

Forschungsbericht 2013-20

Noise Prediction within Conceptual Aircraft Design

Eberhard-Lothar Bertsch

Deutsches Zentrum für Luft- und Raumfahrt
Institut für Aerodynamik und Strömungstechnik
Braunschweig



DLR

**Deutsches Zentrum
für Luft- und Raumfahrt e.V.**
in der Helmholtz-Gemeinschaft

Noise Prediction within Conceptual Aircraft Design

Eberhard-Lothar Bertsch

Institute of Aerodynamics and Flow
Technology
Braunschweig

165 Pages
95 Figures
52 Tables
128 References



DLR

**Deutsches Zentrum
für Luft- und Raumfahrt e.V.**
in der Helmholtz-Gemeinschaft

TU Braunschweig - Campus Forschungsflughafen

Berichte aus der Luft- und Raumfahrttechnik

Forschungsbericht 2013-05

**Noise Prediction within Conceptual
Aircraft Design**

Eberhard-Lothar Bertsch

Deutsches Zentrum für Luft- und Raumfahrt
Institut für Aerodynamik und Strömungstechnik
Braunschweig

Diese Veröffentlichung wird gleichzeitig in der Berichtsreihe „Campus Forschungsflughafen - Forschungsberichte“ geführt.

Diese Arbeit erscheint gleichzeitig als von der Fakultät für Maschinenbau der Technischen Universität Carolo-Wilhelmina zu Braunschweig zur Erlangung des akademischen Grades eines Doktor-Ingenieurs genehmigte Dissertation.

Noise Prediction within Conceptual Aircraft Design

Von der Fakultät für Maschinenbau
der Technischen Universität Carolo-Wilhelmina zu Braunschweig

zur Erlangung der Würde
eines Doktor-Ingenieurs (Dr.-Ing.)
genehmigte Dissertation

von
Dipl.-Ing. Eberhard-Lothar Bertsch, M.Sc.
aus Stuttgart

Eingereicht am: 06.12.2012

Mündliche Prüfung am: 13.08.2013

Berichterstatter: Prof. Dr.-Ing. Jan Delfs
Prof. Dr.-Ing. Peter Horst

Vorsitzender: Prof. Dr.-Ing. Rolf Radespiel

Eidesstattliche Erklärung

Hiermit versichere ich an Eides statt, dass ich die vorliegende Arbeit selbstständig angefertigt habe. Alle benutzten Hilfsmittel sind angegeben. Diese Arbeit ist bisher weder veröffentlicht noch an einer anderen Hochschule eingereicht worden.

Aus Aktualitätsgründen wurden Auszüge der vorliegenden Arbeit in wissenschaftlichen Artikeln vorveröffentlicht [40–44, 84, 94, 104, 112, 123–126].

Göttingen, im Dezember 2012

(Unterschrift)

Eberhard-Lothar Bertsch

Abstract

Motivation for the presented activities is the integration of noise as an additional objective in conceptual aircraft design. Therefore, the Parametric Aircraft Noise Analysis Module (PANAM) is developed to account for individual noise sources depending on their geometry and operating conditions. Each major noise source is modeled with an individual semi-empirical noise source model. These models capture the major relevant correlations, can still be executed on a standard desktop PC, and provide comprehensive simulation results. All models and approximations are based on physics, thus PANAM can be classified as a scientific prediction method. Dedicated validation with experimental data confirms feasible overall aircraft noise prediction. The noise tool is integrated into an existing aircraft design framework in order to realize an overall design process with integrated noise prediction capabilities. A multiple criteria design evaluation is introduced, to quickly assess the environmental and economical performance of different vehicles under various scenarios. The process is applied to identify promising low-noise aircraft concepts with the focus on realizable, medium term solutions. It is demonstrated, that the aircraft designer's influence on the environmental vehicle performance is significant at the conceptual design phase. Extensive engine noise shielding is achieved for over-the-fuselage mounted engines resulting in a 10 EPNdB overall noise reduction. In conclusion, PANAM can be ranked as well suitable to assess all four measures of ICAO's balanced approach.

Keywords: Aircraft noise prediction, low-noise aircraft design, parametric and component noise source modeling, engine noise shielding, scientific prediction method, noise abatement procedure design, helical noise abatement procedure, PANAM, PrADO, SHADOW, HeNAP

Zusammenfassung

Die Motivation der Arbeit ist die Einbindung von Lärm als zusätzlichem Entscheidungskriterium innerhalb des Flugzeugvorentwurfs. Daher wird ein Programm PANAM zur Fluglärmvorhersage entwickelt, das den Beitrag ausgewählter Lärmquellen anhand deren Geometrie und Betriebsbedingungen berücksichtigt. Dabei kommen für jede Einzelquelle individuelle und semi-empirische Rechenmodellen zum Einsatz. Die ausgewählten Modelle berücksichtigen die wesentlichen Zusammenhänge, stellen geringe Rechneranforderungen und generieren dabei nachvollziehbare Ergebnisse. PANAM kann als wissenschaftliches Berechnungsverfahren klassifiziert werden, da alle implementierten Modelle und Näherungsverfahren auf physikalischen Grundlagen basieren. Ein direkter Vergleich von Simulationsergebnissen mit experimentellen Daten bekräftigt die Richtigkeit der berechneten Ergebnisse. Durch die Integration von PANAM in eine existierende Flugzeugentwurfsumgebung wird der konventionelle Entwurfsprozess um die Fähigkeit zur Lärmvorhersage erweitert. Eine neu eingeführte Bewertungsmetrik erlaubt den direkten Vergleich von Wirtschaftlichkeit und erzeugtem Fluglärm für unterschiedlichste Flugzeugkonzepte. Der erweiterte Prozess wird schließlich angewendet, um vielversprechende, lärmarme Entwürfe zu identifizieren. Dabei liegt der Schwerpunkt auf mittelfristig realisierbaren Konzepten und Technologien. Es kann gezeigt werden, dass durch Entscheidungen im Flugzeugvorentwurf ein signifikanter Einfluss auf die ökologische Flugleistung des finalen Entwurfes genommen wird. Dabei können durch geeignete Abschattung des Triebwerklärms lokal bis zu 10 EPNdB Lärmreduktion erreicht werden. Allgemein kann PANAM dazu eingesetzt werden, alle von der ICAO als "balanced approach" vorgeschlagenen Maßnahmen zur Lärmreduktion zu untersuchen.

Schlagwörter: Fluglärmvorhersage, lärmarmen Flugzeugentwurf, parametrische und komponentenweise Lärmquellmodellierung, Triebwerkslärmabschattung, wissenschaftliche Vorhersagemethode, lärmarme An- und Abflugverfahren, Spiralanflug, PANAM, PrADO, SHADOW, HeNAP

Danksagung

Diese multidisziplinäre Arbeit ist parallel zu meiner Tätigkeit als wissenschaftlicher Mitarbeiter am DLR Institut für Aerodynamik und Strömungstechnik entstanden. Jegliche multidisziplinäre Aufgabe ist ohne Unterstützung und gute Zusammenarbeit mit den Experten der jeweiligen Disziplinen nicht denkbar. An dieser Stelle möchte ich die tolle Kollegialität hervorheben, die ich institutsübergreifend innerhalb des DLR und von externer Seite erfahren habe.

Besonders bedanken möchte ich mich bei folgenden ausgewiesenen Experten für die gute Zusammenarbeit: Dr. Wolfgang Heinze (Flugzeugentwurf, TU Braunschweig), Dr. Sebastien Guérin und Dr. Werner Dobrzynski (Lärmquellmodellierung, DLR) und Dr. Markus Lummer (Abschattungseffekte, DLR). Weiterhin danke ich Dr. Ullrich Isermann und Dr. Rainer Schmid (Fluglärmvorhersage, DLR), Dr. Gertjan Looye (Flugmechanik, DLR) und Tom Otten (Triebwerksmodellierung, DLR) für ihre Unterstützung.

Vielen Dank für stets offene Türen und für viele Diskussionen und Anregungen.

Ich bedanke mich bei Prof. Jan Delfs (DLR) für die sehr gute Betreuung dieser Arbeit. Insbesondere bedanke ich mich für viele interessante Diskussionen und Treffen trotz seines prall gefüllten Terminkalenders! Ich habe mich sehr gefreut, Prof. Peter Horst als zweiten Berichterstatter und Prof. Rolf Radespiel als Vorsitzenden zu gewinnen (beide TU Braunschweig) und bedanke mich bei beiden dafür.

Schließlich möchte ich mich an dieser Stelle noch herzlich für den positiven Zuspruch und den Rückhalt durch meine Eltern und Geschwister, sowie im Freundeskreis bedanken.

Contents

1	Introduction	1
1.1	Background	1
1.2	Motivation	3
2	Related Work & Literature Overview	5
2.1	Overall Aircraft Noise Prediction	5
2.2	Aircraft Noise Reduction Concepts	10
3	Methods, Tools, and overall Process	13
3.1	Requirements	13
3.2	Overall Aircraft Noise Prediction Tool	14
3.2.1	Concept	15
3.2.2	Noise Source Modeling	18
3.2.3	Tool Input	42
3.2.4	Modi operandi	44
3.2.5	Tool Output	44
3.3	Aircraft Design with Integrated Noise Prediction Capabilities	46
4	Validation	49
4.1	Conceptual Design vs. Aircraft Data and Specifications	49
4.2	Flight Simulation vs. Recorded Flight Data	50
4.3	Noise Prediction vs. Textbook Theory	51
4.4	Noise Prediction vs. Measurements	59
4.4.1	A319 Flyover Campaign	59
4.4.2	Additional comparison	64
5	Application	67
5.1	Low-Noise Vehicle Design	67
5.1.1	Reference Vehicle and Design Mission	68
5.1.2	Evaluation Metric	70
5.1.3	Solution Space Limitations	73

5.1.4	Vehicle Variants	74
5.1.5	Alternative Propulsion Technologies	83
5.2	Decision Making Support	89
5.2.1	Noise Abatement Flight Procedures	89
5.2.2	Airspace and Airtraffic Management	91
6	Results and Discussion	93
7	Conclusions	97
A	Figures, Tables, and Derivations	107
A.1	Weighting, Sound Propagation, and Ground Effects	107
A.2	Textbook Theory	108
A.3	A319 Flyover Campaign	111
A.4	Low-Noise Vehicle Design	125
B	Additional Items	157

Glosary & Nomenclature

Abbreviations

ACARE	Advisory Council for Aeronautics Research in Europe
ANoPP	Aircraft Noise Prediction Program, NASA
ATA	Air Transport Association
CDA	Continuous Descent Approach
CROR	Counter-Rotating-Open-Rotor
EMPA	Federal Laboratories for Materials Testing and Research, Switzerland
EPNL	Effective Perceived Noise Level
FAA	Federal Aviation Administration
FLULA	Noise prediction tool by EMPA
FW-H	Ffowcs-Williams and Hawkings (equation, surface)
FMP	Fast-Multipole Code, DLR
GTF	Geared Turbofan Engine
HeNAP	Helical Noise Abatement Procedure
HTP	Horizontal Tail Plane
ICAO	International Civil Aviation Organization
IESTA	Infrastructure for Evaluating Air Transport Systems simulation framework, ONERA
INM	Integrated Noise Model, FAA
IOPANAM	PrADO - PANAM interface module
LEQ	Equivalent Sound Pressure Level
LDEN	Day-Evening-Night Sound Level
LNA	DLR's Low Noise Aircraft concept
MLW	Maximum Landing Weight
MTOW	Maximum Take-off Weight
MZFW	Zero-fuel weight
NPD	Noise-Power-Distance tables
OEW	Operational Empty Weight
PANAM	Parametric Aircraft Noise Analysis Module, DLR
PrADO	Preliminary Aircraft Design and Optimization, TU Braunschweig
SAE	Society of Automotive Engineers
SHADOW	Ray-Tracing tool to evaluate engine noise shielding, DLR
SIMUL	Noise prediction tool by DLR
SIMMOD	Fast time airport capacity analysis tool, FAA
SOPRANO	Silencer Common Platform for Aircraft Noise Calculations, ANOTEC
SPL, SPL(A)	Sound Pressure Level, A-weighted SPL
TAS	True Air Speed
TLAR	Top Level Aircraft Requirements

TIVA	Simulation environment, DLR
VTP	Vertical Tail Plane

Scripting

0, ①	Freestream conditions (engine station numbering), characteristic level
2, ②	Fan front face
9, ⑨	Primary exhaust nozzle throat, far-field conditions
13, ⑬	Secondary flow: fan exit plane
19, ⑲	Secondary exhaust nozzle throat, far-field conditions
21, ⑳	Primary flow: fan exit plane
∞	Ambient conditions
a	Airfoil, Axles on selected landing gear
a/c	Aircraft, aircraft fixed
bbn	Broadband noise
c-jet	Coaxial, shock-free jets
con	Convective
ctn	Combination-tone noise
dir	Directivity adjustment
dtn	Discrete-tone noise
e	Emission
eq	Equivalent
ex	Fan exhaust engine station
exp	Experimental data
f	Flap element
fg	Front landing gear
g	Earth-fixed coordinate system, landing gear
geo	Geometry adjustment
i	Impact, immission, scenario
in	Fan inlet engine station
is	Isentropic
ISA	Levels at sea level (0 m) according to the International Standard Atmosphere (ISA)
jet	Isolated, shock-free jet
l	Lift
lam	Laminar
m	Mean value
mg	Main landing gear
norm	Reference normal level (base level)
p	Coaxial jet: primary flow
r	Rotor
ref	Reference value
recX	Flight test no. X, Parchim Campaign (see Tab. A.7)
s	Coaxial jet: secondary flow, slat element, stator
spec	Spectral shape adjustment
t	Total, overall
TE	Trailing edge
vel	Velocity dependent adjustment

Symbols

$\langle a^2 \rangle$	Root-mean-square value (RMS), time average
\tilde{A}	Time average level
\vec{a}^b	Unit vector a in coordinate system b
\vec{A}^b	Vector A in coordinate system b
A_c^b	Component c of vector A in coordinate system b

Variables

A	Area, reference area	m^2
α	Angle of attack	$^\circ$
α^*	Polar noise emission angle	$^\circ$
β	Bank angle	$^\circ$
β^*	Longitudinal noise emission angle	$^\circ$
c	Mean chordlength, speed of sound, correction, local coefficient	$m, m/s, dB, -$
C	Overall vehicle coefficient, empirical constant	$-, -$
d	Relative distance between aircraft and observer: $d = \vec{D}^{a/c} $	m
D	(Hydraulic) diameter, distance	m, m
δ	Boundary layer thickness, cut-off condition, deployment angle, extraction factor	$^\circ, -, m, -$
Δ	Level difference, time difference	dB, s
δ^*	Boundary layer displacement thickness	m
η	Efficiency	$-$
f	Frequency	Hz
$f(x)$	Function of "x"	$-$
γ	Flight path angle, installation angle	$^\circ, ^\circ$
i	Acoustic intensity per noise source volume; normal to trailing edge	W/m^5
I	Acoustic intensity normal to trailing edge	W/m^2
I_{ref}	Reference value of acoustic intensity, $I_{ref} = 10^{-12}$	W/m^2
l	Length	m
L	Sound pressure level (SPL)	dB
Λ	Aspect ratio	$-$
Ma	Mach number	$-$
μ	Observer location	$-$
n	Number of elements	$-$
ν	Dihedral angle, kinematic viscosity	$^\circ, m^2/s$
O	Observer location	m
P	Aircraft location	m
p	Pressure signal	Pa
Π	Total pressure ratio	$-$

Ψ	Sweep angle	°
ρ	Flow density	kg/m^3
rss	Rotor-stator-spacing	m
Str	Strouhal number	-
t	Event time	s
T	Thrust force	N
u	Velocity scale for the turbulence	m/s
v	Velocity (True Air Speed)	m/s
V	Volume	m^3
φ	Aircraft flight position	-
w	Element width, density exponent (hot jet)	m, -
W	Weight force	N
x	Length	m
y	Wall distance of the maximum turbulent kinetic energy	m

Vehicle Design Nomenclature

v	Vehicle variants
V	Final vehicle design

Subscripts

r	Design category: Reference vehicle
0	Design category: Over-the-wing installed engines
1, 1-1, 1-2	Design category: Rear fuselage mounted engines
2	Design category: Over-the-fuselage mounted engines
x	Design category: Wing/empennage integration with covered engines
g	Alternative propulsion: GTF
c	Alternative propulsion: CROR

Multiple criteria design evaluation

κ_i	Predefined (user selected) environmental weighting, applicable to ξ_i
K	Scenario dependent overall environmental weighting, applicable to ξ
λ_i	Predefined (user selected) economical weighting, applicable to ζ_i
Λ	Scenario dependent overall economical weighting, applicable to ζ
σ	Overall scenario score: Environmental and economical performance
ξ_i	Environmental performance indicator (vehicle specific)
ξ	Overall environmental performance indicator (vehicle specific)
ζ_i	Economical performance indicator (vehicle specific)
ζ	Overall economical performance indicator (vehicle specific)

1 Introduction

1.1 Background

According to the *Advisory Council for Aeronautics Research in Europe* (ACARE), the worldwide growth of air traffic over the last 50 years will continue in the future [1]. The demand for air transportation is expected to rise with increasing population density, especially in growing markets; e.g., India and China. Consequently, the percentage of world population subject to aircraft noise is expected to grow significantly. High airspace traffic density, additional runways and airports ultimately require new air traffic routing of approaching and departing aircraft. This means, installation of new routes or displacement of existing flight corridors will affect additional communities. This significant increase in aviation noise pollution can be directly associated with unfavorable effects on people's health and with negative economical effects for individuals as well as for aircraft and airport operators.

According to Smith [16], aircraft can be assigned to the most dominating noise sources of our times. Sound pressure levels close to a jet aircraft engine under take-off conditions can reach the human threshold of pain with respect to noise [76]. Aircraft ground noise levels comparable to a heavy truck passing by, i.e. noise levels in the order of 70 – 80 dBA, can still be measured at large distances up to 20 kilometers from the airport location¹. As a consequence, communities far beyond the direct vicinity of an airport can still be subject to significant aircraft noise perception.

Residents living in close proximity to airports have established numerous consortiums and dedicated citizen's initiatives against aircraft noise pollution in the past. Nearly all communities located in the neighborhood of a German airport are engaged in one of these initiatives in order to fight aircraft noise pollution and the associated negative implications on personal health and local economy. Independent scientific studies directly correlate aircraft ground noise levels in Germany with community annoyance and, more so, with adverse effects on the health of exposed individuals [2]. As identified in various extensive research activities, the communities in close proximity to major airports are subject to increased noise annoyance, occurrences of sleep interruptions, and even cardiovascular diseases [3,4]. Obviously, there is no direct correlation of medical implications into monetary values available, thus it is extremely difficult to assess a feasible economical impact.

In general, no direct local economical impact of aviation noise pollution can be identified. Yet, there are initial studies with respect to real estate values in aviation noise affected communities. A dedicated study correlates real estate value with aviation noise levels for the Rhein-Main-Area according to realtors and monetary institutions [5]. A negative impact of

¹e.g. Frankfurt airport noise monitoring system, <http://franom.fraport.de/franom.php> (accessed 08 January 2012)

high aviation noise levels on real estate values and corresponding economical implications is predicted. In 2010 the German Federal Constitutional Court (Bundesverfassungsgericht) strengthened the legal rights of private property owners against traffic noise exposure. In the event of unacceptable noise exposure they are entitled to increased financial compensation².

According to the German Aviation Noise Protection Law (Fluglärmschutzgesetz), airport operators are required to identify and label areas subject to long-term elevated noise levels. These areas are declared as noise protection zones where affected private homes are entitled to passive noise protection measures on the expense of the airport operator.



Figure 1.1: Ten thousands of people demonstrate in 2011 against Berlin's new international airport BBI³

As a consequence, noise related modifications to the airspace layout and management can have significant economical impact on both aircraft and airport operator.

The airport operator's noise related costs are directly passed on to the airlines in an effort to internalize noise related costs. Most airports have individual noise related landing fees of small to negligible amounts, thus only limited internalization. Some airports have based their noise charges according to actually generated and measured ground noise levels of individual aircraft, e.g. Airport Zurich Kloten⁴. It can

be expected that the situation will change in the future, thus noise related fees could comprise a significant share of the aircraft's direct operating costs.

In addition to an increasing public awareness, significant transnational political attention and intervention to fight aircraft noise pollution has been experienced over the last decade. Extremely ambitious targets, e.g. halving the perceived noise levels of single aircraft movements by 2020 [1], are proclaimed to provide the necessary incentives and establish favorable conditions for new noise-reducing technology. The growing political pressure on aircraft manufacturers and operators is expected to increase noise-regulatory measures and regulations. Under these circumstances advanced technologies will have good chances to be introduced on the market.

According to the International Civil Aviation Organization (ICAO), a so-called *balanced* approach [6] has to be pursued to effectively fight aircraft noise pollution. This approach is comprised of four measures to reduced perceived aircraft noise levels on the ground.

The most obvious measure is (1) *modifications to the noise source*. Application of advanced low-noise technology on-board of an aircraft will reduce overall noise emission for this vehicle. Obviously, such a new low-noise technology would require significant market penetration in order to show any overall effect at all. The second measure is (2) *sophisticated land-use planning and traffic routing* around airports to minimize the number of communities exposed to aviation noise. Land-use management around existing airports is dominated

²Bundesverfassungsgericht 1 BvR 2736/08, 2010

³ddp images/dapd/Klaus-Dietmar Gabbert

⁴Zurich airport's noise monitoring system currently comprises ten noise measurement sites according to the airport website (www.zurich-airport.com, accessed January 2010)

by economical interests and aircraft noise pollution will have only very limited influence. Yet, aircraft noise significantly influences land-use management when planning additional runways at existing airports or investigating locations for new airports. Most major airports reroute their approaching and departing air traffic according to the surrounding population density. Traffic is detoured via selected low-populated areas instead of using the shortest available and most economic route to the airport. The third approach to reduce aircraft noise is (3) *the installation of operational constraints* at a specific airport. These constraints, e.g. night curfews, can limit the overall number of flight operations or reduce overall operating hours of the selected airport. Furthermore, constraints and quota regulations will have an impact on flight schedule and fleet mix at the airport, e.g. noisy aircraft types can be banned from operation in order to reduce surrounding ground noise pollution. A very general and effective approach to reduce overall ground noise levels are (4) *noise abatement flight procedures*. Noise abatement procedures are approach or departure flights that along which the aircraft can be operated with reduced ground noise impact or with favorable noise dislocation effects. Any aircraft with current engine and airframe technology providing the required navigational and flight performance can operate along such a procedure. Implementing new low-noise flight procedures at an airport could immediately reduce community noise levels.

In addition to ICAO's *balanced* approach, modifications to the receiver/observer instantly decrease perceived noise levels for each fly-over event. For example, sound proof windows can be counted toward these so-called passive protection measures.

1.2 Motivation

The focus of the presented work lies on the aircraft designer's influence on overall aircraft noise reduction, e.g. advanced on-board technology and new low-noise vehicles. The full potential of low-noise vehicle design can only be exploited if underlying discipline interdependencies, e.g. modifications to the noise source versus flight performance, are identified and simultaneously accounted for in a so called *concurrent approach* [7]. Maximum noise reduction from the aircraft designer's perspective can only be achieved through a combination of low-noise technology and dedicated overall aircraft design to enable low-noise flight performance.

In the context of overall aircraft design, major interactions of involved engineering disciplines have to be accounted for early within the decision making process. Early within this process, e.g. at the conceptual aircraft design stage, major aircraft and engine design parameters are still subject to change. At this point the dominating design parameters, e.g. wing span, are determined by underlying mission requirements which drive the final aircraft concept. There are only few parameter limitations at the conceptual design stage resulting in an extensive solution space. Low-noise technology needs to be investigated at that design level in order to identify and incorporate resultant and necessary modifications to the overall aircraft and engine layout. Moreover, negative or adverse effects of selected low-noise technology and systems on correlated disciplines can be identified and counteracted. Depending on available noise prediction capabilities, the setting of basic design parameters can be optimized for best economical and acoustical performance according to the selected *Top Level Aircraft Requirements* (TLAR). The identification of such an optimal parameter setting completes the conceptual aircraft design phase that dominates the final

vehicle layout. Major modifications to the basic vehicle layout are ruled out in subsequent and more detailed design stages due to a large number of fixed design parameters and defined constraints. Ultimately, sophisticated noise prediction capabilities at early vehicle design stages are fundamental when it comes to overall aircraft noise reduction.

Despite obvious advantages of noise analysis in conceptual aircraft design, noise evaluation is usually not accounted for in that early design stage due to the lack of appropriate noise prediction methods. Parametric and componential prediction methods are required in order to account for the impact of geometry modifications and operating conditions on both component and overall aircraft noise emission. Such methods would allow to monitor individual noise sources throughout simulated flight operation thus noise related effects could be identified and analyzed. The quantity and complexity of required input parameters for the noise prediction have to be adequate for conceptual design hence impose further requests on a suitable noise prediction methodology. A modular and simple implementation of the method is required to allow for direct integration into existing multidisciplinary conceptual aircraft design codes. High fidelity prediction methods such as Computational Aeroacoustics or time-accurate Computational Fluid Dynamics are ruled out due to their CPU requirements which are not compatible with an iterative conceptual design process. Therefore, fast prediction methods are required to finally determine the level and directivity of the aircraft noise emission according to conceptual aircraft and engine design, configuration, and operating conditions.

In conclusion, the main objective of the presented work is to establish a conceptual aircraft design process with integrated noise prediction capabilities. Thereby it is inevitable to account for both vehicle design and operating condition in order to address noise in the context of the overall aircraft system. A direct process implementation results in noise as a new constraint in the overall design process. This could enable a fully automated low-noise aircraft design optimization. Each new vehicle concept can then simultaneously be evaluated for its resulting economical and environmental performance. Different vehicle concepts out of an available solution space can directly be compared with each other to obtain the most promising solution under preselected requirements. Ultimately, promising design drivers and sensitivities toward economically efficient overall noise reduction can be identified from an aircraft designer's point of view. These findings can be correlated to the modeled physical effects within the simulation, thus can directly be assigned to their cause. Obviously, adequate simulation of the underlying multidisciplinary interdependencies becomes crucial in order to evaluate promising technologies and their impact on the overall system.

2 Related Work & Literature Overview

In this chapter, an overview of related work in the context of aircraft noise prediction and low-noise design is presented. In order to assess the environmental impact of an overall aircraft system, a fast and robust noise prediction software is required [9]. Several tools are available that meet this general requirement. Each of these tools can be assigned to a certain development background and to specific applications in the context of overall aircraft noise prediction. Based on these inherent simulation characteristics, a general classification for noise prediction tools is introduced. In accordance to the new classification, a brief overview of the most important available tools is presented.

Furthermore, a literature overview of existing aircraft noise reduction concepts is presented, including low-noise design modifications and operational concepts. Promising suggestions are discussed and selected for further investigation within this work. Based on these suggestions, an initial solution space for promising low-noise technology can be derived.

2.1 Overall Aircraft Noise Prediction

Existing fast overall aircraft noise prediction tools can be separated into three main categories, referred to as *best practice*, *hybrid*, and *scientific* prediction methodologies.

Best-practice prediction methodology

Tools assigned to the best-practice methods are based on (fully) empirical models derived from ground noise measurements of a specific aircraft. The measured noise immission is corrected by simulated propagation effects in order to determine the originating emission noise level of this aircraft. The underlying noise level database and the applied methods are verified and standardized, as described in corresponding literature [10–12]. The noise source modeling is inherently reduced to one overall noise source for the entire aircraft, i.e. mainly engine noise contribution. As a result, alternating dominance of airframe and engine noise contribution during realistic (approach) flight procedures, precisely the complex schedule of configurational changes along typical flight procedures, can not be accounted for. Consequently, the application of these tools should be limited to the simulation of (take-off) procedures with dominating engine noise contribution. Modeling of the overall aircraft noise is significantly simplified caused by the mixing of noise generation and propagation effects. Defined corrections are applied to the underlying data in order to simulate the influence of flight velocity and/or thrust on noise levels, i.e. under varying operational conditions. Some tools use simple methods to account for directivity effects, others incorporate noise directivity within their underlying data bases.

Initially, the application of a best-practice tool is limited to the existing vehicles and tech-

nology stored in the underlying database. In order to evaluate new technology, the original database can be modified with available data representing the new vehicle, i.e. referred to as substitution.

Best-practice tools are usually developed for the evaluation of medium to long term average noise levels around airports rather than for prediction of single flyover events [14]. Best agreement to experimental data can be achieved if multiple flyover events and airspace scenarios are evaluated. Results can be accurate to approximately ± 1 to ± 2 dB [13, 15] for observers located along the flight ground track with the aircraft operating in lower altitudes. Although, if predicting long-term average noise contours, even these small variations have an impact, i.e. a 20% deviation in predicted isocontour areas per 1 dB [16]. Result accuracy can be significantly reduced for observers located off-side the flight ground track, for shallow angles of incidence, and with increasing distance between aircraft and observer location [15].

Due to their prediction accuracy for longterm scenarios, best-practice tools qualify for application in air traffic management and legislation processes. The focus of applications lies on noise protection zones, land-use planing, and consulting. Potential users are found at airports, airlines, and in legislation. Often, such tools have a commercial or corporate background in order to compensate the high development costs.

The most prominent example for this kind of tool is the Integrated Noise Model (INM) by the Federal Aviation Administration [17]. INM is applied by researchers, airport planners, and authorities world-wide to evaluate the impact of airspace management on community noise impact. With INM, the impact of modifications to flight path, runway / airport layout, and fleet mix on overall ground noise can be accounted for. In this context, INM can for example output maximum or time-integrated noise levels and corresponding isocontour areas.

INM uses Noise-Power-Distance (NPD) tables based on aircraft noise certification data to predict ground noise immission. The NPD data has been normalized to specified, straight horizontal flight segments with constant operational and configurational setting. To predict ground noise immission along a selected flight path, the corresponding trajectory is assembled from these straight flight segments. To account for curved flight segments, specific modifications are applied to the noise data.

At Delft University of Technology INM has been implemented into their trajectory optimization process to study environmental friendly departure procedures for a selected airport scenario [18]. Conventional departure trajectories have been optimized for minimal community noise impact by integrating a geographic information system into the process.

A second example for this group of noise prediction tools is FLULA [19] by the Swiss Federal Laboratories for Materials Testing and Research, EMPA. The noise prediction is based on dedicated aircraft noise measurements recorded along individual flyover events with an array of microphones. Polynomial functions are derived from measured spectral noise levels and directivity patterns for best fitting of experimental data and predictions. Rotational symmetry in noise directivity is assumed hence the polynomials are functions of the polar angle and the distance between aircraft and observer only. Corresponding coefficients are identified and derived from the measurements for each individual aircraft type. To incorporate the influence of aircraft speed, further modifications are applied to the polynomial. Finally, relevant sound propagation effects are accounted for.

Hybrid prediction methodology

In contrast to the best-practice methods, hybrid prediction models separate the overall aircraft noise into its major contributions. Instead of approximating the aircraft as one single noise source, a number of individual noise contributions is accounted for. This componential modeling can be limited to a separation into airframe and engine noise, or be further subdivided into individual components such as high-lift system noise. The noise emission of each noise source is modeled according to an individual database, e.g. derived from flyover noise measurements (array), componential wind-tunnel experiments, and computational findings. Based on this data, physics-based approximations are derived in order to account for specific operational conditions, e.g. flight speed and thrust setting. As a consequence, hybrid prediction models enable to investigate low-noise flight procedures, especially approach procedures with varying configurational setting. Low-noise modifications to individual noise sources can be accounted for by manipulating the corresponding component's data base. Yet, parameter variations with respect to aircraft or engine design are not possible due to the fact that noise source modeling is based on stored and preprocessed data.

As a conclusion, the data-based noise source modeling results in fast computation times and a good agreement of prediction and measurements.

An example for hybrid prediction methods has been developed at DLR, the tool SIMUL [20]. Several flight tests have been performed to identify dominating noise sources and their directivity corresponding to current speed, thrust, and configurational settings [21]. This extensive database allowed to further break down overall aircraft noise into contributions of airframe, jet, and fan. This separation is inevitable for a reasonable overall noise prediction along arbitrary flight procedures, especially for approaching vehicles. Consequently, SIMUL enables a realistic simulation and even optimization of approach and departure procedures accounting for complex configurational changes [22]. A general application of SIMUL is currently limited by the aircraft models available in the data base.

Scientific prediction methodology

Tools that can be assigned to this category are based on a semi-empirical and componential noise prediction, i.e. somewhat similar to the hybrid models. Yet, scientific noise prediction is furthermore characterized by a parametric modeling of each individual noise source. Such a parametric source definition allows to account for the impact of operational settings, i.e. similar to a hybrid model, and moreover to incorporate the impact of airframe/engine geometry modifications on noise generation. Ultimately, the overall aircraft noise is assembled from all these individual noise sources and then propagated to the ground.

Obviously, to identify design trends and run noise sensitivity studies, a scientific prediction methodology is inevitable. As a consequence, other prediction models can be excluded from application within this work. Limitation of the prediction capabilities to existing aircraft technology and fixed aircraft/engine geometries would be in direct contrast to the anticipated comparative low-noise evaluation. The key characteristics of scientific noise prediction, namely semi-empirical, componential, and parametric, are inevitable in order to expand prediction capabilities beyond existing aircraft and radical flight procedures.

Definition of the componential noise source models requires dedicated noise measure-

ments and is characterized by increased scientific complexity. As a consequence, these parametric tools are more likely to be found in state-subsidized environments such as research institutions and universities.

Compared to the best-practice tools, scientific tools represent a good compromise between result accuracy and flexibility toward design modifications. The scientific prediction models enable evaluation of new aircraft/engine concepts, simulate arbitrary flyover scenarios, and still reflect the basic underlying physical effects. Noise sensitivity studies within the aircraft design phase are enabled and promising design trends can quickly be identified.

The most prominent example of this group of tools is the Aircraft Noise Prediction Program (ANoPP) developed at NASA [23]. Initially, the tool was developed to predict noise for single flyover events. Airframe noise components within ANoPP are modeled with Fink's approach [24], whereas engine noise is approximated with the methods of Stone [25] for jet noise and Heidmann [26] for fan noise. To enhance fan noise prediction capabilities to modern high bypass engines, empirical coefficients within Heidmann's original model have been modified. In 2008, two dedicated studies [27, 28] to assess NASA's current jet and fan noise prediction capabilities have been published. It was demonstrated that ANoPP's current methods for jet and fan noise prediction result in reasonably good overall agreement with the experimental data. Optionally, additional engine noise sources can be accounted for such as turbine and core noise. The code is continuously updated and new noise source models are implemented.

ANoPP was embedded within a low-noise aircraft design framework established at Stanford University. The main objective has been to evaluate the feasibility of such a process accounting for the overall environmental impact. Required aircraft design parameters for the noise prediction with ANOPP are provided by the design modules. Certification noise levels are used as an acoustic constraint within the low-noise design process. The initial application of their process was presented in 2004 [29].

Furthermore, ANOPP has been applied in a joint effort of NASA and Georgia Tech. The overall goal was to evaluate the interaction of multiple engineering disciplines at earlier stages in the aircraft design process. A so-called *concurrent approach* including ground noise impact has been established in 2006 [7]. Again, certification noise levels have been used as new design constraints within their process. The focus of the work has been on the overall process and the optimization approach rather than on the noise prediction itself. An extensive number of aircraft and engine design variations has been studied to generate response surface equations for quick overall technology assessment.

NASA announced the release of a new version referred to as ANoPP 2.0 beta for the end of 2011 [30]. The new ANoPP is set up as a framework in order to implement higher fidelity acoustic tools in the overall noise prediction process [31]. According to the selected task, available tools of different fidelity can be arranged into individual processes. The main task for ANoPP 2.0 is to enable a noise prediction process outside the semi-empirical experience base by applying first principles and multi fidelity approaches [31]. Default methods for engine and airframe noise prediction are based on the older AnOPP. Optionally, these basic methods can then be replaced with available tools and methods of similar or higher fidelity. For example, a recent airframe prediction method by Boeing is available [31]. Initial comparison of this up-to-date method with Fink's approach results in significantly different noise levels and level-time histories¹; especially different results are predicted for landing

¹Fig.12 and 13 of Ref. [31]

gear, flap, and slat whereas trailing edge noise remains the same.

In order to enable compatibility and communication among all of the available NASA tools, specific interfaces for tool data I/O are defined. According to the fidelity of a selected tool, the data surfaces only store acoustic pressure data (low fidelity) or are comprised of both pressure and velocity data (high fidelity). Data surfaces containing pressure and velocity data are referred to as *nested Ffowcs Williams and Hawkings surfaces* (FW-H). A FW-H surface completely defines all noise sources within the surface with respect to an outside observer [31]. FW-H surfaces can contain individual or multiple noise sources, e.g. the overall aircraft. Noise sources can be located at their true locations in order to account for interaction effects. FW-H surfaces enable common data exchange for tools of different fidelity in order to make each tool's result directly accessible within the overall process. Finally, the overall noise level is evaluated by assembling the individual results with respect to sound propagation effects.

A second tool example is the European tool SOPRANO (Silencer Common Platform for Aircraft Noise calculations). The tool has been developed within the European aircraft noise research program called *SILENCE(R)*. ANOTEC consulting developed the tool to provide "a common software platform to assess noise reduction techniques within European projects"; cited from Ref. [32]. The 2007 version models several airframe and engine noise components. The airframe noise is currently modeled with Fink's approach [24] as well. Major engine noise components are modeled with the SAE methods, Stone's method [25] (jet noise), and Heidmann's model [26] (fan noise). Furthermore, core and turbine noise are accounted for with models found in the literature. Preprocessed or measured source noise data stored in tables is also accepted. Relevant propagation and installation effects are modeled with public domain approaches. The framework is set up to enable future addition of new models. SOPRANO allows the evaluation of individual sources or sum of several components in order to study noise generating effects. The main focus lies on the noise prediction for single flyover events at multiple observer locations. Direct implementation of the code within an aero engine design process was realized 2010 with the TERA2020 (Techno-economic, Environmental and Risk Assessment for 2020) software, a multidisciplinary optimization tool developed by a consortium of university partners, e.g. Cranfield University [33].

The third example is ONERA's IESTA (Infrastructure for Evaluating Air Transport Systems) simulation framework [34, 35]. IESTA was specifically developed with the focus on multiple flyover events and the modeling of current and future air traffic with respect to the environmental impact. Future air traffic is comprised of new vehicles and advanced operational procedures hence requires more physics-based models. The models for engine noise as implemented in IESTA are similar to the before mentioned methods, i.e. models for jet and fan noise. Predictions by the embedded engine noise models were compared with dedicated experimental data providing reasonably good agreement. Implemented airframe noise sources are modeled according to Fink [24], except of the slat noise which is simulated with Dobrzynski's approach [36]. For the study of advanced new vehicle designs, airframe noise shielding and interaction effects have to be considered. Therefore, these effects are directly incorporated via an ONERA ray tracing method. Overall, IESTA was mainly developed for integration into more complex simulation environments in order to evaluate the overall air transport system.

Other prediction methodologies

It can be expected, that major aircraft manufacturers run their own confidential noise prediction tools. Due to the lack of information, these tools can not be allocated into one specific group. Most likely, the tools are based on each manufacturer's extensive available data base and customized for each specific aircraft and engine type under consideration. Furthermore, the tools are probably still parametric to some extend in order to account for configurational and operational noise generating effects.

2.2 Aircraft Noise Reduction Concepts

In order to achieve relevant aircraft noise reduction, more or less radical solutions have been proposed by various researchers. In the context of the presented work, the focus lies on more realistic, medium term solutions with respect to both aircraft design and operation. Futuristic vehicle concepts such as blended wing bodies with embedded or distributed propulsion will not be in the scope of this work. Dobrzynski has identified feasible approaches and realistic achievements with respect to overall aircraft noise reduction. Based on the experience and knowledge obtained in various DLR research activities over the last decades [22, 36, 59, 61, 100], both operational and vehicle design guidelines have been proposed and published by Dobrzynski in 2007 [62]. Furthermore, earlier DLR low-noise vehicle concepts [37, 38] are revisited in order to identify most promising approaches. The presented design modifications and vehicle layouts within this report are based on (or at least influenced by) these basic concepts and ideas.

Proposed operational guidelines [37, 62] include fast and steep climb-out flight segments along departure procedures. Increasing the flight altitude from d_{ref} to d_{new} would result in an overall noise reduction of $\Delta L = -20 \cdot \log_{10}(d_{new}/d_{ref})$, e.g. doubling the distance could result in a theoretical noise reduction of 6 dB. This applies to any type of sound source, i.e. engine as well as airframe. Low-noise approach procedures are comprised of steep descents with preferably very low flight speeds. Increasing the flight altitude and reducing the flight speed from v_{ref} to v_{new} along the approach would result in an additional airframe noise reduction of $\Delta L = 55 \cdot \log_{10}(v_{new}/v_{ref})$. Low flight velocities could require higher angles of attack which has been found to have only negligible impact on airframe noise generation. The operation of high lift elements should be reduced to a minimum. If required, the deployment and operation of the high lift system should be delayed as long as possible along the approach path. The same guideline can be applied to the most dominating airframe noise source, the landing gear. Obviously, the operation should be reduced to a minimum with late gear extraction along approach procedures and instant gear retraction after take-off. Furthermore, the landing gear should not be used to intentionally increase aircraft drag thus decelerate the aircraft along (steep) approaches [62].

Design Principles are suggested to minimize noise generation and emission from dominating sources [37, 62]. The most dominant individual noise source is the aircraft engine, thus optimization of engine design and operation is very effective. Major parameters with respect to noise generation are jet exhaust velocities, fan (tip) flow conditions, and geometrical details, e.g. lean, sweep, and spacing of fan rotor and stator blades. For a constant thrust, the noise levels of turbofan or jet engines decrease with a reduced exhaust velocity v_{new} by $\Delta L = 60 \cdot \log_{10}(v_{new}/v_{ref})$ with respect to the reference velocity v_{ref} . All modern

turbofan engines come with large bypass ratios, thus already have significantly reduced jet exhaust velocities compared to early designs [16, 39]. Even larger bypass ratios can be achieved by geared turbofan engine concepts. In addition to decreased jet velocities, geared engines can operate with reduced fan rotational speeds, thus reduced fan (tip) velocities. As a consequence, a geared engine concept can be beneficial toward both jet and fan noise reduction.

Noise generation due to the fan and the core engine can effectively be reduced by acoustic lining material. If acoustic lining is installed into the engine inlet and the fan exhaust duct, fan and core noise emission will be significantly reduced. Optimization of acoustic lining material and proper installation on the engine is very promising [16].

Integration of the overall engine on-board of the aircraft should be optimized according to potential noise shielding effects. In order to shield forward fan noise emission, the engine inlet duct could be placed above large airframe structures, e.g. wing or control surfaces. A clever over-the-wing engine installation would allow to fully exploit potential shielding effects. If an engine location is selected, unfavorable noise reflection toward the ground has to be avoided. Jet or fan noise might adversely be reflected by adjacent high-lift elements, extracted control surfaces, vertical or horizontal stabilizers. In general, no airframe components should be installed in the wake of preceding lifting surfaces or along the engine exhaust flow in order to avoid interaction noise. Especially direct contact of the engine exhaust jet with structural elements, e.g. jet flow over the wing or flap deflection into the jet, is not desirable due to strong interaction effects. To reduce fan noise generation, an undisturbed, uniform, and axis-symmetric in-flow is desirable. Therefore, curved or bent engine inlet ducts, e.g. semi-buried engines, are rather disadvantageous with respect to fan noise generation.

To decrease the dominating airframe noise source, i.e. the landing gear, its length should be reduced to a minimum. For example, a low-wing configuration with over-the-wing engine installation could allow for a shortened landing gear, thus significantly decreased noise contribution. On-board of a high-wing aircraft, the landing gear should be integrated into the fuselage rather than into the wing in order to minimize the device length. In general, landing gear noise is highly dependent on the local flow velocities at its location. Therefore, the selection of a feasible landing gear location with reduced local flow velocities is most advantageous. Advanced design of upstream bay doors might enable an active deceleration of the local flow velocities at the landing gear, thus reducing noise generation. At the same time, open landing gear bays should be closed in order to avoid additional cavity noise generation. Complex gear kinematics and linkages should be relocated into the landing gear bay. In general, it is more advantageous to equip a landing gear with few large tires instead of more smaller tires, if there are no adverse effects with respect to fuselage integration.

Noise generation through high-lift elements is proportional to a high order of the normal inflow velocity component, thus can be reduced by sweeping the wing. Compared to slotted leading edge devices, droop nose or Kruger flap designs are more advantageous in the context of noise reduction. If slotted devices are required at the leading or trailing edge, deflection angles and gap widths should be kept at a minimum. Especially, multiple slotted trailing edge devices counteract any high-lift system noise reduction. Isolated side edges of any high-lift or control element are subject to significant noise generation, thus should be avoided. If possible, any in-flight breaking devices such as spoilers could be installed at the rear fuselage so that other devices are not affected by wake interactions.

3 Methods, Tools, and overall Process

3.1 Requirements

The main goal of the presented work is to establish a conceptual aircraft design process with integrated noise prediction capabilities. Such a multidisciplinary approach requires specific characteristics and systematic features of both vehicle design and noise prediction methodology. Therefore, in a first step the essential requirements need to be identified and specified.

Key requirement for a feasible noise prediction is a (1) *parametric* and (2) *componential simulation approach*. Depending on the operating conditions and the configurational setting, overall aircraft noise is dominated by different vehicle components that have to be accounted for. Aircraft noise generation can be separated into contribution of the airframe and the engine. Airframe noise is generated by interaction of the vehicle structure with the surrounding turbulent flow field. All structural elements directly exposed to a relative (turbulent) flow velocity cause fluctuating pressure disturbances thus generate noise [16]. Major airframe noise sources can be identified and allocated to individual structural components.

Each of these components has to be modeled individually as well as parametrically in order to account for the influence of operating condition, configurational setting, and component design parameters on the specific component's noise generation. Obviously, the influence and dominance of individual components is varying during flight operation. Only if each dominating noise source is adequately represented and modeled, overall aircraft noise can be sufficiently approximated during the relevant flight segments. The selected noise source models have to be suitable with respect to data complexity and input availability at the conceptual aircraft design phase. Implementation into an overall design code requires autarkic, script-based operation without user interface. Furthermore, low CPU costs are essential to avoid a slow down of the overall process if a large number of designs is to be evaluated.

Multiple disciplines and research areas are involved if vehicle concepts and technologies are to be evaluated for their environmental performance. Within DLR, specialized institutes and departments investigate different aspects of aircraft noise in detail. Consequently, a new overall noise prediction tool needs to act as an integration framework to combine the impact of individual disciplines and technologies in order to access overall vehicle noise. The corresponding in-house capabilities have to be fully exploited and incorporated into the process to ultimately establish a DLR-wide accessible tool for a wide range of applications. Obviously, a flexible and modular tool setup is required to enable interfaces to other existing tools or methods.

An applicable design method has to allow for the automated execution of three essen-

tial tasks: (1) *provide input information* for the noise prediction, e.g. geometry and operating conditions, (2) *operate the noise prediction* from within the overall design process, and (3) *finally collect the acoustic output data* in order to process it within an overall design optimization. Obviously, prerequisite for the integration of noise prediction capabilities is a modular vehicle design framework with an accessible data structure. Furthermore, such a process requires adequate simulation of all underlying multidisciplinary interdependencies, i.e. from individual component design to vehicle flight performance. Only if major physical effects and interactions between vehicle design and noise generation are accounted for, findings of the overall concept evaluation provide reasonable results thus noise related effects can directly be assigned to their underlying cause. In order to generate input data for the noise prediction, it becomes inevitable to simulate airframe and engine components individually and in a parametric mode. Noise generation of individual noise sources can be highly proportional to specific aircraft and engine parameters. Consequently, these parameters require dedicated and detailed modeling in order to ensure sufficient prediction accuracy. Finally, straightforward implementation of recent findings and methods into the design process is a prerequisite in order to investigate future technology and vehicle concepts. Interfaces to other existing tools or methods require a flexible and modular setup of the design tool.

Meeting these basic requirements for both the noise prediction and the design methodology will enable an overall aircraft design process with integrated noise prediction capabilities. Ultimately, such a process will provide comprehensible solutions for the selected assignments based on scientific and physics-based models.

3.2 Overall Aircraft Noise Prediction Tool

The Parametric Aircraft Noise Analysis Module (PANAM [40–44]) is developed to address overall aircraft noise at the conceptual vehicle design stage where available input data is limited in quantity and complexity. PANAM's main assignments are associated with the investigation of new low-noise technology hence a parametric prediction methodology as outlined in section 2.1 was developed. A noise component break-down is applied, i.e. separation of overall aircraft noise into individual noise contributing components, in order to investigate and optimize individual noise sources, to further reduce complexity, and to speed up computational time. This is a simplification of the overall prediction process since interaction between individual sources will not be accounted for. Instead of simulating the overall system, only selected individual components have to be modeled and accounted for by specific semi-empirical and parametrical source models. These models capture major physical effects and correlations, reflect each component's geometry and operational conditions, and most importantly promise a fast noise prediction of satisfying accuracy. Individual sources can be monitored and rank-ordered throughout simulated flight operation. If the dominating noise components are identified and accounted for, it is possible to sufficiently represent the overall aircraft noise by superposition of these components.

To determine overall aircraft noise of an operating vehicle, mechanisms and disciplines from noise generation to ground impact have to simultaneously be accounted for. Aircraft noise generation is determined by the basic vehicle design, the configurational setting, and the operating conditions along the flight path. Prevailing sound propagation effects, noise source movement, distance and orientation relative to the observer, and surrounding ground properties determine the resulting ground noise impact. Corresponding methods developed

by DLR and other research institutions are available and are implemented into PANAM. Hereby, PANAM acts as a framework for detailed expert knowledge and related methods in order to enable overall aircraft noise prediction. Due to the modular setup of the program frame, one is not restricted to the current stage of source description, but can easily integrate recent findings. Additional or updated noise source models reflecting progress in modeling the physics of noise source mechanisms and their parametrical dependencies can straightforwardly be implemented. This feature is inevitable when it comes to identifying and predicting the impact of new technologies on overall aircraft performance and noise pollution.

3.2.1 Concept

PANAM predicts ground noise impact along a simulated flight path of an aircraft according to Fig. 3.1. Definition of aircraft and observer locations in vector notation within an earth-fixed coordinate system [53] allows for the evaluation of arbitrary three-dimensional flight trajectories [40]. The flight trajectory is discretized into single quasi-stationary aircraft positions. For each position φ , the configuration, location, orientation, and operating conditions of the aircraft are assumed to remain constant, i.e. constant input data for the emission prediction during a time increment $\Delta t_e(\varphi) = t_e(\varphi + 1) - t_e(\varphi)$. A sufficiently fine discretization of the flight trajectory into the quasi-stationary aircraft positions φ is crucial for an adequate accuracy of the predictions¹. Consequently, it is assumed that the received sound signal at the observer location is constant within each one transmission time step. The transmission time step $\Delta t_i(\varphi)$ starts when the observer receives the signal from one aircraft position φ at the time $t_i(\varphi)$. This time step lasts until the emitted sound from the consecutive aircraft position $\varphi + 1$ has reached the observer location at the time $t_i(\varphi + 1)$. According to the aircraft configuration and engine operating condition the relevant noise sources are accounted for and the sound emission at a reference distance of 1 m is predicted. For each time step $\Delta t_i(\varphi)$ the farfield sound pressure level frequency spectrum is computed. Optionally, SPL level differences due to engine noise shielding effects can be applied to the noise emission of affected noise sources.

To transfer the sound field data at the reference distance, i.e. 1 m, to the perceived noise levels at a specific observer location μ , sound propagation effects have to be considered, see Figs. A.1 and A.2, Appendix. PANAM accounts for the effects of geometrical spreading [16,54], atmospheric absorption [56], convection effects (convective amplification, frequency Doppler shift [16,54]) and ground attenuation [10,55] if required.

A large number of models for ground noise attenuation is available. Ref. [52] provides a good overview and detailed comparison of fully empirical models. Preselected methods are implemented in PANAM in order to compare the results: AzB [10], *Flula* [19], *Nortim* [57], and SAE [58]. Each attenuation model has a different development background, e.g. automotive or aviation, with specific applications. As a consequence, the simulation results show similar tendencies but overall levels can be subject to large deviations as depicted in Fig. A.3, Appendix. Yet, all models predict comparable levels for the relevant distances and elevation angles with respect to an aircraft flyover event. For the predictions presented within this report, the ground attenuation model of the German AzB is applied as defined in Ref. [10]. The AzB was specifically derived for aircraft noise prediction and is standardized with straight-forward instructions [10] on its implementation. The ground effect according

¹Flight positions do not have to be uniformly distributed, neither in time nor in space.

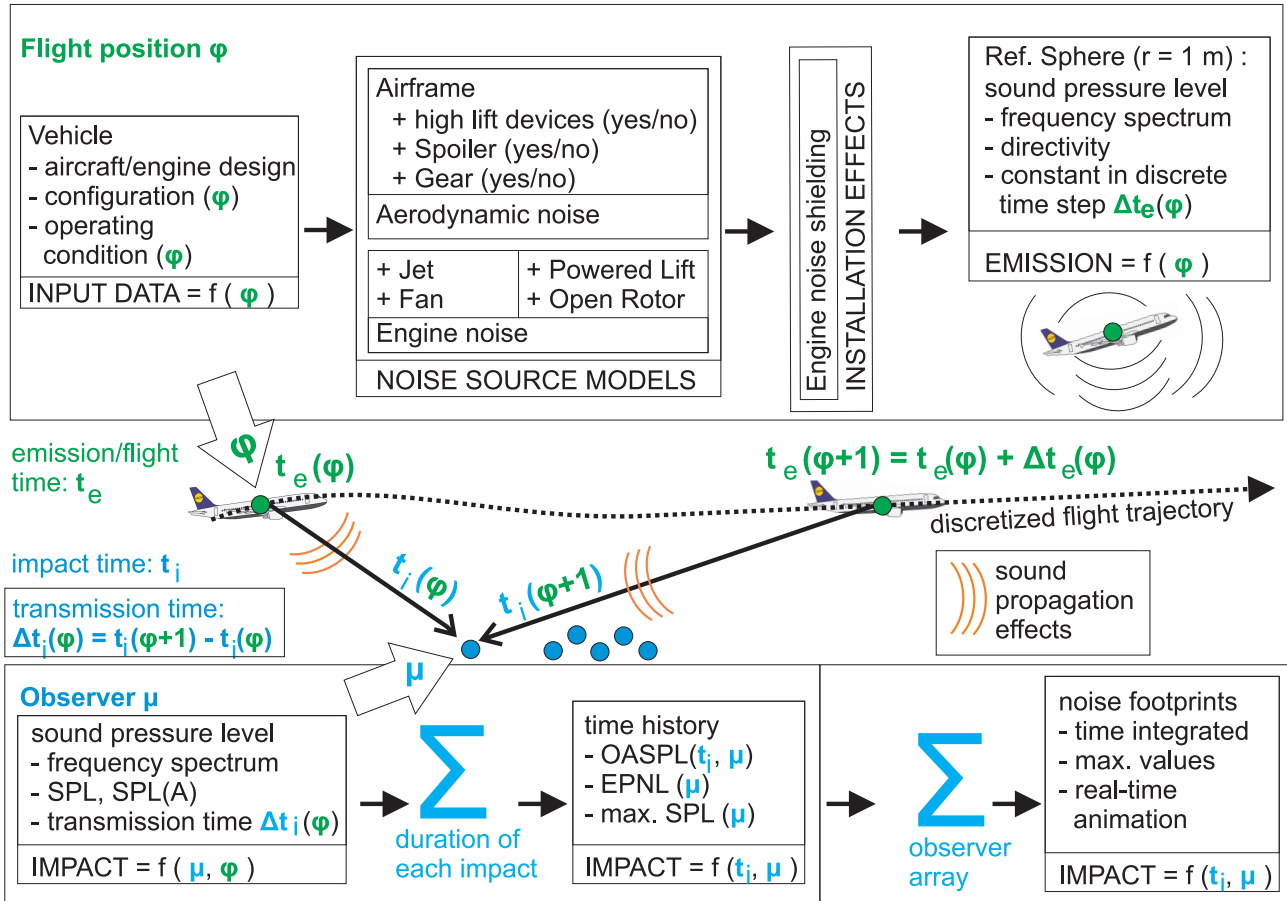


Figure 3.1: Noise prediction concept

to the AzB is approximated by two separate factors to account for reflection and attenuation (section 7.2.5 and 7.2.6, Ref. [10]). The model specifically predicts additional ground noise attenuation effects for elevation angles under 15° .

Weighting functions for the simulation of human sound perception can optionally be applied to the frequency spectrum [16]. The predicted spectrum covers the audible range, namely 20 to 20 kHz, and noise levels are provided in 1/3-octave bands together with the corresponding unweighted or weighted Overall Sound Pressure Level (OASPL). Each OASPL of the discrete time steps $\Delta t_i(\varphi)$ can then be assembled into a level-time-history for each one observer μ . Out of the time-history, time integrated and maximum noise levels for various noise metrics can then be computed. Optional output data can be saved at each observer location for further investigation, e.g. arbitrary level-time-histories. These computations can be repeated for each one observer location μ within a selected array² to provide noise contours on the ground.

Coordinate Systems and Noise Emission Angles

Location and orientation of aircraft and observers are defined in vector notation within an earth-fixed coordinate system [53] as depicted in Fig. 3.2. The origin of this coordinate system is usually placed at the runway threshold of the simulation scenario and implicitly

²Observer arrays can be structured or unstructured to enable arbitrary grid adaption.

defined by the arrangement of aircraft flight trajectory and observer locations. The current aircraft position and the observer location in the earth-fixed coordinate system are referred to as \vec{P}^g and \vec{O}^g respectively. A corresponding aircraft-fixed coordinate system is modeled

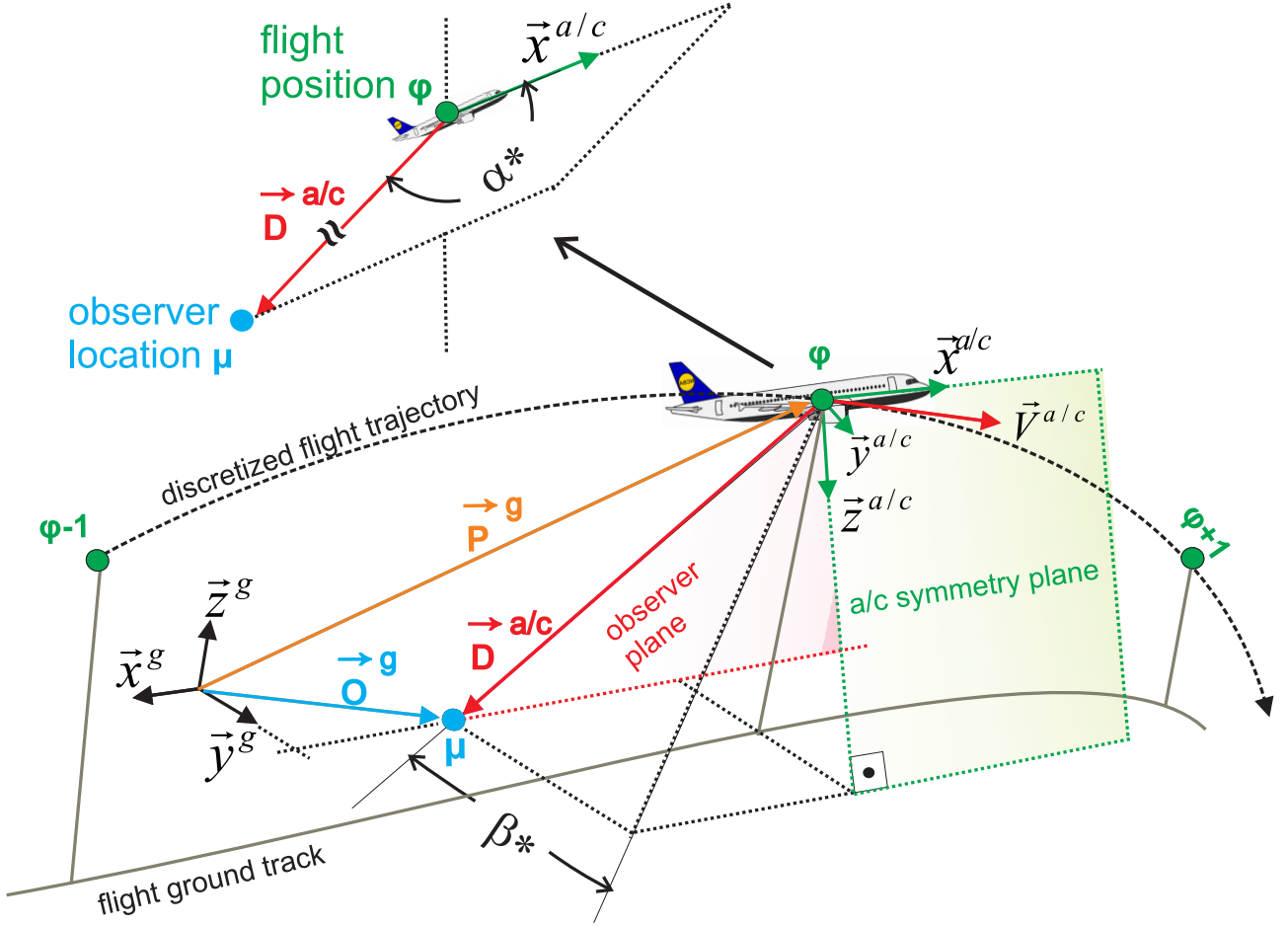


Figure 3.2: Coordinate systems and emission angles

for each quasi-stationary flight position φ along the simulated flight path. To define the aircraft-fixed coordinate system, the discretized flight trajectory is approximated by Lagrange polynomials as a function of flight time. Vector \vec{P}^g together with the corresponding flight time is determined for three subsequent flight positions ($\varphi - 1$, φ , and $\varphi + 1$), then placed into Lagrange polynomials in order to simulate the discretized flight path as a continuous function of time. Derivation of this function at flight position φ with respect to time generates the tangential vector $\vec{V}^{a/c}$, i.e. aircraft velocity over ground. Normalization of the tangent gives the direction vector of the aircraft movement at position φ . Applying the given angle of attack and yaw angle results in the aircraft-fixed symmetry axis $\vec{x}^{a/c}$. Further application of the given roll angle for aircraft position φ to axis $\vec{x}^{a/c}$ defines the missing axis, $\vec{y}^{a/c}$ and $\vec{z}^{a/c}$, of the aircraft-fixed coordinate system.

Selected observer locations are then transformed into this aircraft-fixed system, i.e. vector $\vec{D}^{a/c}$, in order to evaluate the relative observer distance and orientation with respect to the aircraft-fixed system. The relative observer orientation in the aircraft-fixed system is then transformed into two emission angles, i.e. angles α^* and β^* . According to Fig. 3.2, α^* is the angle between the aircraft-fixed axis $\vec{x}^{a/c}$ and the aircraft-fixed vector $\vec{D}^{a/c}$ towards the

observer. Angle β^* is the angle between the aircraft symmetry plane and the observer plane as depicted. The observer plane is the plane between axis $\vec{x}^{a/c}$ and vector $\vec{D}^{a/c}$ toward the observer. The relevant transformations and definitions are according to industry standard LN 9300 [53].

To speed up computations the code can run forward and backward in time along a given trajectory. The noise computation for one selected observer location does not start with the first aircraft position on the trajectory. Instead, the starting point for the computation is selected to be the nearest aircraft position relative to the observer. It is assumed that close to this position the maximum noise levels occur. From this position calculations are performed backward and forward in time. If the noise level for a number of consecutive aircraft positions is below a predefined threshold, calculations are stopped. The levels are set equal to the threshold and the influence of the remaining trajectory is neglected. The number of consecutive positions ξ and the threshold are empirical values. This modification accelerates the computation especially for the combination of large observer arrays and enduring flight simulation.

3.2.2 Noise Source Modeling

Major aircraft noise components have to be simulated for each quasi-stationary flight position. Each component is represented by its individual noise source model. These models account for physics-based influences on the component's noise generation. Consequently, any fully empirical approach can be ruled out and instead parametric and semi-empirical source models are implemented. These models represent a trade-off between fully empirical methods, i.e. best agreement to experimental data, and fully analytical methods, i.e. best agreement to underlying physics and theory.

The models predict static noise emission levels and directivities according to the underlying geometry and operating condition. The selected models allow for low computational demand but yet capture major physical effects throughout simulated flight operations, i.e. influence of aircraft/engine geometry, in-flight configurational setting, and current aircraft/engine operating conditions. According to the emission angles α^* and β^* , depicted in Fig. 3.2, the free-field noise emission out of each noise source, i.e. directional 1/3-octave-band SPL spectra, is predicted on a reference sphere of radius 1 m. To translate these individual contributions into perceived overall ground noise at selected observer locations, the emitted signals are combined and effects of noise source movement are applied³. Furthermore, the influence of noise propagation through the atmosphere, ground noise reflection, and human sound perception⁴ are accounted for.

3.2.2.1 Airframe Noise

The implemented airframe noise source models have been developed by Dobrzynski et al. at the Institute of Aerodynamics and Flow Technology, DLR Braunschweig [59–63]. According to Dobrzynski [9], rank-ordering the major airframe noise sources on-board of a

³Movement of a noise source results in a change in source strength, directivity, and perceived frequencies. These effects have to be accounted for.

⁴weighting functions

conventional aircraft yields (1) the front and main landing gears, (2) leading edge high lift elements, (3) flap or rudder side edges, (4) flap or rudder tracks, (5) spoilers, and (6) component interaction noise sources.

Dobrzynski derived approximation models for the most dominating components as described in Refs. [59–63]. The overall airframe noise is approximated as a combination of these individual models.

1. clean airfoil
2. trailing edge device (fowler flap)
3. leading edge device (slat)
4. spoiler
5. landing gear

An additional prediction model for flap side edge noise is currently under development at DLR [64, 65] but not yet implemented into PANAM. Initial results of the new approach are in good agreement with available experimental data [65]. The results indicate that flap side edge noise of conventional high-lift systems can contribute to overall airframe noise at high frequencies if the landing gear is still retracted [65]. Yet, due to the high frequencies the contribution to overall aircraft flyover noise is strongly reduced by A-weighting and atmospheric damping. Therefore, it is assumed that for the aircraft designs considered within this work, flap side edge noise does not effect the overall aircraft noise as perceived on the ground. Aside from that, the required input parameters for the model, e.g. local velocities, are yet not available at the conceptual aircraft design phase.

Each of the implemented prediction models provides a directional noise emission function for an unmoved source under fixed operating conditions, i.e. comparable to a static windtunnel experiment. For a selected observer location, i.e. distance $d = |\vec{D}^{a/c}|$ and relative source location, i.e. angles α^* and β^* , these functions provide a free-field, 1/3-octave-band SPL emission spectrum. Each SPL spectrum is defined by a summation of individual terms depending on the simulated noise source:

- normalized reference level L_{norm}
- spectral shape function $\Delta L_{spec}(Str)$
- velocity dependent term ΔL_{vel}
- geometry dependent term ΔL_{geo}
- directivity term ΔL_{dir}

L_{norm} is an empirical based reference level for the specific noise source and can be either constant or a function of the Strouhal number Str . The Strouhal number is defined as $Str = f \cdot x_{ref}/v_{ref}$, with f as the frequency, x_{ref} as a noise source reference dimension, and v_{ref} as a reference velocity. In the case that L_{norm} is a constant, the spectral shape can be defined as a dedicated function of the Strouhal number, i.e. $\Delta L_{spec}(Str)$. Then, $\Delta L_{spec}(Str)$ is a simplified function of two linear segments converging at a peak frequency Str_{max} . The slope and shape of each segment and the location of the maximum Strouhal number Str_{max}

are determined according to the specific source's geometry and prevailing flow conditions. The shape of the frequency spectrum is not affected by directivity effects of the source. The inherent emission directivity of certain noise sources is simulated with a dedicated directional term ΔL_{dir} that is directly applied to the overall SPL spectrum. Directivity effects are simulated according to the measured data with respect to known underlying physics. Velocity and geometry dependent adjustments, ΔL_{vel} and ΔL_{geo} , are determined for the selected operating conditions and source geometry with respect to the parameter setting of the underlying experimental data. A relevant freestream velocity v_m is evaluated according to the prevailing angle of attack and yaw, i.e. the velocity component parallel to the aircraft symmetry axis. Finally, for a noise source θ and a given set of reference parameters, the free-field 1/3-octave-band SPL emission spectrum can be evaluated.

$$L_\theta(Str) = L_{norm} + \Delta L_{spec}(Str) + \Delta L_{geo} + \Delta L_{vel} + \Delta L_{dir} \quad (3.1)$$

(1) Clean Airfoil - Clean airfoil noise prediction is based on a concept by Lockard and Lilley [66] adapted by Dobrzynski. Turbulent flow passing a semi-infinite flat plate generates noise. Only the upper surface or suction side of the airfoil has to be considered because it dominates the noise generation. Lockard and Lilley introduce an approximation for the time averaged rate at which this noise energy is emitted perpendicular to the plate trailing edge⁵. The acoustic intensity i per noise source volume is defined at the trailing edge as a function of the characteristic turbulent velocity scale u_0 , ambient flow density ρ_∞ , ambient speed of sound c_∞ , characteristic noise source frequency f_0 , and the observer distance d .

$$i = \frac{c_\infty^3}{\rho_\infty} \cdot \frac{f_0}{2 \cdot \pi^3 \cdot d^2} \cdot \frac{\rho_\infty^2 \cdot u_0^4}{c_\infty^5} \quad \text{per unit source volume} \quad (3.2)$$

Lockard [66] and Dobrzynski [62] show that this formulation is applicable for airfoils under low load conditions, i.e. prevailing lift coefficient ≤ 0.5 . According to Lockard [66] the following Strouhal relation can be defined for the turbulent flow, with l_{ref} as a noise source reference dimension.

$$Str_0 = \frac{f_0 \cdot l_{ref}}{u_0} \approx 1.7 \quad (3.3)$$

Furthermore, the acoustic noise source volume can be defined as the product of airfoil mean chordlength l_a , element length Δw , and boundary layer thickness δ . Evaluating Eq. 3.2 with respect to the source volume V and application of the Strouhal relation lead to a formulation of the acoustic intensity I normal to the flat plate's trailing edge.

$$I = \left[\frac{1.7}{2 \cdot \pi^3} \cdot \frac{\rho_\infty}{c_\infty^2} \cdot \left(\frac{u_0}{v_m} \right)^5 \cdot \frac{l_a \cdot \Delta w \cdot \delta}{l_{ref} \cdot d^2} \cdot v_m^5 \right]_{TE} \quad (3.4)$$

According to Ref. [66] the strength of the acoustic sources is proportional to the maximum turbulent kinetic energy. Furthermore, it is assumed that the reference dimension l_{ref} of the noise source is equal to the source distance from the airfoil wall. The wall distance of the maximum turbulent kinetic energy is denoted by y_m , hence $l_{ref} = y_m$. Lockard sets l_{ref} in the proximity of the wing trailing edge equal to the turbulent boundary layer displacement

⁵Eq. 3 in Ref. [66]

thickness δ^* . The integral can then be evaluated at the wing trailing edge (TE).

$$I = \frac{1.7}{2 \cdot \pi^3} \cdot \frac{\rho_\infty}{c_\infty^2} \cdot v_m^5 \cdot \frac{l_a \cdot \Delta w}{d^2} \cdot \left[\left(\frac{u_0}{v_m} \right)^5 \cdot \frac{\delta}{\delta^*} \right]_{TE} \quad (3.5)$$

$$= \frac{1.7}{2 \cdot \pi^3} \cdot \frac{\rho_\infty \cdot v_m^3 \cdot \text{Ma}^2 \cdot (l_a \cdot \Delta w)}{d^2} \cdot \left[\left(\frac{u_0}{v_m} \right)^5 \cdot \frac{\delta}{\delta^*} \right]_{TE} \quad \text{with } v_m = \text{Ma} \cdot c_\infty \quad (3.6)$$

Eq. 3.6 is according to Lockhard's derivation⁶. Dobrzynski adds a directivity factor to this equation in order to specifically account for the element's trailing edge sweep angle Ψ ⁷:

$$I = \frac{1.7}{2 \cdot \pi^3} \cdot \frac{\rho_\infty}{c_\infty^2} \cdot v_m^5 \cdot \frac{l_a \cdot \Delta w}{d^2} \cdot \left[\left(\frac{u_0}{v_m} \right)^5 \cdot \frac{\delta}{\delta^*} \right]_{TE} \cdot \cos^3(\Psi) \quad (3.7)$$

The ratio of boundary layer and displacement thickness for turbulent flow over a flat plate can be assumed as $\frac{\delta}{\delta^*} = 8$, Ref. [67]. According to recent high fidelity computations and wind tunnel data, Dobrzynski defines the ratio of characteristic velocity scale for the turbulence u_0 and mean inflow velocity v_m as $\frac{u_0}{v_m} = 0.046$, whereas Lockard used $\frac{u_0}{v_m} = 0.066$ in the original version. Obviously, this results in a significant level difference between the two methods, i.e. Lockard predicts intensity levels by ≈ 8 dB higher than Dobrzynski.

In the context of the presented work, the noise source models and inherent assumptions of Dobrzynski have been selected. Therefore, the far field noise emission spectra for clean airfoils under limited load conditions can be predicted as follows, i.e. the noise component that is emitted perpendicular to the airfoil trailing edge.

$$I = \frac{8 \cdot 1.7}{2 \cdot \pi^3} \cdot \frac{\rho_\infty}{c_\infty^2} \cdot \frac{l_a \cdot \Delta w}{d^2} \cdot 0.046^5 \cdot v_m^5 \cdot \cos^3(\Psi) \quad (3.8)$$

Normalizing this equation with the reference value of the intensity $I_{ref} = 10^{-12} \text{ W/m}^2$ provides the corresponding SPL. This value represents a normalized reference level with combined velocity and geometry adjustments, $L_{norm/vel/geo}$.

$$L_{norm/vel/geo} = 10 \cdot \log_{10} \left(\frac{I}{I_{ref}} \right) = 120 + 10 \cdot \log_{10}(I) \quad (3.9)$$

For example, a TE sweep angle of $\Psi = 30^\circ$ would result in an additional 1.9 dB noise level reduction compared to an unswept airfoil (Eq. 3.8). Limited available experimental data indicates no polar emission directivity. Therefore, the clean wing emission directivity ΔL_{dir} is approximated as a function of only the lateral emission angle β^* and the wing segment's dihedral angle ν . The dihedral angle has to be accounted for because the maximum noise is emitted with respect to the airfoil trailing edge.

$$\Delta L_{dir} = 10 \cdot \log_{10} \left(\frac{|\cos(\beta^* - \nu)| + |\cos(\beta^* + \nu)|}{2} \right) \quad (3.10)$$

To describe the spectral noise emission of a clean airfoil element, the Strouhal number is defined as a function of frequency f , mean element chord length l_a , and reference velocity of $v_{ref} = v_m$. The shape is approximated with two segments converging at a peak frequency

⁶Eq. 4 in Ref. [66]

⁷Eq. 3.9 in Ref. [62]

Str_{max} . According to Lockard [66] the max. Strouhal number Str_{max} is defined as a function of l_a , v_m , u_0 , and the boundary layer parameters at the trailing edge, namely δ_{TE} and $\left[\frac{\delta}{\delta^*}\right]_{TE}$.

$$Str_{max} = \frac{1.7}{2 \cdot \pi} \frac{u_0}{v_m} \cdot \frac{l_a}{\delta_{TE}} \cdot \left[\frac{\delta}{\delta^*}\right]_{TE} \quad (3.11)$$

The boundary layer thickness for a turbulent flow over a flat plate is defined as function of the Reynolds number $Re(x)$ along the plate. According to Schlichting, Ref. [67], the thickness can be evaluated as a function of v_m , location x , and the ambient kinematic viscosity ν_∞ .

$$\delta(x) = (0.37 \cdot x) / \left(\sqrt[5]{\frac{v_m \cdot x}{\nu_\infty}}\right) \quad (3.12)$$

With the known quantity $\frac{\delta}{\delta^*} = 8$, Eq. 3.11 can be evaluated at the trailing edge.

$$Str_{max} = \frac{13.6}{0.74 \cdot \pi} \cdot \frac{u_0}{v_m} \sqrt[5]{\frac{v_m \cdot l_a}{\nu_\infty}} \quad (3.13)$$

The spectral shape function can be expressed with respect to the maximum Strouhal number. Thereby, the nearest 1/3-octave-band center frequency is selected for further analysis.

$$\Delta L_{spec}(Str) = \begin{cases} 10 \cdot \log_{10} \left(\frac{Str}{Str_{max}} \right) - 9.0 \text{ dB} & \text{for } Str \leq Str_{max} \\ 10 \cdot \log_{10} \left(\frac{Str_{max}}{Str} \right) - 9.0 \text{ dB} & \text{for } Str > Str_{max} \end{cases} \quad (3.14)$$

Finally, the overall SPL emission is defined as:

$$L_{cl \leq 0.5}(Str) = L_{norm/vel/geo} + \Delta L_{dir} + \Delta L_{spec}(Str) \quad (3.15)$$

This approach is limited to airfoils under low wing loading, i.e. lift coefficients $c_l \leq 0.5$.

In order to account for **natural or hybrid laminar flow** over a clean airfoil, the reduced turbulent run length and boundary layer thickness have to be accounted for. Again, only the noise originating from the upper surface/suction side of the airfoil has to be considered. For simplicity, the new turbulent run length is assumed to be equal to the airfoil chord length l_a minus the simulated laminar run length x_{lam} . For a realistic clean airfoil, a maximum laminar run length x_{lam} of $\approx 55\%$ of the airfoil chord length l_a can be achieved thus the flow over the trailing edge remains turbulent [68]. Therefore, the same noise generating mechanisms as described above are prevailing and the derived equations can be applied as well. Yet, the reduction of turbulent kinetic velocity scale (u_0) and turbulent boundary layer thickness (δ) at the trailing edge have to be known and be accounted for.

The boundary layer thickness at the trailing edge is evaluated with respect to the reduced turbulent run length and kinetic energy.

$$\delta(x)_{lam} = \left(\frac{u_{0,lam}}{v_m} \cdot (l_a - x_{lam}) \right) / \left(\sqrt[5]{\frac{v_m \cdot (l_a - x_{lam})}{\nu_\infty}} \right) \quad (3.16)$$

A modified max. Strouhal number can then be derived:

$$Str_{max,lam} = \frac{13.6}{0.74 \cdot \pi} \cdot \frac{u_{0,lam}}{v_m} \sqrt[5]{\frac{v_m \cdot l_a}{\nu_\infty}} \quad (3.17)$$

With this new Strouhal number, Eq. 3.10, 3.14, and 3.22 or 3.8 can directly be applied. If any high lift devices or control surfaces are deployed, it can be assumed that the flow over the airfoil turns fully turbulent again.

(2) Trailing Edge Device - To predict noise emission of clean airfoils under increased wing loading and to account for deployment of trailing edge devices, modifications to the clean airfoil approach are necessary. Deploying high lift devices will increase wing area and finally results in significantly higher overall lift. To account for these effects, Lockard [66] published scaling factors for the turbulent fluctuation velocity and boundary layer thickness based on recent findings from higher fidelity computations (RANS) and from wind tunnel experiments. It is assumed, that the correlation $y_m = \delta^*$ is no longer valid [66]. Therefore, scaling of the boundary layer thickness with respect to the actual location of the maximum turbulent kinetic energy is applied. Furthermore, the velocity ratio $\frac{u_0}{v_m}$ has to be adapted to higher loads on the wing element. The scaling factors for velocity and length scales given by Lockard are derived from NACA 4412 experiments⁸. Again, the mean reference velocity is assumed equal to the inflow velocity parallel to the main airfoil chord. Furthermore, Dobrzynski's approximation is selected, i.e. $\left[\frac{u_0}{v_m}\right]_{TE, c_l \leq 0.5} \approx 0.046$.

$$\left[\frac{\delta}{y_m}\right]_{TE, c_l > 0.5} \sim \frac{10.0}{\left(1 + \frac{c_l^2}{4}\right)} \quad (3.18)$$

$$\begin{aligned} \left[\frac{u_0}{v_m}\right]_{TE, c_l > 0.5} &\sim \left[\frac{u_0}{v_m}\right]_{TE, c_l \leq 0.5} \cdot \left(1 + \frac{c_l^2}{4}\right) \\ &\sim 0.046 \cdot \left(1 + \frac{c_l^2}{4}\right) \end{aligned} \quad (3.19)$$

A correlation between the low and increased load case can be defined.

$$\left[\left(\frac{u_0}{v_m}\right)^5 \cdot \frac{\delta}{y_m}\right]_{TE, c_l > 0.5} = \frac{10}{8} \cdot \left(1 + \frac{c_l^2}{4}\right)^4 \cdot \left[\left(\frac{u_0}{v_m}\right)^5 \cdot \frac{\delta}{y_m}\right]_{TE, c_l \leq 0.5} \quad (3.20)$$

Finally, an explicit formulation for the acoustic intensity I of wing segments with deployed trailing edge devices and/or increased wing loading can be derived, i.e. emission component perpendicular to the leading edge. The wing element chord length is defined as the sum of airfoil chord length l_a and chord length of the deployed trailing edge flap l_f .

$$\begin{aligned} I &= \frac{1.7}{2 \cdot \pi^3} \cdot \frac{\rho_\infty}{c_\infty^2} \cdot v_m^5 \cdot \frac{(l_a + l_f) \cdot \Delta w}{d^2} \cdot \cos^3(\Psi) \cdot \left[\left(\frac{u_0}{v_m}\right)^5 \cdot \frac{\delta}{y_m}\right]_{TE, c_l > 0.5} \\ &= \frac{1.7}{2 \cdot \pi^3} \cdot \frac{\rho_\infty}{c_\infty^2} \cdot v_m^5 \cdot \frac{(l_a + l_f) \cdot \Delta w}{d^2} \cdot \cos^3(\Psi) \cdot \frac{10}{8} \cdot \left(1 + \frac{c_l^2}{4}\right)^4 \cdot \left[\left(\frac{u_0}{v_m}\right)^5 \cdot \frac{\delta}{y_m}\right]_{TE, c_l \leq 0.5} \\ &= \frac{8 \cdot 1.7}{2 \cdot \pi^3} \cdot \frac{10}{8} \cdot \frac{\rho_\infty}{c_\infty^2} \cdot v_m^5 \cdot \frac{(l_a + l_f) \cdot \Delta w}{d^2} \cdot 0.046^5 \cdot \cos^3(\Psi) \cdot \left(1 + \frac{c_l^2}{4}\right)^4 \end{aligned} \quad (3.21)$$

⁸Note that equations 10 - 11 published by Lockard in Ref. [66] have missing terms. Dobrzynski uses Lockard's scaling factors but Dobrzynski's equation 3.25 yields two typos: factor "1/10" should be "10". Furthermore, the factor $\frac{\delta}{\delta^*}$ on the right hand side of the equation is redundant and should be canceled.

The intensity is transformed into an SPL to obtain the reference level $L_{norm/vel/geo}$.

$$\begin{aligned}
 L_{norm/vel/geo} &= 120 \text{ dB} + 10 \cdot \log_{10} \left(\frac{1.7}{2 \cdot \pi^3} \cdot \frac{\rho_\infty}{c_\infty^2} \cdot v_m^5 \cdot \frac{(l_a + l_f) \cdot \Delta w}{d^2} \cdot \cos^3(\Psi) \right) \\
 &\quad + 10 \cdot \log_{10} \left(\frac{10}{8} \cdot \left(1 + \frac{c_l^2}{4} \right)^4 \cdot \left[\left(\frac{u_0}{v_m} \right)^5 \cdot \frac{\delta}{y_m} \right]_{TE, c_l \leq 0.5} \right) \\
 &= 120 \text{ dB} + 10 \cdot \log_{10} \left(\frac{8 \cdot 1.7}{2 \cdot \pi^3} \cdot \frac{\rho_\infty}{c_\infty^2} \cdot \frac{(l_a + l_f) \cdot \Delta w}{d^2} \cdot \cos^3(\Psi) \cdot (0.046 \cdot v_m)^5 \right) \\
 &\quad + \underbrace{10 \cdot \log_{10} \left(\frac{10}{8} \cdot \left(1 + \frac{c_l^2}{4} \right)^4 \right)}_{\Delta L_{c_l > 0.5}}
 \end{aligned} \tag{3.22}$$

Comparing this equation with the $c_l \leq 0.5$ case, an additional factor $\Delta L_{c_l > 0.5}$ can be identified to account for the increase in lift.

$$\Delta L_{c_l > 0.5} = 0.97 + 40 \cdot \log_{10} \left(1 + \frac{c_l^2}{4} \right) \tag{3.23}$$

According to this additional factor, a wing segment under a typical landing load of $c_l = 2$ would result in a 13 dB level increase compared to the low lift case, i.e. $c_l < 0.5$. Obviously, this effect would be counter-acted by a required increase in flight velocity by a factor "x" for the $c_l < 0.5$ case. As a consequence, additional noise due to the velocity increase is generated, i.e. $\Delta L_{vel} = 50 \cdot \log_{10}(x)$.

The directivity and spectral shape for the high lift wing element is similar to the low lift case because of the inverse lift dependency of equations 3.18 and 3.20. Therefore, Eq. 3.10 and 3.14 remain valid and can be applied to the high lift airfoil.

$$L_{c_l > 0.5} = \underbrace{L_{norm/vel/geo}}_{c_l > 0.5} + \Delta L_{dir} + \Delta L_{spec}(Str) \tag{3.24}$$

(3) Leading Edge Devices - Leading edge devices can dominate airframe noise as long as the landing gear is retracted [9]. The prediction method as proposed by Dobrzynski is applicable to two- and three-position leading-edge slats as described in Ref. [69]. The method is based on the concept of a spanwise distribution of uncorrelated dipole noise sources, i.e. so-called *lift* and *drag dipoles*. Both *lift* and *drag dipoles* are aligned along the trailing edge of each slat element but have different dipole reference axis orientation. Reference axes of *lift dipoles* are oriented approximately perpendicular with respect to the slat chord line [21, 36]. This arrangement results in major noise emission perpendicular to the slat chord. Prediction accuracy can be improved with respect to the measurements by adding *drag dipoles* at the location of the *lift dipoles*. *Drag dipoles* are aligned parallel to the element chord hence are emitting noise primarily in this direction. To evaluate the noise emission of an installed and deployed slat element, the dipole noise sources are finally rotated along with the slat element according to the slat installation angle γ and the selected slat deployment angle δ_s . The final orientation of the dipoles with respect to the overall aircraft symmetry axis influences the noise emission directivity.

Each slat element is defined by four geometry parameters, i.e. slat mean chord length l_s ,

mean element width Δw , mean sweep angle Ψ of the element, and installation angle γ between aircraft symmetry axis and element mean chord line. The reference velocity for the Strouhal number is v_∞ hence the dimensionless frequency can be defined as $Str = \frac{f \cdot l_s}{v_\infty}$.

The normalized reference level $L_{norm/spec}$ is expressed as a function of the Strouhal number and of the high lift configurational setting, i.e. deployment of leading and trailing edge devices. An empirical relation was developed to account for the impact of flap and slat deflection, i.e. angles δ_f and δ_s , on the local flow conditions. Two empirical constants are introduced as $C_1 = 104.6 \text{ dB}$ and $C_2 = 113.1 \text{ dB}$. For Strouhal numbers below a certain limit, $Str \leq Str_{max}$, an adjustment factor ΔL_{conf} to account for the selected configurational setting is defined.

$$\Delta L_{conf} = -15.6 + 0.416 \cdot (\delta_s + \delta_f) - 0.0025 \cdot (\delta_s + \delta_f)^2 \quad \text{for } Str \leq Str_{max} \quad (3.25)$$

The maximum Strouhal number Str_{max} is related to the empirical constants and the adjustment factor for the configurational setting.

$$Str_{max} = 10.0^{\frac{C_2 - C_1 - \Delta L_{conf}}{21.0}} \quad (3.26)$$

Finally, the normalized reference level $L_{norm/spec}$ is a function of the Strouhal number Str , comprised by two linear segments converging at the peak frequency Str_{max} .

$$L_{norm/spec}(Str) = \begin{cases} C_1 + 3 \cdot \log_{10}(Str) + \Delta L_{conf} & \text{for } Str \leq Str_{max} \\ C_2 - 18 \cdot \log_{10}(Str) & \text{for } Str > Str_{max} \end{cases} \quad (3.27)$$

The geometry dependent adjustment factor ΔL_{geo} is defined with respect to the parameter setting of the underlying experimental data (marked with $_{exp}$). With the known geometry parameters, a reference noise source area can be defined as $\mathfrak{A} = l_s \cdot \Delta w / \cos(\Psi)$. The ratio of these source areas and the observer distances determines the adjustment factor.

$$\Delta L_{geo} = 10 \cdot \log_{10} \left(\frac{d_{exp}^2}{d^2} \right) + 10 \cdot \log_{10} \left(\frac{l_s \cdot \Delta w / \cos(\Psi)}{l_{s,exp} \cdot \Delta w_{exp} / \cos(\Psi_{exp})} \right) \quad (3.28)$$

The formulation is simplified by plugging in the given experimental reference parameters, i.e. slat sweep angle $\Psi_{exp} = 27^\circ$, slat chord $l_{s,exp} = 0.0701 \text{ m}$, slat width $\Delta w_{exp} = 4.03 \text{ m}$, and observer distance $d_{exp} = 1 \text{ m}$.

$$\Delta L_{geo} = 5.0 + 10 \cdot \log_{10} \left(\frac{l_s \cdot \Delta w}{\cos(\Psi) \cdot d^2} \right) \quad (3.29)$$

The velocity dependence is approximated as a function of leading edge sweep angle Ψ and the reference velocity v_∞ with respect to the corresponding experimental parameters, i.e. $v_{exp} = 100 \text{ m/s}$.

$$\Delta L_{vel} = 50 \cdot \log_{10} \left(\frac{v_\infty}{100 \text{ m/s}} \right) + 30 \cdot \log_{10} \left(\frac{\cos(\Psi)}{\cos(27^\circ)} \right) \quad (3.30)$$

According to the predefined emission angles α^* and β^* , the emission directivity correlation ΔL_{dir} is subdivided into two components, i.e. $\Delta L_{dir} = \Delta L_{dir}(\alpha^*) + \Delta L_{dir}(\beta^*)$. The polar directivity factor $\Delta L_{dir}(\alpha^*)$ with respect to angle α^* is defined as a function of polar angle α^* , installation angle γ , slat deployment δ_{slat} , and the aircraft angle of attack α .

$$\Delta L_{dir}(\alpha^*) = 10 \cdot \log_{10} \left(\sin^2(|\alpha^* - \gamma - \delta_s + \alpha|) + 0.1 \cdot \cos^2(|\alpha^* - \gamma - \delta_s + \alpha|) \right) \quad (3.31)$$

Lateral directivity is defined as a function of emission angle β^* and the wing dihedral angle ν .

$$\Delta L_{dir}(\beta^*) = 10 \cdot \log_{10} \left(\frac{|\cos(\beta^* - \nu)| + |\cos(\beta^* + \nu)|}{2} \right) \quad (3.32)$$

Finally, the SPL spectrum can be evaluated.

$$L_{slat} = L_{norm/spec}(Str) + \Delta L_{geo} + \Delta L_{vel} + \Delta L_{dir} \quad (3.33)$$

(4) Spoiler - Spoiler noise is currently modeled with a very simple and fully empirical model. Spoiler operation obviously has huge impact on the overall flow field around the corresponding wing segment hence has a dominating influence on adjacent noise sources as well. Spoiler deflection significantly reduces the overall lift hence changes the flow conditions at both leading and trailing edge of the wing. To evaluate these effects, local flow conditions would have to be evaluated and accounted for. Since these data are not available, a simple and fully empirical model has been developed by Dobrzynski [62]. Due to limited experimental data, only fully extracted spoilers can be accounted for with the model. A reference source dimension of $x_{ref} = 1m$ is selected, thus the Strouhal number is defined as $Str = \frac{f \cdot 1m}{v_{\infty}}$.

The normalized reference level L_{norm} is defined as a function of the Strouhal number.

$$L_{norm} = 91.6 - 9.0 \cdot \log_{10}(Str + 1.0) \quad (3.34)$$

According to the experimental data base, geometry and velocity depending adjustments are defined. The underlying experimental data only comprises spoilers of constant height and full deflection. Therefore, geometry dependence is defined as a function of the actual spoiler width Δw and the observer distance d . The ratio of reference and measured velocity defines the velocity correction factor; with $v_{exp} = 100m/s$ as the measured velocity of the underlying experiment.

$$\Delta L_{geo} = 20 \cdot \log_{10} \left(\frac{\Delta w}{d} \right) \quad (3.35)$$

$$\Delta L_{vel} = 50 \cdot \log_{10} \left(\frac{v_{ref}}{v_{exp}} \right) = 50 \cdot \log_{10} \left(\frac{v_{ref}}{100 m/s} \right) \quad (3.36)$$

Spectral shape function and directivity effects are combined into one approximation formula $\Delta L_{dir/spec}(Str)$. Lateral directivity effects are negligible hence only polar directivity effects with respect to emission angle α^* are accounted for.

$$\Delta L_{dir/spec}(Str) = |A_1| \cdot \cos^2 \left(\frac{\alpha^*}{2} \right) + |A_2| \cdot \cos^2 \left(\frac{\alpha^*}{2} + 90^\circ \right) \quad (3.37)$$

$$\text{with } A_1 = 7.0 - 10 \cdot \log_{10}(Str + 1.0)$$

$$\text{and } A_2 = -2.0 + 10 \cdot \log_{10}(Str + 1.0)$$

Overall, spoiler SPL levels are defined as:

$$L_{spoiler} = L_{norm} + \Delta L_{geo} + \Delta L_{vel} + \Delta L_{dir/spec}(Str) \quad (3.38)$$

(5) Landing Gear - Landing gear can be the most dominating airframe noise source of conventional transportation aircraft during approach due to bluff body vortex shedding [8,9]. The implemented noise source models [59,60,63] simulate noise emission of each landing gear according to the specific geometry parameters, installation effects and flow conditions. Geometry parameters are extended length l_g of the gear, wheel diameter D_g , and number of axles n_a as an empirical indicator for the component's overall complexity [62]. Operational parameters are gear extraction factor δ_g (0 - 1) and the corresponding mean flow velocity at the bogie⁹ of the landing gear.

The mean flow velocity v_m is approximated for each landing gear by taking local installation effects into account, i.e. possible variation of the freefield velocity due to circulation effects. The focus of this work lies on tricycle landing gear arrangements as described in Ref. [51], i.e. one gear in front of the aircraft and two main gears located at the wing/fuselage junction. The front gear is subject to a mean velocity equal to the freestream velocity v_∞ whereas v_m at the main landing gear bogie is reduced by the flow field around the main wing. The local wing circulation at the spanwise gear position is modeled according to the wing chord length and any presence of extended high lift devices. The mean flow velocity v_m at the main gear bogie is then approximated as the freefield velocity v_∞ subtracted by the circulation induced velocity component v_Γ . v_Γ is simply approximated by application of Kutta-Joukowski's theorem, i.e. the relation of freestream velocity, lift and circulation around an airfoil.

Experimental data has shown no significant directivity effect [62], thus each landing gear is modeled as a non-directional noise source, i.e. $\Delta L_{dir} = 0$. The normalized level L_{norm} is an empirical constant of 110.0 dB whereas ΔL_{vel} and ΔL_{geo} are determined by flow conditions and geometry of the specific gear, respectively. With a selected reference velocity from the underlying experiment of $v_{exp} = 100 \text{ m/s}$ and the known geometry parameters, the corrections can be defined.

$$\Delta L_{geo} = 10 \cdot \log_{10} \left(\frac{(l_g \cdot \delta_g) \cdot D_g \cdot \sqrt[4]{n_a}}{d^2} \right) \quad (3.39)$$

$$\Delta L_{vel} = 60 \cdot \log_{10} \left(\frac{v_m}{v_{exp}} \right) \quad (3.40)$$

According to the type of landing gear, i.e. main or front installation, a different spectral shape function is applied [62]. With the corresponding Strouhal number Str the shape functions can be evaluated. The Strouhal number is defined as $Str = \frac{f \cdot l_{ref}}{v_m}$, with a selected source reference dimension of $l_{ref} = 1 \text{ m}$. The spectral shape function of a main landing gear (mg) is given as:

$$\Delta L_{spec, mg}(Str) = \begin{cases} \log_{10} (Str^{-0.769}) & \text{for } Str \leq 20 \\ 12.96 + \log_{10} (Str^{-10.7301}) & \text{for } Str > 20 \end{cases} \quad (3.41)$$

The spectral shape function of a front landing gear (fg) is given as:

$$\Delta L_{spec, fg}(Str) = \begin{cases} \log_{10} (Str^{1.1143}) & \text{for } Str \leq 10 \\ 10.45 + \log_{10} (Str^{-9.3367}) & \text{for } Str > 10 \end{cases} \quad (3.42)$$

Ultimately, the SPL spectra for a main or front landing gear can be evaluated.

$$L_{gear} = L_{norm} + \Delta L_{geo} + \Delta L_{vel} + \begin{cases} \Delta L_{spec, mg}(Str) & \text{main gear} \\ \Delta L_{spec, fg}(Str) & \text{front gear} \end{cases} \quad (3.43)$$

⁹According to Dobrzynski [62], the bogie is considered to be the main source of noise generation on a conventional landing gear.

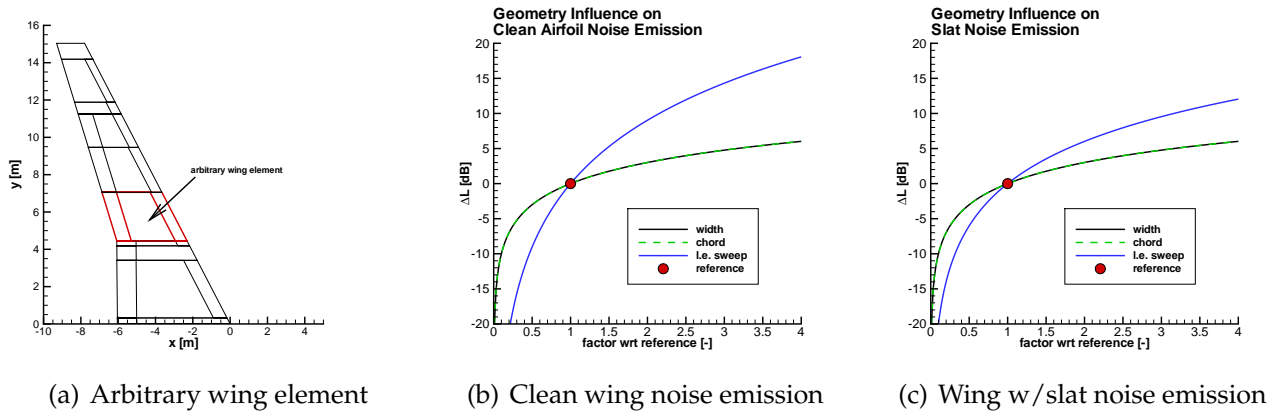


Figure 3.3: Impact of geometry parameters on noise emission (note: depicted is the cosine of the sweep angle)

Furthermore, Dobrzynski introduces empirical adjustment factors c to account for additional system complexity and to account for the overall landing gear size [62]. Elimination of breaking devices that are directly installed at the landing gear reduces overall noise levels by $c = -2$ dB. Wide body aircraft are subject to a noise increase of $c = +2$ dB due to the higher landing gear size and complexity compared to narrow body aircraft.

Limitations and Applicability - The implemented noise source models are derived from computational and experimental data. This data base is comprised of actual measurements or simulations, e.g. high fidelity computation, windtunnel, and flyover experiments, see Refs. [59–63]. Obviously, derivation of models and approximations from a fixed data base sets up inherent limitations to the applicability. General application of a noise source model is not feasible. Each noise source model can only be applied according to the underlying and case-specific data, i.e. general noise generating mechanisms and physics need to be consistent with the data. Reasonable and reliable results are achieved, if principal design features are kept constant or if empirical constants are adapted. For example, if a device's layout and mechanism is kept constant, geometry parameters can be modified in order to investigate the impact on noise generation [61], see Fig. 3.3. If empirical factors within the noise source models are adapted, a good prediction accuracy was achieved for such diverse vehicles as the A319 and the B747-300 [70]. According to Ref. [71], the prediction accuracy for the selected airframe noise source models is within ± 1 dB(A). Result uncertainty increases if existing noise source models are applied toward vehicle concepts far off the design space specified by the underlying empirical data base.

3.2.2.2 Turbofan/Turbojet Engine Noise

Noise prediction for turbofan and turbojet engine concepts is based on semi-empirical methods found in the literature. Two major noise components are modeled and accounted for in PANAM, i.e. the two dominant noise sources.

1. jet noise (turbofan, turbojet)
2. fan noise (turbofan)

Jet noise is predicted with the well-known Stone's method [25] whereas fan noise is based on Heidmann's method [26] but with a modified underlying data base. Both models assume a symmetric noise emission with respect to the engine reference axis, i.e. a function of the relative emission angle α^* . Ultimately, both models yield far field third-octave band SPL spectra for a lossless noise propagation under free-field conditions. The engine noise

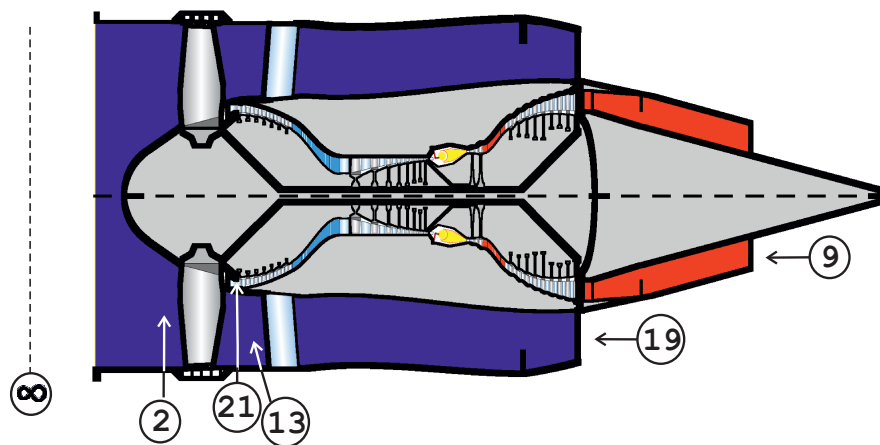


Figure 3.4: Station numbering for turbofan and turbojet engines¹⁰

module as implemented in PANAM was developed by Dr. S. Guérin, Institute of Propulsion Technology, DLR Berlin. The provided FORTRAN subroutines are somewhat modified and adapted in order to integrate them into PANAM. The models predict directional, free-field 1/3-octave SPL spectra. In order to evaluate engine ground noise impact, only sound propagation through the atmosphere, ground noise reflection, and spectral weighting has to be accounted for.

The two semi-empirical noise models require specific input data with respect to geometry and operational conditions of the selected engine. Engine operation along a simulated flight is determined by flight altitude, flight speed, and the engine operational setting (thrust setting or rotary speed). According to the engine operation, required input data for each noise source model has to be generated and provided, i.e. specific engine aerodynamic and thermodynamic parameters. In addition, specific geometric engine design parameters are required.

The applied nomenclature for turbofan engine stations is in accordance with SAE's *Aerospace Recommended Practices* [72]. Fig. 3.4 is adapted from Ref. [73] and shows the applied station numbering. For example, the fan total pressure ratio $\Pi_{t,2-13}$ is defined as the ratio of $p_{t,13}$ at the fan exit plane ⑬ and the pressure $p_{t,13}$ at the fan front face ②.

¹⁰Figure is adapted from Ref. [73]

It has to be noted, that stations ⑨ and ⑰ denote the fully expanded far-field exit conditions for core and bypass flow, respectively.

The jet noise model can address single and mixed dual jets. A normalized reference level L_{norm} is predicted for the single jet. L_{norm} is defined according to the nozzle geometry and the operating condition. Based on an empirical data base, a combined term for spectral shape and directivity $\Delta L_{dir/spec}$ as a function of Strouhal number Str is applied. An additional term ΔL_{c-jet} and a modified $\Delta L_{dir/spec}$ is defined to account for the secondary jet.

$$L_{jet} = \begin{cases} L_{norm} + \Delta L_{dir/spec}(Str_9, \alpha_{cor}^*) & \text{for single jet} \\ L_{norm} + \Delta L_{dir/spec}(Str_{c-jet}, \alpha_{cor}^*) + \Delta L_{c-jet} & \text{for coaxial jets} \end{cases} \quad (3.44)$$

Fan noise L_{fan} is separated into fan inlet $L_{fan,in}$ and fan exhaust $L_{fan,ex}$ noise contribution. Both contributions are modeled individually and are each comprised of 4 basic terms and additional correction factors c if required. The basic terms are comprised of a normalized reference level, i.e. constant for inlet and exhaust, and the contributions of (a) broadband, (b) discrete-tone, and (c) combination-tone noise, if applicable. Energetic summation of these individual contributions yields the overall fan inlet and outlet noise emission.

$$L_{fan,in} = L_{norm} + \underbrace{L_{bbn,in}}_{(a)} + \underbrace{L_{dtn,in}}_{(b)} + \underbrace{L_{ctn,in}}_{(c)} + c_i \quad (3.45)$$

$$L_{fan,ex} = L_{norm} + \underbrace{L_{bbn,ex}}_{(a)} + \underbrace{L_{dtn,ex}}_{(b)} + c_j \quad (3.46)$$

$$L_{fan} = L_{fan,in} + L_{fan,ex} \quad (3.47)$$

(1) Jet noise - The method by Stone can be applied to predict jet noise for single (turbojet) and mixed dual jets (turbofan) up to bypass ratios of 15 [25,27]. The predicted noise levels are free-field, far field, and lossless [25]. According to Bridges [27], the results for round jets are very good with nearly all predicted noise levels within the underlying experimental uncertainty bands, i.e. a standard deviation of 1.8 dB for jet velocities up to 800 m/s. In general, the model can be applied to subsonic or supersonic jet flows up to exhaust Mach numbers of 2.5 and higher [27]. There are a few inherent limitations to the applicability of the method [25]: required conditions are (1) co-axial and coplanar nozzle¹¹, (2) no low-noise nozzle modifications¹², and (3) no inverse velocity profile¹³.

If jet flows are supersonic, broadband shock noise is generated in addition to the jet mixing noise. For coaxial supersonic flow, it is assumed that there is no interaction with respect to broadband shock noise, hence each individual jet [25] can separately be evaluated. In the context of the presented work, shock noise is not an issue because exhaust velocities of considered turbofan engines remain subsonic during the considered approach and departures flight segments. Therefore, overall jet noise is simulated as jet mixing noise only.

The first step in order to evaluate mixed coaxial jets is the simulation of an isolated (primary) jet without refraction effects¹⁴. Stone defines a normalized sound pressure level

¹¹No short or long buried nozzles can be simulated.

¹²No serrations or a lobbed mixer can be simulated.

¹³The method cannot be (directly) applied, if bypass or flight velocity are greater than the velocity of the core flow.

¹⁴Note: In the following simplified description of the noise source model, possible engine installation angles γ are not accounted for.

L_{norm} for mixing noise of an isolated and shock-free jet. L_{norm} is defined as a function of (a) atmospheric conditions, (b) area, density, and velocity of the jet, (c) eddy convective amplification, (d) flight effects, and (e) nozzle shape. The required parameters to evaluate these effects can be derived from the following basic input parameters for the isolated (primary) jet, i.e. exhaust flow velocity, exhaust flow total temperature, nozzle exhaust area, mean free flow velocity, ambient temperature, ambient speed of sound, and ambient density. All of these parameters are required input information to the jet noise prediction.

(a) The ambient flow density ρ_∞ and speed of sound c_∞ are evaluated. Reference levels are defined at sea level (0 m) according to the International Standard Atmosphere, i.e. $p_{\infty, ISA} = 1013 \text{ N/m}^2$ and $T_{\infty, ISA} = 288 \text{ K}$.

(b) Parameters of the isolated (primary) jet, i.e. density ρ_9 , nozzle exhaust area A_9 , and an effective jet speed \bar{v}_9 , are accounted for with respect to observer distance d , ambient density ρ_∞ , and ambient speed of sound c_∞ . Stone defines the effective jet speed \bar{v}_9 as a function of v_∞ ¹⁵, and jet exhaust velocity v_9 .

$$\bar{v}_9 = v_9 \cdot \left[1 - \frac{v_\infty}{v_9} \cdot \cos(\alpha^*) \right]^{2/3} \quad (3.48)$$

Furthermore, Stone introduces a density exponent ω as a function of the effective jet speed \bar{v}_9 and the ambient speed of sound c_∞ . This exponent applies to hot jets.

$$\omega = \frac{3.0 \cdot (\bar{v}_9/c_\infty)^{3.5}}{0.6 + (\bar{v}_9/c_\infty)^{3.5}} - 1 \quad (3.49)$$

(c) Eddy convective amplification is determined as a function of a convective Mach number Ma_{con} and the polar angle α^* . Stone defines the convective Mach number Ma_{con} as a function of v_∞ , jet exhaust velocity v_9 , the ambient speed of sound c_∞ , and the polar angle α^*

$$\text{Ma}_{con} = 0.62 \cdot \frac{v_9 - v_\infty \cdot \cos(\alpha^*)}{c_\infty} \quad (3.50)$$

(d) Flight effects are defined as a function of v_∞ and the polar angle α^* .

(e) Nozzle shape of the jet exhaust is determined as a function of nozzle area A_9 and the nozzle hydraulic diameter D_9 .

Finally, the reference noise level of an isolated and shock-free jet without refraction ef-

¹⁵For simplicity, it is assumed that the mean inflow velocity is parallel to the engine symmetry axis, i.e. $v_m = v_\infty$.

fects can be defined as:

$$\begin{aligned}
 L_{norm} = 141.0 &+ \underbrace{10 \cdot \log_{10} \left[\left(\frac{\rho_{\infty}}{\rho_{\infty, ISA}} \right)^2 \cdot \left(\frac{c_{\infty}}{c_{\infty, ISA}} \right)^4 \right]}_{\text{(a) atmosphere}} \\
 &+ \underbrace{10 \cdot \log_{10} \left(\frac{A_9}{d^2} \right) + 10 \cdot \omega \cdot \log_{10} \left(\frac{\rho_9}{\rho_{\infty}} \right) + 75 \cdot \log_{10} \left(\frac{\bar{v}_9}{c_{\infty}} \right)}_{\text{(b) jet parameters}} \\
 &- \underbrace{15 \cdot \log_{10} [(1 + \text{Ma}_{con} \cdot \cos(\alpha^*))^2 + 0.04 \cdot \text{Ma}_{con}^2]}_{\text{(c) eddy amplification}} \\
 &- \underbrace{10 \cdot \log_{10} [1 - \text{Ma} \cdot \cos(\alpha^*)]}_{\text{(d) flight effects}} \\
 &+ \underbrace{3 \cdot \log_{10} \left(\frac{2 \cdot A_9}{\pi \cdot (D_9)^2} + 0.5 \right)}_{\text{(e) nozzle shape}}
 \end{aligned} \tag{3.51}$$

Jet noise directivity is assumed to be rotationally symmetric, hence is only a function of the polar angle α^* . Stone does not define specific directivity functions but accounts for directivity effects implicitly. Stone introduces a corrected directivity angle α_{cor}^* as a function of the primary jet speed and the ambient speed of sound: $\alpha_{cor}^* = \alpha^* \cdot (v_9/c_{\infty})^{0.1}$. With this new angle, Stone defines an effective Strouhal number for the jet as the product of specific empirical terms.

$$\begin{aligned}
 Str_9 = f \cdot \frac{\sqrt{4 \cdot A_9/\pi}}{\bar{v}_9} \cdot \left(\frac{D_9}{\sqrt{4 \cdot A_9/\pi}} \right)^{0.4} \cdot \left(\frac{T_{t,9}}{T_{t,\infty}} \right)^{0.4 \cdot [1 + \cos(\alpha_{cor}^*)]} \cdot (1 - \text{Ma} \cdot \cos(\alpha^*)) \\
 \cdot \left[\frac{\left(1 + 0.62 \cdot \frac{v_9 - v_{\infty}}{c_{\infty}} \cdot \cos(\alpha^*) \right)^2 + 0.01538 \cdot \left(\frac{v_9 - v_{\infty}}{c_{\infty}} \right)^2}{\left(1 + 0.62 \cdot \frac{v_9}{c_{\infty}} \cdot \cos(\alpha^*) \right)^2 + 0.01538 \cdot \left(\frac{v_9}{c_{\infty}} \right)^2} \right]^{0.5}
 \end{aligned} \tag{3.52}$$

Spectral shape and emission directivity of the shock-free isolated jet noise are defined as a function of the effective Strouhal number Str_9 and the corrected directivity angle α_{cor}^* . Empirical level differences $\Delta L_{dir/spec}$ applicable to L_{norm} with respect to directivity and spectral shape are listed in Table 1 of Ref. [25]. With this empirical data, turbulent mixing noise L_{jet} of a shock-free and isolated jet, i.e. a turbojet concept, can be evaluated according to Str_9 and α_{cor}^* .

$$L_{jet} = L_{norm} + \underbrace{\Delta L_{dir/spec}(Str_9, \alpha_{cor}^*)}_{\text{data: Table 1, Ref. [25]}} \tag{3.53}$$

These equations can also be applied to turbofan engines with a buried core nozzle. In that case, the resulting exhaust flow parameters for one common and mixed exhaust flow have to be determined and accounted for. An equivalent jet model is applied according to Ref. [78], in order to translate the mixed flow into one equivalent jet of equal mass flow, momentum, and enthalpy (see Section B).

Simulation of coaxial jets with separate exhaust nozzles requires input with respect to both primary and secondary flow; primary flow parameters are marked with subscript "9" and secondary flow parameters with "19". To determine the mixing noise of a shock-free

coaxial jet, i.e. heated primary and cold secondary flow, Eq. 3.51 has to be expanded and modified in order to account for the effects of area, temperature, and velocity ratio between the two jets. According to Stone, the additional term ΔL_{c-jet} or ΔL_{19} is defined as¹⁶:

$$\Delta L_{c-jet} = 5 \cdot \log_{10} \left(\frac{T_{t,9}}{T_{t,19}} \right) + 10 \cdot \log_{10} \left[\left(1 - \frac{v_{19}}{v_9} \right)^m + 1.2 \cdot \frac{\left(1 + \frac{A_{19}}{A_9} \cdot \frac{v_{19}^2}{v_9^2} \right)^4}{\left(1 + \frac{A_{19}}{A_9} \right)^3} \right] \quad (3.54)$$

The exponent m is defined as a function of the area ratio.

$$m = \begin{cases} 1.1 \cdot \sqrt{A_{19}/A_9} & \text{for } A_{19}/A_9 < 29.7 \\ 6.0 & \text{for } A_{19}/A_9 \geq 29.7 \end{cases} \quad (3.55)$$

Stone assumes that the spectrum of the coaxial flow is simply shifted relative to the isolated jet. Based on work by Olsen and Friedman [74] Stone introduces a frequency shift parameter f_{freq} as a function of the area ratio¹⁷; empirical values for f_{freq} are given in Fig. 2 of Ref. [25].

$$\begin{aligned} f_{freq} = & 0.1709 \cdot \left(\log_{10} \left(1 + \frac{A_{19}}{A_9} \right) \right)^3 \\ & - 0.6335 \cdot \left(\log_{10} \left(1 + \frac{A_{19}}{A_9} \right) \right)^2 + 1.1037 \cdot \log_{10} \left(1 + \frac{A_{19}}{A_9} \right) \end{aligned} \quad (3.56)$$

Knowing f_{freq} and Str_9 , a resulting Strouhal number Str_{c-jet} for the coaxial jet noise can be evaluated.

$$Str_{c-jet} = Str_9 \cdot \left(1 - f_{freq} \cdot \left[\frac{1}{2} + \frac{(T_{t,19} \cdot v_{19} \cdot A_{19}) / (T_{t,9} \cdot v_9 \cdot A_9)}{1 + (T_{t,19} \cdot v_{19} \cdot A_{19}) / (T_{t,9} \cdot v_9 \cdot A_9)} \right]^2 \right) \quad (3.57)$$

Finally, the mixing noise L_{jet} for a shock-free coaxial jet without refraction effects can be derived. The spectral shape and emission directivity is evaluated according to the relevant Strouhal number Str_{c-jet} of the coaxial jet and the corrected directivity angle α_{cor}^* .

$$L_{jet} = \underbrace{L_{norm}}_{Eq. 3.51} + \underbrace{\Delta L_{dir/spec}(Str_{c-jet}, \alpha_{cor}^*)}_{\text{data: Table 1, Ref. [25]}} + \Delta L_{c-jet} \quad (3.58)$$

If the engine is simulated along common approach procedures, often the resulting engine operating conditions are off-design. Along approach procedures, the engine is operated at low thrust settings while at the same time the flight velocity is still high. This can cause an inverse velocity profiles for core and bypass flow, i.e. the bypass is higher than the core flow velocity. Furthermore, there are situations when the aircraft flight velocity is larger than the engine exhaust velocities, i.e. core and/or bypass flow velocity. The presented noise source models are not capable of predicting engine noise emission for these operating conditions. In this case, an equivalent jet model is applied according to Ref. [78], see Section B. The core and bypass flow are translated into one mixed equivalent jet of equal mass flow, momentum,

¹⁶Note: Typo in Eq. 1 of Ref. [25]; missing division sign between " A_1 " and " V_1^2 ".

¹⁷Stones "frequency shift parameter" f_{freq} is not equal to the ratio of the Strouhal numbers! Furthermore, there is a typo in Eq. 3 and Fig. 2: the ratio of S_1/S is not correct, it should be S/S_1 . The typo results in increasing peak frequencies for the coaxial jet compared to a single jet. The opposite is true according to Olsens measurements depicted in Fig. 6 of Ref. [74]. The data clearly indicates the expected decrease in peak frequencies for coaxial jets compared to a single jet.

and enthalpy. For this equivalent jet, the corresponding jet noise is then evaluated according to Eq. 3.53. If the aircraft flight velocity is larger than this equivalent jet velocity, the flight speed is assumed to be equal to the jet velocity¹⁸.

(2) Fan noise - Overall fan noise generation at inlet and exhaust is separated into specific contributions, namely broadband, discrete-tone, and combination-tone noise. Whereas broadband and discrete-tone noise contribution originates from both the fan inlet and exhaust nozzle, combination-tone noise is located at the inlet station only. Depending on the operating condition of the fan, i.e. especially the flow velocity at the fan tip, only discrete tones or both discrete and combination-tones are prevailing [76]. At subsonic fan tip speeds, discrete tones dominate the overall noise emission and can be identified in the spectra. These tones occur at the so-called *blade passage frequency* f_b and higher harmonics of this frequency causing a noticeable whining sound at these higher frequencies [76]. The discrete tones are clearly visible in Fig. 3.5 at the corresponding harmonics. Increasing the engine thrust setting shifts the tones to higher frequencies according to the new engine rotation speed. For the presented forward emission angle of 40° , the discrete tone directivity yields a maximum. Backward emitted tones show decreased levels because the angle is slightly off the peak emission. The cyclic pressure field and the periodic wake interactions between

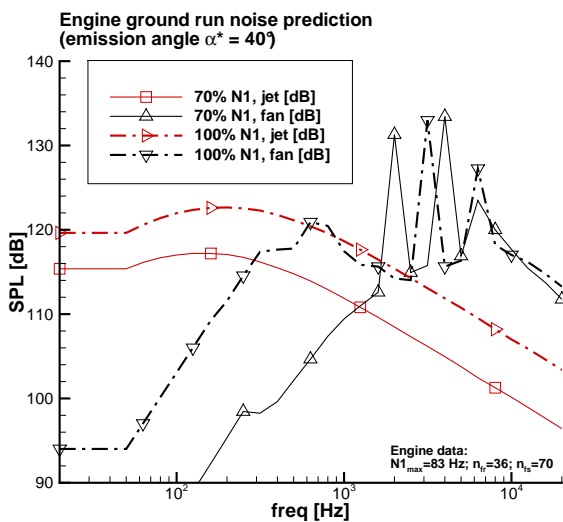


Figure 3.5: Engine noise spectra, emission angle $\alpha^* = 40^\circ$

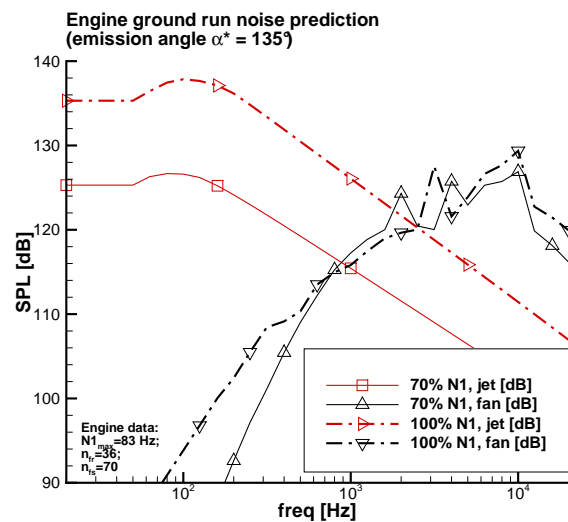


Figure 3.6: Engine noise spectra, emission angle $\alpha^* = 135^\circ$

fan rotors and stators are the source of these tones [16]. At lower and higher frequencies, broadband noise is predominant and perceptible as roaring or hissing [76]. The broadband or random noise contribution is caused by the interaction of the turbulent flow with both rotor and stator elements. Random pressure fluctuations on each blade can be induced by the turbulent inflow, eddy shedding in the wake of a blade or obstacle, and due to the interaction of a preceding blade row's turbulent wake with the subsequent blade row. Hereby, the major broadband noise contribution can be attributed to the fan blade tips. Each fan blade tip is exposed to the highest relative flow velocities and is furthermore moving through the turbulent boundary layer along the wall of the inner fan casing [16]. Overall, the broadband noise depends on the flow turbulence intensity, the relative flow velocity,

¹⁸Modification to the jet velocity would result in larger deviations. Reducing the flight speed does eliminate the jet mixing noise contribution as it can be expected in such an operating condition.

and the aerodynamic efficiency of the blades [16].

Reaching higher fan tip velocities modifies the spectral shape of the fan noise emission. If the fan tip speed reaches supersonic flow conditions, shock waves form in front of the blade and cause the so-called combination-tone noise in addition to the before mentioned broadband and discrete-tone noise. The combination-tone noise originates from the fan inlet and is dominant at lower frequencies due to atmospheric damping [16]. Combination-tone contribution causes a distinctive noise signal comparable to a sawmill, thus is often referred to as buzz-saw noise. The overall fan noise is dominated by these tonal noise contributions in the supersonic velocity regime [76]. The buzz-saw noise contribution is clearly visible in Fig. 3.5, when the engine setting is increased to full thrust. According to the specific emission directivity of buzz-saw noise, no contribution is observed for increased engine setting under backward emission angles, see Fig. 3.6.

As previously mentioned, the fan exhaust and inlet noise are each based on a common reference level L_{norm} . This level is proportional to the shaft power P times the specific work w of the fan stage. The shaft power P is in turn proportional to the total temperature rise $\Delta T_{t,2-13}$ over the fan stage multiplied with the airflow mass \dot{m} [77]. The specific work w , i.e. work per airflow mass, is proportional to the temperature rise only [77]. The temperature rise across the fan stage can be evaluated with the total pressure ratio $\Pi_{t,2-13}$ and the isentropic efficiency η_{is} [79], i.e. the ratio of the isentropic specific work and the actual required specific work over the fan stage.

For conventional turbofan engines, $\Delta T_{t,2-13}$ is usually in the order of 20 to 60 K and η_{is} of 0.7 to 0.9 according to the engine design and current operating condition [79]. With the assumption, that the total temperature $T_{t,2}$ remains constant over the fan inlet, the temperature rise can be evaluated¹⁹.

$$\Delta T_{t,2-13} = T_{t,2} \cdot \frac{1}{\eta_{is}} \cdot \left[\left(\Pi_{t,2-13}^{\frac{\kappa-1}{\kappa}} \right) - 1 \right] \quad (3.59)$$

Heidmann normalizes the temperature rise and the mass flow parameters with predefined reference levels, i.e. $\Delta T_{t,ref} = 0.555 \text{ K}$ and $\dot{m}_{ref} = 0.453 \text{ kg/s}$. Finally, the reference level L_{norm} can be evaluated.

$$\begin{aligned} L_{norm} &= 10 \cdot \log_{10} \left(\frac{\Delta T_{t,2-13}}{\Delta T_{t,ref}} \right) + 10 \cdot \log_{10} \left(\frac{\Delta T_{t,2-13} \cdot \dot{m}}{\Delta T_{t,ref} \cdot \dot{m}_{ref}} \right) \\ &= 20 \cdot \log_{10} \left(\frac{\Delta T_{t,2-13}}{\Delta T_{t,ref}} \right) + 10 \cdot \log_{10} \left(\frac{\dot{m}}{\dot{m}_{ref}} \right) \end{aligned} \quad (3.60)$$

In addition to L_{norm} , the contributions of (a) broadband, (b) discrete-tone, and (c) combination-tone are accounted for. Furthermore, additional correction factors c can be applied to the inlet or outlet noise levels.

$$L_{fan,in} = L_{norm} + \underbrace{L_{bbn,in}}_{(a)} + \underbrace{L_{dtn,in}}_{(b)} + \underbrace{L_{ctn,in}}_{(c)} + c_{in} \quad (3.61)$$

$$L_{fan,ex} = L_{norm} + \underbrace{L_{bbn,ex}}_{(a)} + \underbrace{L_{dtn,ex}}_{(b)} + c_{ex} \quad (3.62)$$

The components (a) - (c) are separately evaluated at both fan inlet and exhaust nozzle. At both stations, each of the components is defined according to three underlying functions, i.e.

¹⁹ κ denotes the specific heat of the medium.

a directivity function ΔL_{dir} , a spectral shape function $\Delta L_{spec}(f)$, and term ΔL_{vel} depending on the specific flow velocity at the fan tip. Within the presented work, Heidmanns original directivity and spectral shape functions are applied. Yet, the original formulations for ΔL_{vel} by Heidmann²⁰ have been adapted by Guérin to account for recent findings in fan design²¹. The modified formulations are still functions of the relative Mach numbers²², i.e. under selected (off-design) operating condition (Ma_{rel}) and for the design point (Ma_{rel}^d), but with different coefficients. Knowing Ma_{rel} and Ma_{rel}^d , the velocity dependent terms for (a) broadband, (b) discrete-tone, and (c) combination-tone can be evaluated at the corresponding engine station.

At the fan inlet, i.e. station ②, the broadband noise contribution $L_{bbn,in}$ is defined. Fully empirical data is provided for the emission directivity of the inlet broadband noise, i.e. L_{dir} ²³. Assuming rotational symmetry, the directivity is a function of the emission angle α^* only. Heidmann's original data defines the characteristic fan noise peaks for α^* in the range of 20 – 45°.

The spectral shape of the broadband emission is approximated as a function of frequency f and engine rotation speed times the blade count, i.e. blade passing frequency f_b .

$$\Delta L_{spec}(f) = 10 \cdot \log_{10} \left(\exp \left[-0.5 \cdot \left(\log \left(\frac{f}{2.5 \cdot f_b} \right) / \log(2.2) \right)^2 \right] \right) \quad (3.63)$$

This characteristic 1/3-octave spectrum for fan broadband noise is assumed constant for both fan inlet and discharge.

In contrast to the directivity and the spectral shape function, the original velocity dependent term L_{vel} has been adapted to account for current findings in fan design. Modifications by Guérin to the semi-empirical factors of the original Heidmann model result in accuracy improvement for modern turbofan engines with high by-pass ratios [44]. The parameter adaption results in the following new formulation.

$$\Delta L_{vel} = \begin{cases} 58.5 & \text{for } Ma_{rel}^d \leq 1.0 \wedge Ma_{rel} \leq 0.9 \\ 58.5 + 20 \cdot \log_{10}(Ma_{rel}^d) & \text{for } Ma_{rel}^d > 1.0 \wedge Ma_{rel} \leq 0.9 \\ 58.5 + 20 \cdot \log_{10}(Ma_{rel}^d) & \\ - 50 \cdot \log_{10}(Ma_{rel}/0.9) & \text{for } Ma_{rel}^d > 1.0 \wedge Ma_{rel} > 0.9 \\ 58.5 - 20 \cdot \log_{10}(Ma_{rel}^d/0.9) & \text{for } Ma_{rel}^d \leq 1.0 \wedge Ma_{rel} > 0.9 \end{cases} \quad (3.64)$$

Finally, broadband noise emission from the fan inlet at station ② can be defined.

$$L_{bbn,in} = L_{norm} + \Delta L_{dir} + \Delta L_{spec}(f) + \Delta L_{vel} \quad (3.65)$$

(b) Discrete-tone contribution to the fan inlet noise is referred to as $L_{dtn,in}$. As for the broadband contribution, the directivity is a fully empirical function, i.e. ΔL_{dir} ²⁴. The peak emission is predicted for α^* in the range of 20 to 40°.

²⁰Term "F1", Fig. 4 in Ref. [26]

²¹Institute of Propulsion Technology, DLR Berlin. Modifications are based on a NASA Contractor Report: K.B.Kontos, B.A.Janardan, P.R.Gliebe: *Improved NASA-ANOPP Noise Prediction Computer Code for Advanced Subsonic Propulsion Systems*, NASA-CR-195480, 1996

²²"Relative" Mach numbers are relative with respect to fan blade tip, i.e. contribution of axial and radial flow velocity.

²³Fig. 7 (a) in Ref. [26]

²⁴Term "F1", Fig. 13 (a) in Ref. [26]

For the rotor-stator interaction, levels for each discrete tone are defined by Heidmann. A noise level delta $\Delta L_h(i)$ is assigned to each harmonic "i". Heidmann assumes a 3 dB falloff per harmonic "i" and only accounts for the first five harmonics. For the first harmonic $\Delta L_h(1)$, a cut-off condition is evaluated in order to check whether the harmonic is propagable. The cut-off condition δ is defined according to the fan blade tip axial Mach number Ma and the number of rotors n_r and stators n_s .

$$\delta = \left| \frac{Ma}{1 - n_s/n_r} \right| \quad (3.66)$$

For $\delta > 1.05$, the first harmonic is propagable. Guérin defines different level deltas according to Ma , i.e. for $Ma < 1.15$, the following delta levels are applied:

$$\Delta L_h(i) = \begin{cases} 6.0 - 6.0 \cdot i & \text{for } \delta > 1.05 \\ -8.0 & \text{for } \delta > 1.05 \wedge i = 1 \\ 6.0 - 6.0 \cdot i & \text{for } \delta > 1.05 \wedge i \in [2, 5] \end{cases} \quad (3.67)$$

For $Ma_{rel} \geq 1.15$ the following delta levels are applied:

$$\Delta L_h(i) = \begin{cases} 9.0 - 9.0 \cdot i & \text{for } \delta > 1.05 \\ -8.0 & \text{for } \delta > 1.05 \wedge i = 1 \\ 9.0 - 9.0 \cdot i & \text{for } \delta > 1.05 \wedge i \in [2, 5] \end{cases} \quad (3.68)$$

According to the frequency of harmonic "i", the discrete tones are arranged into 1/3-octave bands. If multiple harmonics fall into one frequency band, energetic summation is applied. Finally, a spectral contribution can be defined, i.e. $\Delta L_{spec}(f)$.

Again, a velocity dependent term ΔL_{vel} is defined as a function of the Mach numbers at a representative blade section. As mentioned before, the empirical factors have been adapted by Guérin [44].

$$\Delta L_{vel} = \begin{cases} 60.5 & \text{for } Ma_{rel}^d \leq 1.0 \wedge Ma_{rel} \leq 0.72 \\ 60.5 + 20 \cdot \log_{10}(Ma_{rel}^d) & \text{for } Ma_{rel}^d > 1.0 \wedge Ma_{rel} \leq 0.72 \\ C & \text{for } Ma_{rel}^d > 1.0 \wedge Ma_{rel} > 0.72 \end{cases} \quad (3.69)$$

The auxiliary term C is evaluated with one of the following formulations. The formulation with the lowest value for the selected Mach numbers is selected.

$$C = \begin{cases} 60.5 + 20 \cdot \log_{10}(Ma_{rel}^d) + 50 \cdot \log_{10}(Ma_{rel}/0.72) \\ 64.5 + 80 \cdot \log_{10}(Ma_{rel}^d/Ma_{rel}) \end{cases}$$

If the engine is operated in flight, an empirical correction for the inlet flow distortion is applied, i.e. c_{dist} . Operation on the ground does not require a correction.

Finally, the discrete tone contribution to the forward fan emission can be defined.

$$L_{dtn,in} = L_{norm} + \Delta L_{vel} + \Delta L_{dir} + \Delta L_h(f) + c_{dist} \quad (3.70)$$

(c) Combination-tone noise is defined as L_{ctn} and occurs if the relative tip Mach number $Ma_{rel} \geq 1$, thus no combination-tone noise is generated for the subsonic case. Heidmann describes the directivity of the buzzsaw noise with empirical functions, i.e. ΔL_{dir} ²⁵. The

²⁵Fig. 16 in Ref. [26]

buzzsaw noise spectral content is approximated by three functions according to Heidmann's model²⁶. Noise peaks are defined at a half, fourth, and eighth of the blade passing frequency f_b . Noise levels are linearly increasing up to the peak and decreasing after the peak. Three combination-tone noise functions are defined: $\Delta L_{1/2 f_b}$, $\Delta L_{1/4 f_b}$, and $\Delta L_{1/8 f_b}$. Individual peak levels with respect to the engine operating condition, i.e. Ma_{rel} , are assigned to each of these functions. For each function, such a empirical and velocity dependent peak value ΔL_{vel} is defined. Due to the somewhat antique underlying database for Heidmann's original model, especially the buzzsaw noise contribution has been overpredicted in the past. Therefore, modifications to each ΔL_{vel} are applied by Guérin to account for recent findings.

$$\Delta L_{vel, 1/2 f_b} = \begin{cases} 30.0 & \text{for } Ma_{rel} \leq 1.0 \\ 72.5 & \text{for } 1.0 < Ma_{rel} \leq 1.14 \\ 4.4 & \text{for } 1.14 < Ma_{rel} \leq 2.0 \end{cases} \quad (3.71)$$

$$\Delta L_{vel, 1/4 f_b} = \begin{cases} 30.0 & \text{for } Ma_{rel} \leq 1.0 \\ 68.6 & \text{for } 1.0 < Ma_{rel} \leq 1.25 \\ 10.5 & \text{for } 1.25 < Ma_{rel} \leq 2.0 \end{cases} \quad (3.72)$$

$$\Delta L_{vel, 1/8 f_b} = \begin{cases} 36.0 & \text{for } Ma_{rel} \leq 1.0 \\ 60.6 & \text{for } 1.0 < Ma_{rel} \leq 1.61 \\ 56.5 & \text{for } 1.61 < Ma_{rel} \leq 2.0 \end{cases} \quad (3.73)$$

Finally, the three spectral shape functions can be defined.

$$\Delta L_{1/2 f_b} = \Delta L_{vel, 1/2 f_b} + \begin{cases} -30.0 \cdot \log_{10}\left(\frac{2f}{f_b}\right) & \text{for } \frac{f}{f_b} > 0.5 \\ +30.0 \cdot \log_{10}\left(\frac{2f}{f_b}\right) & \text{for } \frac{f}{f_b} \leq 0.5 \end{cases} \quad (3.74)$$

$$\Delta L_{1/4 f_b} = \Delta L_{vel, 1/4 f_b} + \begin{cases} -50.0 \cdot \log_{10}\left(\frac{4f}{f_b}\right) & \text{for } \frac{f}{f_b} > 0.25 \\ +50.0 \cdot \log_{10}\left(\frac{4f}{f_b}\right) & \text{for } \frac{f}{f_b} \leq 0.25 \end{cases} \quad (3.75)$$

$$\Delta L_{1/8 f_b} = \Delta L_{vel, 1/8 f_b} + \begin{cases} -30.0 \cdot \log_{10}\left(\frac{8f}{f_b}\right) & \text{for } \frac{f}{f_b} > 0.125 \\ +30.0 \cdot \log_{10}\left(\frac{8f}{f_b}\right) & \text{for } \frac{f}{f_b} \leq 0.125 \end{cases} \quad (3.76)$$

These separate shape functions are finally arranged into 1/3-octave bands to yield the overall spectrum, i.e. $\Delta L_{spec}(f)$.

Ultimately, the combination-tone or buzzsaw noise contribution for $Ma_{rel} \geq 1$ can be defined. If required, some empirical correction is applied in order to account for inlet flow distortion, i.e. c_{dist} .

$$L_{ctn, in} = L_{norm} + \Delta L_{dir} + \Delta L_{spec}(f) + c_{dist} \quad (3.77)$$

²⁶Fig. 14 in Ref. [26]

Two contributions, namely (a) broadband and (b) discrete-tone noise are defined at the fan exhaust, i.e. station ⑬.

$$L_{fan,ex} = L_{norm} + \underbrace{L_{bbn}}_{(a)} + \underbrace{L_{dtn}}_{(b)} \quad (3.78)$$

In accordance with the fan inlet definition, each of the contributions (a) and (b) is comprised of directivity, spectral shape, and velocity dependent terms.

(a) The velocity dependence of the fan broadband noise is defined as ΔL_{vel} . In contrast to Heidmanns original formulation, Guérins modifications are applied.

$$\Delta L_{vel} = \begin{cases} 63.0 & \text{for } Ma_{rel}^d \leq 1.0 \wedge Ma_{rel} < 1.0 \\ 63.0 + 20 \cdot \log_{10}(Ma_{rel}^d) & \text{for } Ma_{rel}^d > 1.0 \wedge Ma_{rel} \leq 1.0 \\ 63.0 + 20 \cdot \log_{10}(Ma_{rel}^d) - 30 \cdot \log_{10}(Ma_{rel}) & \text{for } Ma_{rel}^d > 1.0 \wedge Ma_{rel} > 1.0 \end{cases} \quad (3.79)$$

For the directivity of the broadband exhaust noise emission, Heidmann's original empirical functions are selected²⁷. The directivity function ΔL_{dir} predicts noise peaks under emission angles of $\alpha^* = 120 - 140^\circ$. Furthermore, the characteristic 1/3-octave broadband noise spectrum, i.e. $\Delta L_{spec}(f)$, is applied as described in Eq. 3.63.

An additional contribution c is defined to account for the spacing between rotor and stator disc, ξ_{rss} . In contrast to Heidmanns original formulation, Guérin only applies c to the fan discharge at station ⑬.

$$c = -5 \cdot \log_{10}\left(\frac{1}{3} \cdot \xi_{rss}\right) \quad (3.80)$$

Ultimately, broadband noise emission from the fan discharge is defined as:

$$\Delta L_{bbn,ex} = L_{norm} + \Delta L_{vel} + \Delta L_{dir} + \Delta L_{spec}(f) + c \quad (3.81)$$

(b) A velocity dependent term is defined for the discrete-tone noise contribution at the fan exhaust. In contrast to the formulations for the fan inlet, no modifications to Heidmanns original definitions are applied²⁸.

$$\Delta L_{vel} = \begin{cases} 63.0 & \text{for } Ma_{rel}^d \leq 1.0 \wedge Ma_{rel} \leq 1.0 \\ 63.0 + 20 \cdot \log_{10}(Ma_{rel}^d) & \text{for } Ma_{rel}^d > 1.0 \wedge Ma_{rel} \leq 1.0 \\ 63.0 + 20 \cdot \log_{10}(Ma_{rel}^d) - 20 \cdot \log_{10}(Ma_{rel}) & \text{for } Ma_{rel}^d > 1.0 \wedge Ma_{rel} > 1.0 \end{cases} \quad (3.82)$$

Furthermore, the empirical functions for spectral shape and directivity of the discrete-tone emission are Heidmanns original formulations, i.e. $\Delta L_{freq}(f)$ and ΔL_{dir} ²⁹. To account for geometrical effects, the correction factor c_ξ , as described in Eq. 3.80, is applied. Ultimately, the discrete-tone noise contribution of to the fan exhaust noise can be evaluated.

$$L_{dtn,ex} = L_{norm} + \Delta L_{vel} + \Delta L_{dir} + \Delta L_{spec}(f) + c_\xi \quad (3.83)$$

Limitations and Applicability - Reliability and validity of results is limited to the underlying database because extrapolation is not recommended [75]. Stone's database does not impose significant restrictions to jet noise modeling because the relevant parameter domain for the presented work is covered, i.e. preferred engine sizes and thrust requirements

²⁷Fig. 7 (b) in Ref. [26]

²⁸Fig. 10 (b) in Ref. [26]

²⁹Figs. 8 and 13 (b) in Ref. [26]

are mapped. The selected fan noise model by Heidmann is based on a somewhat antique database hence application should be limited to older engine types with low bypass ratios. In order to apply Heidmann's approach to modern turbofan engines, adaption and modification of the inherent empirical constants becomes necessary. Recent studies from NASA [28] show that such a modified approach can be applied for quite a wide range of fan pressure ratios, tip speeds, and bypass ratios. It is demonstrated, that predicted results are usually within a ± 4 dB margin with respect to the measurements [28] for bypass ratios up to 13.3, i.e. a satisfying agreement to the experimental data. PANAM's implemented fan noise model features similar modifications of Heidmann's original constants. Therefore, it is assumed that the implemented engine noise source models can be applied to modern turbofan engines up to high bypass ratios around 15. Application of the methods to engine concepts other than turbofan or even higher bypass ratios does not seem feasible. Applying the models that far off from the experimental and knowledge database will result in unpredictable uncertainties [28,75].

3.2.2.3 Noise Shielding Effects

The analysis of noise shielding effects is of growing importance with regard to future aircraft concepts, e. g. blended wing bodies or the DLR low-noise aircraft (LNA). At DLR, the ray tracing tool SHADOW [83] has been developed in order to investigate different engine installations with respect to structural noise shielding. The tool by M. Lummer³⁰ combines fast computation and at the same time simplified input requirements. As a consequence, the tool is well suited for application within conceptual aircraft design. The required input data for SHADOW, i.e. aircraft geometry and engine alignment, can directly be generated at the conceptual design phase. For a selected aircraft/engine design, frequency dependent noise attenuation factors are predicted with SHADOW and then fed back into PANAM for further processing. The attenuation factors are then accounted for in PANAM when simulating the fan noise contribution [84].

SHADOW is based on a high frequency approximation of the linearized Euler equations where the pressure field is calculated by solving ordinary differential equations along lines in space, so-called rays. These rays originate in a point source, which approximates the center of the fan disc. Furthermore, no mean flow effects are taken into account and the aircraft geometry is approximated by a triangulated surface. If required, the triangulated surfaces may optionally be refined with tools such as ADMesh. This surface definition allows for great flexibility in representation of complex geometries. Furthermore, a local 2nd-order polynomial geometry approximation is applied to take into account the surface curvature, thus enable proper calculation of the ray reflection.

The pressure amplitude along each ray is calculated based on an energy conservation principle, which requires the calculation of the Jacobian of the ray-field. Evaluating the Jacobian with a difference approximation can lead to problems due to strong divergence of the rays after multiple reflections. Therefore, a differential equation for the Jacobian was derived and integrated along with the ray equations [83].

In order to calculate the acoustic shielding at prescribed points in space, a shooting procedure using a Newton algorithm is applied. In the high frequency limit the diffractive part of

³⁰Institute of Aerodynamics and Flow Technology, DLR Braunschweig

the solution of the wave equation is lost. Thus, in ray-tracing the diffraction has to be taken into account by special approximations, like, e.g., the geometrical theory of diffraction [85]. While this approach yields quite accurate results, its implementation for arbitrary geometries is complicated. Therefore, a more simple approach based on the Maggi-Rubinowicz formulation of the Kirchhoff diffraction theory has been implemented [86,87]. In this case, the diffracted field is calculated by a line integral along the shadow boundary on the surface of the diffracting body. In contrast to the ray field, the diffraction correction is frequency dependent. Since only the acoustic far field is calculated in the implemented form of the high frequency approximation, it is sufficient to consider acoustic point sources [83].

3.2.2.4 Acoustic Lining

A model to account for noise absorption due to acoustic liners has been implemented. The method as developed by Moreau, Guérin, and Busse [81] improves result accuracy especially under take-off conditions [125]. The original source code by Guérin is adapted and integrated into PANAM. The liner damping model is derived from the ray theory which makes it fast enough for applications at the conceptual aircraft design phase. Liners mounted in both the engine intake and bypass duct can be investigated. As a consequence, the respective length of the lining is required as an input. The following brief description is based on Ref. [125].

In a first step, the sound field generated by the fan stage is synthetically decomposed into relevant acoustic modes (m, n) . Assuming hard-wall boundary conditions and applying a ray theory, the ray structures of the cut-on modes can be determined. According to the angle at which a ray impinges on the wall and the number of bounces along this ray, a sound attenuation is predicted for each mode. Here, it is assumed that the liners do not significantly modify the propagation angles nor induce mode scattering. The far-field directivity is supposed to remain unchanged despite an existing effect by acoustic lining in real applications. A model based on the liner geometry and inflow conditions is applied to predict the wall impedance. A modal content is synthesized for each individual engine operating point of the simulation. A specific approach is used for the three noise components identified by Heidmann [26]. For broadband noise, all the cut-on modes are contained and supposed to propagate the same acoustic energy (*Equal Modal Energy Model*). Furthermore, in order to reduce computational requirements, the liner attenuation is calculated only for the center-frequencies of each one-third octave band. The tones at multiple of the blade passing frequency are all assumed to be generated by the rotor-stator interaction mechanism. The azimuthal order of those modes can be calculated according to the number of rotor and stator blades with the Tyler and Sofrin rule [82]. The same power amplitude is given to all the radial orders. Finally, the modal content of buzz-saw noise has to be determined in the transonic regime of the fan [81]. Since buzz-saw is a rotor-locked mechanism, the azimuthal order of each engine order tone can be assumed to have the same value as the engine order itself. Then, within a given one-third octave band all the engine orders are considered to have the same amplitude [81]. The energy of the radial order components is chosen to be equal, too. The implementation of Guérin's liner model makes it possible to predict and investigate the influence of the acoustic lining on the noise contribution of the fan.

3.2.3 Tool Input

Input data requirement is defined according to the implemented noise source models for both airframe and engine. The required input data for PANAM is comprised of (1) aircraft design, (2) engine design parameters with a detailed engine performance deck, (3) a simulated flight trajectory with configuration settings/operating conditions, and (4) the location of the respective observer. Relevant input data can be generated with corresponding tools or has to be provided by the user in order to initiate a noise prediction.

PANAM simulates the overall aircraft noise as a combination of relevant components, i.e. wing/control surface(s), landing gear(s), and engine(s). Each type of component is simulated with a corresponding noise source model as described in the previous sections. The selected models are defined by a broad parameter set, especially if compared to other prediction models such as Fink's Airframe Noise Prediction Method [24]. According to this parametrical definition, specific input data is required for each modeled noise source. More than one noise source of the same type but with different parameter setting can exist, e.g. if a wing or control surface is represented by several segments. In this case, each segment has to be defined according to the individual shape, high lift, and spoiler design.

As a consequence, the amount of required input data can become quite extensive. Nevertheless, the complexity of these parameters is well suitable for conceptual aircraft design and the required information can be generated with available and standard vehicle design methods. If only limited input data is available, it is possible to switch back to a simplified geometry representation, i.e. only accounting for one representative and averaged element per noise source type.

3.2.3.1 Aircraft design

Wing and control surfaces are separated into acoustically relevant segments, i.e. segments with constant flap, slat, and airfoil geometry. Dealing with unconventional aircraft configurations, such a segmentation is inevitable to guarantee feasible representation of the geometry. Each segment is defined by multiple and individual parameters instead of working with averaged and representative dimensions for each major noise source. The required input parameters are segment type and corresponding geometry details. Four segment types are accounted for: (1) clean airfoil, (2) airfoil with leading edge devices (led), (3) airfoil with trailing edge devices (ted), and (4) airfoil with led and ted. Each of these segment types is defined by 9 parameters: (a) width, (b) chord length, (c) twist distribution, (d) dihedral angle, (e) leading and (f) trailing edge sweep angle of the segment. Furthermore, if equipped with a high lift devices, the corresponding chord length of leading (g) and/or trailing edge (h) device is required. Additional installation of a spoiler element on a segment requires (i) the width of this component.

Each landing gear is defined by three parameters: (a) wheel diameter, (b) extended length of the gear, and (c) number of axles. Furthermore, if an under-the-wing installation is selected, a fourth parameter, the main wing chord length (d) has to be evaluated at the location of the gear-wing-junction.

The relative location of each engine and the actual overall weight of the vehicle complete the list of required aircraft design parameters for a PANAM run. If all parameters are generated, the individual noise sources can be assembled into one acoustically analogous model of the overall aircraft.

An additional 3D vehicle description has to be provided, if noise shielding effects are

investigated. To evaluate shielding effects with the DLR ray tracing tool SHADOW [83], a surface mesh of the corresponding vehicle is required, e.g. a triangulated surface model in Standard Tessellation Language (STL). Furthermore, the precise location of the engines is evaluated and provided as an input for SHADOW.

Engine design

Engine design parameters and performance decks are required for the engine noise simulation. The required input data is comprised of detailed engine geometry parameters and an overall engine performance map. This so-called engine performance deck is comprised of precomputed thermodynamic and aerodynamic parameters for each one combination of flight altitude, flight speed, and engine operational setting (thrust or rotational speed setting). According to the simulated engine operation, relevant parameters are extracted from the stored performance deck.

Required geometry parameters and design constants are (1) number of fan rotor and stator blades, (2) spacing between rotor and stator, (3) fan hub-to-tip ratio, (4) fan diameter, (5) maximum rotation speed, (6) fan blade chord length, (7) design Mach number at the fan tip, and (8) core and bypass flow exhaust areas.

For each selected operating condition of the engine, multiple input variables are required. These performance parameters depend on the operating condition and comprise (1) bypass/core exhaust jet velocities, (2) bypass/core exhaust temperatures, (3) bypass/core exhaust flow densities, (4) fan total pressure ratio, (5) isentropic fan efficiency, and (6) maximum turbine entry temperature. All additional input parameters for a PANAM noise prediction can be derived from these basic requirements.

If acoustical lining is accounted for, additional geometry parameters are required, i.e. the liner length in both bypass and core duct, if available.

Flight trajectories

For each simulated flight position of the vehicle, specific data is required with respect to location, orientation and operation of the aircraft. Hereby, the aircraft location can be provided as either GPS information, including flight altitude over ground, or directly in relative coordinates with respect to a defined ground location. Aircraft orientation is described by the three Euler angles with respect to the flight path angle or inflow direction. The inflow direction is determined according to three consecutive flight positions, as previously described. Finally, the aircraft operation is described by (1) the flight velocity, (2) the commanded engine operation (thrust or rotational speed setting), and (3) the vehicle configuration. The configurational setting is defined by the deflection angles of (a) trailing edge and leading edge high lift device, (b) spoiler elements, and (c) the position of each landing gear.

Observer locations

Arbitrary observer locations can be selected for the noise prediction. Depending on the selected task, level-time-histories or isocontour areas, individual observers or microphone arrays can be processed. Individual observer property settings can be defined for each location, i.e. ground resistivity to air, observer altitude, microphone height, and population density if required. This allows to define and simulate arbitrary airport surroundings with a realistic population distribution, if available.

3.2.4 Modi operandi

Providing the required input data as previously described, a PANAM run can be initiated. PANAM's flexible setup allows for three different run-modes: (1) *autarkic/stand-alone mode*, (2) *controlled operation* within a multidisciplinary simulation environment, and (3) *modular operation* directly embedded within an overall aircraft design process.

For the (1) autarkic/stand-alone operation, the necessary input data has to be provided by the user. In this modus, a simple graphical user interface supports the user to command and operate the noise prediction process³¹. After the computation, the prediction results can then manually be evaluated by the user.

If PANAM is operated within a (2) simulation environment, required input data is automatically generated if corresponding tools are embedded in the simulation process under consideration. To enable automated operation within the simulated process, PANAM features script-based operation without user interface.

PANAM can be operated within DLR's TIVA [45] simulation environment. DLR has established a common system to enable distributed multidisciplinary conceptual aircraft design [46]. The TIVA system is based upon a common data exchange format to establish a framework for the integration of tools and methods from multiple disciplines and experts. The implemented tools come from specialized DLR institutes, are harmonized in input/output format and are integrated into one fully automated analysis process. The PHX ModelCenter framework [47] allows for a DLR-wide accessible server/client architecture. Currently, tools from corresponding disciplines are available and can be implemented into individual process chains to provide input data for the noise prediction. Interfaces to various DLR high fidelity and expert tools are established, e.g. flight simulation tools.

Ultimately, noise prediction input and output data can be made accessible for other tools via network connection. Parts of the input data for the noise prediction can remain constant whereas other input parameters will be generated and provided by embedded expert tools. For example, to investigate low-noise flight operation of a specific aircraft, PANAM is connected to a flight performance tool whereas predefined aircraft and engine parameters are made accessible as stored input data [84, 92, 93]. Furthermore, linking PANAM to high fidelity simulation tools can improve result accuracy, e.g. due to detailed engine cycle analysis with the VarCycle [80] tool³².

PANAM's (3) modular run-mode allows for direct operation within an overall aircraft design process. This third PANAM run-mode is of dominating importance in the context of the presented work, enabling an aircraft design process with integrated noise prediction capabilities.

3.2.5 Tool Output

3.2.5.1 Individual Flyover Event

Individual flyover events are the default application for PANAM. The data output includes noise levels for each individually modeled aircraft component as well as levels for the overall aircraft. Noise level frequency spectra for individual components can be provided for

³¹GUI is based on a concept by IFL, Technical University Braunschweig

³²VarCycle is an one-dimensional, off-design performance calculation program developed by the Institute of Propulsion Technology (AT)

any specified operating condition along a simulated flight path. Furthermore, level-time-histories, weighted or time-integrated noise metrics can be predicted for each flyover event. The time-integrated and weighted output data includes the standard flyover noise measures, e.g. (A-weighted) Sound Pressure Level and Effective Perceived Noise Level (EPNL). For a grid of observer locations the distribution of noise levels as received on the ground can be generated. Animated noise footprints for each one time step as well as visualizations of time-integrated noise footprints can be generated. This allows for real-time evaluation of the influence of aircraft operating conditions and configurational settings on the overall noise radiation. Noise related effects can be identified, visualized, and ultimately analyzed [84]. Isocontour areas of the max. Sound Pressure Level (SPL) can be translated into a probability distribution of aircraft noise induced awakenings [3]. Multiplied with a given population density, one can evaluate the number of affected people, i.e. awake people due to a single aircraft flyover noise event. This scalar value is well suited as a design objective within an optimization process. Obviously, the population density around a typical airport is very inhomogeneous. But due to the complexity of modeling the communities around a real airport and the lack of available data, usually an average and constant population density is assumed³³.

3.2.5.2 Multiple Flyover Events

Multiple flyover events can be simulated with the code as well. Arbitrary combinations of individual flyover events are arranged into a multiple flyover scenario. Equivalent Sound Pressure Levels (*aequivalenter Dauerschallpegel*, L_{eq}) are computed for arbitrary combinations of aircraft, fleet mix, flight operation, and runway layout. The computations are performed according to Ref. [90].

$$L_{eq} = k \cdot \log_{10} \left(\frac{t_{ref}}{T} \cdot \sum_{i=1}^N g_i \cdot 10^{L_{E,i}/k} \right) + C \quad (3.84)$$

The flyover events (N) within a predefined time span (T) are summed up for an arbitrary observer location. $L_{E,i}$ is the noise level for one individual flyover event (i), t_{ref} is the specific time span defined for L_E , g_i is the time dependent weighting factor. Parameter k depends on the summation of the individual noise levels, e.g. $k = 10$ for energetic summation. Finally, the resulting levels are scaled/normalized by factor C . The most common noise metrics can be evaluated according to the parameter setting defined in Section B, Appendix. To speed up computational time, the ground noise distribution for each combination of (1) aircraft, (2) flight procedure, and (3) selected runway is precomputed and stored within a database. Simulating a selected flight plan, comprised of arbitrary combinations of available settings (1) to (3), is then predicted based on the precomputed database within seconds.

The most commonly used L_{eq} is the Day-Evening-Night Sound Level (L_{DEN}). A noise response relationship by the European Commission translates the L_{DEN} into aircraft noise induced annoyance [91]. Ultimately, L_{DEN} isocontour areas for multiple flyover events/scenarios can be reduced to one scalar value applicable as a design objective within an optimization process.

³³For example, current population density of Germany with 231 people per square kilometer.

3.2.5.3 Optional Output Data

Geographical Noise Impact Visualization Geographical noise impact visualization enables a better understanding on how aviation impacts local communities and their annoyance toward noise pollution. Overlapping noise isocontour plots with maps of local communities will identify noise affected areas and population. Hereby, noise impact on sensitive areas such as highly populated residential areas can directly be evaluated. For a predefined airport scenario with given runway layout and airspace routing, PANAM transforms the flight trajectories and resulting noise isocontour areas into WGS84 coordinates to load them into a geographical visualization tool, e.g. Google Earth [89]. Various noise metrics for individual or multiple flyover events can be visualized.

Gaseous Engine Emissions Gaseous engine emissions are summed up along simulated flight procedures. Obviously, this optional output depends on the availability of emission data for the selected engine. If emission data is available, e.g. by DLR tool VarCycle [80], flight procedures can be modified for best environmental performance, i.e. evaluation of noise vs. gaseous emissions vs. required fuel. Results of an initial trade study for individual flyover events have been published in 2009 [84].

3.3 Aircraft Design with Integrated Noise Prediction Capabilities

PANAM was specifically developed for direct application within the aircraft design synthesis code PrADO [48–50], an in-house development of the Technical University Braunschweig, Germany. PrADO can assess the feasibility of new aircraft concepts at the conceptual aircraft design stage. The PrADO framework is comprised of individual design modules, each dedicated to a certain task or discipline. All modules are embedded into a monolithic structure resulting in one large program code and therefore very fast computation times [45]. Each of PrADO's design modules offers a selection of methodologies to solve its designated task. The selected methodology determines the overall computational requirement, result accuracy, and most importantly the input data requirement.

The top level aircraft requirements and a basic vehicle layout comprise the input for the design synthesis process. The overall design process is a sequential execution of individual PrADO design modules in a predefined order. This simulation sequence is repeated until predefined design parameters reach convergence. Selected design parameters can be for example aircraft mass, thrust requirement, design mission performance, and field length requirement. If the predefined parameters reach convergence, the simulation process is successfully ended and a final vehicle design is identified. Implementation of new methodologies into preexisting modules as well as integration of new design modules into the framework are possible due to PrADO's flexible setup.

A dedicated module for noise related data I/O is implemented into the PrADO framework to connect the aircraft design process to PANAM [40, 42]. This additional module, referred to as IOPANAM, was developed to perform three specific tasks: (1) provide required data input for PANAM, (2) execute the noise prediction, and (3) collect output data and return the PANAM results into the PrADO process. IOPANAM performs these tasks fully automatically, thus can be operated as one of the self-contained modules within the

PrADO framework [44, 88, 94]. Returning PANAM results back to the PrADO framework establishes a design process with integrated noise prediction capabilities, i.e. introducing noise as a new design constraint. Thereby, arbitrary PANAM results can be selected as overall design criteria, e.g. noise isocontour areas along approach and departure.

The three essential tasks of IOPANAM are briefly discussed in following sections.

IOPANAM can be operated in an autarkic and PrADO independent run-mode, if a complete PrADO data set is available. Saving the complete data set after a successful PrADO vehicle synthesis, comprises the required basic information for IOPANAM to generate the PANAM input data. Based on the PrADO data set, IOPANAM can then perform the flight simulation and finally initiate the noise prediction. In conclusion, having the corresponding PrADO data set for a specific aircraft, enables an autarkic IOPANAM analysis of low-noise flight operation for the underlying vehicle.

In order to investigate engine noise shielding effects, an interface to the tool SHADOW [83] is implemented into IOPANAM. IOPANAM automatically generates the required input data for a SHADOW run, i.e. a triangulated surface of the vehicle and the position of the engine (fan disc center). Yet, SHADOW is not fully automated within the conceptual design process but still an external process. After IOPANAM generates the input, SHADOW is executed as a postprocess and the simulation results can then be returned back for the final overall aircraft noise simulation with PANAM.

Input data

Based on PrADO simulation results, IOPANAM generates the required input data, i.e. aircraft geometry, engine data, and the flight procedure.

Vehicle design - A geometry separation algorithm for wing and control surfaces is implemented into IOPANAM [44, 88]. Relevant acoustical component segments are automatically identified and assigned according to their classification as described in Section 3.2.3.1. Dealing with complex and exotic configurations, the segmentation approach becomes inevitable to guarantee feasible representation of the geometry, see Fig. 3.7. Yet, if a conventional aircraft design is evaluated, the segmentation only seemingly improves the prediction accuracy [70, 71].

Engine data - PrADO's standard engine simulation model is based on the concept of Mattingly³⁴, thus considered to be very sophisticated and computationally expensive for a conceptual aircraft synthesis code. Due to this profound engine simulation, most of PANAM's required input data can be generated after some IOPANAM data transformation. While general thermodynamic performance parameters, e.g. exhaust jet velocities, are direct outputs of the Mattingly model, additional effort is required to generate engine rotational speed according to a selected thrust setting [88, 94]. Any correlation between thrust setting and rotation speed is a simplification, thus can be subject to large uncertainties. Specific engine geometry parameters and performance characteristics, e.g. maximum turbine entry temperature, can not be generated at the conceptual design phase. These detail parameters have

³⁴Mattingly, Heiser, Pratt: *Aircraft Engine Design*, AIAA Education Series, 2002, 2nd Edition, 719 pages, ISBN: 1-56347-538-3.

to be provided as user specified input for PrADO due to their complexity. The "manual" selection of these specific parameters can dominate the performance simulation and any subsequent noise prediction. If the input parameters are adequately selected and adapted to a specific existing engine, a satisfying agreement of simulation and existing experimental data can be achieved [88,94]. If significant engine noise overprediction is experienced, it can directly be attributed to uncertainties in the PrADO engine simulation or to a poor selection of the user specified parameters [88,94].

In general, a tendency of noise level overprediction is experienced if the PANAM noise prediction is solely based on PrADO engine data. To avoid possible input data uncertainties, the noise prediction within this work is based on VarCycle results [80]. If not otherwise indicated, the presented engine noise predictions within this work are based on a fixed VarCycle engine concept. In this case, the user specific engine parameters are pre-evaluated and directly provided by DLR engine specialists.

Flight simulation - PrADO comes with dedicated software libraries for flight simulation [48]. IOPANAM is using these PrADO libraries in order to simulate predefined flight operation of a PrADO vehicle. All relevant input parameters for the flight simulation are available after a successful PrADO design synthesis. An approach or departure flight trajectory can be simulated according to predefined user input. The principle layout of these procedures depends on the selection of fixed waypoints and corresponding flight segments. Each flight segment can be defined by constraints to flight path angles, flight speed, thrust setting, and configurational setting. The final flight trajectory is ultimately assembled from these individual segments. Thereby, IOPANAM generates smooth transitions between individual flight segments, i.e. avoiding artificial jumps and discrepancies in the resulting flight parameters. After the IOPANAM run, all the required data as described in Section 3.2.3.1 is available.

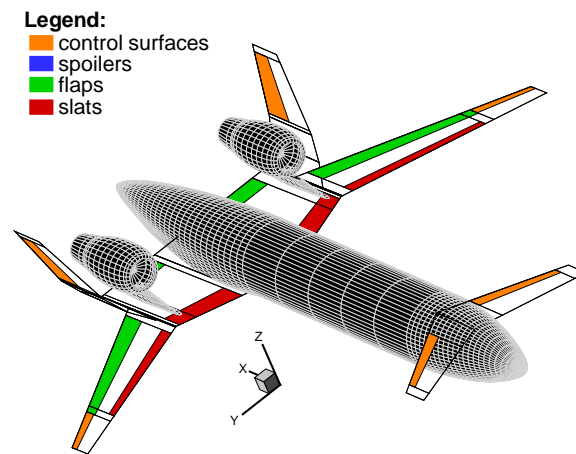


Figure 3.7: PANAM acoustical analogous model

4 Validation

4.1 Conceptual Design vs. Aircraft Data and Specifications

PrADO simulation results for existing aircraft can directly be compared with available literature and manufacturer data. Very good agreement between simulated and real vehicles can be achieved for conventional and subsonic transport aircraft [48–50]. Simulating these vehicles, prediction uncertainties for the most important design parameters are usually in the order of $\pm 2\%$, i.e. for maximum take-off weight, operational empty weight, mission range, and required block fuel¹.

The magnitude of prediction uncertainties of a PrADO run depends on the selected modules and on the case specific input data quality. Input data for a PrADO run comprises detailed vehicle geometry parameters, design constraints, and preselected mission requirements. Based on this input PrADO computes aircraft weights and simulates the vehicle along preselected missions and flight segments, in order to evaluate the overall vehicle performance.

For the selected reference aircraft, an Airbus A319-100 (weight variant *WV012*), the vehicle weights are underpredicted by less than 4% compared to manufacturer data [101], see Tab. 4.1. The PrADO payload-range diagram as depicted in Fig. 4.1 is in very good agreement to published diagrams by the manufacturer [101] and other published data [102]. If breaking coefficients and rotation rates are adequately selected², the predictions and published data for take-off and landing field length requirements [102] can be shifted to excellent accordance, i.e. prediction vs. publication of 1434.78 vs. 1430 m (landing) and 1701.86 vs. 1720 m (take-off). To further enhance the overall agreement of prediction results and

OEW [kg]			MTOW [kg]			MLW [kg]			MZFW [kg]		
P	M	Δ	P	M	Δ	P	M	Δ	P	M	Δ
38641	39725	-2.7%	60815	62400	-2.5%	58588	61000	-3.9%	55637	57000	-2.4%

Table 4.1: Reference Aircraft A319-100: PrADO (P) weight predictions vs. manufacturer data (M) [101]

available vehicle data [101, 102], empirical PrADO technology factors can be applied to specific simulation results, e.g. to artificially decrease an overpredicted wing weight. Within this work the PrADO standard setting is kept constant for all design variants.

Overall, the conceptual design with PrADO yields simulation results that are in accordance

¹Private communication with the PrADO chief developer, Dr. W. Heinze, TU Braunschweig, Germany, May 2011 and Ref. [48].

²PrADO default settings for breaking coefficients and rotation rates are too low, resulting in increased required field lengths. With exception of this specific comparison, all vehicle variants within the presented work are evaluated with the PrADO default settings, e.g. a relatively small breaking coefficient of 0.3. Consequently, presented field lengths of the PrADO designs show increased values.

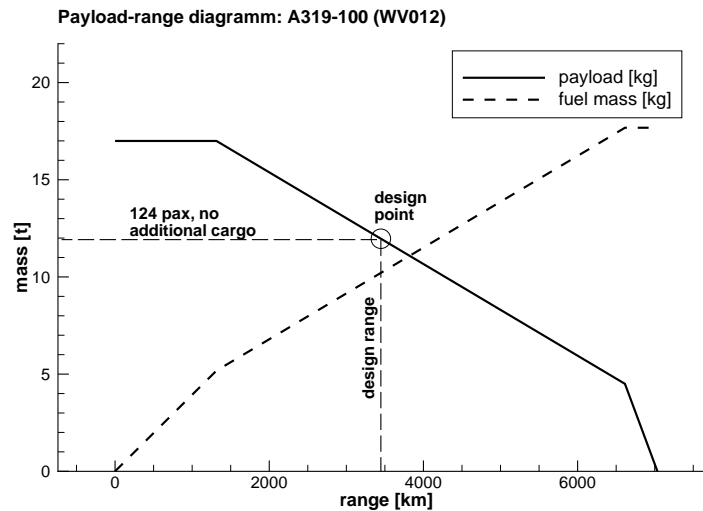


Figure 4.1: Reference Aircraft A319-100: PrADO payload range diagram

with available data. Inherent deviations due to approximations and simplifications in PrADOs computations are systematic and affect all vehicles in equal measure. Furthermore, the context of the presented work lies on level differences rather than precise absolute values. Consequently, the performance ranking of individual vehicles should not be significantly affected due to uncertainties in the PrADO conceptual design phase.

4.2 Flight Simulation vs. Recorded Flight Data

Within the presented work, PrADO is applied to simulate vehicle flight procedures. To check the feasibility of the simulation results, recorded flights of an A319-100 are re-simulated with PrADO and simulation results are compared to actual flight data recordings [21,61,95]. The recorded flight data is of course dominated by underlying weather influences, e.g. increased thrust setting due to wind. Therefore, the prediction is not directly comparable to the flight data but is used as an indicator for the feasibility of the simulated trajectories, i.e. a qualitative comparison.

Aircraft weight and configurational setting along the simulated flight path is adapted from the recorded flight data. Relevant simulation outputs with respect to noise prediction are thrust setting, altitude, vehicle orientation, and vehicle velocity along the simulation. The simulated flight trajectories are inspected if interdependencies among these dominating parameters are plausible.

A departure procedure somewhat similar to a modified ATA with flexible thrust is simulated with PrADO. Fig. 4.2(a) depicts the thrust, velocity, and altitude profile of the PrADO flight simulation. The simulation shows a comparable flight performance as the real vehicle, see Figs. 4.2(a) and A.12(a). Both vehicles reach an altitude of ≈ 2100 m at a distance of 20 km to the runway threshold. Along the climb, velocities and thrust settings are predicted that are comparable to available flight data. At the final departure flight position, flight velocity, altitude, and thrust setting are of similar magnitude compared to the measured flight. Obviously, thrust setting and actual velocity can deviate from the recordings due to the simplified modeling of the environmental impact. Yet, the thrust levels and velocities

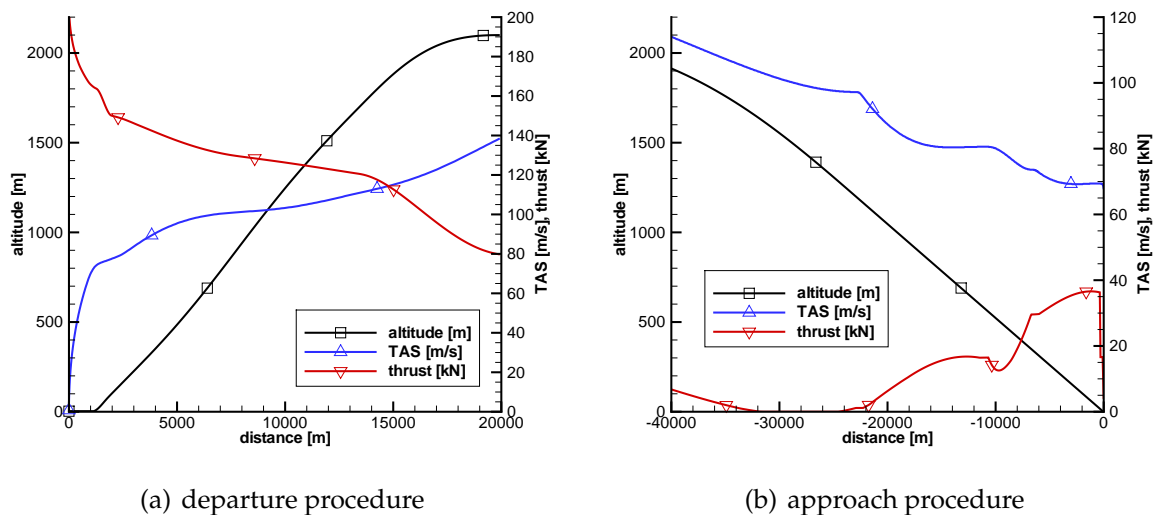


Figure 4.2: PrADO flight simulation for A319-100

along the simulation are well within the limits of the real aircraft's flight performance. Overall, the simulated trajectory is in conformity with recorded flight performance of the reference aircraft.

The simulated approach is similar to a Continuous Descent Approach with late gear extension. Along the simulated continuous descent, the selected flight path results in thrust setting of comparable magnitude to the recorded flight data. Along the simulated descent, the selected flight velocities are below the actual measurement. Yet, the required flight performance remains in conformity with the actual vehicle performance, see Figs. 4.2(b) and A.13(b).

In conclusion, the PrADO flight simulation predicts reasonable flight trajectories compared to realistic vehicle operation. Therefore, simulated flight trajectories are considered to be fully valid as input data for the overall noise prediction. PrADO is applied to simulate flight operation for all design variants and vehicles within the presented work. As presented in Ref. [88], very good agreement between simulation and flight data can be achieved, if the control parameters of the PrADO flight simulation are furthermore adapted.

4.3 Noise Prediction vs. Textbook Theory

Representative approach and departure operating conditions and simplified flyover events are simulated. Noise emission and resulting ground noise impact is predicted in order to identify noise related effects. A-weighting of the predicted noise levels is applied to account for human sound perception. Noise source dominance of individual components under preselected and defined operating conditions is evaluated. Representative flight conditions along approach and departure are selected based on available flight data [21]. Feasibility of the simulation results is then checked against known theoretical and experimental findings according to textbook theory [9, 16, 76, 97].

In a first step, the influence of A-weighting and sound propagation effects on predicted noise spectra is simulated. The second step is the evaluation of noise generation and ground

impact during representative approach and departure flight conditions. Componential noise contribution is rank-ordered in order to identify typical noise sources during approach and departure. Noise sources are rank-ordered directly at the source (emission) as well as on the ground (impact). In a final step, simplified flyover events are simulated. These flyover events are simulated under varying configurational and operational settings in order to identify noise related effects. Influence of flight altitude, speed, and configurational setting is investigated.

Representative Flight Conditions

In order to visualize the noise emission directivity for representative approach and departure operating conditions, noise levels on a reference sphere are predicted (Fig. 4.3). The colors are selected to indicate the various noise sources, e.g. yellow represents trailing edge noise. Furthermore, the radius of the depicted "noise bubbles" is linearly scaled according to the underlying components noise level in order to visualize the noise emission directivity. Obviously, a large extension of such a bubble in one direction indicates an increased noise emission.

The selected approach operating condition results in dominating landing gear and some fan noise contribution³. The predictions show an almost spherical emission directivity of the landing gear, which is in coherence to theoretical findings [16]. Due to its dominance, land-

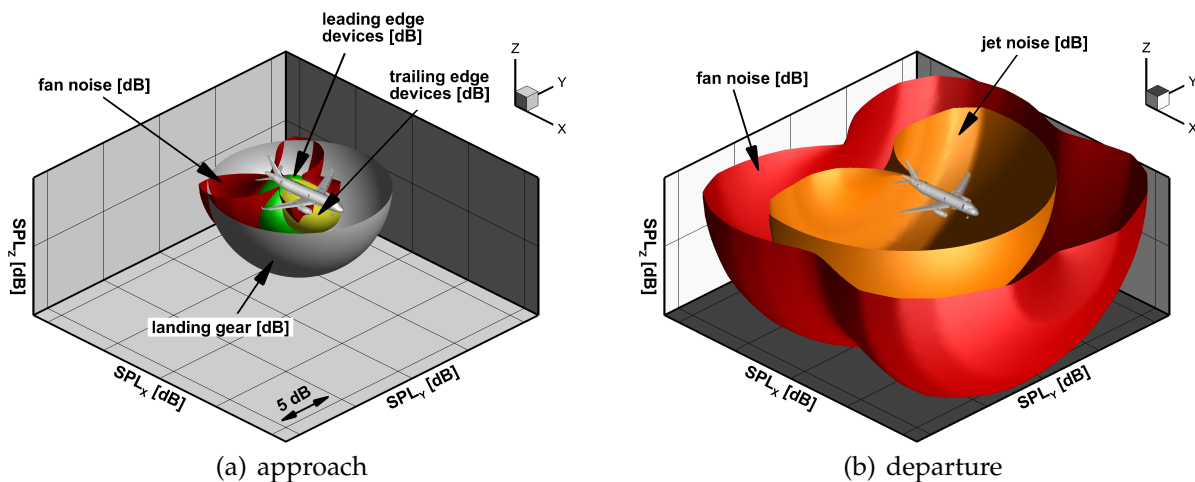


Figure 4.3: SPL(A) emission directivities

ing gear noise modifies the overall aircraft noise directivity to near-spherical. According to the operating condition, the predicted level increase due to the landing gear is in the order of 5 to 10 dB, thus in good agreement with textbook theory [16].

Obviously, departure noise is dominated by engine noise⁴. For the selected engine with a bypass ratio of 6, fan exceeds jet noise contribution. Fig. 4.3(b) shows that the predicted

³Flight speed is 75.0 m/s, altitude 500 m, and engine runs on idle, i.e. 35%. Gear, flaps, and slats are fully extracted.

⁴Flight speed is 85.0 m/s, altitude is 500 m, clean configuration, and engine runs at 88.6%.

emission directivities of the engine noise sources are similar to known engine noise radiation patterns [16,76]. Airframe noise generation is tens of dB below engine noise levels, thus airframe noise sources are not depicted in the figure.

Propagating the noise emission to an observer on the ground can change noise source dominance due to frequency dependent level weighting, atmospheric, and ground attenuation effects. Maximum levels of SPL(A) are predicted at representative observer locations directly along the approach and departure flight ground track⁵. The predicted SPL(A) ground noise levels are separated into the contribution of individual noise sources as depicted in Fig. 4.4.

Rank-ordering the noise sources for the approach observer yields a similar contribution of airframe and engine noise sources⁶. Further breakdown of airframe noise into its com-

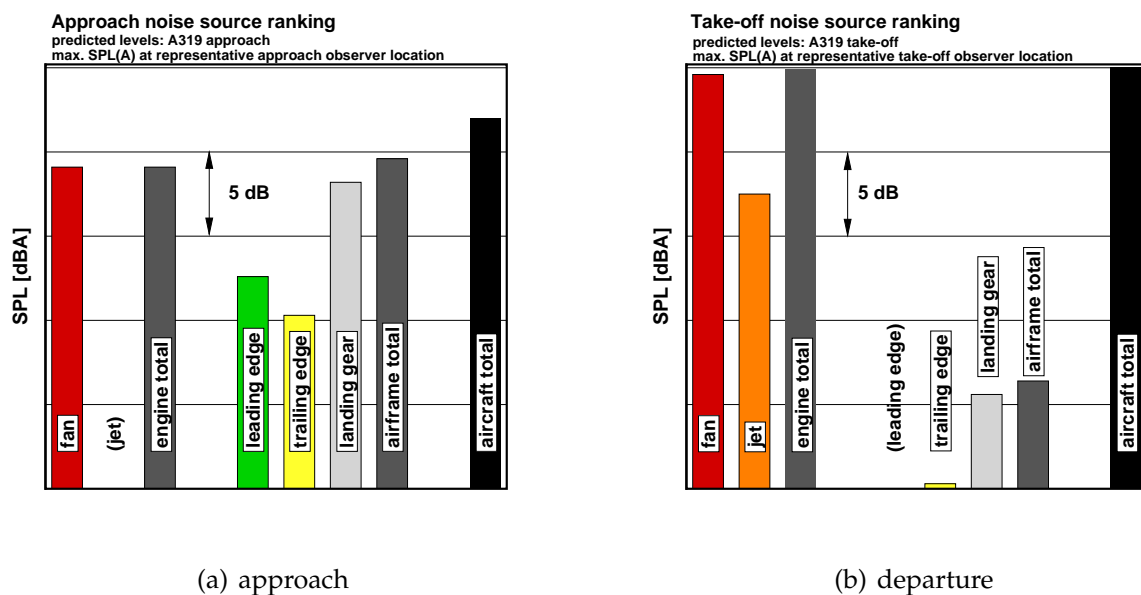


Figure 4.4: Ground noise impact: Noise source ranking

ponents is in good agreement with existing measurements and theoretical approaches [9]. Predicted airframe contribution to approach noise is dominated by the landing gear, then followed by leading and trailing edge devices.

As can be expected, noise source ranking along the departure procedure yields engine noise dominance. Airframe noise levels are tens of dB(A) below the engine noise contribution, thus are negligible.

Predicted approach and departure EPNL levels on the ground yield similar noise source contributions, (see Fig. A.4, Appendix). For the selected approach operating condition, airframe contribution toward the overall EPNL lies above the engine contribution. The prevailing moderate engine EPNL levels can be attributed to this typical approach engine setting. This near-idle engine operation leads to only insignificant tonal penalties for the EPNL evaluation. Yet, these tonal corrections can ultimately dominate engine noise EPNL

⁵Representative observer locations are selected from the Parchim campaign, see Fig. 4.8. Observers 10 and 16 are selected along the departure and the approach flight, respectively.

⁶Note: the presented levels are A-weighted. Not A-weighting the predictions would result in approximately 3 - 5 dB higher airframe than engine noise levels. This can be attributed to the prevailing spectral shapes of airframe and engine for this operating condition.

for increasing thrust settings. This is the case for the departure situation as depicted in Fig. A.4, Appendix.

Overall, the noise source ranking and emission directivities for the selected flight conditions are in good agreement with existing experimental data and theoretical knowledge, e.g. published data from aircraft manufacturers [97] and textbook theory [16,76].

Simplified Flyover Events

The selected procedures are comprised of non-accelerated and straight flight segments with preselected and constant speed, thrust setting, configuration, and flight path angle. The simulated reference aircraft is a PrADO [48] model of an A319-100. Additional required input parameters come from VarCycle [80], i.e. a detailed engine performance map. The selected aircraft mass for the simulation is 45000 kg, the wing area is 122.6 m, and the center of gravity is located at 14.4% mean airfoil chord (MAC). The forces on the overall aircraft if simulated as a point mass can be written according to Ref. [96]. C_d and C_l are the overall aircraft drag and lift coefficients, T the thrust force, W the weight force, \dot{v} the vehicle acceleration, γ the flight path angle, and g the gravitational acceleration. Accounting for the selected flight conditions, i.e. non-accelerated and horizontal flight segments⁷, further simplifies the equation.

$$\sin(\gamma) + \frac{\dot{v}}{g} = \frac{T}{W} - \frac{C_d}{C_l} \rightarrow \frac{T}{W} = \frac{C_d}{C_l} \quad (4.1)$$

With known weight and wing area, the required C_l can be evaluated for each selected flight speed v and ambient density ρ .

$$C_l = \frac{2 \cdot W}{\rho \cdot A \cdot v^2} \quad (4.2)$$

Depending on the configuration and ambient flow conditions, the required lift coefficient is directly linked to the overall drag coefficient via the aircraft polar. Overall aircraft polars are generated with PrADO for each selected flight condition, i.e. altitude, speed, and configurational setting. From these PrADO polars, the corresponding C_d can be determined for each required C_l . With known values for W , C_l and C_d , the required thrust force is evaluated according to Eq. 4.1.

For the required thrust force, thermodynamic engine cycle modeling yields the corresponding engine rotation speed. The selected reference aircraft produces the required thrust levels with two engines, thus each engine has to generate a thrust force of $T/2$. At this point, all required geometrical and operational input parameters for the overall noise prediction are available.

Three noise related effects are simulated and investigated in more detail, i.e. (1) source distance, (2) flight speed, and (3) configurational setting. The resulting main operational parameters are provided in Tab. A.1, Appendix. The selected flight conditions and parameter settings along the simulated flights are comparable to real flight data recorded under similar operational conditions [21, 61, 95]. Therefore, the simulated flight conditions are

⁷ $\dot{v} = 0, \gamma = 0$, lift force equals weight force

somewhat representative for typical approach and departure flight operation⁸.

The simulation of these simplified flights allows to separate noise related effects and identify the operational influences on each individual noise source. Direct flyover events are simulated for observers located sideways and directly along the flight ground track. Time-level-histories, spectra and max. SPL levels are predicted and evaluated.

(1) To study the influence of source distance, three flight altitudes are simulated, i.e. 500, 1000, and 2000 m. Flight speed of 130 m/s, the engine setting, and a clean high-lift configuration are kept constant during the simulated flights (flights 1 to 3 in Tab. A.1, Appendix). The influence of the selected altitude on the overall flight performance is negligible. Fig. 4.5 shows predicted max. SPL(A) levels and time-level-histories with and

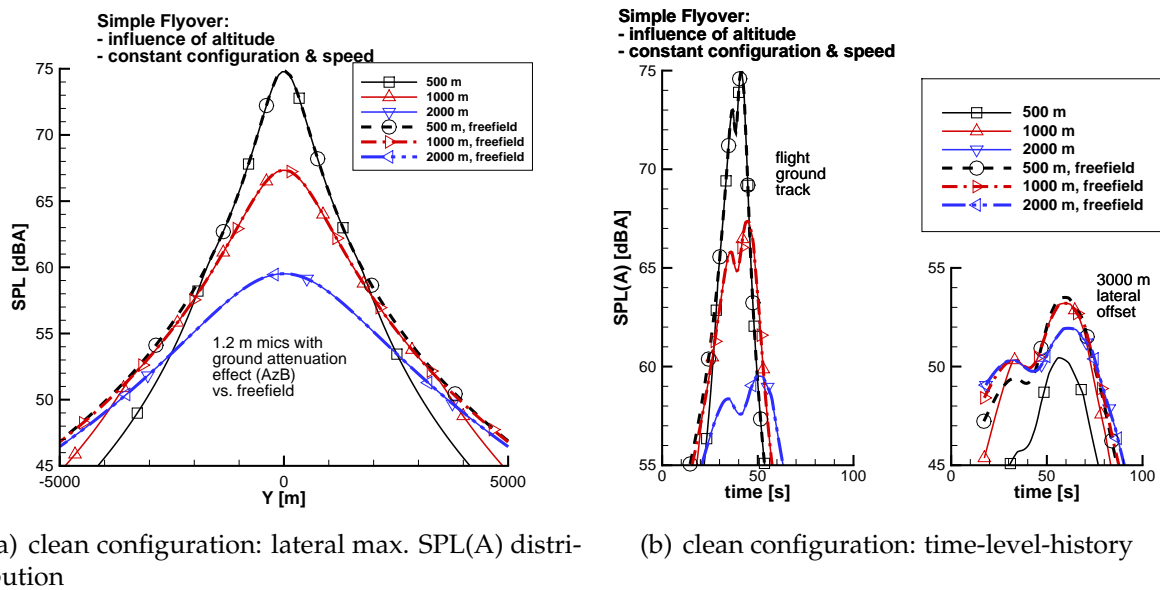


Figure 4.5: Influence of source altitude and ground attenuation: max. levels and time-level-history

without additional ground noise attenuation. Compared to the lowest flight (flight 3), noise levels of the highest flyover (flight 1) are decreased by $\Delta L \approx 12$ dBA solely due to the difference in source-observer distance. Furthermore, sound propagation effects along the increased distance between flight 1 and the observer reduce the noise levels. Altogether, a 15 dBA offset is predicted between the lowest flight (flight 3) and the highest flyover (flight 1).

If no ground attenuation is accounted for (dashed lines), the lateral max. SPL(A) levels for all flights are converging with increasing lateral distance to the flight ground track. If lateral distances are significantly greater than flight altitudes, there is no relevant difference between the source-observer distances for these flights. Not accounting for ground noise attenuation, source-observer distance will dominate sound propagation, thus the predicted ground noise levels. From approximately 4000 m lateral offset on, the source-observer distances are similar, thus the ground levels along all three flights are within one dB.

If empirical ground noise attenuation is accounted for [10], the situation changes with

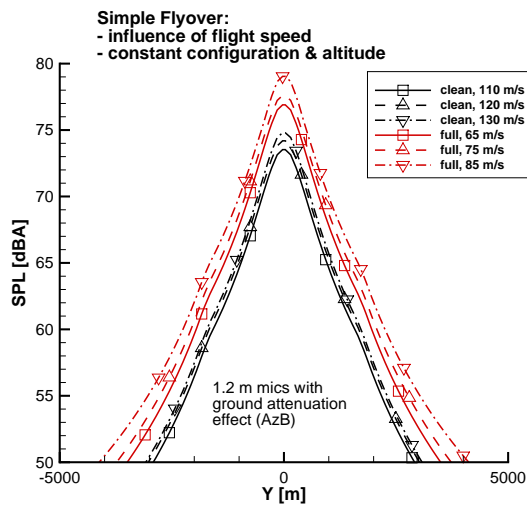
⁸Note: realistic approach and departure flights could be subject to significant de- or acceleration compared to the simulated simple flight segments. On the one hand, deceleration could result in reduced engine thrust setting, minimize engine noise contribution. On the other hand, acceleration could require higher thrust setting resulting in increased engine noise.

increasing lateral distance to the flight ground track (solid lines). The levels along the flight ground track are not affected by ground noise attenuation. Yet, if lateral distance is increased, especially toward a grazing incidence, noise levels are significantly reduced due to ground noise attenuation. At a lateral distance of approximately 4000 m, maximum ground noise levels for the lowest flight (flight 3) are already 3 dBA below the levels for the highest flyover (flight 1). Obviously, high flight altitude results in wide-spread noise distribution compared to lower flight operations due to ground attenuation. This effect is especially noticeable when evaluating ground noise isocontour areas, i.e. so-called noise footprints. Fig. A.5, Appendix, shows the max. SPL(A) ground noise isocontours along a non-accelerated approach with a constant glide slope, constant configuration, and constant flight speed. Reducing flight altitude along an approach procedure does clearly reduce lateral expansion of the predicted noise level isocontours while the noise levels magnitudes are increasing. On the contrary, higher flight operation reduces absolute levels on the ground due to the increased noise source distance but at the same time results in broader and more wide-spread noise isocontour areas. A description of this effect can be found in the known literature, e.g. ground attenuation is discussed in Ref. [76]. Furthermore, in Ref. [14] the authors emphasize the dominating influence of ground noise effects on isocontour areas.

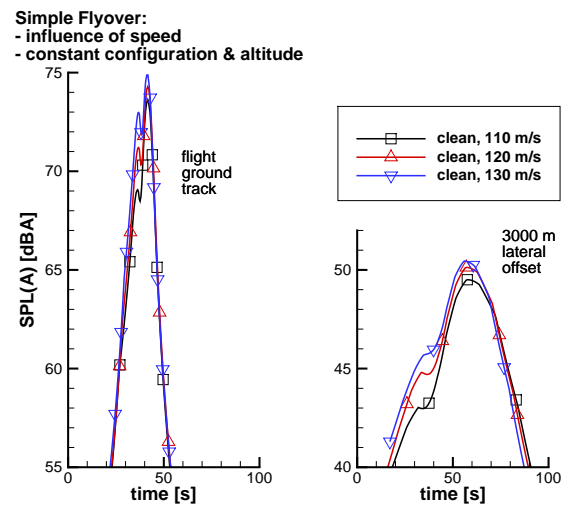
(2) To investigate the impact of flight velocity on ground noise impact, flights with different velocities are simulated. Two configurational settings are simulated, i.e. clean (flights no. 4-6) and fully configuration⁹ (flights no. 7-9). Flight speeds of 110, 120, and 130 m/s are simulated for the clean configuration. The vehicle under landing configuration is simulated with 65, 75, and 85 m/s. The flight altitude is kept constant at 500 m and the corresponding engine setting is selected according to configuration and flight speed. Assuming a correlation of airframe noise with the fifth power of flight speed, the speed increase from 110 to 130 m/s for the clean configuration results in $\Delta L \approx 4$ dB additional airframe noise. Likewise, airframe noise increases by $\Delta L \approx 6.4$ dB changing flight speed from 65 to 85 m/s for the full configuration. Fig. 4.6 shows the prediction results, i.e. lateral max. SPL(A) distribution and level-time-histories for both configurational settings. The predicted noise levels indicate a much smaller level increase for both configurations. This can be traced back to an increase in engine noise contribution. For both configurations, increasing the flight speed results in reduced lift to drag ratios and therefore, higher engine thrust settings are required. Obviously, the increased engine noise contribution works against the airframe noise reduction. Both presented level-time-histories show significant level increases with velocity due to forward fan noise contribution, i.e. comparing levels prior to main peak. Due to the emission directivity for the full configuration and mostly due to the slow flight speeds, especially lateral level-time-histories indicate sustained ground noise impact. A speed increase by 10 m/s results in noise level increase of ≈ 2 dB for the clean and ≈ 3 dB for the full configuration. Noise levels for full configuration are 4 - 5 dB above the noise levels for the clean configuration while both configurations operate in appropriate velocity regimes. This is in accordance with other published investigations [9,16]. Obviously, aircraft with full and clean configuration can not operate at similar velocities thus any comparison at constant velocities seems not feasible.

Predicted noise emission directivities are presented in Fig. A.6, Appendix. Noise levels are predicted on a reference sphere in order to visualize the noise directivities. The characteristic shapes are in good agreement with available data and theory [9,16].

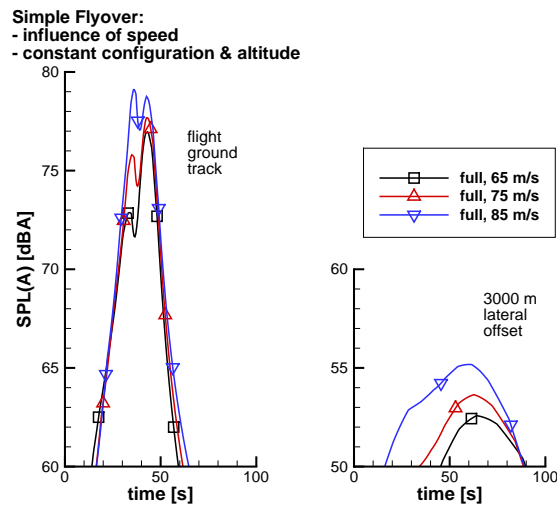
⁹fully deployed high-lift system and extracted landing gears



(a) clean/full configuration: lateral max. SPL(A) distribution



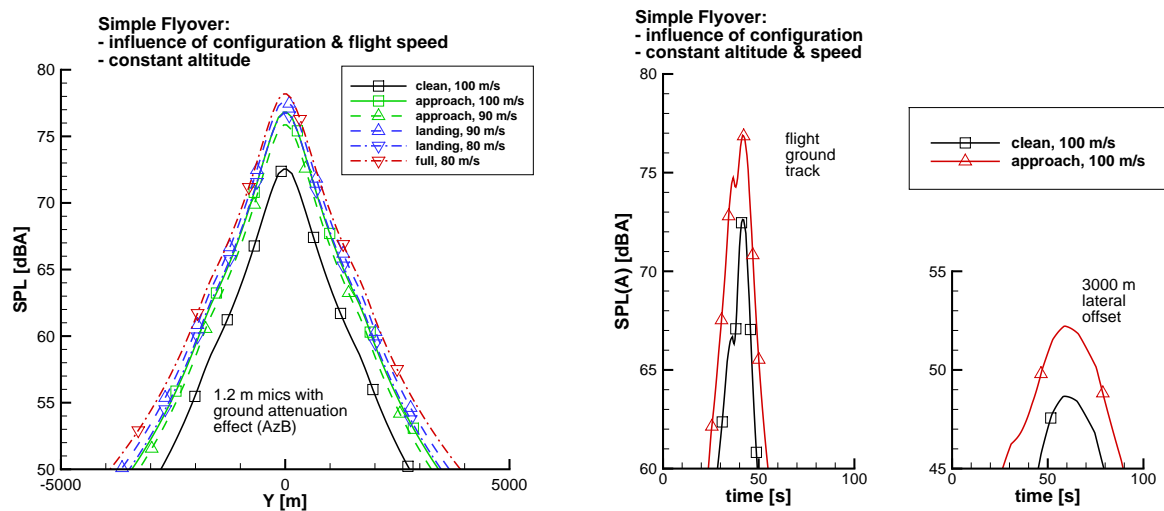
(b) clean configuration: time-level-history



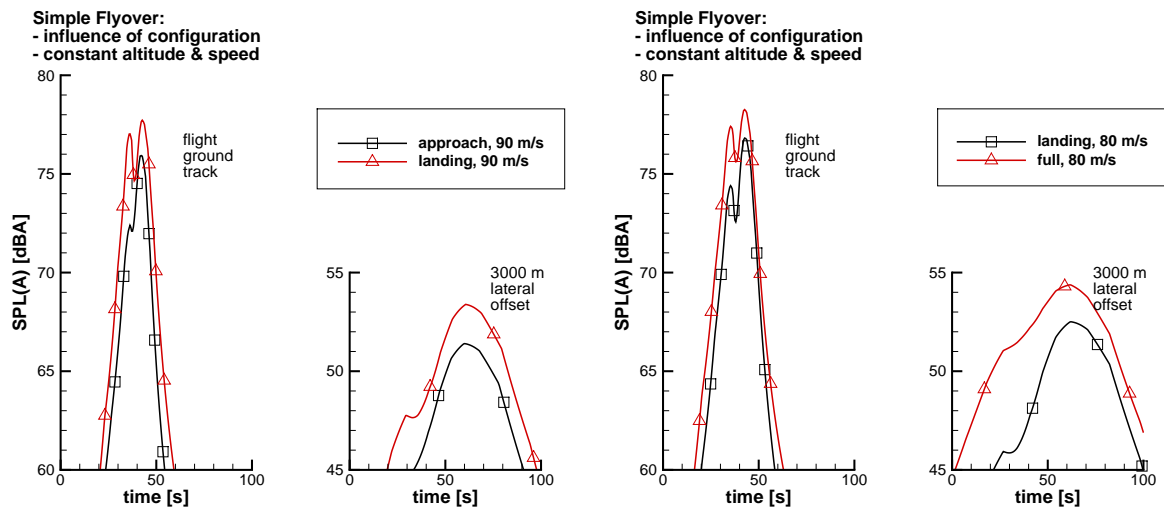
(c) full configuration: time-level-history

Figure 4.6: Influence of flight velocity: max. levels and time-level-history

(3) Impact of the high-lift system and the landing gear is evaluated along horizontal flight segments with corresponding flight velocities. Selected configurational settings are evaluated, i.e. clean, approach, landing, and full configuration. Depending on the configurational setting, a specific flight velocity, angle of attack, and thrust setting is required. Each setting is evaluated and compared against the previous setting at the same velocity and similar thrust settings, i.e. comparison of clean (flight 10) vs. approach (flight 11), approach (flight 12) vs. landing (flight 13), and landing (flight 14) vs. full configuration (flight 15). Fig. 4.7 shows the predicted lateral max. SPL(A) distribution and level-time-histories for



(a) all configuration: lateral max. SPL(A) distribution (b) clean vs approach configuration: time-level-history



(c) approach vs landing configuration: time-level-history (d) landing vs full configuration: time-level-history

Figure 4.7: Influence of configurational setting: max. level and time-level-history

each comparison. Based on the max. SPL(A) distribution all flights can be rank-ordered according to their ground noise impact. Noise levels increase starting with clean, then approach, then landing, and finally reach maximum levels when fully configured. Any noise reducing effect of slower flight velocities is outweighed by additional noise generation due to deployment of high-lift system and gear. As a consequence, high-lift and gear operation should be reduced to a minimum which is in compliance with available instructions for

low-noise procedures, see Section 2.2 and Ref. [9]. Again, characteristic directivity shapes are in good agreement with available data and theory [9, 16], see Fig. A.7, Appendix.

In conclusion, predicted influence of flight altitude, speed, and configurational setting is consistent with existing experimental and theoretical findings. The presented comparison of PANAM results with textbook theory indicates that the major noise generating effects are adequately accounted for. In general, the predicted shape of level-time-histories is in good agreement with theoretical level variations for turbofan vehicles. In consistence with Ref. [76], the time-histories show two level peaks before and after the time step corresponding to a direct overhead position of the aircraft. The level peaks can be more or less intensified depending on the dominating sources noise emission and the flyover event, i.e. flight speed and altitude.

4.4 Noise Prediction vs. Measurements

Each implemented noise source model has individually been validated with component windtunnel and or computational data [21, 28, 36, 95]. Experimental windtunnel data is recorded under steady laboratory conditions and computations are defined by simplified and artificial boundary conditions. Therefore, it is necessary to judge the feasibility of the assumptions and models under realistic operating conditions. Studies indicate an accuracy for dedicated airframe noise prediction of ± 1 dB [71] and ± 4 dB for engine noise prediction [28]. Yet, it has to be verified, that overall aircraft noise can be approximated by an assembly of these separate noise sources in a real environment. A feasible validation requires a comparison with actual aircraft flyover noise measurements. Such flyover noise data reflects realistic operating conditions, thus is compromised by noise source movement and sound propagation effects. If working with flyover noise measurements one has to keep in mind that such data is subject to inherent imprecision and limited replicability [15]. Therefore, very good overall agreement of predicted noise levels with actual measurements becomes very difficult and can only be achieved to a certain extend. Furthermore, PANAM only accounts for the most dominating noise sources and simplifies noise source interaction. Various design details, e.g. cavities, on-board of real aircraft can contribute significantly to the overall noise levels [9] but cannot be accounted for. As a consequence, Dobrzynski accentuates that perfect or very good agreement of measurements and simple predictions can not be achieved and if so they would not be plausible [9]. Nevertheless, if the major dominating noise sources are accurately modeled, a satisfying overall accuracy can be expected. Only a dedicated comparison of simulated versus measured aircraft ground noise levels can indicate the feasibility and the quality of the applied prediction methodology.

4.4.1 A319 Flyover Campaign

Within the presented work, the focus lies on medium-range, single-aisle transport aircraft. Therefore, the prediction results are compared to flyover noise measurements for such an aircraft type. Due to extensive available data, especially detailed engine design, an A319 with CFM56 engines is selected. The required input data for PANAM comes from PrADO [48] (vehicle geometry), SHADOW [83] (noise shielding effects), Varcycle [80] (engine performance map and detail design), and recorded flight data (trajectory with configuration and engine setting).

In 2006, this aircraft was operated along 9 approach and 9 departure procedures [21,61,95]. The procedures are referred to as *rec001* to *rec018*, see section A.3. A detailed description of the test flights can be found in Ref. [100]. Ground noise measurements have been recorded at 12 departure and 13 approach observer locations. Initial comparison for this campaign has been presented earlier [43]. Modifications to airframe and engine noise source models and the implementation of an acoustic lining model improved the overall conformity of prediction with experimental data; compare Ref. [43] and [44]. In contrast to what has been presented in Refs. [43,44], the prediction input data is furthermore revised. Now, the original and raw flight data recordings are directly transformed into PANAM input, without any data simplification and unknown corrections. The underlying data for the past comparisons [43,44] was somewhat simplified and smoothed out according to a subsequent and ground based simulation of the actual test flights. The flights have been subject to

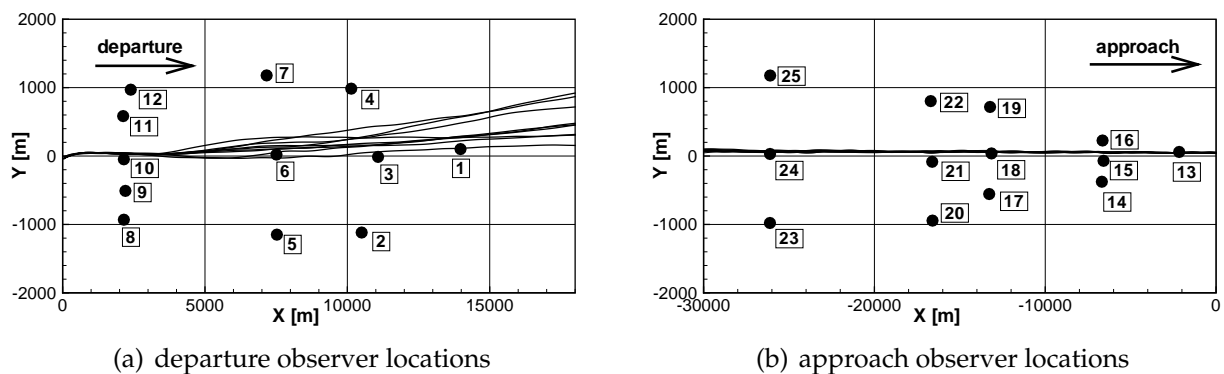


Figure 4.8: Parchim Campaign 2006: Observer locations

subsequent ground based simulation in order to get access to additional data such as engine thrust. Compared to this simplified input data, the original raw flight data shows slightly reduced flight speeds¹⁰. Compared to older predictions, the corrected flight velocities result in a reduction of predicted airframe noise contribution. Furthermore, the raw flight data shows increased distances between flight ground path and observer locations compared to the simplified input data. The maximum deviation of observer and ground flight path is as high as 400 m at the furthest departure observer location whereas the old and smooth input data does not show these discrepancies at all [43,44]. Fig. 4.8 depicts the ground noise observer locations and the flight ground tracks.

In addition to the input data modifications, the jet noise model is revised and adapted to recent findings. This required modification to the jet spectral shape increases predicted jet noise contribution especially during take-off compared to older prediction results [43,44]. As a consequence, the overall engine noise contribution is now slightly amplified. During take-off, the modified jet model results in almost similar overall noise contribution of the jet and the fan. This is conform with known engine noise theory [16].

To perform flyover noise measurements is of course very complex and costly, thus the recorded data base is very limited. The data base is comprised of independent flyover events, thus no feasible statistics can be applied. Instead of working with standard deviation, each individual event is separately evaluated to ultimately judge the overall prediction

¹⁰Corrected Air Speed (CAS) from the flight data recorder is translated into True Air Speed (TAS) for the predictions.

quality.

At each observer location, measured SPL(A) time-histories are evaluated and compared to PANAM predictions, i.e. approach and departure flyover events. Detailed event reports are available for each installed observer station of the campaign. In addition, the reports include results of a detailed aural feasibility check of each recorded sound file¹¹. According to these reports, certain recordings can (mainly) be attributed to foreign noise source contribution. The recorded departure noise data is valid except of three corrupted measurements¹². Due to generally lower approach noise levels, more problems are encountered for the approach measurements due to external noise contribution and prevailing background noise. According to the event report, several noise measurements are corrupted by strong wind gusts or close-by ground vehicle operation¹³. The corrupted approach measurements

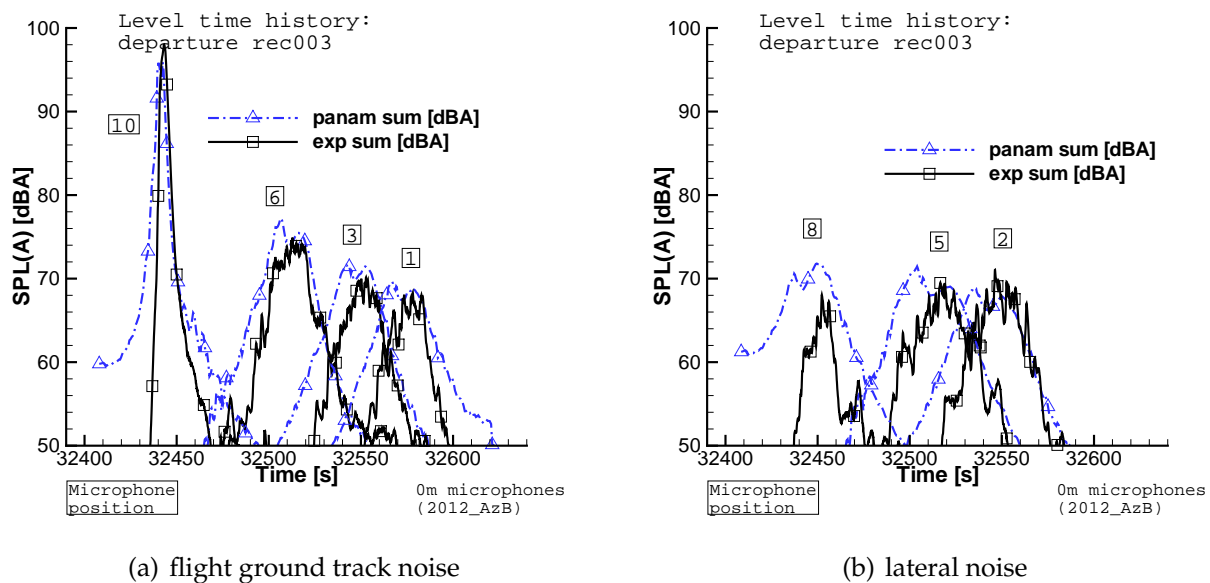


Figure 4.9: Parchim Campaign 2006: departure *rec003*

are all located at relatively large distances to the nearest fly-by of the aircraft. All corrupted departure and approach recordings are indicated by gray colored and dotted lines in the corresponding time-history plot. Recordings with documented additional noise contribution sufficiently below the aircraft ground noise levels are considered as fully valid for a comparison with the predictions.

Multiple measurements and predictions are aligned within one figure for each flyover event. The measured and simulated SPL(A) time-histories along all test flights are depicted in Figs. A.14 to A.19 of Section A.3. Exemplary, level-time-histories for selected departure and approach procedures are presented here, i.e. flights *rec003* (Fig. 4.9) and *rec004* (Fig. 4.10). Both observers directly along the flight ground track, i.e. Figs. 4.9(a) and 4.10(a), and observers with a lateral offset to the flight ground track are evaluated, i.e. Figs. 4.9(b) and 4.10(b).

¹¹With friendly permission of U. Isermann, Institute of Aerodynamics and Flow Technology, DLR Goettingen

¹²Corrupted departure noise recordings: *rec009* at location 3; *rec001* at location 1; *rec015* at observer location 5.

¹³Corrupted approach noise recordings: *rec002* and *rec006* at location 24; *rec002*, *rec010* and *rec006* at location 23; *rec008* and *rec018* at location 25; *rec004* at location 22

4.4.1.1 SPL(A) time-history

Predicted departure noise along the flight ground track is in agreement to the measured levels, i.e. both predicted maximum levels and predicted time-histories. As depicted in Fig. 4.9(a), the prediction results indicate, that forward noise emission is somewhat overpredicted. Overall agreement in shape of the time-histories is reduced if observers experience the flyover event under small angles of incidence. During the departure, this is especially the case for observer locations 8, 9, 11, and 12. These observers have intentionally been located at lateral offsets and close to the runway threshold in order to study ground attenuation effects in detail. Furthermore, locations 5 and 7 see the noise source under relatively small angles. Predictions for these locations are significantly below the measured levels as depicted in Figs. 4.9(b), A.15, and A.16. This is mainly attributed to sound propagation effects under small angles of incidence and increased distances to the noise source. Sound waves propagating nearly parallel to the earth surface can be subject to large attenuation or even amplification due to the impact of topography¹⁴ and local weather¹⁵. As a consequence, the prediction of these so-called grazing incidences is error-prone and associated with large uncertainties in the order of several dB. Ref. [54] presents empirical findings to account for the variability in predicted noise levels for a vehicle at low altitudes. Solely due to meteorological effects the noise prediction uncertainties for a vehicle operating on the ground can be in the order of ± 10 dB [54].

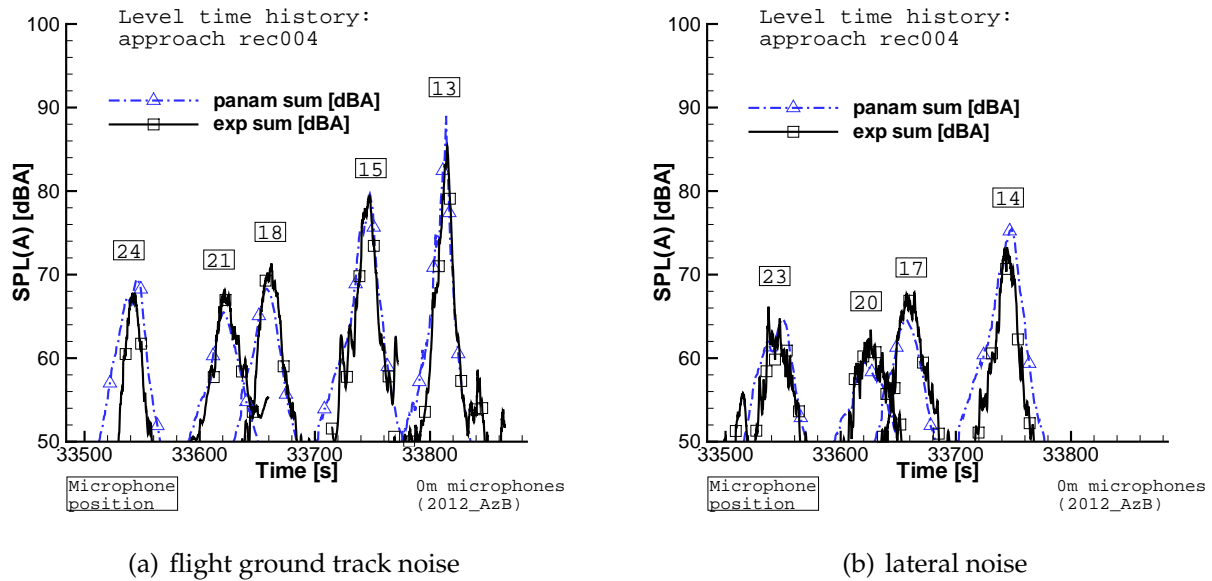
Along the approach flight ground track, absolute SPL values as well as the level variation in time are generally in conformity with the experimental data for all flights (Fig. 4.9(a) and Fig. A.17 of Section A.3). Significant deviations are not experienced along the approach flight ground tracks. Predictions along the flight ground track for all 9 approach procedures are promising, see Fig. A.17. If deviations exist, they can be tracked down to their cause according to the reported disturbances and errors within the measurements. Again, with increasing distance to the aircraft, deviations are slightly increasing as well, e.g. at locations as far as 20 km from the runway threshold. Maximum levels are still in reasonably good agreement but time-histories show deviations. The simplified simulation overpredicts the experimental data. "Natural" noise level attenuation under grazing incidences due to complex local terrain influences, or atmospheric turbulences along extensive propagation paths up to the observers can not be simulated. Yet, maximum perceived noise levels show better agreement because the peak is reached when the aircraft is at close distances but higher altitudes, i.e. large elevation angle of the vehicle.

4.4.1.2 Sound Exposure Level

Each of the SPL(A) time-histories is translated into a corresponding Sound Exposure Level (SEL). The SEL is selected because it is a commonly applied measure for the evaluation of aviation noise [103]. It is a measure of the total energy impact on the ground produced by a single flyover event, thus seems like an optimal indicator for evaluation of the prediction quality. For the experimental SEL data (symbol "x") an ± 2 dB error margin is assumed as depicted in each figure. Predictions that lie within this margin are considered to be in close conformity with the measurements. Corrupted departure and approach measurements are indicated by a symbol "o". The SEL predictions for the departure and approach observer

¹⁴Topography: ground reflection and terrain effects

¹⁵local weather: atmospheric turbulences, wind shear layers, and temperature gradients

Figure 4.10: Parchim Campaign 2006: approach *rec004*

locations are presented in Figs. A.20 and A.21 of Section A.3. Due to the grazing incidents, departure observer locations 7, 8, 9, 11, and 12 are excluded from the SEL evaluation. Exemplary, one observer location for approach and one for departure are presented here, i.e. departure observer location 6 (Fig. 4.11(a)) and approach observer location 21 (Fig. 4.11(b)).

The simulated energy impact at observer location 6 is slightly overpredicted for all departure flights. An overprediction is prevailing at all departure locations and can be addressed to still existing, but reduced, engine noise overprediction. Fan noise prediction has been significantly improved due to modifications compared to earlier results as presented in Ref. [44]. Overall, the predicted SEL levels at all observers are still in a feasible range compared to the measurements.

The selected approach observer 21 is in good accordance with the measurements, i.e. all predictions are within the preselected error margin for the measurements. For the other approach observers similar results are obtained, see Fig. A.21 of Section A.3. Yet, most distant observers, e.g. locations 23-25, are subject to some overprediction of the total sound energy impact.

4.4.1.3 Summary

In summary, it can be concluded that the presented noise prediction method generates reasonable and comprehensible ground noise levels (for the reference aircraft). Both the predicted approach and departure noise levels are in satisfying conformity with the measurements. Taking the known simulation uncertainties into account, i.e. ± 1 dB for airframe and ± 4 dB for engine noise contribution [28, 70, 71], the predicted results are in good overall agreement with the measurements. Maximum levels, time-histories, and consequently the perceived energy impact are predicted reasonably well. Good agreement with measured data can be demonstrated along different flight procedures and for various configurational settings, see Tab. A.7. Componential noise source dominance according to the configurational changes in flight, see Figs. A.12 and A.13, are adequately modeled. The results indicate a feasible componential noise source ranking along each flight path, i.e. departure and

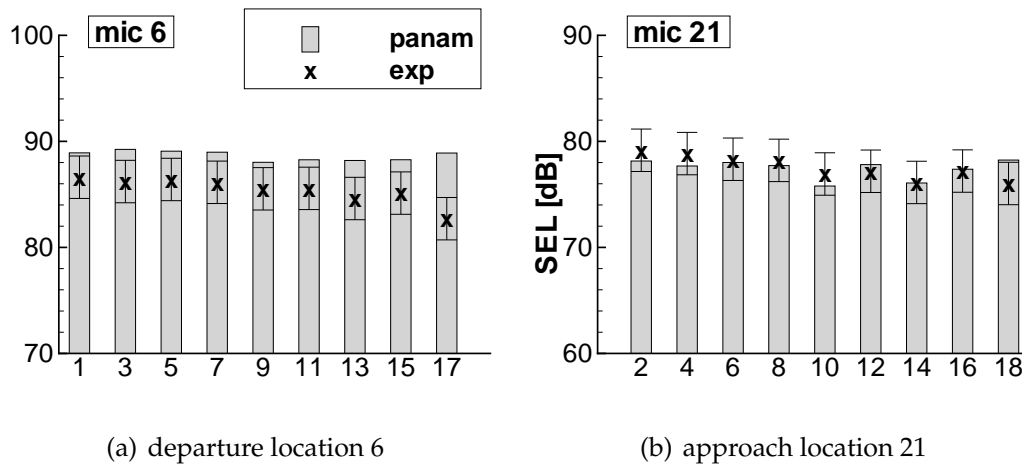


Figure 4.11: Parchim Campaign: Sound Exposure Level (SEL)

approach procedures.

Departure engine noise is slightly overpredicted but is still of acceptable magnitude. Airframe noise prediction is in accordance with measurements at most observers. If observers are subject to noise impact under grazing angles, large deviations between prediction and measurements are experienced. This is the case along both approach and departure procedures. Yet, these observers are usually not relevant to an aircraft noise evaluation because of their specific location. Either these observers are too close to the runway in order to represent any affected population or they are too far away from the aircraft, thus perceive very low aircraft ground noise. Obviously, the relevant areas for an aircraft noise evaluation depend on the specific flight procedure. These areas usually begin at least 2-3 km away from the runway threshold and are extended around the ground flight track until the aircraft reaches a certain altitude. Noise predictions within these relevant areas are consistent and in conformity with the measurements.

As a consequence of the uncertainties related to grazing incidences, the presented noise prediction methodology should not be applied to predict certification sideline noise levels¹⁶. The ground-to-ground noise simulation for these observers is subject to inherent and unpredictable errors due to the grazing incidences [54].

Other than that, the prediction results indicate that the underlying noise models allow for a dependable prediction. Individual components as well as the overall noise is reasonably good simulated. Furthermore, results at observer locations with lateral offsets affirm the feasibility of the simulated noise emission directivities.

4.4.2 Additional comparison

Initial and simplified comparison of prediction results versus other aircraft types is available but not in the scope of the presented work. PANAM predictions are compared to experimental data for DLR's former flying testbed ATTAS (Refs. [43, 84]), the new DLR Airbus ATRA (not published yet), a Boeing B737 (Ref. [125]), and a Boeing B747 (not published yet). Comparison of prediction results according to the implemented noise source models with the experimental data is quite promising for all four vehicles. Yet, alternative high lift and landing gear design principles (e.g. B747) require modifications to the empirical

¹⁶Sideline observers are located parallel to the runway in a distance of 450 m.

factors. If the empirical factors are modified, the results show good agreement with the measurements [70,71].

A sophisticated prediction for these various vehicles would require detailed engine design with higher fidelity tools, e.g. Varcycle [80], not being available at the time of finalization of this work. Therefore, initial predictions of ATRA, B737, and B747 are based on simplified PrADO engine models. Obviously, the major and dominating influence of engine operating conditions on noise emission is crucial to accurate modeling for a feasible noise prediction. It is demonstrated, that result accuracy can be significantly improved if more detailed engine data is available, e.g. high-fidelity thermodynamic engine modeling [125].

A direct tool-to-tool comparison with other existing scientific noise prediction tools has been initiated and is currently under progress. As presented in Ref. [104], an initial comparison with the University of Manchester's FLIGHT code confirms the feasibility and result accuracy of PANAM. In the long run, these tool-to-tool comparisons will contribute to establish defined validation standards and realistic accuracy margins for scientific noise prediction tools.

5 Application

The presented applications of PANAM can be grouped into two research areas, i.e. low-noise vehicle design and decision making support. The main focus of the presented applications lies on low-noise vehicle retrofit and overall design.

Low-noise design modifications do not only apply to the corresponding noise source geometries, but can have an influence on the overall flight performance. The flight performance defines the operating conditions for all noise sources, thus overall noise generation can be influenced. Consequently, for the evaluation of low-noise concepts and promising technologies, individual flyover events have to be simulated for each new or modified vehicle design. The second area of application for PANAM is to support (political) decision making with respect to noise abatement flight procedures and airspace management. Single and multiple flyover events can be analyzed in order to support the identification of promising low-noise flight procedures, spatial airtraffic routing, and flight schedules.

5.1 Low-Noise Vehicle Design

The focus of the presented design study lies on single-aisle, medium-range transport aircraft. The two main reasons for this selection are today's large market share for this aircraft category and the availability of extensive validation data. Independent market forecasts of major aircraft manufacturers even predict an increase in market share to over 70% for these aircraft types by the year 2030 [105, 106]. As a consequence, single-aisle aircraft represent the majority of all flight operations at larger airports thus have a dominating impact on airport community noise pollution.

The main goal of this study is the identification of promising low-noise design trends and technologies within the conceptual aircraft design phase, i.e. a reduction of perceived ground noise levels without adverse effects on economical performance of the vehicle. At this early design level, only few key parameters are fixed so that major geometry and concept modifications are still feasible. This flexibility allows for an extensive solution space. Existing and new low-noise concepts can directly be compared within the common multidisciplinary design process as described in Section 3.3. New low-noise vehicles are evaluated according to their individual flight performance along a predefined reference flight procedure.

Optional and further detail investigations of the identified vehicles through "high fidelity" methods or wind tunnel tests are not in the scope of the presented work.

Noise level reduction in certain frequency ranges is less important due to human noise perception and prevailing sound propagation effects [16, 54]. Noise levels below 250 and above 10 000 Hz are significantly reduced in human sound perception, i.e. A-weighted

noise levels as depicted in Fig. A.2, Appendix. Furthermore, noise levels above 2000 Hz are subject to extensive atmospheric attenuation with increasing distance between source and observer. The effect of atmospheric damping is depicted in Fig. A.1, Appendix. For example, relevant distances between source and observer along typical approach procedures are in the range of 200 to 1000 meters. For these distances, atmospheric damping significantly reduces high frequency noise. Noise emission around 8000 Hz is reduced by as much as 15 (200 m) to 50 dB (1000 m) under ISA weather conditions.

As a consequence, aircraft noise emission in the frequency range from 250 to 2000 Hz is most dominant with respect to ground noise perception¹, thus most promising to any low-noise modification and technology. Reducing noise emission within this limited frequency range can effectively decrease perceived overall noise levels.

Starting from a predefined reference aircraft, various approaches toward overall noise reduction are investigated. Hereby, the solution space is limited to the overall vehicle layout, i.e. vehicle shape and engine installation effects. Changes to the specific design of the engines are excluded and not in the scope of the presented work. A fixed engine design is selected as the reference engine for all vehicle variations. Simulation of future and non-validated engine concepts with the existing engine performance tools results in unpredictable uncertainties, thus falsifies the overall vehicle evaluation. Consequently, all selected vehicle variations are equipped with the identical reference engine thus can be simulated with available and validated methods. New vehicles and retrofit solutions can directly be compared and rank-ordered according to their individual performance.

To give a forecast on future developments with respect to alternative engine concepts, an initial and rough evaluation of two promising engine concepts is presented. Due to the lack of experimental data and validated simulation models, simulation results for these concepts can not directly be compared to results of the previous design study. The results for these alternative concepts only indicate trends with respect to the reference engine concept, i.e. based on noise emission directivities.

5.1.1 Reference Vehicle and Design Mission

A representative single-aisle transport aircraft is the A319-100 with CFM56 engines. For this aircraft, an extensive DLR in-house data base is available thus allowing to validate computational results, see Chapter 4. Validation data includes aircraft geometry and engine design, flight data recordings, and detailed noise measurements from the Parchim flyover campaign [21, 61, 95]. Thermodynamic engine data and required engine design details for the CFM56 are provided by T. Otten, DLR Institute of Propulsion².

Having access to this extensive validation data base offers a unique opportunity for feasibility checks of simulated design modifications. The simulated impact of arbitrary design modifications on flight performance and noise emission can be checked for feasibility according to experimental data for the underlying original design. Ultimately, the plausibility of predicted noise level differences for new technologies can be assessed, thus enabling a quick identification of unrealistic predictions.

The A319-100 originates from the bigger A320 aircraft with a shortened fuselage due to

¹The frequency range of relevant ground noise levels is based on experience, thus is a best-practice value. Private communication with U. Isermann and R. Schmid, DLR Goettingen, April 2012.

²Engine cycle modeling is performed with the DLR tool Varcycle [80] by the Institute of Propulsion.

reduced payload and range requirements. Due to the Airbus family concept, the A319 is equipped with identical wing, control surfaces, and high lift system as the A320. The Top

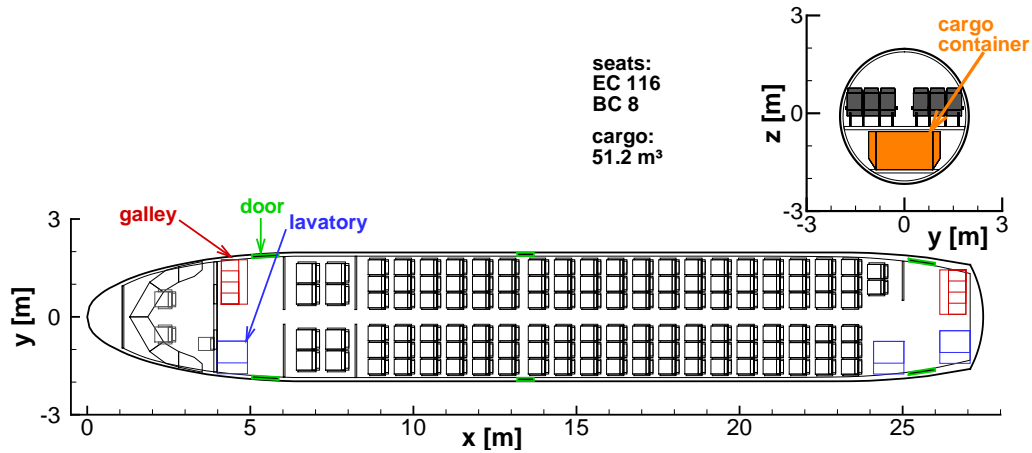


Figure 5.1: Reference aircraft cabin layout

Level Aircraft Requirements (TLAR) are comprised of a design mission range of 3330 km, 124 passengers, and a cruise Mach number of 0.76. Furthermore, all considered vehicle variants have a cabin layout similar to the reference vehicle, see Fig. 5.1. The reference vehicle is referred to as V-R and depicted in Fig. A.10. Basic aircraft design and performance parameters according to the PrADO synthesis are summarized in Appendix A.3.

In order to enable direct comparability of different vehicle concepts, each aircraft is simulated along predefined and constant (1) departure and (2) approach procedures. The flights are simulated according to preselected flight segments under defined climb angle, altitude profile, and configurational setting. The segmental definition is in accordance with common procedures at major airports, i.e. fixed waypoints with specified altitude and flight speed requirements. The actual flight performance of each vehicle, e.g. required engine operation, depends on the individual flight performance along the prescribed procedure.

(1) Departure - The departure procedure is defined by 5 consecutive flight segments. After take-off, the first segment with a 7° climb angle is initiated up to an altitude of 100 m. This climb segment is simulated with extracted gear, high-lift system in take-off configuration, and full thrust setting. In the subsequent flight segment the gear and high-lift system are retracted while the flight speed and climb angle are held constant. This segment ends when reaching clean configuration of the aircraft. This configurational setting allows for a steeper climb angle, thus a climb angle of 9° is selected for the third flight segment. This segment is defined up to an altitude of 900 m with a thrust setting of 98%. The climb angle and thrust setting are reduced during the forth flight segment, i.e. 7° climb angle with a thrust setting of 96%. The fourth flight segment is defined up to an altitude of 1700 m when the final flight segment is initiated. During the final flight segment, the climb angle is furthermore reduced until reaching stationary horizontal flight with a thrust setting of 65%. This fifth and final segment of the departure simulation is defined up to an altitude of 2100 m over ground where the departure simulation ends.

(2) Approach - The approach procedure is comprised of seven consecutive flight segments. The approach simulation is initiated at a constant altitude of 2100 m over ground, a flight

speed of 420 km/h, and the vehicle in cruise configuration. The first flight segment is a -3° descent down to an altitude of 1200 m. While the aircraft remains in clean configuration, the airspeed is uniformly reduced down to 320 km/h. At 1200 m a second, short flight segment is initiated. During this flight segment, the previous glide path and speed are kept constant. Flaps and slats are extracted into the approach configuration prior initiation of the next flight segment. Maintaining the -3° descent, flight altitude is reduced to 600 m and flight speed down to 280 km/h. The subsequent flight segment holds the glide slope and speed settings, while the configurational setting is uniformly modified. Flaps and slats are furthermore extracted in order to initiate the final approach. The final approach is comprised of three more descent segments. Along the first segment of the final approach, the velocity is reduced to 250 km/h until the aircraft reaches an altitude of 350 m. During this descent, the flaps and slats are fully extracted. During the next short flight segment the landing gear deployment is initiated. Starting from this segment on, the flight velocity is finally reduced down to the aircraft specific individual landing speed, i.e. the stall speed multiplied with a constant safety factor. Hereafter, along the final segment the flight altitude is reduced to 50 ft in order to enable flare-out, touch-down, and deceleration.

The defined reference flight procedures are not equal to available and practical procedures as established at major airports. A simplified and more general definition of the flight procedures is required to ensure that each vehicle variant can be operated along these procedure. Only if similar procedural constraints are established for each vehicle variant, a comprehensive analysis and fair comparison of the predicted effects is enabled.

5.1.2 Evaluation Metric

At this point, a generic metric would be required in order to directly compare cost efficiency and environmental performance of new vehicles within the conceptual design phase. Such an approach could translate the predicted noise levels directly into monetary values. These noise expenses could simply be accumulated with the direct operating costs in order to evaluated and rank-order the economical efficiency of each vehicle. Obviously, such a correlation is extremely difficult to assess. In order to establish a general and comprehensive approach seems rather impossible. Up to this day, there is no accepted and common agreement on how to fix a price for ground noise pollution. For each airport individual and local noise charges and fees can be established, if any. As a consequence, the European Union plans to harmonize the various existing noise based charges for Europe within the next decade [107]. Existing local noise related fees and scientific models are only based on measurements at the three noise certification points, thus a low-noise modification or improvement to an existing aircraft or flight procedure has very limited to no direct effect [108,109]. Consequently, existing models for noise related charges are apparently meaningless in context of the presented work, thus can be ruled out.

More importantly, as long as existing noise related fees remain at insignificant magnitudes [108,109], there is no incentive to investigate and establish more sophisticated metrics and systems. This situation might change in the future due to the unpredictable influence of politics and rulemakers, e.g. legislation of more radical environmental hurdles for airports.

Multiple criteria design evaluation

As a consequence, no direct translation of predicted noise levels into monetary values is applied within the presented work. Instead, a simple multiple criteria approach is implemented. Normalized³ and weighted environmental and economical performance indicators are predicted and can directly be compared.

Relevant vehicle parameters are preselected and evaluated for each vehicle, i.e. n parameters with respect to environmental and m parameters with respect to economical performance. The environmental parameters are labeled as x_j with $j \in \{0..n\}$. Economical performance parameters are z_k with $k \in \{0..m\}$. Each of these vehicle specific performance parameters is normalized with respect to the corresponding value for the reference aircraft ("ref") to yield dimensionless performance indicators, i.e. ξ_j for the environmental and ζ_k for the economical performance.

$$\begin{aligned}\xi_j &= \frac{x_j}{x_{ref,j}}, & j \in \{0..n\} \\ \zeta_k &= \frac{z_k}{z_{ref,k}}, & k \in \{0..m\}\end{aligned}\tag{5.1}$$

The n environmental performance indicators ξ_j are then combined into one overall environmental indicator ξ . A predefined weighting function κ_j is assigned to each one of the performance indicators to finally sum them up into one value ξ . The same approach is applied to the m economical performance indicators, i.e. application of weightings λ_k . These weightings κ_j and λ_k are predefined and constant, thus are independent of the underlying scenario. The ranking among individual economical and environmental parameters is constant throughout the presented work.

$$\begin{aligned}\xi &= \underbrace{\sum_{j=1,n} \kappa_j \cdot \xi_j}_{environment} \\ \zeta &= \underbrace{\sum_{k=1,m} \lambda_k \cdot \zeta_k}_{economy}\end{aligned}\tag{5.2}$$

Performance parameters - The selected environmental performance parameters x_j are aircraft noise induced awakenings along approach and departure operation. For a quick and initial evaluation of the acoustic performance, it is sufficient to compare noise levels along the flight ground track. Max. SPL(A) is predicted along representative flight segments of the reference approach and departure procedure. These levels are then translated into aircraft noise induced awakenings⁴. Awakenings along the departure are labeled as x_1 and approach awakenings as x_2 .

The economical parameters are block fuel (z_1), operational empty weight (z_2), and balanced field length (z_3). Block fuel is selected as an indicator for the direct operating costs of the vehicle. The operational empty weight is selected as an indicator for the overall vehicle price [51]. Furthermore, the field length requirement is selected in order to reward short

³Results are normalized with respect to the preselected reference condition.

⁴A constant population density along the flight ground track is assumed. Such an assumption yields valid results because (1) all vehicles are simulated along constant and predefined reference trajectories and (2) no absolute but level differences are of interest.

take-off and landing operation (STOL). Such low-noise STOL vehicle could be operated at underutilized airports with shorter runways enabling new transportation business models [110].

Obviously, in order to improve the overall vehicle performance the selected individual parameters have to be minimized. The corresponding environmental and economical predictions for the reference vehicle are summarized in Tab. 5.1. The specific performance param-

environment, $x_{ref,i}$		economy, $z_{ref,k}$		
dep. awakenings [-]	app. awakenings [-]	oew [kg]	bal. field length [m]	block fuel [kg]
$x_{ref,1}$	$x_{ref,2}$	$z_{ref,1}$	$z_{ref,2}$	$z_{ref,3}$
8.15	14.37	38664	1949	10222

Table 5.1: Reference vehicle performance parameters

eters are selected based on engineering judgment and the opinion of the author. Obviously, a different selection is feasible and would probably lead to more or less different results for the overall vehicle evaluation.

Weighting factors and overall performance indicators - The corresponding weighting factors for departure and approach noise are selected to be equal, $\kappa_1 = \kappa_2$. Reduction of noise along approach and departure procedures is assessed to be of equal importance. Block fuel is selected as the far most important economical factor, thus an appropriate weighting factor of $\lambda_1 = 0.7$ is selected. Operational empty weight is defined as twice the factor for balanced field length, i.e. $\lambda_2 = 0.2$ and $\lambda_3 = 0.1$. The weighting factors λ_1 to λ_3 are predefined independently of the underlying scenario. The factors are selected to reflect the major cost drivers for aircraft acquisition and operation.

No specific business case is represented and different weighting factors or additional performance parameters could be selected by other users.

Now, the overall environmental and economical performance indicators, i.e. ξ and ζ can be evaluated.

$$\begin{aligned}\xi &= \underbrace{\frac{1}{2}}_{\kappa_1} \cdot \xi_1 + \underbrace{\frac{1}{2}}_{\kappa_2} \cdot \xi_2 \\ \zeta &= \underbrace{\frac{7}{10}}_{\lambda_1} \cdot \zeta_1 + \underbrace{\frac{2}{10}}_{\lambda_2} \cdot \zeta_2 + \underbrace{\frac{1}{10}}_{\lambda_3} \cdot \zeta_3\end{aligned}\tag{5.3}$$

These two overall performance indicators ξ and ζ are predefined and vehicle specific constants, thus independent of the selected scenario.

Scenario specific vehicle ranking - In order to evaluate a vehicle under specific boundary conditions, e.g. dominating environmental requirements, corresponding weighting can be applied to the vehicle specific performance indicators ξ and ζ (as specified in Eq. 5.4). Specific weighting of environmental, i.e. K_i , and economical performance, i.e. Λ_i , in a scenario "i" determines the overall ranking of a vehicle within this scenario. K_i and Λ_i are defined under the following conditions:

$$K_i + \Lambda_i = 1 \quad \wedge \quad K_i \in [0, 1] \quad \wedge \quad \Lambda_i \in [0, 1]\tag{5.4}$$

Applying these scenario weighting factors to the vehicle specific and constant performance indicators ξ and ζ results in a scenario specific ranking. Within an arbitrary scenario "i", defined by the ratio of K_i and Λ_i , each vehicle can be assigned a score σ_i according to its environmental and economical performance within this specific scenario.

$$\begin{aligned}
 \sigma_i &= K_i \cdot \xi + \Lambda_i \cdot \zeta \\
 &= K_i \cdot \sum_{j=1,n} (\kappa_j \cdot \xi_j) + \Lambda_i \cdot \sum_{j=1,m} (\lambda_j \cdot \zeta_j) \\
 &= K_i \cdot \left(\frac{1}{2} \cdot \frac{x_1}{x_{ref,1}} + \frac{1}{2} \cdot \frac{x_2}{x_{ref,2}} \right) + \Lambda_i \cdot \left(\frac{7}{10} \cdot \frac{z_1}{z_{ref,1}} + \frac{2}{10} \cdot \frac{z_2}{z_{ref,2}} + \frac{1}{10} \cdot \frac{z_3}{z_{ref,3}} \right)
 \end{aligned} \tag{5.5}$$

Economical and environmental performance weighting factors are varied in 10% steps resulting in 11 different scenarios. These scenarios include an economically driven scenario "0" ($K_0 = 0.0$ and $\Lambda_0 = 1.0$) and a low-noise scenario "10" ($K_{10} = 1.0$ and $\Lambda_{10} = 0.0$). An aircraft ranking within today's scenario could be described by a dominating economical and negligible environmental weighting, i.e. $\Lambda_{now} > 0.99$ and $K_{now} \leq 0.01$.

5.1.3 Solution Space Limitations

The design synthesis code PrADO and the implemented noise source models restrict the potential solution space. Obviously, only parameters that are both simulated in PrADO and are captured by the noise source models affect the noise prediction thus can be subject to any low-noise analysis. Furthermore, each noise source model imposes specific requirements with respect to data input and component design principles as outlined in section 3.2.2. According to section 3.2.2, each modification to the reference engine or airframe design has to be checked for compatibility against the inherent design principles of the corresponding noise model.

According to Dobrzynski [9], operational effects have a dominating impact on noise generation. Relevant operational parameters along a simulated flight path are captured by the models. Therefore, the operational impact on noise generation can be studied in detail, i.e. engine thrust setting, flight speed, altitude, flight path angle, selected configuration along the simulated flight path. Furthermore, overall aircraft design can be modified in order to support low-noise flight operation, i.e. steeper flight segments and reduced flight velocities [37,62]. Improving the vehicles Lift-to-Drag ratio allows to reduce wing area⁵ thus enabling slower approach flight velocities. Reduction of vehicle take-off weight increases the thrust-to-weight ratio for a fixed engine, thus enables steeper climb angles during departure. Obviously, modification to these basic aircraft parameters does not only influence the overall aircraft performance with respect to low-noise flight operation but also changes the noise emission of the corresponding airframe noise sources.

Both airframe and engine noise source models are parametric with respect to predefined major design parameters, see section 3.2.2. Variation of these design parameters will determine the componential noise emission, thus can be investigated. Due to the required simplicity of the source models, detailed geometry parameters, e.g. local cavities, kinematics, or linkages, can not be accounted for. As a consequence, Dobrzynski's suggestions with respect to certain design details can not be investigated with the available models. Although a direct parameter study is not possible, these geometry details could be accounted for by

⁵Reduction of wing loading is the main driver for reducing the flight velocity [37].

reading in measured noise level deltas. The significant influence of structural shielding on engine noise emission can be accounted for with the DLR ray-tracing tool SHADOW [83], see Section 3.2.2.3. Engine location and airframe layout can be modified in order to investigate engine noise shielding effects.

In the context of the presented aircraft design study, only preselected engine concepts are considered. For these concepts, underlying noise models have been checked in detail prior each application. Variation of engine design details is not investigated, thus engine performance decks and geometry parameters are precomputed for each selected engine concept and kept constant during further vehicle design modifications.

5.1.4 Vehicle Variants

Based on the solution space limitations, different basic vehicle layouts are selected for further investigation. As outlined in section 2.2, Dobrzynski and others identified several promising short- to mid-term solutions towards aircraft ground noise reduction [37,38,62]. Several of these suggestions are within the limitations, thus can be investigated within the presented process.

The selected vehicle variants can be assigned to 5 main categories according to their most important noise related design features. Obviously, this has to be the approach toward a reduction of perceived engine noise levels on the ground. Engine noise is still the most dominant noise source on-board of any flying vehicle. Not considering advanced engine nor futuristic vehicle design, e.g. a blended wing body with fully embedded engines, the situation is not likely to change within the next decades. Within this timeframe, no significant noise reduction is expected for existing, conventional turbofan engines [79]. Other, more optimistic references estimate a theoretically achievable, maximum noise reduction within the next decades to be in the order of 3 to a maximum of 5 dB [113,114].

Alternative propulsion concepts could have a significant impact on engine noise contribution, i.e. either positive or negative. Yet, this impact is difficult to assess due to the lack of simulation models and (unrestricted) validation data. As a consequence, the selected vehicle variants are simulated with the reference engine.

As an outlook on future applications, some alternative propulsion concepts are discussed in a reduced detail level according to available data and simulation methods.

Consequently, exploitation of structural noise shielding is the most effective vehicle design solution to significantly reduce perceived engine noise levels. The implemented fan noise source model [26] yields a characteristic noise emission directivity for the fan. For aircraft under take-off conditions, maximum fan noise levels are observed for polar angles α^* between 20 and 60° in the forward direction and 110 to 140° in the backward direction. Under approach conditions, i.e. low engine thrust settings, significant fan noise contribution is limited to the backward direction with polar angles between 110 and 140°. Consequently, noise barriers should be placed directly in these relevant emission directions for effective fan noise shielding.

The selected vehicle variants are assigned into the following main categories.

- main wing shielding of over-the-wing installed engines: Design variants *v-0*

- empennage shielding of rear fuselage mounted engines: Design variants $v-1$
- fuselage/wing shielding of over-the-fuselage mounted engines: Design variants $v-2$
- wing/empennage integration for engine covering: Design variants $v-x$
- alternative propulsion concepts
 - geared turbofan engine: Design variant $v-g$
 - counter-rotating-open-rotor: Design variant $v-c$

Investigation of over-the-wing engine installation is selected because this concept is already realized on-board of existing vehicles. Vehicles of category $v-1$ represent a compromise between economical and environmental performance whereas the remaining categories are defined to maximize noise shielding effects.

Fig. 5.2 shows the major design features for each selected vehicle category. The depicted variants, referred to as v , do not represent final vehicles but illustrate the design changes and steps toward feasible low-noise aircraft configurations. Yet, all variants v have reached convergence with respect to major design parameters, e.g. operational empty weight (OEW), thus can be considered as valid designs but not as practical or optimized solutions. The dashed line in Fig. 5.2 points out the initial and less detailed discussion of selected alternative propulsion concepts.

The vehicle variants with the conventional reference propulsion system are subject to a detailed design study. For each vehicle category, key design parameters are selected and modified in order to identify the most promising parameter setting, see Appendix. In order to generate the required environmental and economical performance data, all resulting 460 design variants are subject to an analysis with PrADO, SHADOW, and PANAM. Each of these vehicle variants can directly be compared with each other variant and with the reference vehicle. The environmental and economical performance indicators are evaluated for each vehicle as depicted in Fig. 5.3. An improvement in vehicle performance is indicated by reduced ξ and ζ values compared to the reference vehicle at $\xi = \zeta = 1.0$. For example, an environmental performance indicator $\xi = 0.95$ could be caused by a 6.6 % reduction in aircraft noise induced awakening probability along the simulated approach operation compared to the reference case.

Depending on the impact of the preselected parameters on the vehicle performance, patterns and trends can be identified in the ξ and ζ distribution. Improvements to the environmental performance without huge economical losses can be achieved according to Fig. 5.3. Several design variants even promise both environmental and economical benefit. Yet, these design variants are no final and practical vehicles but represent the most promising choices out of the preselected parameter range. According to Fig. 5.3 and Tab. A.32, the most promising design variant out of each category can be identified and selected for a final overall design check. The selected design studies and the resulting final vehicle design for each category are presented in the following sections. Known uncertainties are discussed for each vehicle variation in order to identify and stress out these issues for a more detailed investigation at a subsequent design phase.

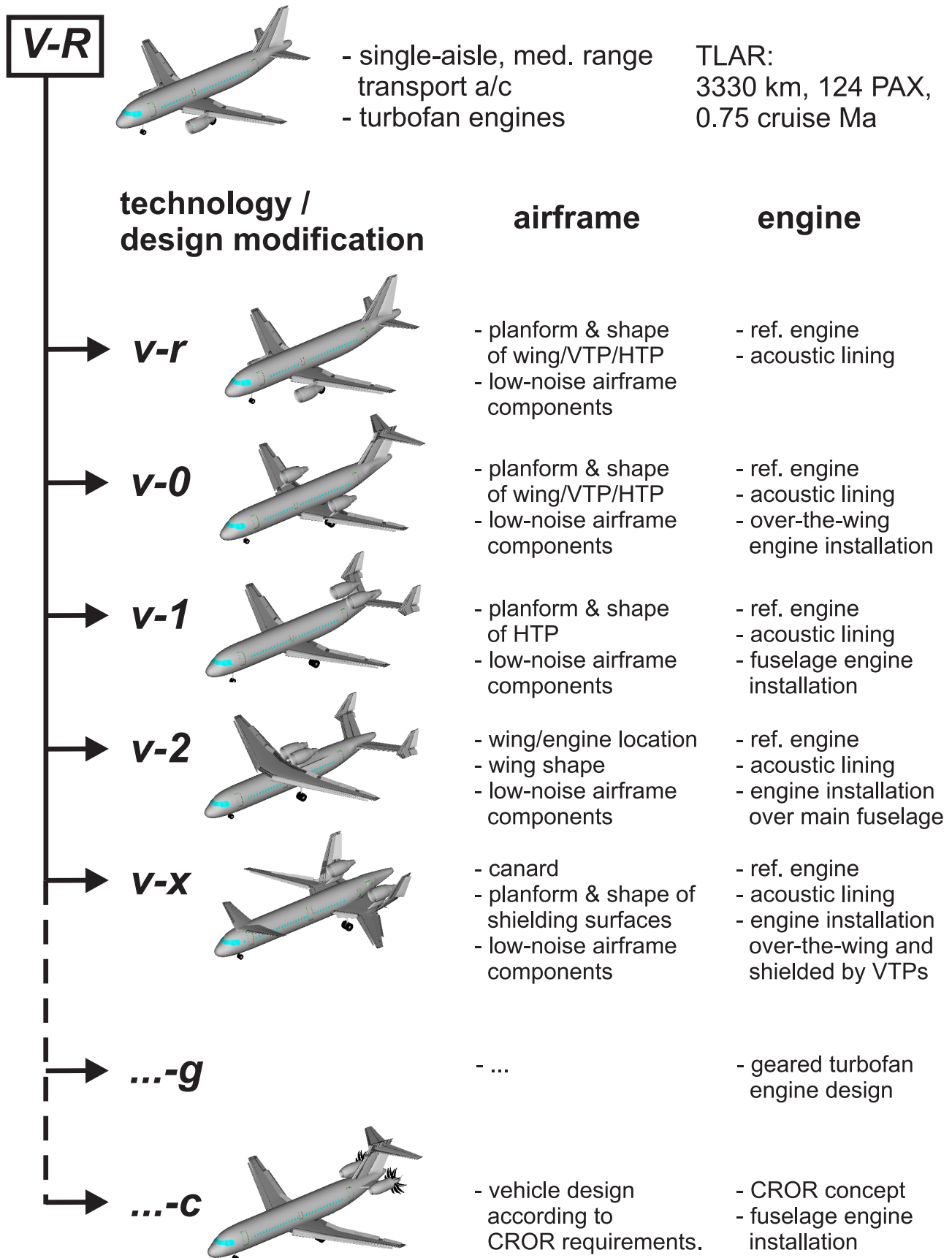


Figure 5.2: Design Evolution Chart

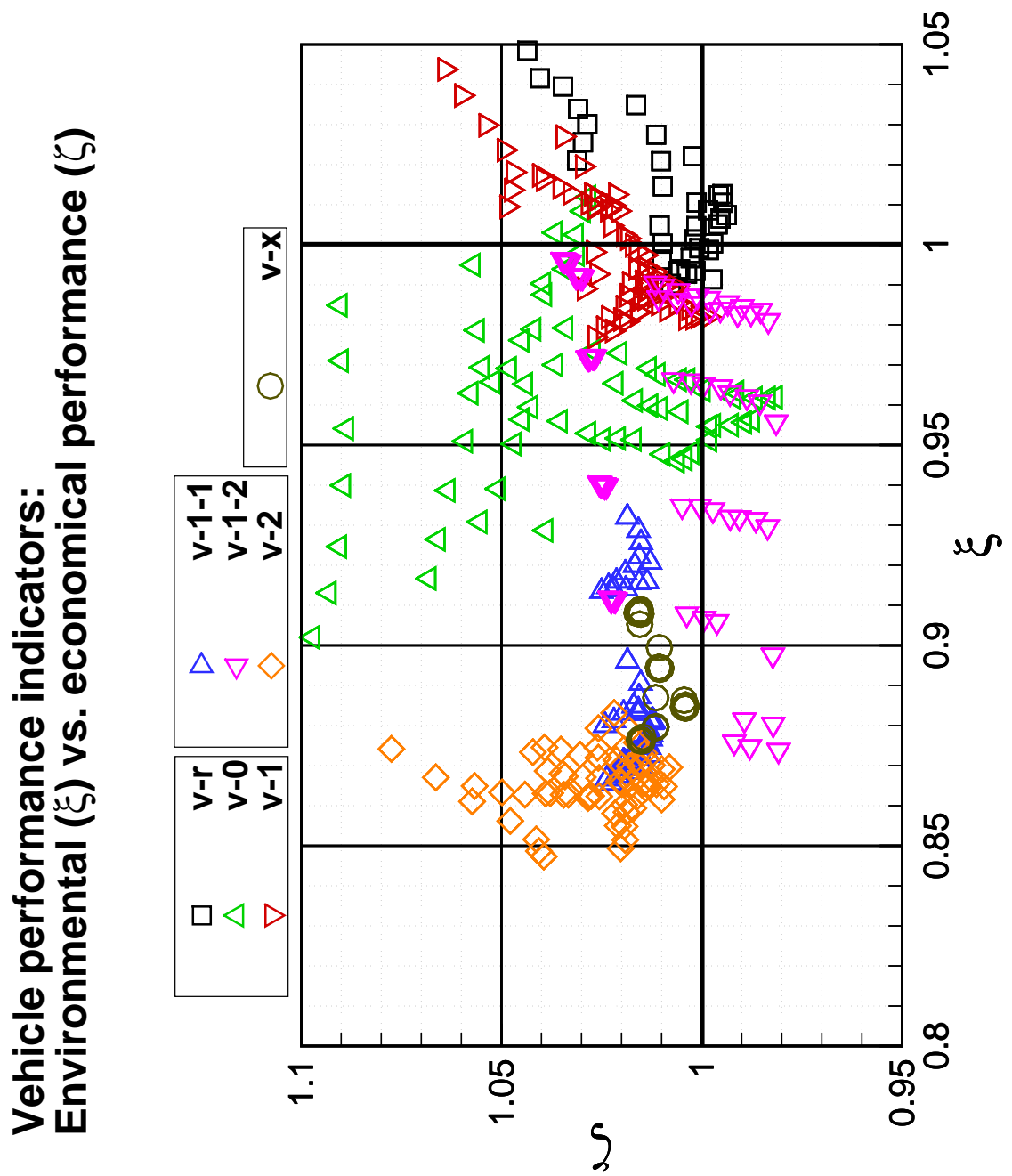


Figure 5.3: Performance indicators: all design variants

5.1.4.1 Vehicle Geometry Variation

For some of the selected vehicle variants, engine noise is shielded by the main wing. Moreover, the flight performance of each vehicle depends on the lift and control surfaces. Therefore, all variants are subject to a parameter variation of the main wing planform and relative location along the fuselage. Thereby, the high lift system components are linearly adapted according to the new wing planform.

From an aerodynamic point of view, a large aspect ratio is desirable because it improves the vehicle aerodynamics. As a result, this could reduce required engine thrust settings along the predefined flight procedures. A large wing area A_w , i.e. reduced wing loading, enables slow aircraft specific flight velocities along the final approach resulting in reduced airframe noise generation [37]. Reducing the wing loading decreases aerodynamic loading on high lift and lifting surfaces thus furthermore decreases airframe noise. Yet, wing weight does increase with both area and aspect ratio, thus has negative implications on flight performance. Furthermore, reduced wing loading can have negative implications on passenger ride quality during cruise, i.e. buffeting. Obviously, a trade-off between additional wing weight and desirable flight performance is necessary.

The resulting vehicle variants are valid PrADO designs but might require further design adaptations due to the new wing planform. These variants are therefore no final or optimized PrADO designs. From each category, the most promising vehicle variant is identified and selected for a final detail investigation.

Modified reference vehicle (category $v-r$) - According to each parameter variation, the resulting global aircraft parameters (PrADO) and the selected environmental prediction results (SHADOW, PANAM) are evaluated (Tab. A.9 and Fig. A.23, Appendix). Normalizing these results with the reference data yields ξ and ζ , as depicted in Fig. A.24.

The most promising variants out of the parameter space feature high aspect ratios. Especially, the environmental impact is strongly influenced by Λ_w , as it is clearly visible in Fig. A.23. This can be mainly attributed to reduced thrust requirement along the predefined approach procedure, i.e. significantly reduced ground noise levels for $\Lambda_w = 11$ compared to a vehicle with $\Lambda_w = 7$. The advantageous economical impact of high Λ_w is based on the reduction in block fuel, which is furthermore accentuated by a strong weighting factor. An obvious increase in wing weight, thus overall empty weight, due to high aspect ratio does not counteract the overall advantage. Furthermore, the most promising design variant has a reduced wing area (-7.7%) compared to the reference vehicle. This is in good agreement with the known oversizing of the reference wing due to the Airbus family concept.

Ultimately, the most promising design variant is no. 20 of parameter variation 1. The second parameter variation is not discussed in detail because no improvements with respect to neither environmental nor economical performance could be achieved, see Fig. A.24.

Main wing shielding (category $v-0$) - The V-R is modified to exploit fan noise shielding due to an over-the-wing engine installation. Due to flight stability reasons, the main wing is shifted closer to the fuselage tail. Furthermore, a T-tail arrangement is selected in order to avoid direct jet impingement on the control surfaces. The engine arrangement pushes the center of gravity (CG) backward along the fuselage, thus requires increased control surface areas at the tail. Fig. A.25 depicts the principal vehicle layout. For this concept, variation of A_w and Λ_w does not only influence the flight performance but directly determines en-

engine noise shielding. To increase noise shielding, increasing A_w and low values of Λ_w are most promising. The second parameter variation is based on a relatively small A_w , therefore an increased economical performance but reduced shielding effects. A direct impact of increased A_w on noise shielding is clearly visible in Fig. A.27(a). Therefore, the most promising vehicle variant from parameter variation 1 is selected, precisely variant 24. This variant yields a significantly increased environmental performance although flight operation is less economical compared to vehicles from parameter variation 2.

Empennage Shielding (category *v-1*) - If engines are mounted at the back of the fuselage, the empennage can be applied for noise shielding. Compared to the reference vehicle, this design shifts the overall center of gravity (CG) to the back of the vehicle. This can cause problems with respect to the overall aircraft flight stability.

In a first step, an H-tail design with rear-mounted engines is selected as depicted in Figs. A.29 and A.30, Appendix. The H-tail design promises some shielding of the backward fan noise and at the same time assures stable flight behavior of the vehicle. Yet, the H-tail design increases the empennage weight, thus results in generally increased OEW compared to the reference layout. With this initial, backward-swept H-tail design, no shielding of forward fan noise is achieved, thus the concepts results in low environmental performance (Fig. A.31(a)).

As a consequence, a forward-swept H-tail is investigated in order to achieve sufficient engine noise shielding (Figs. A.33 and A.34, Appendix). This new design *v-1-1* results in significantly improved environmental performance, i.e. an extensive reduction in aircraft noise induced awakenings (Fig. A.35(a)). Yet, due to the forward-swept H-tail, distances between aircraft CG and control surfaces are significantly reduced, thus massive control surfaces would be required for reasonable flight stability and control. Because the required tail volume coefficient can not be realized, the *v-1-1* variants are not considered as practical solutions.

In a next step, a third vertical tailplane is added to the *v-1-1* variant. This third tailplane is supposed to reduce the required size of the former H-tail. The so-called *v-1-2* variant, as depicted in Fig. A.37, results in improved flight stability, yet is still not sufficient for a practical flight operation. The *v-1-2* has similar shielding characteristics compared to the *v-1-1* but increased economical performance. This can be attributed to the three-tailplane design which results in reduced weight of the empennage, i.e. reduced overall weight of the aircraft.

The previous findings indicate, that a forward-swept empennage is promising but a forward-swept H-tail can be excluded as a practical solution. Consequently, a conventional tail layout with forward-swept horizontal stabilizers is selected for further investigation (Fig. A.38, Appendix). This empennage layout promises sufficient tail volume coefficients for stable flight operation. Yet, the acceptable margin for a CG movement during flight is little, i.e. under 1 m, so that safe flight operation would require further dedicated investigation. The general layout results in reduced weight of the aircraft and consequently a low block fuel requirement. These *v-1-2* variants (2nd parameter variation) show the best economical flight performance of all *v-1* design variants. Compared to the reference vehicle, the simulations even indicate an improvement in economical performance for the *v-1-2* (Fig. A.40, Appendix).

For the v -1-2 variants, an optimal shape of the horizontal stabilizer is identified, i.e. with respect to aspect ratio and sweep angle. The design variant 1 of parameter variation 2 is selected for further investigation.

Fuselage/wing shielding (category v -2) - Maximum engine noise shielding requires an extensive shielding barrier. A high wing design provides such a barrier, precisely above the fuselage-wing junction. Extensive noise shielding can be achieved, if both engines are directly mounted above this junction. As a consequence, a H-tail is required to avoid direct jet impingement. Due to the H-tail, the aircraft structural weight is increased. Compared to the reference vehicle, all v -2 variants result in decreased economical performance (Fig. A.44, Appendix).

Starting with a basic design (Fig. A.41), further parameter variations are applied in order to find the most promising wing planform and location. According to the simulation results, extensive noise shielding is achievable (Fig. A.43(a), Appendix).

For the final assessment, variant 27 of parameter variation 1 is selected. This design variant promises significant noise shielding at the price of reduced economical flight performance.

Wing/empennage integration (category v -x) - The original DLR Low-Noise Aircraft (LNA) concept [37, 38] is modified in order to meet the TLAR as described in Section 5.1.1. The modifications result in a reduced fuselage length and decreased wing/control surface areas. The underlying PrADO input data set is adapted from an earlier short-range LNA model (LNA-SR) by C. Liersch, Institute of Aerodynamics and Flow Technology, DLR, Braunschweig.

The selected canard configuration allows to move the main wing toward the rear section of the fuselage. Such a backward main wing location enables an integrated design of main wing and vertical tail plane (VTP). The fuselage mounted VTP of the reference aircraft is thus modified into two VTPs. The engines can then be mounted over-the-wing, in-between fuselage and VTP, thus are subject to significant polar and lateral fan noise shielding. Starting from this initial geometry (Fig. A.45), the main wing planform and the final arrangement of the two VTPs are modified in order to maximize noise shielding effects. Out of the available vehicle variants, variant 25 is selected due to efficient noise shielding and still feasible economical performance.

With respect to the reference aircraft, the cabin layout had to be rearranged, i.e. a new location of main door and emergency exit.

5.1.4.2 Final Vehicle Designs

The selected most promising vehicle variants are subject to a feasibility check and some design modifications, if required. Some parameters that have been kept constant during the parameter variations might require further adaption, e.g. final matching of main wing and empennage due to control and stability issues. These modifications do not affect the identified optimal engine noise shielding but can have an impact on the overall flight performance, e.g. due to increased aircraft weight. The final PrADO vehicles are labeled with an upper-case letter, namely V , and detailed results are presented in Section A.4, Appendix. Key design and performance parameters for each vehicle are listed. The resulting environmental and economical performance indicators for each vehicle are collected and subject to a final scenario evaluation.

To rank-order the final vehicles under various boundary conditions, different economical and environmental weighting factors are applied. K_i and Λ_i are varied in 10% steps resulting in 11 different scenarios, including an economically driven scenario "0" and a low-noise scenario "10". Each vehicle is assigned its individual scenario score σ_i within a scenario "i". Fig. 5.4 shows the scenario dependent vehicle ranking for the final six vehicles. According to the selected importance of environmental and economical performance, each scenario results in a different score for one specific vehicle. By definition, the reference vehicle has a constant score of 1 in all scenarios. If economical performance is weighted 100 %, the highest score is achieved by the modified reference vehicle. Starting from 30% weighting of environmental performance up to the low-noise scenario, the $V - 2$ is the most promising design. According to these findings, fuselage/wing shielding is the most promising design feature with respect to low-noise vehicle design.

If engine noise contribution is adequately reduced, airframe noise generation is more and more dominating along the approach procedures. Fig. 5.5 shows the predicted maxi-

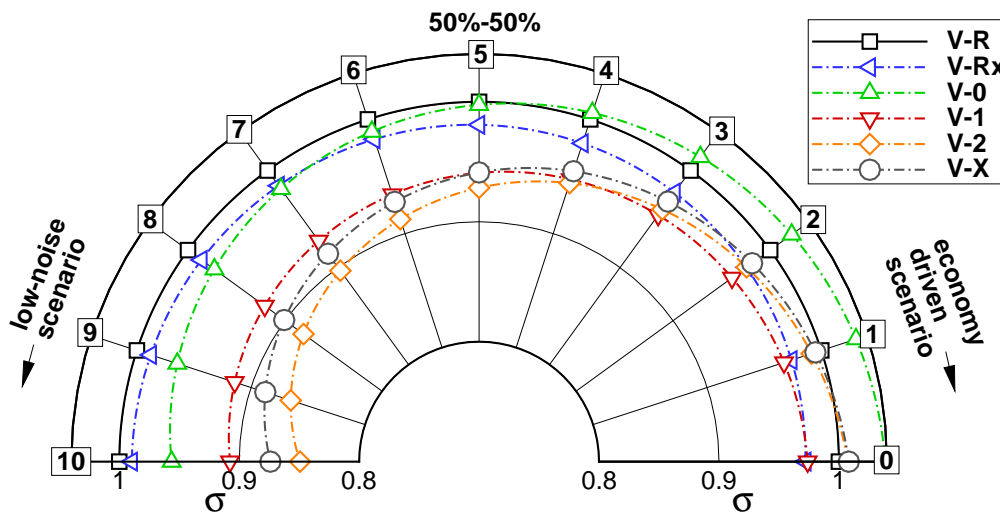


Figure 5.4: Scenario dependent vehicle ranking

imum SPL(A) levels along the simulated approach flight ground track. The ground noise distribution is predicted according to the individual flight performance of each vehicle along the selected reference approach. Around 24 km prior to the runway threshold, the flaps and slats are deployed on-board all vehicles. This happens at relatively high velocities, thus results in an airframe noise level increase up to 10 dBA as depicted in Fig. 5.5. Furthermore, the landing gear extraction around 7-8 km prior to the runway can be identified in the plot.

For the vehicles $V - 1$, $V - 2$, and $V - X$, the achieved engine noise reduction is extensive, thus results in dominating airframe noise along most of the approach procedure. As a consequence, any reduction of the dominating airframe noise sources will have a direct overall effect, i.e. high-lift system and gear. According to Dobrzynski [9], noise level reductions due to modifications of flap and slat design are limited to about 1 dB. An additional 5 dB noise reduction can be achieved due to low-noise modifications to the landing gear. Obviously, this effect is limited to flight operation with extended gear, thus only affects an area from the extraction of the gear until touch-down or until higher thrust settings cause engine noise dominance. A more effective way to reduce the dominating airframe noise for these vehicles is a decreased approach flight speed. Alternative approach procedures

with a decreased flight speed v_{new} would immediately result in an overall noise reduction. Depending on the configurational setting, significant reductions in the order of 5 dB can be achieved, e.g. approach velocities of the $V-2$ can be reduced up to 25%. Yet, the flight speed reduction should not require additional deployment of the high-lift system because this will counteract any noise reduction. Furthermore, a reduced flight speed might be not practicable along a common approach path toward major airports. Due to the prevailing high traffic densities, these slow vehicles would choke the incoming traffic routes. Yet, a slower low-noise approach could be a promising alternative during night hours.

Along the departure procedures, the overall noise reduction due to the fan shielding is limited. All vehicles with extensive fan noise shielding are limited to a maximum of 2-3 dBA overall noise reduction compared to the reference vehicle. The reason for that is the dominance of remaining jet noise contribution (Fig. A.63, Appendix).

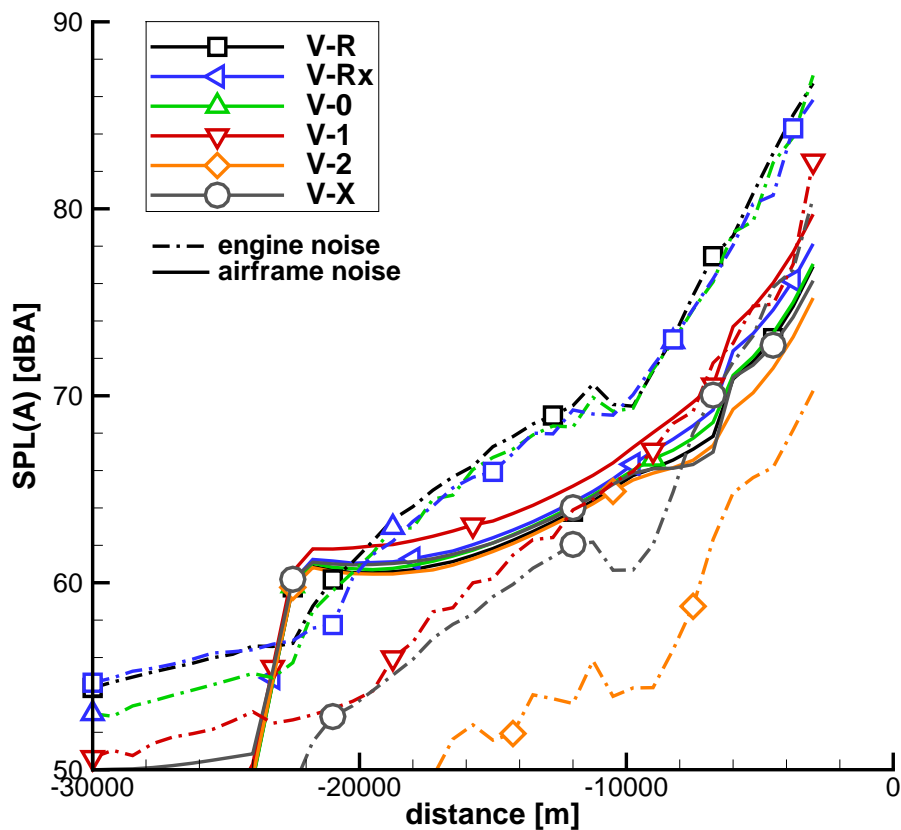


Figure 5.5: Max. SPL(A) along approach flight ground track

5.1.5 Alternative Propulsion Technologies

In this section, alternatives to the selected reference propulsion concept are discussed without detailed flight simulation nor vehicle/engine geometry variations. Geared Turbofan (GTF) and propeller driven engine concepts are identified as plausible alternative propulsion units for the reference aircraft.

A GTF has promising characteristics with respect to both noise reduction and efficiency improvement [79]. For conventional turbofan engines, fan and low-pressure compressor/turbine are directly linked via one shaft, thus run at the same rotation speed. While increased speeds would be preferable for the compressor and the turbine [79], the maximum fan rotations are limited to avoid supersonic fan tip velocities. As a result, the components are not operated at their individual optimum. Installation of a gearbox breaks up this linkage and enables the desired adaption of rotational speeds. If higher rotation speeds can be achieved for the low-pressure engine components, the overall pressure ratio of the core engine is increased [79]. This results in an increased engine advance ratio, which defines the overall efficiency of the engine. Furthermore, decoupling of fan and low-pressure components enables to increase the fan diameter according to a reduced rotation speed but still meet the requirements for subsonic tip velocities [79]. As a result, higher bypass ratios can be achieved, i.e. increased mass flow and decreased flow velocities through the bypass duct. Obviously, this has a beneficial effect on jet noise generation at the bypass exhaust [79]. Modern GTF have bypass ratios in the order of twice the ratio for conventional turbofan engines [79], thus are very promising propulsion systems for low-noise aircraft concepts.

Compared to a turbofan engine, a propeller offers significantly reduced specific fuel consumption due to extensive bypass ratios [77]. The optimum propeller design comes with a large diameter and only few blades which results in moderate acceleration of a massive air flow, thus yields in maximum propulsion efficiency⁶. As a consequence, single propeller disk concepts require huge engine diameters to generate appropriate thrust levels for the reference aircraft. A recent study of a turboprop on-board of a vehicle similar to the V-R requires a propeller diameter in the order of 6 m [115]. A comparable existing engine, the EPI TP400-D6 of the new A400M, provides a shaft power of over 8000 kW and has an engine diameter of 5.3 m [102]. These huge engine diameters cause difficulties with respect to the vehicle integration and therefore would require further detailed analysis of feasible installation concepts.

In general, vehicles with propeller engines are limited to slower cruise velocities. The maximum cruise velocity is determined according to an inherent limitation to the fan tip Mach numbers. At the fan tip, velocities in the higher supersonic regime should be avoided due to considerably increasing aerodynamic losses [79]. The cruise speed limitations for efficient flight operation are in the order of Mach 0.5 for older turboprops and can be as high as 0.65 for advanced high-speed propellers [115]. In addition to the speed limitation, propellers inherently have extensive thrust excess. Consequently, these engine concepts are more advantageous for short take-off and landing (STOL) flight operation [115] but less promising for the selected TLAR as described in Section 5.1.1. Due to the required mission range, the propeller flight speed limitation would have a significant impact on overall flight time.

⁶Private communication with C. Lenfers, DLR Braunschweig, June 2012, Ref. [115].

A more promising concept for a propeller engine is the Counter-Rotating-Open-Rotor (CROR). The CROR promises significant advantages over the conventional turboprop design according to Refs. [116–119]. Most importantly, flight cruise Mach numbers of up to 0.75 can be achieved for an optimized CROR design as presented in Refs. [116,117]. According to Ref. [116], CROR engines mark a "step change in propulsion efficiency" due to their ultra-high bypass ratios. Compared to turboprop concepts, the CROR offers an increased efficiency for the same disk loading [118]. This can be attributed to the counter-rotating rotors, precisely the avoidance of swirl behind the engine, thus reducing additional efficiency losses to a minimum [118]. Consequently, for a required disk loading and propulsion efficiency, the CROR design results in significantly reduced fan diameters compared to a turboprop⁷. For example, a recent DLR concept for an aircraft similar to the *V-R* has a maximum diameter of 4.2 m [116,117]. Compared to a turboprop design, the engine integration on-board of the vehicle is simplified.

Due to the low specific thrust, extremely favorable specific fuel consumption (SFC) is achievable. Simulations indicate a potential SFC reduction in the order of 30% compared to a conventional turbofan concept [119].

Another advantage of a counter-rotating engine is the avoidance of dynamic rotor torque and therefore reduced loads on engine mountings [118]. Transmitting the engine power and torque via two shafts, reduces the loads and simplifies the gearing of the propellers according to Ref. [118].

In conclusion, an advanced CROR almost fulfills the predefined TLAR for the reference aircraft *V-R* and is therefore preferred over a conventional turboprop.

5.1.5.1 Geared Turbofan Engine

Investigation of a geared turbofan is straight forward due to its (geometrical) similarity with the reference engine. Vehicle installation considerations are similar but the increase in diameter and engine weight has to be accounted for. While the implemented noise prediction methods are still valid for a GTF, the generation of required input data for the noise prediction is not possible within conceptual aircraft design. The complexity of the required engine details is not suited for conceptual design, thus simplified engine performance simulation cannot be applied. Tools of higher fidelity are required in order to simulate interactions and interdependencies of fan, compressor, and turbine with respect to the gear box.

The (re-) design of a current geared turbofan engine concept, e.g. PW-1000 on-board of the new A320neo, is still under investigation at DLR. So far, no simulation results nor measurements are available. Due to the lack of alternatives, an existing but outdated GTF design is selected for further investigation⁸. The DLR engine concept as introduced in 2009 [112] is not optimized for low-noise performance but was designed for short take-off and landing flight operation (STOL), thus comes with significant thrust excess. Consequently, the GTF engine is overdimensioned for the reference aircraft *V-R*. During standard and non-STOL flight operation of the *V-R*, the selected GTF can therefore be operated with reduced thrust settings. In Ref. [112], the predicted extensive noise reduction for the GTF is mainly attributed to this effect and not directly to conceptual advantages. Furthermore, low-noise performance of the GTF is overestimated in Ref. [112] due to predominant PANAM fan noise overprediction

⁷Private communication with C.O. Márquez, DLR Braunschweig, June 2012, Ref. [117].

⁸The engine performance map and detail design parameters are VarCycle [80] results provided by Tom Otten, DLR Institute of Propulsion Technology.

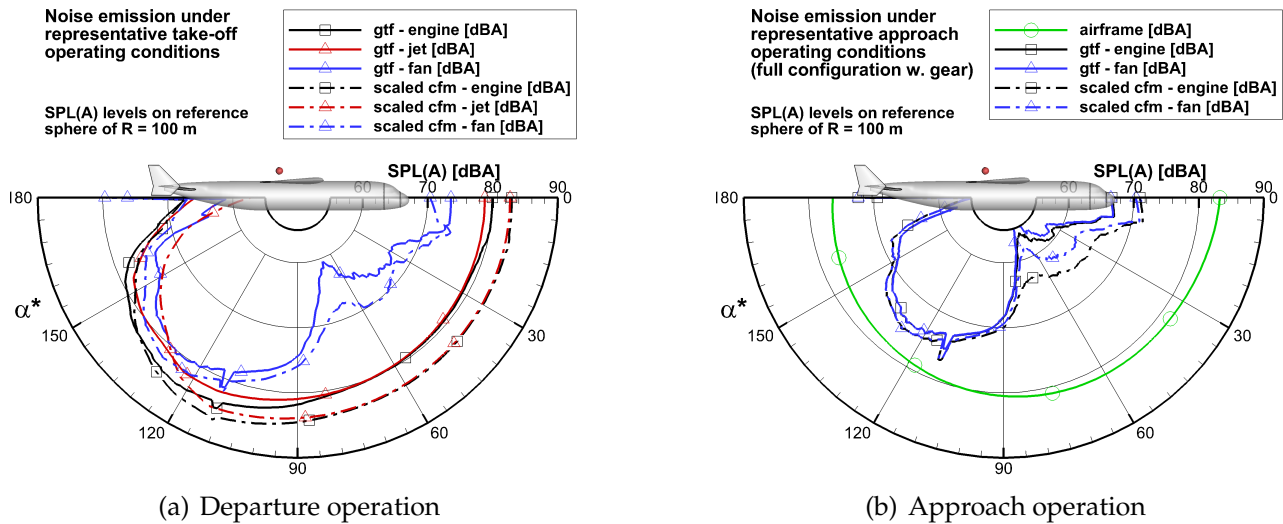


Figure 5.6: Vehicle V-2: Engine noise SPL(A) directivities for geared turbofan versus scaled reference engine

back in 2009. As a consequence, the impact of a GTF's reduced rotation speeds on noise generation is overpredicted if compared to current PANAM simulations [125].

Nevertheless, in context of the studied vehicle variants, the GTF engine is a promising concept. Due to the high bypass ratio of almost 16, jet exhaust velocities and thereby jet noise generation is reduced. Exhaust velocities for the engine bypass are reduced by up to 20%. Consequently, a GTF concept in combination with structural fan noise shielding yields significant noise level reduction for both major engine noise components.

In contrast to what was presented in Ref. [112], the overdimensioned GTF is now directly compared to a scaled version of the reference engine⁹. Both engines generate identical maximum thrust at sea level, thus can directly be compared under identical operating conditions. As a result, any artificial advantage of an oversized engine under reduced operation can be avoided. Prediction results for both concepts can now directly be attributed to the corresponding engine design.

The two engines are evaluated on-board of a V-2 vehicle design. A variant with the GTF and one with the scaled CFM are simulated under identical take-off and approach conditions. For take-off operation this is a required thrust of 75 kN per engine at a flight speed of 80 m/s and an altitude of 500 m. The scaled CFM runs at 81% (4020 rpm) and the GTF at 93% (2760 rpm) of the corresponding maximum revolution speed in order to deliver the required thrust. The representative approach flight condition is defined as 22.5 kN thrust per engine, 75 m/s flight speed, and 500 m altitude. The required approach thrust results in 65% (1960 rpm) max. engine rotations for the GTF and 55% (2760 rpm) for the scaled reference.

The SPL(A) emission directivity is evaluated on a reference sphere of 100 m radius as depicted in Fig. 5.6. Departure noise emission of the V-2 is dominated by jet contribution due to very efficient fan noise shielding as depicted in Fig. 5.6(a). Reduced jet velocities for the GTF decrease the overall vehicle noise emission by 3-4 dBA for all relevant emission angles, i.e. a clearly perceptible noise level difference. Obviously, no difference is observed

⁹The scaled reference engine is provided by T. Otten, DLR Institute of Propulsion Technology.

for the approach condition due to dominating airframe noise contribution, i.e. landing gear dominance (Fig. 5.6(b)). Consequently, the incentive to exploit any low-noise modifications to the airframe is increased. The increased level difference between airframe and engine noise make modifications to the airframe more promising. For example, the overall impact of a low-noise landing gear is significantly increased.

Although the presented results are based on an outdated engine design, the results support the application of GTF engines with respect to noise reduction. The results indicate a potential to reduce both fan and jet noise contribution. More recent GTF designs, e.g. the PW-1000, are subject to both componential and overall low-noise design modifications compared to the presented initial GTF concept. Therefore, it can be expected that future GTF designs are subject to decreasing noise generation compared to this initial design.

In conclusion, the combination of structural fan noise shielding and a GTF engine design shows a great potential for overall aircraft noise reduction.

5.1.5.2 CROR Engine

For the noise prediction of a CROR, no appropriate simple noise source model is available or will be in the foreseeable future. So far, CROR simulation is either based on input from dedicated experiments in combination with high fidelity computation (CFD & CAA), or entirely based on the computation. Due to the extensive effort and required data complexity in the context of a CROR, only very limited prediction results are available, especially if dealing with installation effects. Installation effects are yet expected to significantly influence the noise directivity of a CROR, thus have to be accounted for in order to produce feasible and physical results [120].

If existent at all, available experimental data is usually confidential and proprietary, thus not available for validation of the computational models. In the context of the presented work, these circumstances and restrictions permit only an initial estimation on the noise emission of a CROR.

According to available literature [116, 118], extensive CROR noise emission can be expected for emission angles around $\alpha^* = 90^\circ$. As a consequence, solely tail-mounted engine installation is acceptable in order to avoid intolerable cabin noise exposure [118]. For this investigation, an appropriate and initial PrADO vehicle is designed as depicted in Fig. 5.7. The selected vehicle, referred to as $V - c$ is a rather conventional design, because an investigation of advanced structural noise shielding for a CROR is not in the scope of the presented work.

In order to simulate an installed CROR concept such as the $V - c$, the Fast-Multipole Code (FMP) by M. Lummer¹⁰ is applied. This code is still under development but initial results are promising [120]. According to the selected reference CROR design [116, 117] and the vehicle layout, two different simulations have been performed by Lummer, i.e. an isolated and the installed CROR ($V - c$, see Fig. 5.7). FMP results for the uninstalled CROR can directly be compared to available high fidelity computations by J. Yin¹¹ based on the Ffowcs-Williams and Hawkings equation (FW-H). This comparison is understood as a feasibility check of the FMP predictions. Original FW-H data from Yin as presented in

¹⁰Institute of Aerodynamics and Flow Technology, DLR Braunschweig

¹¹Institute of Aerodynamics and Flow Technology, DLR Braunschweig

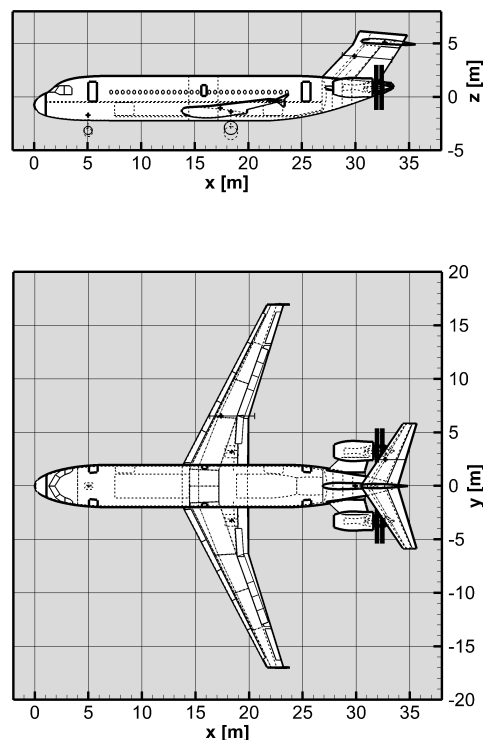


Figure 5.7: CROR: vehicle layout

Ref. [116] is used for this tool feasibility check.

For predefined take-off operating conditions¹², farfield noise emission levels are available by Yin. These predicted levels correspond to observers on straight lines parallel to the CROR axis of rotation¹³. For the comparison, this original FW-H data is transformed onto a corresponding reference sphere of radius 42.7 m.

As depicted in Fig. 5.8, the FW-H (red dashed line) and the FMP simulation (black dashed line) of the uninstalled CROR are in good agreement, thus confirm the plausibility of the FMP approach. It has to be noted, that both simulations are modified in order to account for 2 CROR engines.

If acoustic installation effects are accounted for, increasing noise levels are experienced due to noise reflection and interaction effects with the empennage and fuselage. It is noted, that source installation effects due to a change of the local aerodynamics on the CROR are neglected. For the specific vehicle layout, the noise level increase is in the order of 2-4 dB (black, solid line) compared to the uninstalled engine.

Finally, the FMP simulations are compared to a conventional turbofan engine, i.e. CFM-56, under identical operating conditions. Yet, it has to be kept in mind that both concepts are simulated with different tools and methods! The presented results can only indicate trends and tendencies with respect to conventional propulsion technology.

Comparing the uninstalled CFM (dashed blue line) with the uninstalled CROR (dashed black line) indicates a noise level increase in the order of 3 - 5 dBA. If both engines are installed onboard of the $V - c$, the CROR generates noise levels up to 8 dBA above the

¹²Ma = 0.2, T = 75 kN per engine.

¹³Original data is depicted in Fig. 21-b, Ref. [116]

levels for the installed CFM-56. Most importantly, the CROR noise peaks are predicted for relevant emission angles α^* of 90 - 120° with respect to ground noise immission. As a consequence, further investigation of noise shielding barriers is essential. A CROR installation as presented in Fig. 5.7 might yield acceptable cabin noise levels but is not suitable with respect to ground noise immission. The presented initial results necessitate the exploitation of CROR noise shielding. Only if the direct CROR noise emission towards the ground can be shielded by structural barriers, the overall noise impact might be reduced to a level comparable to a conventional engine.

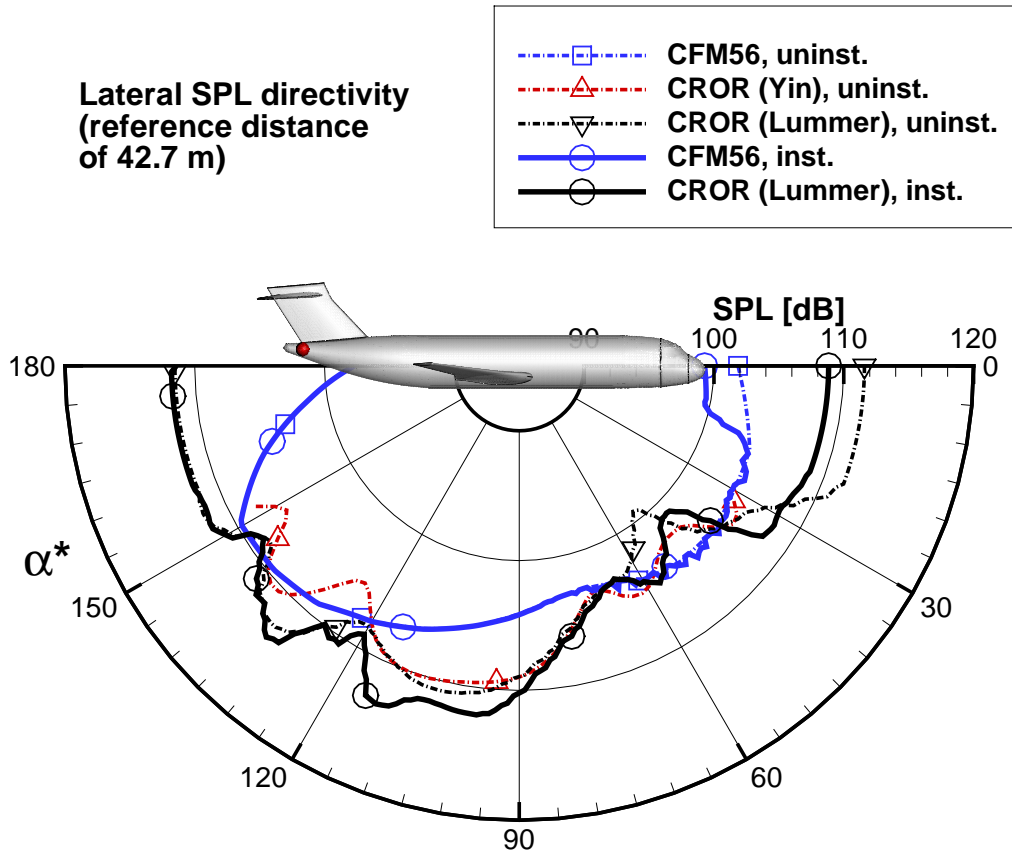


Figure 5.8: CROR: polar noise directivity

5.2 Decision Making Support

In addition to conceptual aircraft design, a significant demand for parametric aircraft noise prediction can be identified in the field of decision making support toward environmental friendly aviation¹⁴. The inherent characteristics and capabilities of parametric aircraft noise prediction, are most promising for applications towards flight procedure design and air traffic management [121]. The key capabilities are componential noise source modeling, highly flexible applicability, and the possibility for real-time noise analysis. The environmental impact of new vehicles and technologies, e.g. advanced navigational performance, and spacial air traffic routing can be evaluated. Furthermore, in combination with local population densities, airport specific scenarios can be analyzed. The community noise annoyance due to existing and future air traffic can be simulated, e.g. in order to identify optimal locations for future residential areas with minimal exposure to aviation noise.

Two example applications of PANAM in the context of decision making support are presented in the following sections.

5.2.1 Noise Abatement Flight Procedures

The focus of the presented analysis lies on approach procedures due to their significant contribution to community noise annoyance. The entire approaching air traffic is generally concentrated along common approach paths whereas departing aircraft rapidly increase their flight altitude and can soon be assigned to different flight directions. Common approach paths are defined in order assure horizontal distances between two subsequent aircraft as required by aviation safety regulations. A minimum distance according to the wake-vortex classifications of both aircraft is required along the final approach toward the airport. Possible delays and the variety of aircraft specific flight speeds make the spacial air traffic routing even more difficult and result in increased distances. As a consequence, approaching aircraft are assigned to enter the common approach path at large distances to the airport. Around major German airports, the spacial alignment causes extensive air traffic re-routing in the order of 40 to 100 km¹⁵ as depicted in Fig. 5.9¹⁶. Therefore, communities along the common approach path are exposed to a fly-by or a direct flyover of each incoming aircraft. Due to the small descent angles in the order of 3°, all vehicles operate at low flight altitudes, thus furthermore intensify community noise annoyance.

Any approaching aircraft is subject to a complex schedule of configurational modifications along with flight speed and altitude reduction, thus ground noise levels are dominated by both engine and airframe noise. If the configurational setting of the aircraft is modified, significant contribution of individual airframe noise sources can be observed [8,9]. To minimize ground noise along a typical approach flight, the timing of the configurational settings along with the selected flight velocities and altitudes need to be optimized [22]. Prediction

¹⁴Attendance of dedicated workshops with representatives of airlines, aircraft/engine manufacturers, and government agencies: (1) "Active High Lift and Impact on Air Transportation", April 2011, DLR Braunschweig, <http://www.aircraft-noise.info> (accessed 13 July 2012). (2) "Virtual Air Traffic System Simulation", June 2011, RWTH Aachen University, <http://vatss.ilr.rwth-aachen.de/doku.php> (accessed 13 July 2012). (3) "Innovative An- und Abflugverfahren zur Erhoehung der Lebensqualitaet am Flughafen Salzburg", June 2012, Salzburg Airport

¹⁵Stefan Mauel, Fraport AG: Presentation *Die Bedeutung von Maßnahmen des aktiven Schallschutzes für den Flughafen Frankfurt Main*, Institutskolloquium Institut für Flugführung, DLR Braunschweig, 16. November 2010.

¹⁶Web-application by <http://casper.umwelthaus.org/dfs/>, accessed 02.08.2012



Figure 5.9: Frankfurt Airport: Departing and approaching Airtraffic routing¹⁶

tools that can only account for engine noise are apparently meaningless. Moreover, noise contribution due to a specific configurational setting can only be accounted for if individual airframe noise sources are modeled. Noise abatement procedure design is an optimal application for tools with componential noise source modeling. Ultimately, the prediction results support decision making with respect to future low-noise flight operations and air traffic routing.

Initial application towards low-noise approach procedures for DLR's flying testbed AT-TAS are presented in Ref. [84] and [125]. PANAM can directly be linked to a flight trajectory generator¹⁷ called FlightSim [92]. If required vehicle and engine data are provided as input for one specific aircraft, arbitrary flight operation can be simulated and evaluated for environmental implications. FlightSim simulates the vehicle along a predescribed flight path and accounts for configurational setting [92, 93]. Required input parameters for PANAM are automatically generated and provided as input. The input includes vehicle location and orientation, flight speed, setting of engine thrust, landing gear, and configuration.

Inspired by earlier NASA concepts [98, 99], the study led to the development of a spiraling approach procedure called *Helical Noise Abatement Procedure* (HeNAP). The procedure is comprised of an initial flight segment at high altitudes toward the airport boundaries. The altitude is then reduced along a helical flight segment before the final approach is initiated, see Fig. 5.10. The significantly increased altitude along the initial flight segment results in wide-spread ground noise reduction until the helix is reached. High ground noise levels can be concentrated in preselected areas and dislocated away from highly populated communities by a clever selection of the helix location and orientation. Obviously, the preselected area for the helical descent is subject to increased noise impact, i.e. multiple flyover events per approaching aircraft, thus should be non-residential, an industrial zones, or lie within the airport boundaries. The HeNAP has been flight tested and evaluated through a dedicated flyover noise campaign. Noise level reductions along the high altitude approach in excess

¹⁷FlightSim is developed by Gertjan Looye, DLR Institute of Robotics and Mechatronics.

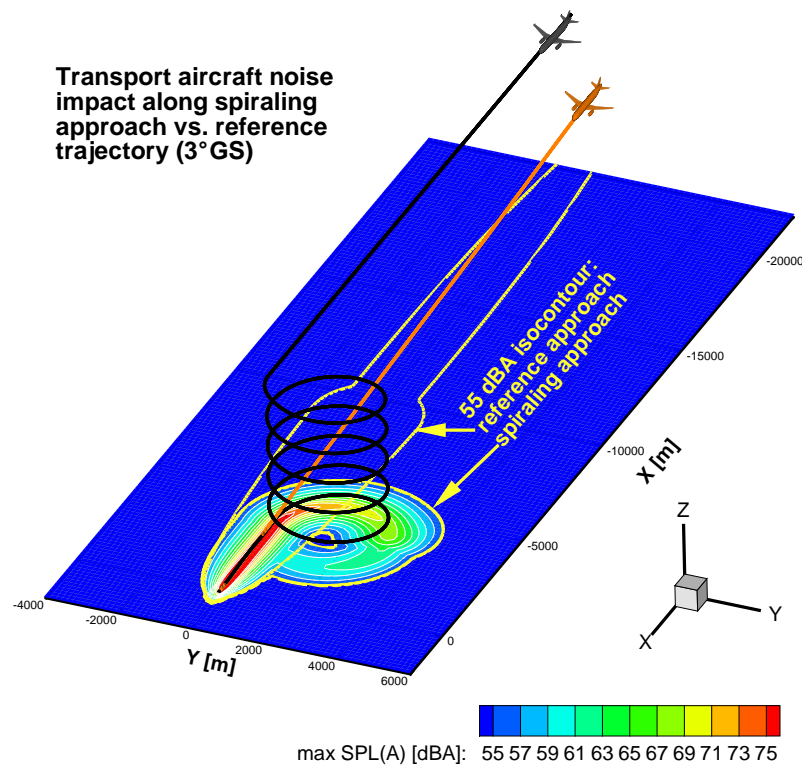


Figure 5.10: Helical Noise Abatement Procedure (HeNAP), Ref. [125]

of 8 dBA have been measured. Computational predictions and simulations are in good agreement to the recorded flight data and the ground noise measurements [84, 92, 93, 125]. These initial study proves the feasibility of the concept by simulation (and even flight test), thus supports a decision in favor of further investigations of this radical concept.

5.2.2 Airspace and Airtraffic Management

In the context of airspace layout and air traffic routing, environmental implications are of dominating importance¹⁸. Airport profitability is in direct contrast to the extensive re-routing of air traffic in order to protect surrounding communities from aircraft noise. If new flight routes are installed or existing routes are modified, simulations can support the decision for or against certain solutions.

Existing airspace/airport scenarios can be modified in order to evaluate various alternative flight routes. Modification of spacial air traffic routing according to underlying population densities can result in minimal community noise annoyance. As presented in Ref. [126], a simplified scenario is defined in order to investigate the impact of a new low-noise approach. Based on CORINE landcover data [127], residential areas can be identified to account for populated areas. Because the CORINE data does not provide any number of people, a simplified population density is assumed in order to assess a somewhat realistic estimate on aircraft noise induced awakenings. Fig. 5.11 shows the scenario layout and prediction results for two approach procedures, the reference and a noise abatement procedure. The

¹⁸Stefan Maue, Fraport AG: Presentation *Die Bedeutung von Maßnahmen des aktiven Schallschutzes für den Flughafen Frankfurt Main*, Institutskolloquium Institut für Flugführung, DLR Braunschweig, 16. November 2010

significant difference in aircraft noise induced awakenings [3] is clearly visible. At a later

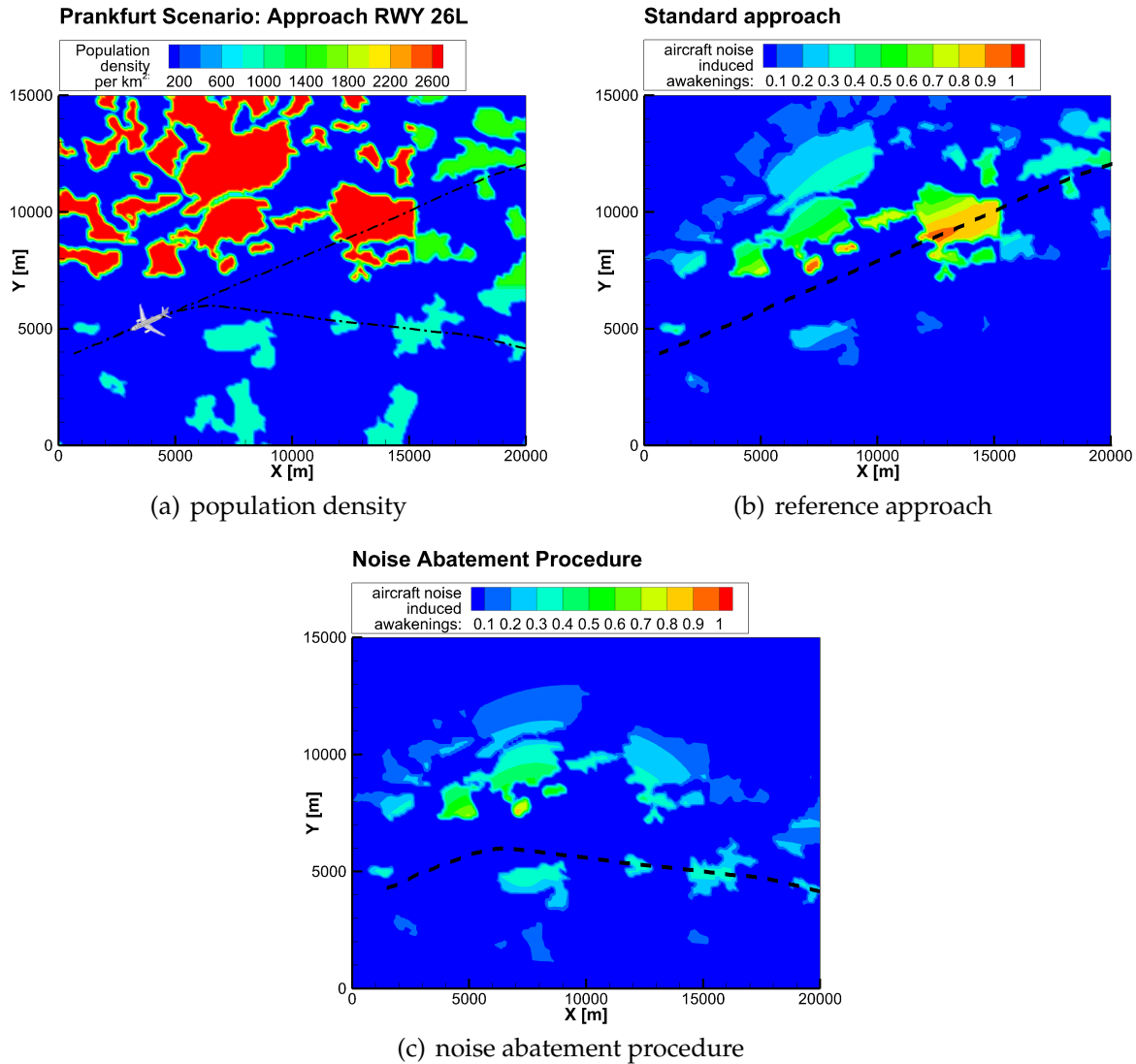


Figure 5.11: Parametric Noise Prediction for Airspace Routing

point, the simplified population distribution of this scenario can be exchanged by more realistic data [128] in order to evaluate a specific airport. Yet, the focus of this initial study lies on a comparative analysis rather than a precise simulation of absolute values. In conclusion, the example applications demonstrate the considerable potential for parametric noise prediction methods in airspace and air traffic management.

6 Results and Discussion

In the preceding chapter, the new aircraft design process is applied to identify low-noise aircraft concepts and technologies. Each new vehicle is based on the overall reference aircraft with similar mission requirements and basic design features, i.e. high-lift system, landing gear, and engine. As a consequence, PANAM noise source models are still applicable within their defined limitations and overall result reliability is consolidated. Individual PrADO, SHADOW, and PANAM runs are executed for each individual design variant in order to evaluate the corresponding economical and environmental performance. Several practical concepts for overall noise reduction are identified, thus the conceptual aircraft design phase is successfully completed. By definition, detailed or high fidelity analysis is not in the scope of the presented conceptual design process.

Results

The predicted environmental and economical parameters for each final vehicle are listed in Table 6.1. For each final vehicle, the difference to the reference aircraft is presented.

The economical performance is evaluated along the predefined design mission as defined in Section 5.1.1. The predicted aircraft weights are increased for all vehicles except of

-	V-Rx	V-0	V-1	V-2	V-X
approach noise delta [dBA, EPNdB]					
max. SPL(A)	-1.0	0.0	-6.4	-10.7	-6.6
EPNL	-1.1	-3.5	-7.5	-12.0	-7.2
departure noise delta [dBA, EPNdB]					
max. SPL(A)	0.7	-1.9	-0.7	-2.9	-2.1
EPNL	0.0	-4.2	-6.1	-10.0	-6.6
design mission delta [%]					
OEW	3.4	2.6	3.8	-1.6	1.4
field length	11.1	4.2	14.1	-8.4	-1.0
block fuel	-3.6	5.2	-2.7	3.6	2.1

Table 6.1: Environmental and economical vehicle performance

the V-2. The OEW reduction for this vehicle is due to the centered engine installation. In case of one-engine-out, significantly reduced tail surfaces are required to counterbalance the torque, thus decrease the overall vehicle weight. An one-engine-out case requires much larger tail surfaces if the engines are offset from the centerline. Increased OEW of the V-Rx and the V-1 can be tracked down to their large wing aspect ratios, thus increased wing weight. Large tailplanes on-board of the V-1 and the V-0 further increase the OEW. A small

increase is predicted for the *V-X* due to the unconventional airframe structure with two large VTPs.

Compared to the reference vehicle, the *V-Rx* and the *V-1* have wings of high aspect ratio (+13%) and reduced area (-6% and -10%). As a consequence, the high wing loading extensively decreases the landing performance [51]. The overall field length requirement for these aircraft is dominated by the landing, precisely the landing field length is 10% larger than the required take-off field length. The overall field length requirement of the *V-X* is similar to the reference, whereas a significantly reduced value is predicted for the *V-2*. This reduction can mainly be attributed to the lower aircraft weight.

Finally, significant differences can be identified for the predicted fuel requirements along the design mission. For the presented vehicle ranking, the block fuel requirement is selected by far the most important economical design objective. Vehicle *V-Rx* is a modification of the reference vehicle for best economical performance. The adapted wing size results in a reduced wetted area, thus decreased parasitic drag for the vehicle. Furthermore, a high aspect ratio is selected to improve the lift-to-drag ratio to almost 20 during cruise. As a consequence, a saving in block fuel of 3.6% can be achieved. Vehicle *V-1* is also equipped with an optimized wing for economic cruise performance, i.e. high aspect ratio and reduced wing area. Again, this results in a small wetted area and a high lift-to-drag ratio in cruise flight. The other vehicle designs are optimized for maximum noise shielding, thus result in increased block fuel requirements. Increasing the wing or tailplane surfaces for noise shielding leads to large wetted areas, thus high parasitic drag.

Noise levels are predicted along the defined approach and departure procedures. The underlying flight procedures as specified in Section 5.1.1 enable feasible flight operation of all selected vehicle variants. As a consequence, each vehicle can be evaluated based on identical assignments but is therefore not operated along an optimal procedure. Differences in maximum SPL(A) and EPNL with respect to the reference vehicle are evaluated at selected observer locations.

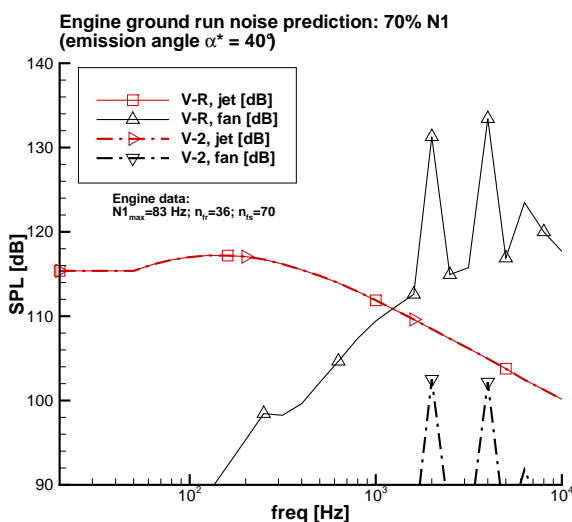


Figure 6.1: Take-off SPL spectrum: *V-R* vs. *V-2*
V-Rx.

These observer locations are located 5000 m prior touch-down and 3000 m after break-release. Significant EPNL level reductions are predicted for all vehicles except of the modified reference aircraft. This can be attributed to the fan noise shielding, thus reduced tonal noise contribution which dominates the EPNL. The largest approach and departure noise reduction can be achieved by design *V-2*, i.e. in the order of 10 EPNdB. Comparing engine noise level spectra of the reference and the *V-2* design clearly shows the extensive reduction in high frequency tonal contribution, see Fig. 6.1. Due to the unchanged fan noise contribution, similar SPL(A) and EPNL reductions are achieved for the modified reference vehicle

Discussion

The presented vehicle ranking is based on a selection of environmental and economical performance parameters. These parameters are then weighted in order to evaluate the overall ranking of a design variant. The selection of these parameters and the corresponding weightings reflect the opinion of the author, thus can seem somewhat arbitrary. Yet, the presented selection results in feasible and comprehensive simulation results, thus is recommended as a best practice or default setting.

For example, selecting different weighting factors can change the overall rank-order of the final designs. Different environmental weightings κ_j have no relevant influence on the rank-order of the presented vehicles because noise shielding is advantageous along both approach and departure procedures. Yet, the situation changes with a different λ_i setting. For example, a stronger weighting of the balanced field length does change the vehicle ranking within the economically driven scenarios (Fig. A.64, Appendix). Vehicles with a reduced field length would get better ratings despite higher block fuel or increased vehicle weight. Moreover, the preceding selection of promising vehicle variants out of the available solution space could change with different weighting factors, i.e. selecting variants with short field length requirements.

Furthermore, it has to be kept in mind, that the presented vehicle ranking takes place at the conceptual design phase. At this early design phase, simulations can be subject to systematic errors and inherent uncertainties due to simplified methods and approximations. If vehicle variants within one category are compared, it is expected that these uncertainties and errors in the simulation process equally affect each variant. If that is the case, the comparative variant ranking within a specific category is not influenced. Yet, uncertainties can have an impact if comparing substantially different vehicles, thus necessitate a subsequent and "manual" feasibility check. Therefore, simulation results should be compared with validated and reliable reference data.

At the conceptual aircraft design phase, detailed investigations for inherent disadvantages due to specific engine installation are not possible. This would require a simulation with far more advanced methods and higher fidelity tools. As a consequence, some inherent disadvantages with respect to the new vehicles cannot be evaluated but are identified for a more detailed investigation at later design phases.

Uncertainties are most likely to affect vehicles V-0, V-2, and V-X. For example, over-the-wing engine installation can cause a negative impact on the cruise performance due to the development of shocks between engine and fuselage. As a consequence, such concepts might require strict limitations on maximum flight speed, e.g. as it is the case for the VFW-614.

Engine installation above the fuselage can result in disadvantageous or even critical operational conditions. If flow separation occurs at the wing-fuselage junction or above the fuselage, the engines can directly be subject to disturbed inflow conditions. This can have severe effects on the performance and efficiency of the engine. Furthermore, when the aircraft is stalled in case of an emergency, the engines can be fully exposed to a separated flow and can not assist to recover a stable flight condition.

Early within the design process, only few and selected structural load cases can be accounted for. Whereas certain load cases are of no significance to some vehicles they can require structural reinforcement for others. High fidelity investigations of the DLR LNA, as presented in Ref. [50], indicate further performance disadvantages compared to the simpli-

fied PrADO analysis. This can be attributed to a dedicated load case, precisely the landing impact. During the landing impact, extensive fuselage bending moments are predicted for the LNA configuration, which require an increased fuselage wall thickness [50]. The default PrADO sizing does not account for this special load case, thus does not lead to a fuselage thickness increase. This underprediction of the overall empty weight results in artificially improved flight performance. High fidelity analysis indicates an additional fuselage and wing weight in the order of 15%, respectively. Accounting for these additional weights in PrADO, increases the balanced field length (+13%), block fuel (+3.6%), and OEW (+8%) of the V-X. More awakenings along both the departure (+2.6%) and the approach procedure (+1%) are predicted due to an increase in required thrust setting. Consequently, worse vehicle specific performance indicators are achieved.

In conclusion, simplified methods at the conceptual aircraft design phase cannot identify inherent disadvantages of certain design details. Therefore, a feasibility check with available data and similar vehicle designs is performed for each final vehicle design. This check indicates, that certain design specifics and load cases need further and higher fidelity investigation. Especially, for vehicle V-X it can be demonstrated, that conceptual design leads to artificially improved vehicle performance. The V-X concept needs further detail investigations at a later design phase. For the other presented vehicles it can be assumed, that feasible results are achieved with the PrADO simulation. Yet, certain design details require further adaption, e.g. improving the flight stability of the V-1 with an advanced defueling scheme. Furthermore, it can be expected that specific absolute values can show discrepancies if compared to results of high fidelity computational analysis.

Ultimately, the reliability of the new simulation process is confirmed due to feasible and comprehensive results, i.e. all relevant effects can directly be attributed to a physical cause.

7 Conclusions

The main motivation for the presented research activities is the integration of noise as an additional design objective and the identification of promising low-noise aircraft concepts. Thereby, it is most effective if noise is accounted for as early as possible within the overall design process. At early design levels only few key parameters are fixed, thus major geometry modifications are still feasible and significantly varying concepts can directly be compared. For all modifications and new concepts, the impact on environmental and economical performance has to be assessed. This requires a concurrent approach, i.e. all relevant interdependencies among the involved disciplines have to be accounted for at the same time. In conclusion, two main topics have to be addressed, i.e. development of an appropriate noise prediction tool and integration of noise into the design process of new aircraft. Thereby, the intended investigations aim at realizable, medium term solutions with respect to both aircraft and engine design. Futuristic vehicle concepts such as blended wing bodies with embedded or distributed propulsion are not in the scope of this research activity.

A new noise prediction software is developed for application at the conceptual aircraft design phase, the Parametric Aircraft Noise Analysis Module (PANAM). PANAM features componential and parametric noise prediction, thus can consider individual noise sources depending on their geometry and operating conditions during simulated flight operation. Thereby, each major noise source is modeled with an individual semi-empirical noise source model. These models capture the major physical effects and correlations but yet allow for quick noise predictions, i.e. executable on a standard desktop PC. This simulation approach provides comprehensive results as each noise relevant effect can be attributed to its cause.

The selected semi-empirical models as implemented into PANAM come from various DLR Institutions and are derived from flyover noise measurements and different full-scale or model scale component wind-tunnel tests. These models are well suitable for the available quantity and complexity of input data at the conceptual aircraft design phase. All models and approximations are based on physics, thus PANAM can be classified as a scientific prediction method. Recent findings and detail solutions from related disciplines can be integrated into the PANAM framework to enable an evaluation on a system level.

Dedicated comparison of simulation and measurement indicates feasible overall aircraft noise prediction capabilities. Prediction results and noise related effects are in good agreement to available experimental data and theoretical knowledge. The result reliability is reduced, if the noise source models are applied toward vehicle concepts far off the design space as specified by the underlying empirical data. Yet, if general noise generating mechanisms are kept consistent with the empirical data base, i.e. fixed design principles for individual noise sources, reasonable and reliable results can be expected.

In order to establish an overall low-noise design process, the existing design synthesis code PrADO is selected and modified. The PrADO tool, as developed at the Technical

University of Braunschweig, is updated with noise prediction capabilities. PANAM is directly executed within the modular and sequential PrADO design process. The prediction results are then collected and returned to the overall design process. Any of these results can be selected as final design objectives. To quickly assess the environmental versus the economical performance under different scenarios, a multiple criteria design evaluation is introduced. As a result, different vehicle concepts can directly be compared in order to identify the most promising concepts within a certain scenario. Ultimately, a comparative analysis of both environmental and economical performance under various boundary conditions is established. The identification and initial evaluation of promising concepts out of the available solution space concludes the assigned task. Subsequently, these concepts can be subject to further and more detailed investigations, e.g. high fidelity computation or wind tunnel tests, which is not in the scope of the presented activities.

It is demonstrated, that the aircraft designer's influence on the environmental vehicle performance is significant at the conceptual design phase. Early modifications to the basic vehicle layout result in extensive reduction of ground noise levels. Initial PrADO evaluations indicate, that this can be achieved for small decreases in economical vehicle performance. Maximum engine noise shielding is achieved for fuselage/wing shielding of over-the-fuselage mounted engines. Compared to the reference vehicle, noise level reductions in excess of 10 EPNdB are predicted along both approach and departure procedure. Reduction in maximum SPL(A) is smaller along the departure because SPL does not account for tonal corrections and broadband jet noise is dominating. But at the same time, block fuel increases by 3.6%. As an alternative propulsion concept for this vehicle, a geared turbofan promises reduced block fuel requirements and further reduction of jet noise contribution. If economical performance is selected as the highest priority, modifications to the reference vehicle can decrease block fuel by 3.6% under similar ground noise immissions. In conclusion, promising and feasible concepts are identified at an early design phase and can be recommended for subsequent investigations at increased fidelity levels.

Ultimately, PANAM can be ranked as well suitable to assess all four measures of ICAO's balanced approach, including (1) modifications to the noise source, (2) sophisticated traffic routing, (3) operational constraints, and (4) noise abatement flight procedures. Furthermore, real-time noise prediction could support pilots or air traffic controllers to identify ideal flight routes with respect to ground noise pollution. A real-time noise evaluation could augment cockpit in-flight information or enable pilot environmental awareness training in ground-based flight simulators.

Future work has to focus on the weighting of individual noise sources. Especially, the weighting of jet versus fan noise contribution under various operating conditions needs further validation. Additional noise sources are under investigation at DLR and will be implemented into PANAM.

The focus of the presented work lies on low-noise vehicle design but it will become inevitable for future analysis to optimize both aircraft and operational procedure at the same time. In order to achieve maximum noise reduction, a low-noise vehicle needs to be operated on its individual, aircraft type specific noise abatement flight procedure. The development of PANAM provides the key prerequisites for any of these future activities.

Bibliography

- [1] ACARE - *Beyond Vision 2020*, LEAFLET_ACARE_beyond_V2020_exe_summary.pdf, online version, <http://www.acare4europe.com> (accessed 10 January 2010)
- [2] U. Heudorf: *Fluglärm und Gesundheit, Ergebnisse epidemiologischer Studien - Literaturübersicht*, Amt für Gesundheit Frankfurt, Abteilung Medizinische Dienste und Hygiene, Frankfurt, Dec 2008
- [3] M. Basner, B. Griefahn, M. Berg: *Aircraft noise effects on sleep: mechanisms, mitigation and research needs*, Noise & Health Journal, Vol. 12 (47), pages 95-109, 2010
- [4] *Burden of disease from environmental noise - Quantification of healthy life years lost in Europe*, World Health Organization, 108 pages, ISBN 978928-900229-5, 2011
- [5] F. Thiessen, S. Schnorr: *Immobilien und Fluglärm*, Fakultät für Wirtschaftswissenschaften, Technische Universität Chemnitz, Bericht Nr. WWDP 69/2005, ISSN 1618-1352, 2005
- [6] International Civil Aviation Organization (ICAO), Air Transport Bureau (ATB): *Concept of a balanced approach principle to aircraft noise management*, appendix C of Assembly Resolution A35-5, 2007, <http://www.icao.int/env/noise.htm> (accessed 21 April 2011)
- [7] E.D. Olson, D.N. Mavris: *Aircraft Conceptual Design and Risk Analysis Using Physics-Based Noise Prediction*, AIAA 2006-2619, 12th AIAA/CEAS Aeroacoustics Conference, 8 - 19 May 2006, Cambridge, Massachusetts, USA
- [8] F. Farassat, J.H. Casper: *Towards an Airframe Noise Prediction Methodology: Survey of Current Approaches*, AIAA-2006-0210, 44th AIAA Aerospace Sciences Meeting and Exhibit, Reno, Nevada, January 9-12, 2006
- [9] W. Dobrzynski: *Almost 40 Years of Airframe Noise Research: What did we Achieve?*, Journal of Aircraft, Vol. 47 (No. 2), pages 353-367, DOI: 10.2514/1.44457, March - April 2010
- [10] Bundesministerium der Justiz: *Erste Verordnung zur Durchführung des Gesetzes zum Schutz gegen Fluglärm (Verordnung über die Datenerfassung und das Berechnungsverfahren für die Festsetzung von Lärmschutzbereichen - 1.FlugLSV)*, Bundesgesetzblatt BGBl I, 27th December 2008
- [11] European Civil Aviation Conference (ECAC): *Methodology for Computing Noise Contours around Civil Airports*, Vol. 1 and 2 (applications and technical guide), ECAC/CEAC Doc.29, 3rd Edition, December 2005
- [12] International Civil Aviation Organization (ICAO): *ICAO DOC 9911 Recommended Method for Computing Noise Contours Around Airports*, Order Number 9911, ISBN 978-92-9231-225-1, 2008
- [13] Society of Automotive Engineers SAE, A-21 Aircraft Noise Measure Noise Aviation Emission Modeling: *Procedure for the Computation of Airplane Noise in the Vicinity of Airports*, SAE-AIR-1845, 1986
- [14] U. Isermann, R. Schmid: *Description and Calculation of Aircraft Noise (German)*, DLR-Forschungsbericht 2000-20, German Aerospace Center (DLR), ISSN 1434-8454, June 2000
- [15] S. Fidell, P. Schomer: *Uncertainties in measuring aircraft noise and predicting community response to it*, Noise Control Engineering Journal (NCEJ), Vol. 55 (No. 1), pages 82 - 88, ISSN 0736-2501

- [16] M.J.T. Smith: *Aircraft Noise*, Cambridge Aerospace Series, Cambridge University Press, ISBN 0-521-61699-9, 2004
- [17] J.R. Olmstead, G.G. Fleming, J.M. Gulding, C.J. Roof, P.J. Gerbi, and A.S. Rapoza: *Integrated Noise Model (INM) Version 6.0 Technical Manual*, U.S. Department of Transportation Federal Aviation Administration, Report No. FAA-AEE-02-01, January 2002, Washington, D.C., USA
- [18] S. Hartjes, H.G. Visser, S.J. Hebly: *Optimization of RNAV Noise and Emission Abatement Departure Procedures*, AIAA-2009-6953, 9th AIAA Aviation Technology, Integration, and Operations Conference (ATIO), September 2009, Hilton Head Island, South Carolina, USA
- [19] W. Krebs, G. Thomann, R. Buetikofer: *FLULA2 - Ein Verfahren zur Berechnung und Darstellung der Fluglaermbelastung*, Technical Manual Version 4, EMPA, (Flula2-V4-mBV1.pdf), 2010
- [20] U. Isermann: *Calculation of Aircraft Noise in the Vicinity of Civil Airports by a Simulation Procedure (German)*, Dissertation, Report 7/1988, Max-Planck-Institut fuer Stroemungsforschung, 1988
- [21] M. Pott-Pollenske, W. Dobrzynski, H. Buchholz, S. Guérin, G. Saueressig, and U. Finke: *Airframe Noise Characteristics from Flyover Measurements and Predictions*, AIAA-2006-2567, 12th AIAA/CEAS Aeroacoustics Conference (27th AIAA Aeroacoustics Conference), May 2006, Cambridge, Massachusetts, USA
- [22] R. Koenig, J. Heider, M. Maierhofer: *Aircraft Flight Procedure Design with Respect to Noise Abatement as well as Economical and Pilot Workload Aspects*, Inter-noise Congress and Exposition on Noise Control Engineering 2005, August 2005, Rio de Janeiro, Brazil
- [23] R.E. Gillian: *Aircraft Noise Prediction Program User's Manual*, NASA Langley Research Center, 1982
- [24] M.R. Fink: *Airframe Noise Prediction Method*, FAA Research Report, FAA-RD-77-29, March 1977
- [25] J.R. Stone, D.E. Groesbeck, C.L. Zola: *Conventional profile coaxial jet noise prediction*, AIAA Journal, 21(1) (1983), pp. 336-342
- [26] M.F. Heidmann: *Interim prediction method for fan and compressor source noise*, NASA Technical Report TM-X-71763, 1979
- [27] J. Bridges, A. Khavaran, C.A. Hunter: *Assessment of Current Jet Noise Prediction Capabilities*, AIAA-2008-2933, 14th AIAA/CEAS Aeroacoustics Conference (29th AIAA Aeroacoustics Conference), 5 - 7 May 2008, Vancouver, British Columbia Canada
- [28] E. Envia, D.L. Tweedt, R.P. Woodward, D.M. Elliott, E.B. Fite, C.E. Hughes, G.G. Podboy, and D.L. Sutliff: *An Assessment of Current Fan Noise Prediction Capability*, AIAA-2008-2991, 14th AIAA/CEAS Aeroacoustics Conference (29th AIAA Aeroacoustics Conference), 5 - 7 May 2008, Vancouver, British Columbia Canada
- [29] N. Antoine, I. Kroo, K. Willcox, and G. Barter: *A Framework for Aircraft Conceptual Design and Environmental Performance Studies*, AIAA-2004-4314, 10th AIAA/ISSMO Multidisciplinary Analysis and Optimization Conference, August 2004, Albany, New York, USA
- [30] C. Burley, L. Lopez: *ANOPP2: Progress Update*, NASA Spring Acoustics Technical Working Group, presentation, April 21-22 2011, Cleveland, OH
- [31] L. Lopez, C. Burley: *Design of the Next Generation Aircraft Noise Prediction Program: ANOPP2*, AIAA-2011-2854, 17th AIAA/CEAS Aeroacoustics Conference, Portland, Oregon, June 2011
- [32] N. Van Oosten: *SOPRANO Presentation* (PDF), SOPRANO Workshop, 21 - 22 June 2007, Madrid, Spain
- [33] A.M. Rolt, K.G. Kyprianidis: *Assessment of new aeroengine core concepts and technologies in the EU framework 6 NEWAC programme*, paper icas-408, 27th International Congress of the Aeronautical Sciences (ICAS 2010), 19 - 24 September 2010, Nice, France
- [34] Y. Rozenberga, J. Bultéb: *Fast Aircraft Noise Prediction Including Installation Effects for the Evaluation of Air Transport Systems*, paper in08-0342, 37th International Congress and Exposition on Noise Control Engineering (inter-noise 2008), 26 - 29 October 2008, Shanghai, China

- [35] M. Brunet, T. Chaboud, N. Huynh, P. Malbequi, and W. Ghedhaifi: *Environmental Impact Evaluation of Air Transport Systems Through Physical Modeling and Simulation*, AIAA-2009-6936, 9th AIAA Aviation Technology, Integration, and Operations Conference (ATIO), September 2009, Hilton Head Island, South Carolina, USA
- [36] W. Dobrzynski, M. Pott-Pollenske: *Slat Noise Source Studies for Farfield Noise Prediction*, AIAA-2001-2158, 7th AIAA/CEAS Aeroacoustics Conference, 28 - 30 May 2001, Maastricht, Netherlands
- [37] M. Hepperle: *Environmental Friendly Transport Aircraft*, Notes on Numerical Fluid Mechanics and Multidisciplinary Design, Vol. 87, pages 26-33, Springer Verlag, 13th STAB/DGLR Symposium, 12 - 14 Nov 2002, Muenchen, Germany, ISBN 3-540-20258-7
- [38] M. Lummer, M. Hepperle, J. Delfs: *Towards a Tool for the Noise Assessment of Aircraft Configurations*, Aeroacoustics of New Aircraft and Engine Configurations, 8th ASC-CEAS Workshop, Budapest, Hungary, 11 - 12 Nov 2004, ISBN 963-420-842-8
- [39] R. Schmid: *Half-empirical, physical model for the directional characteristic of sound radiated by modern turbofan engines*, Doctoral Thesis University of Goettingen, Germany, DLR-Forschungsbericht 1999-47, ISSN 1434-8454, 2000
- [40] L. Bertsch: *Stand der Arbeiten zur akustischen Bewertung von Flugzeugkonfigurationen im Projekt QSTOL*, Internal Report IB 124-2007/4, Institute of Aerodynamics and Flow Technology, German Aerospace Center, ISSN 1614-7790
- [41] L. Bertsch, P. Krammer: *PANAM - a noise prediction tool for conceptual aircraft design*, Internal Report IB 124-2008/902, Institute of Aerodynamics and Flow Technology, German Aerospace Center
- [42] L. Bertsch, W. Dobrzynski, S. Guérin: *Tool development for Low-Noise Aircraft Design*, AIAA-2008-2995, 14th AIAA/CEAS Aeroacoustics Conference, Mai 2008, Vancouver, British Columbia, Canada
- [43] L. Bertsch, W. Dobrzynski, S. Guérin: *Tool Development for Low-Noise Aircraft Design*, Journal of Aircraft, 47 (2), Seiten 694-699, DOI: 10.2514/1.43188, March - April 2010
- [44] L. Bertsch, S. Guérin, G. Looye, M. Pott-Pollenske: *The Parametric Aircraft Noise Analysis Module - status overview and recent applications*, AIAA-2011-2855, 17th AIAA/CEAS Aeroacoustics Conference, 5-8 June 2011, Portland, Oregon, USA
- [45] C. Liersch, M. Hepperle: *A Unified Approach for Multidisciplinary Preliminary Aircraft Design*, accepted for presentation at the CEAS 2009 European Air and Space Conference, 26 - 29 Oct 2009
- [46] M. Kunde, A. Bachmann, M. Litz: *A dynamic data integration approach to build scientific workflow systems*, Institute of Electrical and Electronics Engineers, International Workshop on Workflow Management (IWWM 2009), pages 27-33, May 2009
- [47] Phoenix Integration: *PHX ModelCenter and Analysis Server*, <http://www.phoenix-int.com>
- [48] W. Heinze: *Ein Beitrag zur quantitativen Analyse der technischen und wirtschaftlichen Auslegungsgrenzen verschiedener Flugzeugkonzepte für den Transport großer Nutzlasten*, ZLR-Forschungsbericht 94-01, ISBN 3-928628-14-3
- [49] W. Heinze, C.M. Oesterheld, P. Horst: *Multidisziplinäres Flugzeugentwurfsverfahren PrADO - Programmwurf und Anwendung im Rahmen von Flugzeugkonzeptstudien*, DLRK 2001-194, Deutscher Luft- und Raumfahrtkongress 2001, September 2001, Bonn, Germany
- [50] W. Werner-Westphal, W. Heinze, P. Horst: *Multidisciplinary Integrated Preliminary Design Applied to Unconventional Aircraft Configurations*, Journal of Aircraft, 45 (2), pages 581-589, DOI: 10.2514/1.32138, March - April 2008
- [51] D.P. Raymer: *Aircraft design: a conceptual approach*, third edition, AIAA education series, American Institute of Aeronautics and Astronautics, ISBN 1563472813, 1999

- [52] G. Thomann: *Uncertainties of measured and calculated aircraft noise and consequences in relation to noise limits*, PhD Thesis ETH Zuerich, No. 17433, 2007
- [53] International Organisation for Standardisation, ISO: *ISO LN 9300, Luftfahrtnorm*, Juli 1976
- [54] D.A. Bies: *Engineering Noise Control, Theory and Practice*, Third Edition, Spon Press, ISBN 0-415-26714-5, 2003
- [55] A. Le Duc, P. Spiegel, F. Guntzer, M. Lummer, J. Goetz, and H. Buchholz: *Simulation of complete helicopter noise in maneuver flight using aeroacoustic flight test database*, American Helicopter Society, 64th Annual Forum, and Technology Display, Montreal, Canada, April 2008
- [56] *Method for the Calculation of the Absorption of Sound by the Atmosphere*, ANSI S1.26-1978, 1995
- [57] I.L.N. Granoien, R.T. Randeberg: *Corrective measures for aircraft noise models, new algorithms for lateral attenuation*, Baltic-Nordic Acoustics Meeting 2004, BNAM, 8-10 June 2004, Mariehamn, Alan
- [58] Society of Automotive Engineers, Committee A-21: *Prediction Method for Lateral Attenuation of Airplane Noise During Takeoff and Landing*, Aerospace Information Report No. 1751, Warrendale, Society of Automotive Engineers, Inc., March 1981
- [59] W. Dobrzynski, L. Chow, P. Guion, D. Shiells: *A European Study on Landing Gear Airframe Noise Sources*, 6th AIAA/CEAS Aeroacoustics Conference, 12-14 June 2000, La-haina Hawaii/USA
- [60] W. Dobrzynski, L.C. Chow, P. Guion, and D. Shiells: *Research into Landing Gear Airframe Noise Reduction*, AIAA-2002-2409, 8th AIAA/CEAS Aeroacoustics Conference, June 2002, Breckenridge, USA
- [61] DLR: *Entwicklung von Quellmodellen für den Umströmungslärm von Verkehrsflugzeugen durch Auswertung von Windkanal-Messdaten und Überflugmessungen an einem Airbus A319 - Arbeiten im Rahmen des Projekts LAnAb*, Abschlussbericht für den BMFT, DLR IB 124-2006/05
- [62] W. Dobrzynski: *Konfigurationen 2020 Abschlussbericht - Konfigurative Lärmkriterien*, final project report, ref.-nr.: K2020-DLR-000-017-P4-Final_Report, Braunschweig, Germany, 16 July 2007
- [63] W. Dobrzynski, L.C. Chow, M. Smith, A. Boillot, O. Dereure, and N. Molin: *Experimental Assessment of Low Noise Landing Gear Component Design*, AIAA 2009-3276, 15th AIAA/CEAS Aeroacoustics Conference, 11 - 13 May 2009, Miami, Florida, USA
- [64] K.-S. Rossignol: *Development of an empirical prediction model for flap side-edge noise*, AIAA-2010-3836, 16th AIAA/CEAS Aeroacoustics Conference, 7 - 9 June 2010, Stockholm, Sweden
- [65] K.-S. Rossignol: *Empirical Prediction of Airfoil Tip Noise*, AIAA-2011-273, 17th AIAA/CEAS Aeroacoustics Conference, 6-8 June 2011, Portland, Oregon, USA
- [66] D.P. Lockard, G.M. Lilley: *The Airframe Noise Reduction Challenge*, NASA Technical Manual TM-2004-213013, 2004
- [67] H. Schlichting, E. Truckenbrodt: *Aerodynamik des Flugzeuges - Erster Band*, second edition, Springer-Verlag, ISBN 3-540-03970-8, 1967
- [68] M. Braun, K. Wicke, A. Koch, T. Wunderlich: *Analysis of Natural Laminar Flow Aircraft based on Airline Network Design and Fleet Assignment*, 11th AIAA Aviation Technology, Integration, and Operations (ATIO) Conference 2011, paper AIAA-2011-6807
- [69] P.K.C. Rudolph: *High-Lift Systems on Commercial Subsonic Airliners*, NASA Contractor Report CR 4746, Sept. 1996
- [70] W. Dobrzynski, K.S. Rossignol, and D. Almonet: *Handbuch zum modularen Quellmodell fuer das Umstroemungsgeraeusch von Verkehrsflugzeugen*, Version 4.0, Internal Report IB 124-2011/? (t.b.d.), Institute of Aerodynamics and Flow Technology, German Aerospace Center

- [71] W. Dobrzynski, M. Herr, M. Pott-Pollenske: *Airframe Noise Source Modeling - Application and Limitations*, Presentation, Campus Research Airport Symposium 2011: Active High Lift and Impact on Air Transportation, DLR Braunschweig, 11-12 April, 2011, <http://www.aircraft-noise.info> (accessed 23 July 2011)
- [72] *Gas Turbine Engine Performance Station Identification and Nomenclature*, Aerospace Recommended Practice, ARP 755A, Society of Automotive Engineers, Warrendale, Pennsylvania, USA
- [73] J. Kurzke: *Fundamental Differences between Conventional and Geared Turbofans*, GT-2009-59745, Proceedings of ASME Turbo Expo 2009 Gas Turbine Technical Congress and Exhibition June 8-12, 2009, Orlando, Florida, USA
- [74] W. Olsen, R. Friedman: *Jet noise from co-axial nozzles over a wide range of geometric and flow parameters*, NASA Technical Report TM-X-71503, Lewis Research Center, Cleveland, Ohio 44135, 1979
- [75] S. Guérin, A. Moreau, C. Weckmüller: *Engine Noise Source Modeling - Limitations and Perspectives*, Presentation, Campus Research Airport Symposium 2011: Active High Lift and Impact on Air Transportation, DLR Braunschweig, 11-12 April, 2011, <http://www.aircraft-noise.info> (accessed 23 July 2011)
- [76] G.J.J. Ruijgrok: *Elements of Aviation Acoustics*, Delft University Press, ISBN 90-6275-899-1, 1993
- [77] P.G. Hill, C.R. Peterson: *Mechanics and thermodynamics of propulsion (2nd revised and enlarged edition)*, Reading, MA, Addison-Wesley Publishing Co., ISBN 0-201-14659-2, 1992
- [78] S. Guérin: *Impact on Serrations on the Circumferential Structure of Jet Turbulence and Relation to Jet Noise Reduction*, 14th AIAA/CEAS Aeroacoustics Conference 2008, paper AIAA-2008-3025
- [79] W.J.G. Braeunling: *Flugzeugtriebwerke*, Springer Verlag, ISBN 3-540-40589-5, 2004
- [80] F. Deidewig: *Ermittlung der Schadstoffemissionen im Unter- und Ueberschallflug*, German Aerospace Center, DLR Forschungsbericht 98-10, Cologne, Germany, 1998
- [81] A. Moreau, S. Guérin, and S. Busse: *A method based on the ray structure of acoustic modes for predicting the liner performance in annular ducts with flow*, NAG/DAGA International Conference on Acoustics, Rotterdam, 23 - 26 March 2009
- [82] J.M. Tyler, T.G. Sofrin: *Axial flow compressor noise studies*, SAE Transactions 70, 309-332, 1962
- [83] M. Lummer: *Maggi-Rubinowicz Diffraction Correction for Ray-Tracing Calculations of Engine Noise Shielding*, 14th AIAA/CEAS Aeroacoustics Conference 2008, paper AIAA-2008-3050
- [84] L. Bertsch, G. Looye, T. Otten, M. Lummer: *Integration and application of a tool chain for environmental analysis of aircraft flight trajectories*, AIAA-2009-6954, 9th AIAA Aviation Technology, Integration, and Operations Conference (ATIO), September 2009, Hilton Head Island, South Carolina, USA
- [85] J.B. Keller: *Geometrical Theory of Diffraction*, Journal of the Optical Society of America, vol. 52, no. 2, pages 116-130, Feb 1962
- [86] K. Miyamoto, E. Wolf: *Generalization of the Maggi-Rubinowicz Theory of the Boundary Diffraction Wave - Part I*, Journal of the Optical Society of America, vol. 52, no. 6, pages 615-625, June 1962
- [87] K. Miyamoto, E. Wolf: *Generalization of the Maggi-Rubinowicz Theory of the Boundary Diffraction Wave - Part II*, Journal of the Optical Society of America, vol. 52, no. 6, pages 626-637, June 1962
- [88] C. Kott: *Entwurf von laermarmen Flugzeugkonfigurationen unter Beruecksichtigung von Abschattungseffekten (German)*, final diploma thesis, German Aerospace Center in cooperation with Fachhochschule Aachen, Faculty of Aerospace Engineering, Aachen, Germany, 2010
- [89] Google: Google Earth software, <http://earth.google.com>
- [90] G. Mueller, M. Moeser: *Taschenbuch der Technischen Akustik*, 3rd edition, Springer Press, Berlin, ISBN 978-3-540-41242-7, 2004

- [91] *Position paper on dose response relationships between transportation noise and annoyance*, European Communities, 2002
- [92] G. Looye: *Flight testing of autopilot control laws: fly the helix!*, German Aerospace Congress 2009, paper DLRK-2009-1375
- [93] G. Looye: *Aircraft Mission Simulation for Environmental Analysis with Flight Test Validation*, Presentation, DGLR workshop "Umweltfreundliches Fliegen", Braunschweig, Germany, June 16-17, 2010, <http://www.dglr.de> (accessed 23 January 2011)
- [94] P. Krammer, L. Bertsch, C. Werner-Spatz: *Multidisciplinary Preliminary Aircraft Design with Integrated Noise Analysis Capabilities*, DLRK 2009 121177, Deutscher Luft- und Raumfahrtkongress 2009, September 2009, Hamburg, Germany
- [95] S. Guérin, U. Michel: *Prediction of aero-engine noise: comparison with A319 flyover measurements*, Tech. Rep., DLR, 2007, IB 92517-04/B3
- [96] W. Durham: *Aircraft Dynamics and Control*, Vorlesungsskript an der Virginia Polytechnic Institute and State University, Blacksburg, VA, USA, 2004
- [97] Airbus Flight Operations Support & Line Assistance: *Getting to grips with aircraft noise*, PDF, "Getting to grips" advisory publications, Airbus Customer Services, rond-point Maurice Bellonte 1, BP 33, 31707 Blagnac, France
- [98] C. Hange: *Assessment of a C-17 flight test of an ESTOL transport landing approach for operational viability, pilot perceptions and workload, and passenger ride acceptance*, AIAA 2007-1398
- [99] C. Hange: *Trajectory kinematics of a simultaneous non-interfering landing approach and the impact on ESTOL regional transport performance and flight control*, AIAA 2003-6857
- [100] R. Koenig: *Lärmoptimierte An- und Abflugverfahren, Zusammenfassender Schlussbericht*, Forschungsverbund Leiser Verkehr, Bereich Leises Verkehrsflugzeug, Projekt 1600 Lärmoptimierte An- und Abflugverfahren (LANAb), 2007
- [101] Airbus: *A319 airplane characteristics for airport planning*, PDF, technical document, AIRBUS S.A.S., Customer Services, Technical Data Support and Services, 31707 Blagnac Cedex, France, Issue: Jul 01/95, Rev: May 01/11
- [102] P. Jackson, K. Munson, L. Peacock (Editors): *Jane's All the World's Aircraft [Hardcover]*, 2009 - 2010 Version, Jane's Information Group, United Kingdom, ISBN 0-710-62837-4, June 2008
- [103] Brüel & Kjaer: *Leq, SEL, what? Why? When?*, Application Notes 1989 - 1980, Brüel & Kjaer, Sound & Vibration Measurement A/S, Denmark, <http://www.bksv.com/doc/BO0051.pdf> (accessed 12 May 2011)
- [104] A. Filippone, L. Bertsch, M. Pott-Pollenske: *Validation Strategies for Comprehensive Aircraft Noise Prediction Methods*, AIAA 2012-5411, 12th AIAA Aviation Technology, Integration, and Operations (ATIO) Conference, 17 - 19 September 2012, Indianapolis, Indiana, USA
- [105] Airbus Company: *Airbus Market Forecast 2011-2030*, online pdf, http://www.airbus.com/company/market/forecast/passenger-aircraft-market-forecast/Airbus_GMF_2011-2030_delivering_the_future_-_full_book.pdf (accessed 09 January 2012)
- [106] Boeing Company: *Boeing Current Market Outlook 2011-2030*, online version, <http://www.boeing.com/commercial/cmo/> (accessed 12 January 2012)
- [107] European Union: *Noise Charge Harmonization within Europe*, online version, <http://ec.europa.eu/environment/noise/home.htm> (accessed 02 January 2012)
- [108] Berlin Airport: *Airport Charges*, pdf version, http://www.berlin-airport.de/EN/GeschaeftskundenUndPartner/Entgelte/Download/110401_Entgeltordnung_engl.pdf (accessed 02 January 2012)

- [109] Frankfurt Airport: *Airport Charges*, pdf version, http://www.fraport.com/content/fraport-ag/en/misc/binaer/products_services/airport-charges/Flughafenentgelte_Airport_charges_202012.pdf (accessed 02 January 2012)
- [110] R. Henke, T. Lammering, E. Anton: *Impact of an Innovative Quiet Regional Aircraft on the Air Transportation System*, Journal of Aircraft, 47 (3), pages 875-886, DOI: 10.2514/1.45785, May - June 2010
- [111] S. Guérin, A. Moreau, C. Menzel, C. Weckmueller: *Open-rotor noise prediction with a RANS-informed analytical method*, abstract proposed for presentation at the 18th AIAA/CEAS Aeroacoustics Conference (33rd AIAA Aeroacoustics Conference), 4 - 6 June 2012, Colorado Springs, Colorado, USA
- [112] L. Bertsch, O. Schneider, H. Hemmer, M. Hepperle, O. Macke: *Process Implementation for the System Evaluation of new Low-Noise STOL Transportation Concepts*, Paper No. 2, CEAS/KATnet II Conference on Key Aerodynamic Technologies, May 2009, Bremen, Germany
- [113] N. Arndt: *Environmentally friendly aero-engines for the 21st century*, Rolls-Royce presentation, First CEAS European Air and Space Conference, 10 - 13 September 2007, Berlin, Germany, http://www.dlr.de/pa/Portaldata/33/Resources/dokumente/ceas/CEAS_WS_Arndt.pdf (accessed 02 March 2011)
- [114] J.J. Korsia: *VITAL Project overview*, Snecma presentation, Aeronautics Days 2006 - Sustainable Solutions for New Horizons, 19 - 21 June 2006, Vienna, Austria, http://www.aeroday2006.org/sessions/A_Sessions/A4/A44.pdf (accessed 12 June 2011)
- [115] C. Lenfers: *Propeller Design for a future QESTOL Aircraft in the BNF Project*, AIAA 2012-3334, 30th AIAA Applied Aerodynamics Conference, 25 - 28 June 2012, New Orleans, Louisiana, USA
- [116] A. Stuermer, J. Yin: *Low-Speed Aerodynamics and Aeroacoustics of CROR Propulsion Systems*, AIAA-2009-3134, 15th AIAA/CEAS Aeroacoustics Conference, 11-13 May 2009, Miami, Florida, USA
- [117] C.O. Márquez, A. Stuermer, C. Clemen: *Installation Effects of a CROR Propulsion System on a Modified DLR-F6 Aircraft Configuration*, ISABE-2011-1307, 20th International Society of Airbreathing Engines Conference, 12-16 September 2011, Goeteborg, Sweden
- [118] H. Grieb, D. Eckardt: *Turbofan and Propfan as Basis for Future Economic Propulsion Concepts*, AIAA-86-1474, AIAA/ASME/SAE/ASEE 22nd Joint Propulsion Conference, 16-18 June 1986, Huntsville, Alabama
- [119] M. Kingan, R.H. Self: *Advanced Open Rotor Noise Modelling Tool and Comparison Study Technical Dissemination Workshop*, Institute of Sound and Vibration research, University of Southampton, December 2008, <http://www.omega.mmu.ac.uk/workshop-integrated-study-of-advanced-open-rotor-powered-aircraft.htm> (accessed 02 June 2012)
- [120] L. Mueller: *Quellformulierung für Fernfeldschallberechnung mit einem Schallstrahlenverfahren bei installierten gegenläufigen Propellern*, Diploma thesis, University of Braunschweig, Germany, 2009
- [121] M. Arntzen, T.A. van Veen, H.G. Visser, D.G. Simons: *Aircraft Noise Simulation for a Virtual Reality Environment*, AIAA-2011-2991, 17th AIAA/CEAS Aeroacoustics Conference, 5-8 June 2011, Portland, Oregon, USA
- [122] S. Kreth: *Projekt LEISA Abschlussbericht*, final project report, DLR-IB 111-2011/24, Institute of Flight Systems, German Aerospace Center (DLR)
- [123] L. Bertsch, G. Looye, E. Anton, S. Schwanke: *Flyover noise measurements of a spiraling noise abatement approach procedure*, AIAA-2010-11, 47th AIAA Aerospace Sciences Meeting and Exhibit, Januar 2010, Orlando, Florida, USA
- [124] O. Schneider, S. Kreth, L. Bertsch: *Towards a Quiet Short Take-Off and Landing Transportation System: Concept Evaluation and ATM Integration*, IPLC-2010-0037, International Powered Lift Conference, October 2010, Philadelphia, USA

- [125] L. Bertsch, G. Looye, E. Anton, S. Schwanke: *Flyover Noise Measurements of a Spiraling Noise Abatement Approach Procedure*, Journal of Aircraft, 48 (2), pages 436-448, DOI: 10.2514/1.C001005, March - April 2011
- [126] H.H. Toeppen, V. Mollwitz, L. Bertsch, B. Korn, D. Kuegler: *Flight Testing of Noise Abating RNP Procedures and Steep Approaches*, abstract proposed for presentation at the 28th International Congress of the Aeronautical Sciences (ICAS), 23 - 28 September 2012, Brisbane, Australia
- [127] *CORINE Land Cover (CLC2006)*, Umweltbundesamt (German Federal Environmental Agency), DLR-DFD 2009
- [128] F. Batista E Silva, J. Gallego, C. Lavalley: *A high resolution population grid map for Europe*, under review process, Journal of Maps

A Figures, Tables, and Derivations

A.1 Weighting, Sound Propagation, and Ground Effects

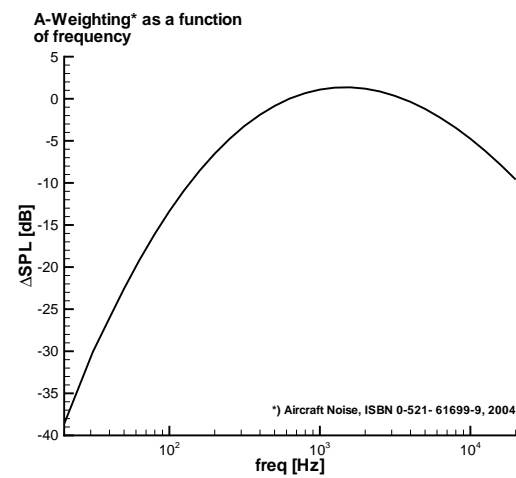
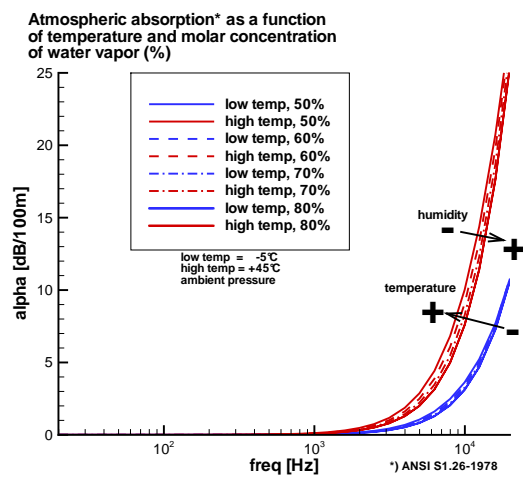


Figure A.1: Atmospheric sound absorption

Figure A.2: Sound Pressure Level: A-weighting

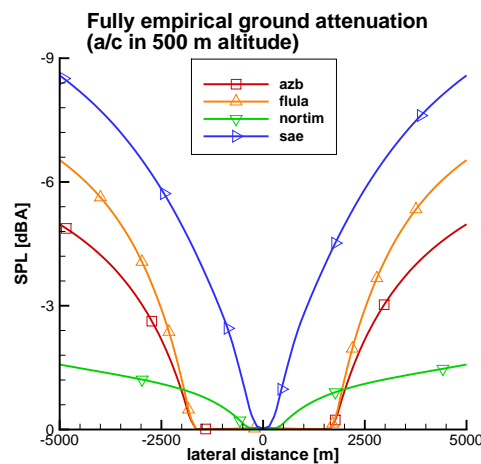


Figure A.3: Predicted ground attenuation for flyover event in 500 m altitude

A.2 Textbook Theory

-	config	speed [m/s]	mach [-]	alt [m]	C_l [-]	α [°]	C_d [-]	thrust/engine	N1 [%]
1	clean	130	0.382	500	0.3479	2.47	0.024427	15497.7	61.21
2	clean	130	0.382	1000	0.3479	2.47	0.024427	15497.7	61.21
3	clean	130	0.382	2000	0.3479	2.47	0.024427	15497.7	61.21
4	clean	110	0.324	500	0.4858	4.20	0.029123	13232.1	55.32
5	clean	120	0.353	500	0.4082	3.22	0.026218	14176.8	58.16
6	clean	130	0.382	500	0.3479	2.47	0.024427	15497.7	61.21
7	landing & gear	65	0.191	500	1.391	2.91	0.187709	29785.8	62.68
8	landing & gear	75	0.221	500	1.045	-1.41	0.153626	32448.9	66.45
9	landing & gear	85	0.25	500	0.814	-4.26	0.135809	36826.1	71.31
10	clean	100	0.294	500	0.5879	4.68	0.031470	11815.3	51.84
11	approach	100	0.294	500	0.5879	-0.82	0.064771	24318.0	64.02
12	approach	90	0.265	500	0.726	0.89	0.071991	21887.3	60.18
13	landing	90	0.265	500	0.726	-5.33	0.107793	32772.2	69.11
14	landing	80	0.235	500	0.919	-2.97	0.121554	29194.8	64.71
15	landing & gear	80	0.235	500	0.919	-2.97	0.143552	34478.3	68.80

Table A.1: Horizontal, non-accelerated flight segments

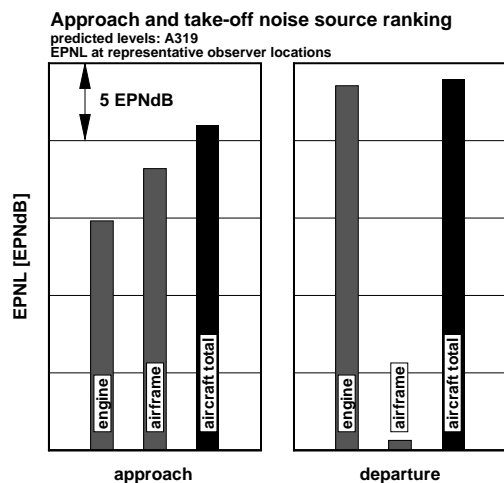


Figure A.4: EPNL predictions: Aircraft noise source ranking

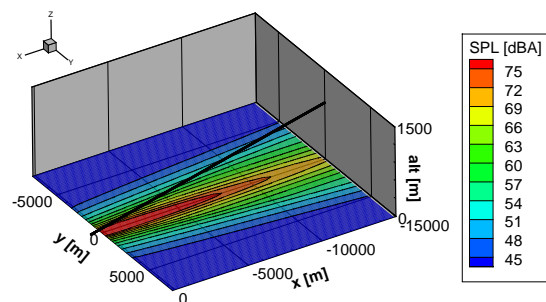


Figure A.5: Noise isocontour areas along simplified approach trajectory

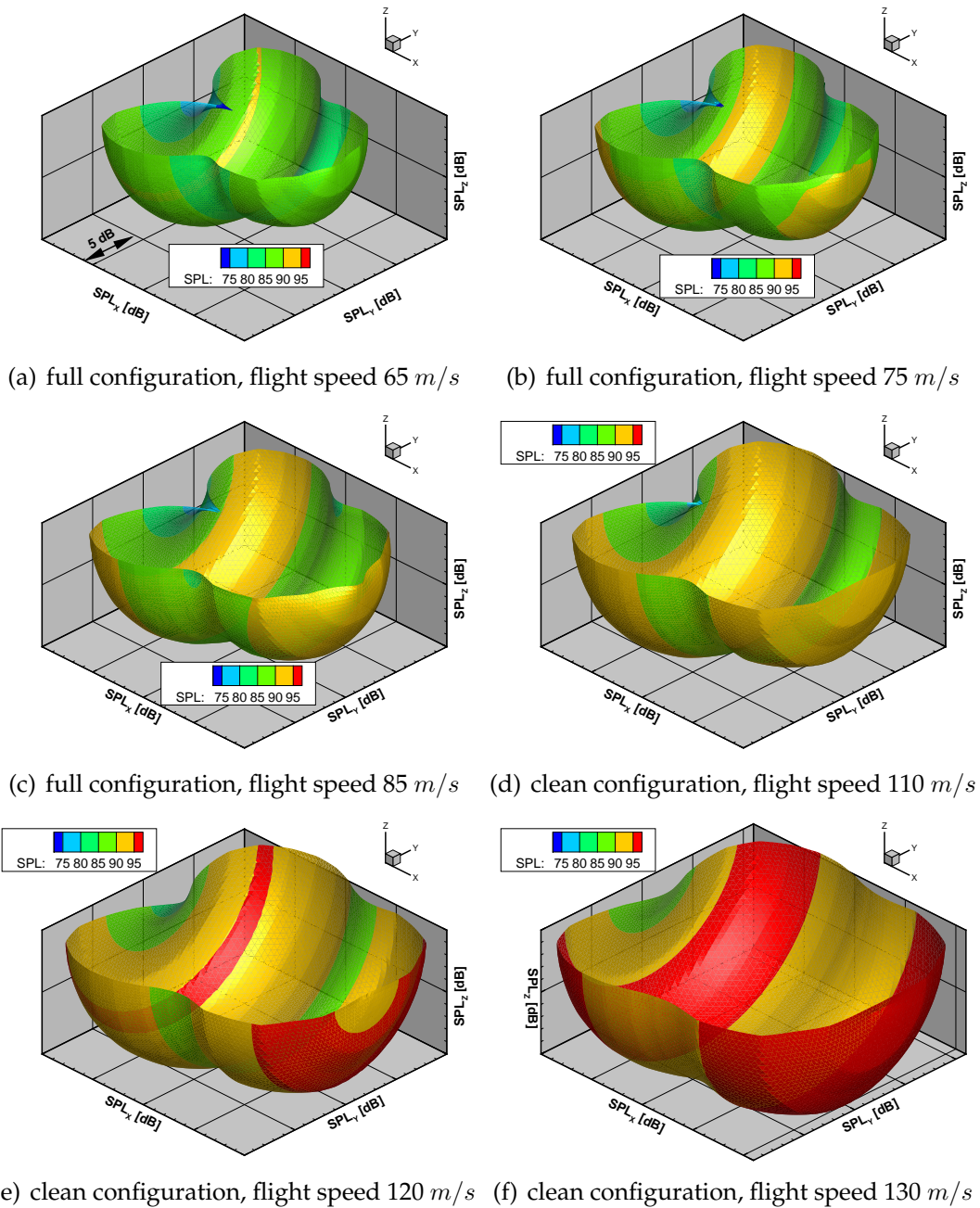


Figure A.6: Influence of flight velocity: noise emission directivity (in 80 m source distance)

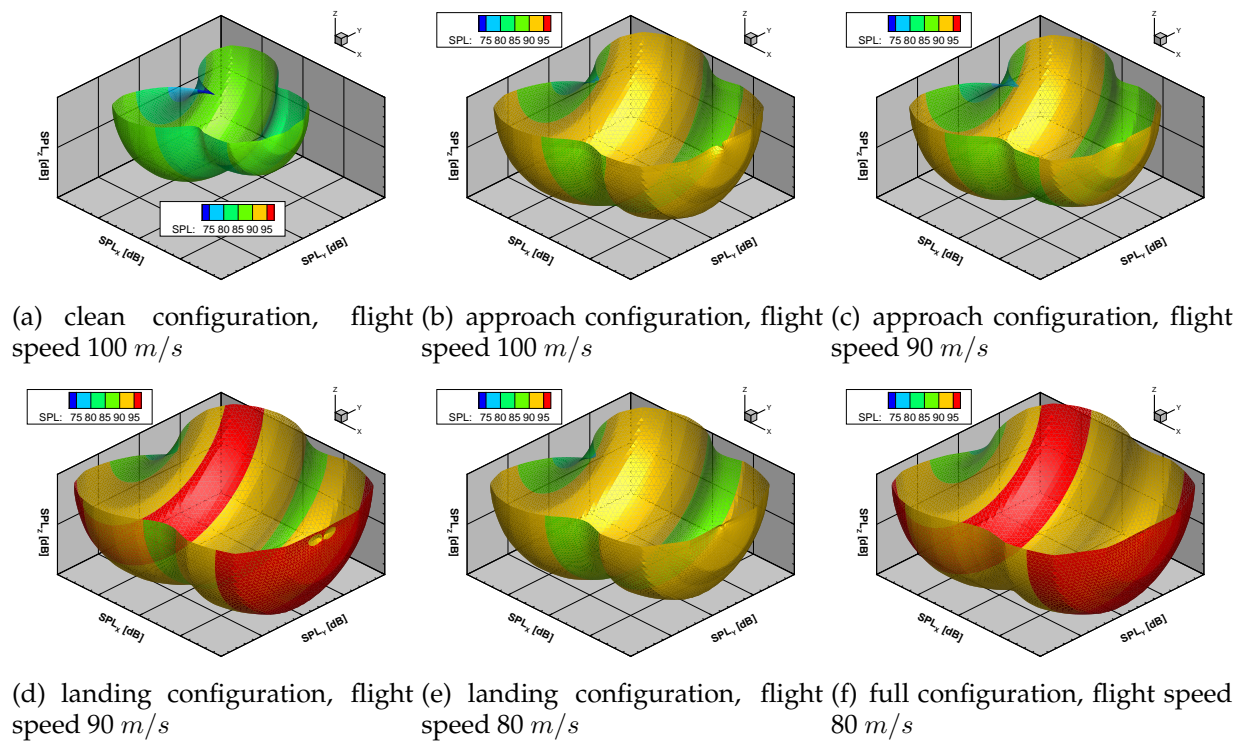


Figure A.7: Influence of configurational setting: noise emission directivity (in 80 m source distance)

A.3 A319 Flyover Campaign

Reference Aircraft PrADO Redesign

range [km]	PAX [-]	freight [kg]	cruise mach [-]
3333.6	124	0.00	0.76

Table A.2: Top Level Aircraft Requirements

Reference vehicle V-R

Weights	
operational empty	38641.02
max. take-off	60815.30
max. landing	58588.28
Geometry	
max. width [m]	33.96
max. height [m]	12.14
max. length [m]	33.84
wheel base [m]	10.44
wheel guage [m]	7.60
max. rotation angle [°]	15.54
max. bank angle [°]	16.33

Table A.3: V-r global aircraft parameters

Parameter	Wing	HTP	VTP
span width [m]	33.94	11.83	5.87
ref. area [m ²]	122.60	28.00	21.50
aspect ratio [-]	9.40	5.00	1.60
taper ratio [-]	0.25	0.33	0.35
root chord [m]	6.09	3.12	0.00
wing tip chord [m]	1.50	1.17	1.90
aerod. mean chord [m]	4.19	2.57	3.95
t/4 sweep angle [°]	23.98	27.91	37.20
leading edge sweep [°]	27.49	32.21	42.60
trailing edge sweep [°]	12.33	12.88	16.12
t/4 dihedral angle [°]	4.26	5.00	90.00

Table A.5: V-r lift and control surfaces

no. of engines [-]	2
static thrust/engine [N]	104043.
bypass ratio [-]	6.00
overall pressure ratio [-]	25.30
max. turbine temp. [°K]	1550.00
SFC [kg/N/h]	0.05900

Table A.4: V-r engine data

Design mission	
flight speed [km/h]	813.34
block time [h]	4.31
balanced field length ^a [m]	1908.99
fuel req. [kg]	10178.52
Max. fuel mission	
max. fuel	17676.16
fuel req. [kg]	14916.19
range [km]	6614.00
Max. payload mission	
max. payload	16995.76
fuel req. [kg]	3426.99
range [km]	1315.67

Table A.6: V-r vehicle performance

^aPrADO default settings, e.g. breaking coefficient of 0.3.

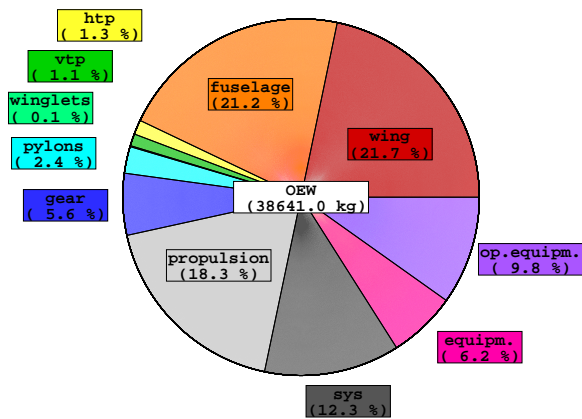


Figure A.8: V-r oew breakdown

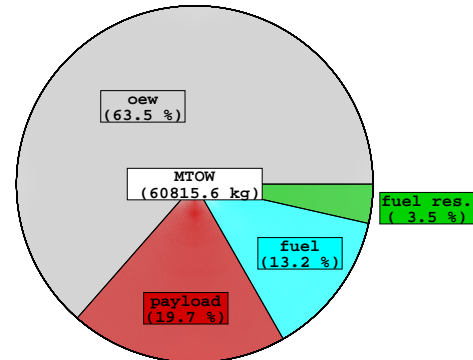


Figure A.9: V-r design mission mass breakdown

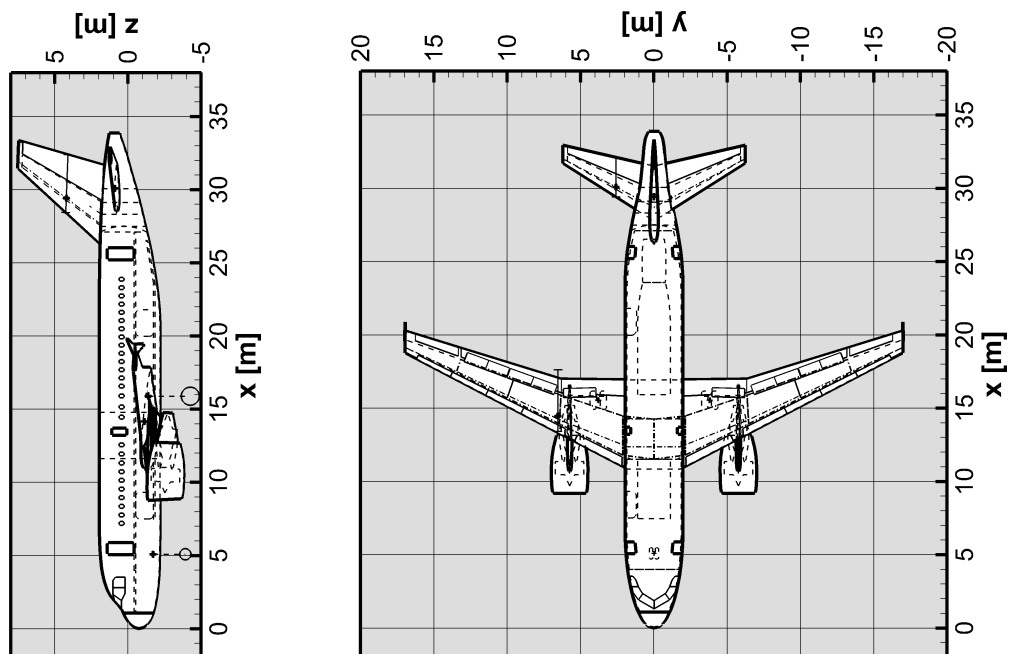
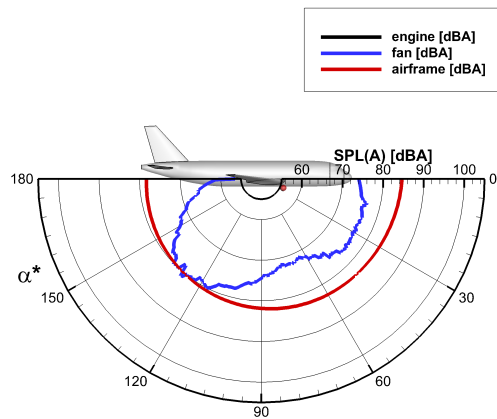
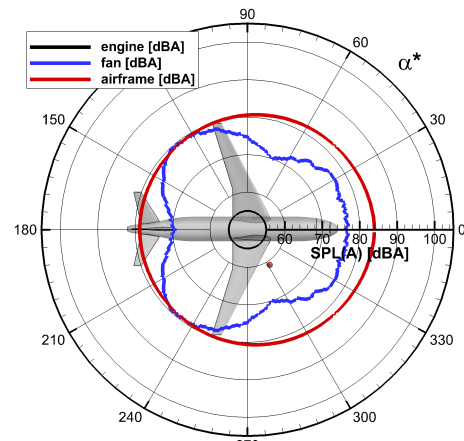


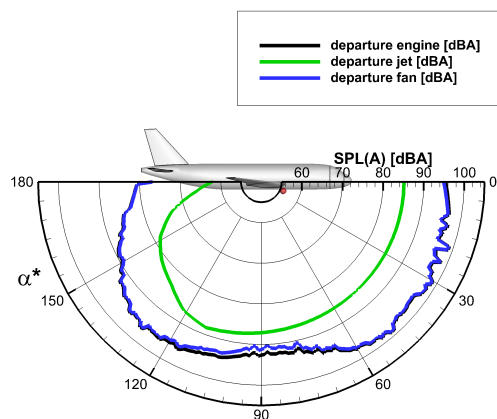
Figure A.10: V-r geometry layout



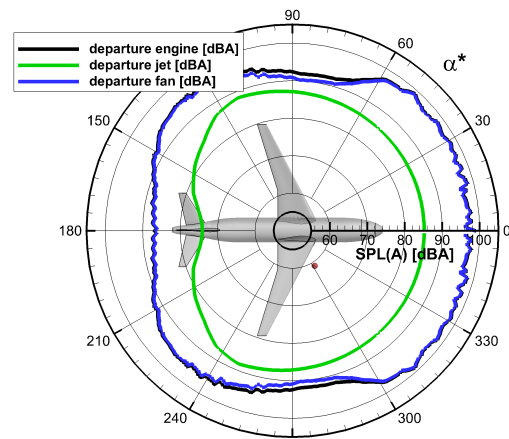
(a) approach: polar directivity



(b) approach: lateral directivity



(c) take-off: polar directivity



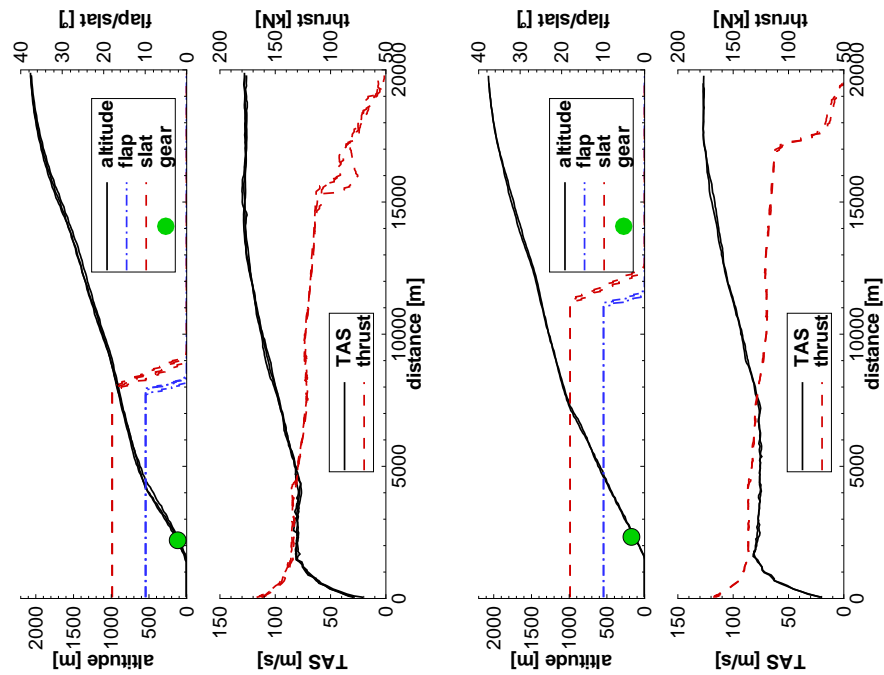
(d) take-off: lateral directivity

Figure A.11: $V-r$ noise emission directivities

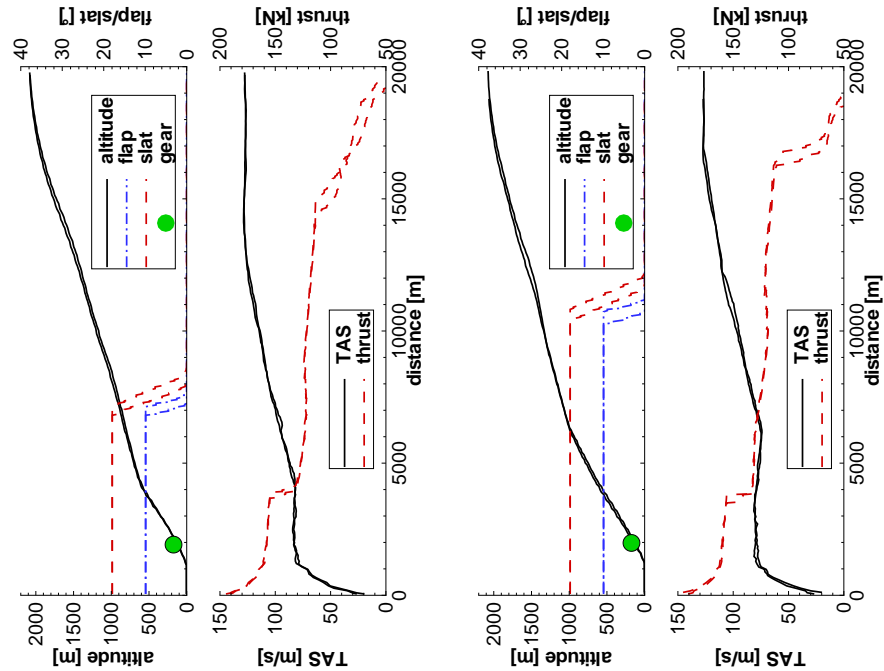
Test Flights

-	procedure	name
<i>rec001</i>	dep	modified IATA with flexible thrust setting
<i>rec002</i>	app	Low-Drag-Low-Power (LDLP)
<i>rec003</i>	dep	modified IATA with flexible thrust setting
<i>rec004</i>	app	LDLP
<i>rec005</i>	dep	ICAO with flexible thrust setting
<i>rec006</i>	app	Continuous Descent Approach (CDA) with late gear extension
<i>rec007</i>	dep	ICAO with flexible thrust setting
<i>rec008</i>	app	CDA with late gear
<i>rec009</i>	dep	modified IATA procedure, take-off and go-around thrust setting
<i>rec010</i>	app	LDLP with steep final segment
<i>rec011</i>	dep	modified IATA procedure, take-off and go-around thrust setting
<i>rec012</i>	app	LDLP with steep final segment
<i>rec013</i>	dep	ICAO with take-off and go-around thrust setting
<i>rec014</i>	app	segmented CDA
<i>rec015</i>	dep	ICAO with take-off and go-around thrust setting
<i>rec016</i>	app	segmented CDA
<i>rec017</i>	dep	modified IATA with flexible thrust setting
<i>rec018</i>	app	LDLP

Table A.7: Parchim Flyover Campaign: Test Flights (**standard** procedures), according to Ref. [100]



(a) mod. IATA with flex. thrust: (b) ICAO with flex. thrust: *rec005*,
rec001, *rec003*, *017* *rec007*



(c) mod. IATA with TOGO thrust: (d) ICAO with TOGO thrust: *rec013*,
rec009, *rec011* *rec015*

Figure A.12: Parchim Flyover Campaign: Departure procedures

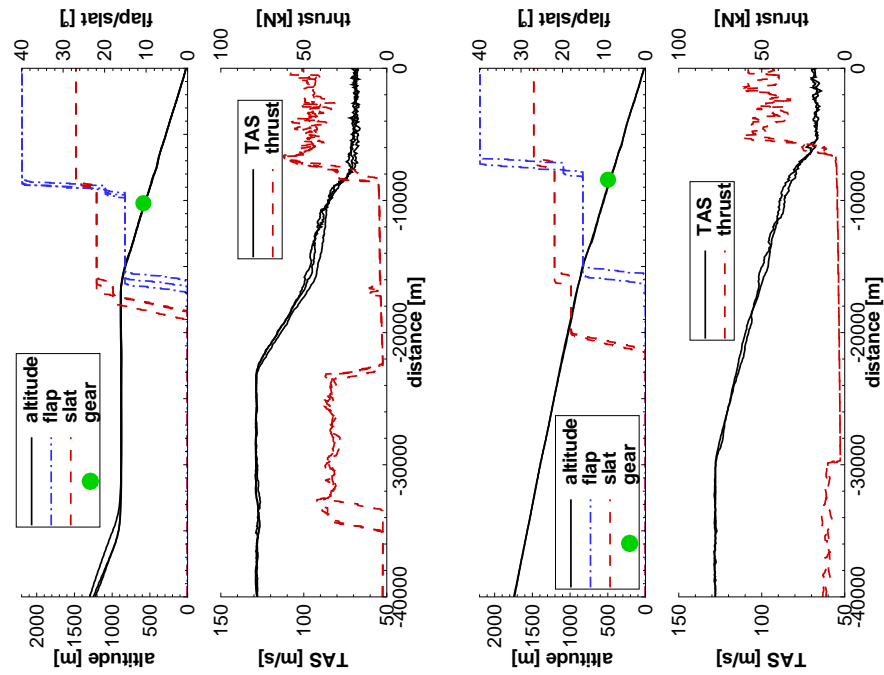
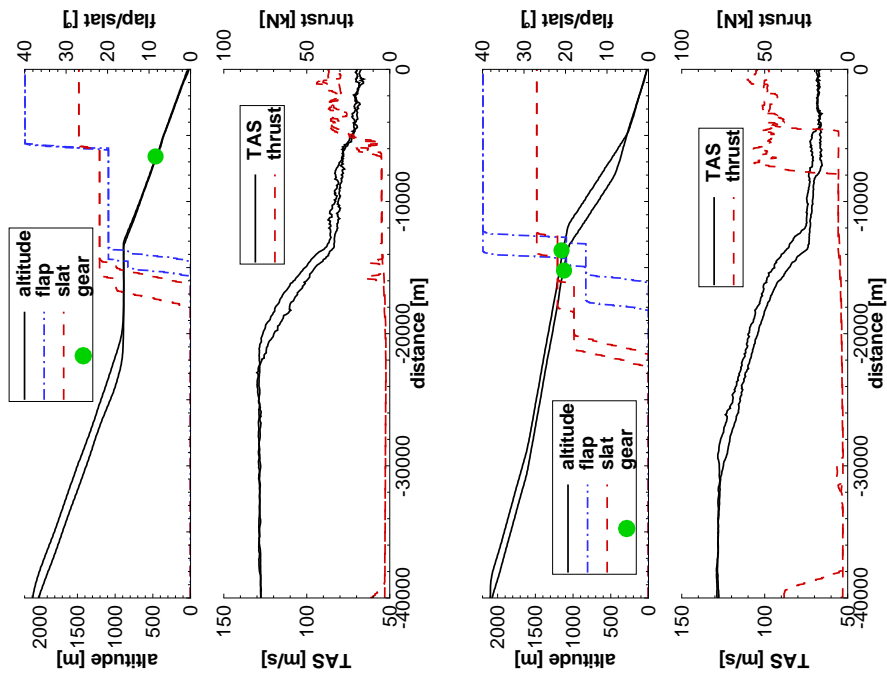
(a) LDLP: *rec002, rec004, 018*(b) CDA with late gear: *rec006, rec008*(c) LDLP with steep final: *rec010, rec012*(d) Segmented CDA: *rec014, rec016*

Figure A.13: Parchim Flyover Campaign: Approach procedures

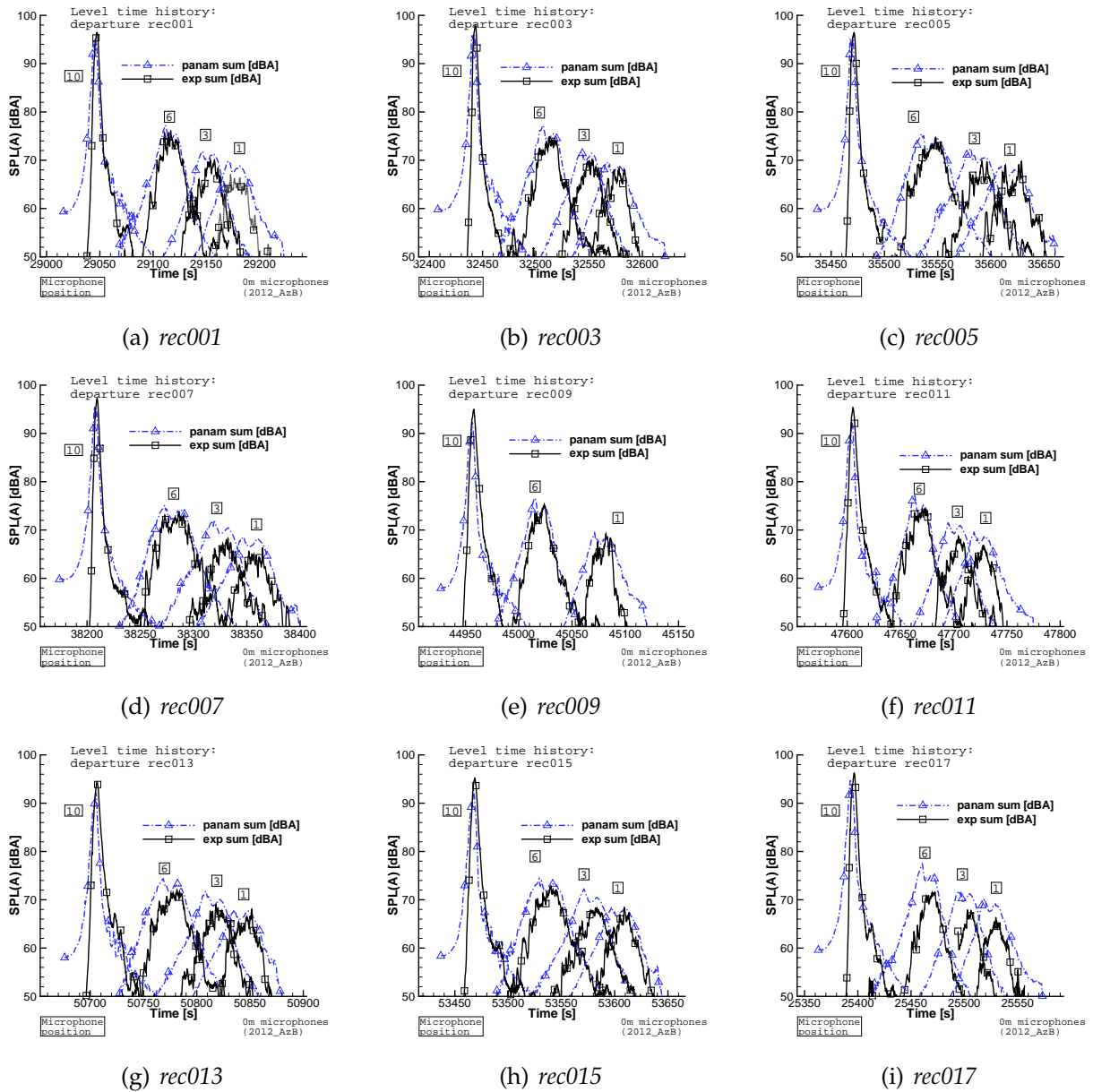
Departure¹

Figure A.14: Predicted vs. measured departure SPL(A) time-history: ground mics along flight ground track

¹Corrupted Measurements are indicated with gray dotted lines.

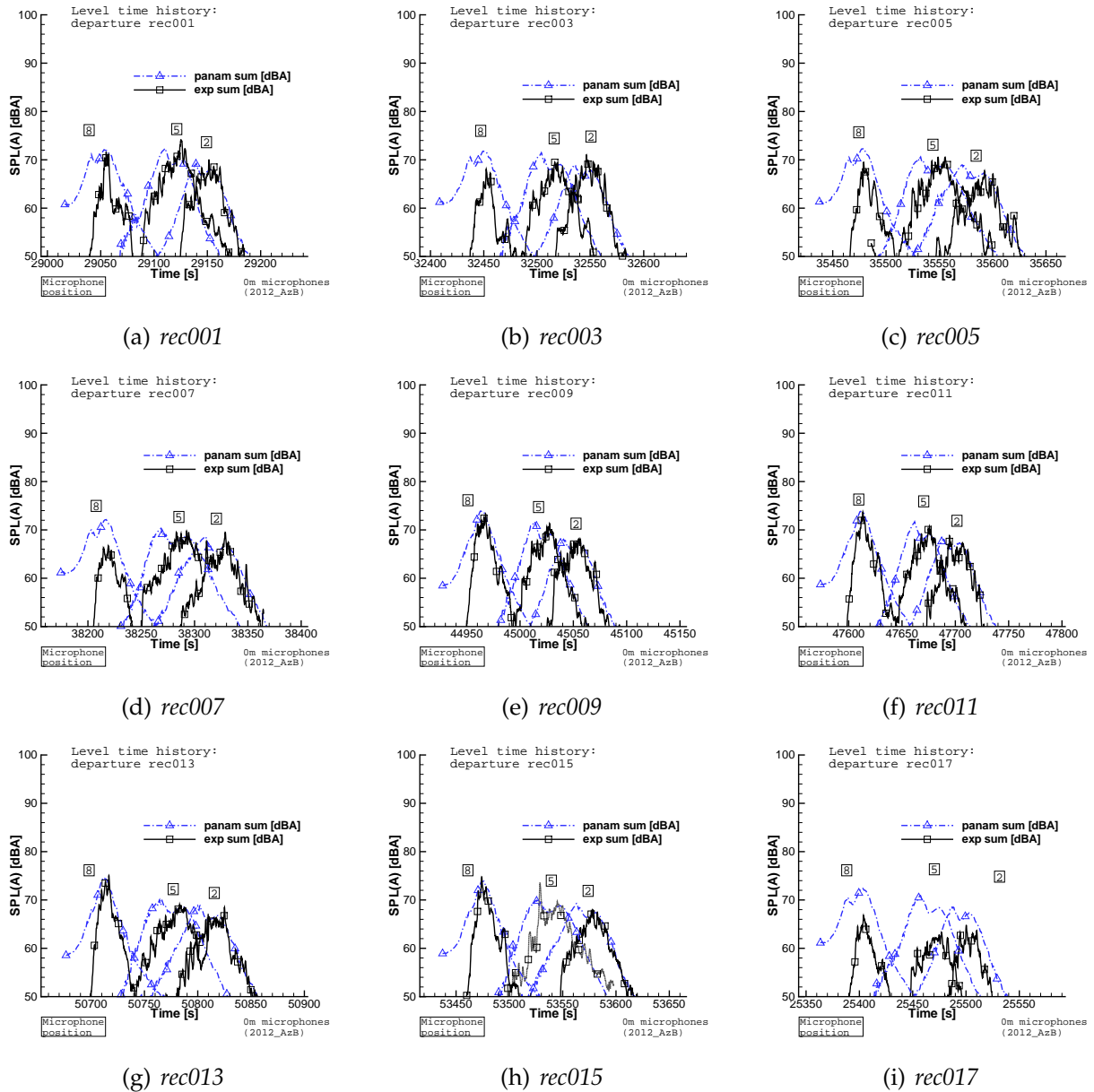


Figure A.15: Predicted vs. measured departure SPL(A) time-history: ground mics with lateral offset to flight ground track, 1

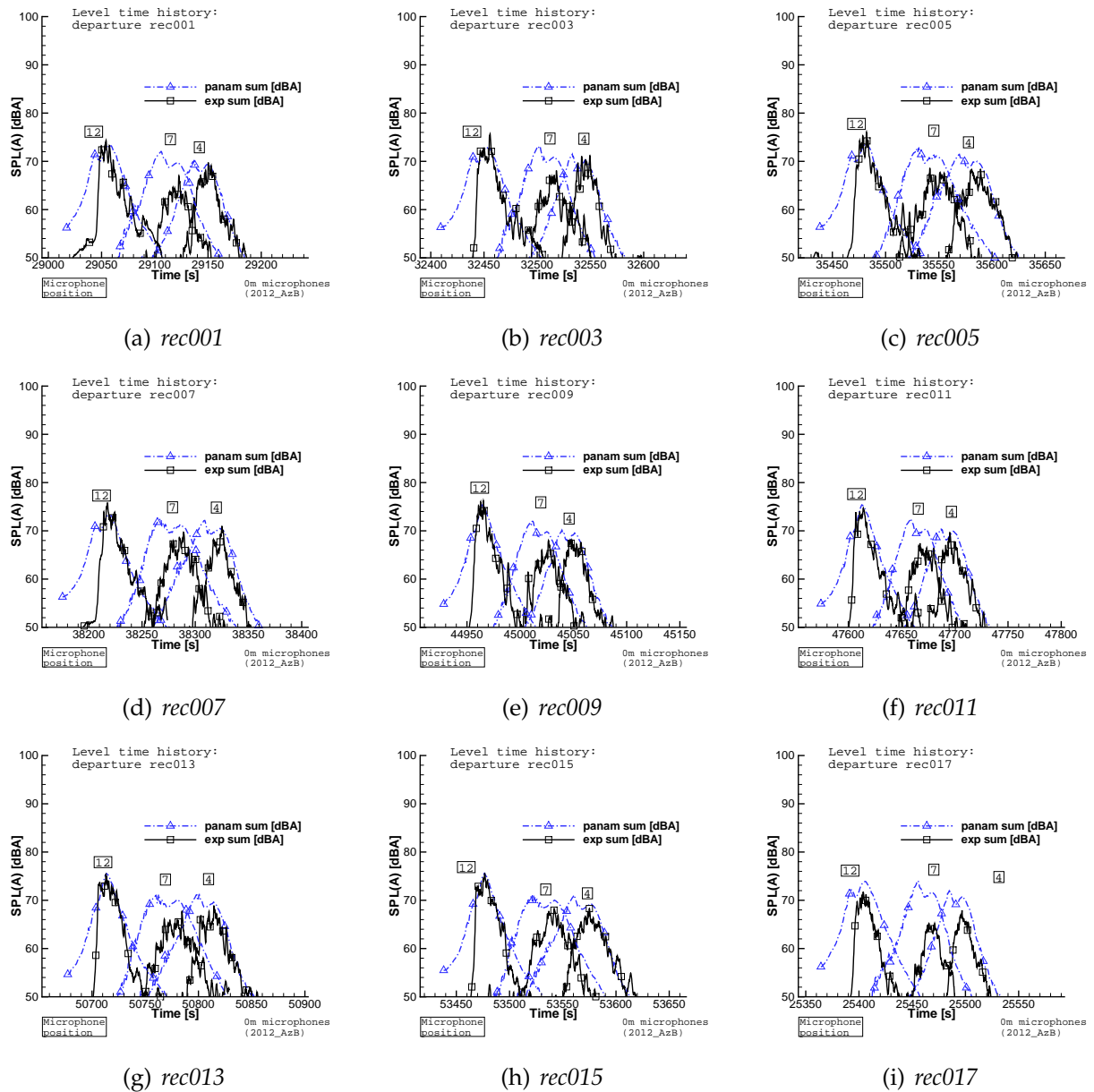


Figure A.16: Predicted vs. measured departure SPL(A) time-history: ground mics with lateral offset to flight ground track, 2

Approach²

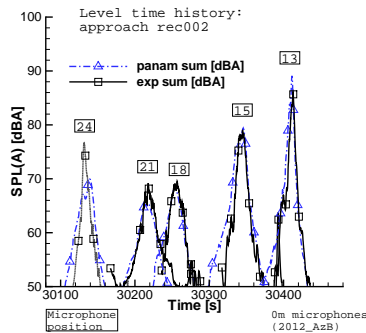
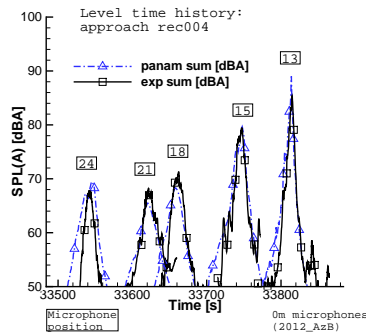
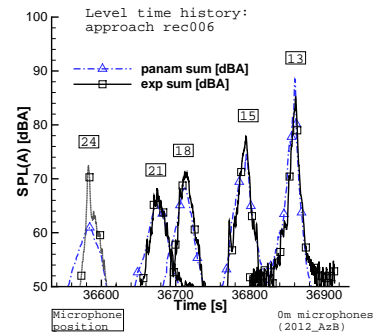
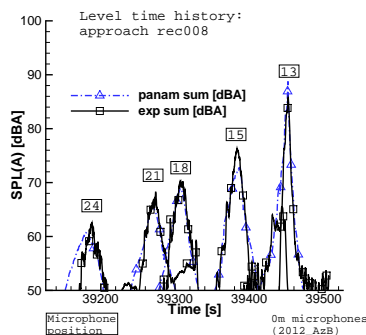
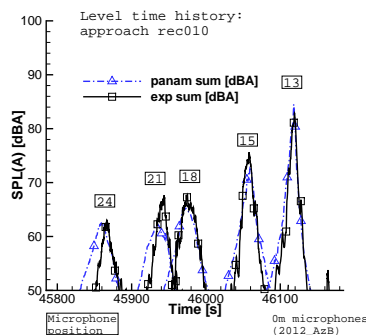
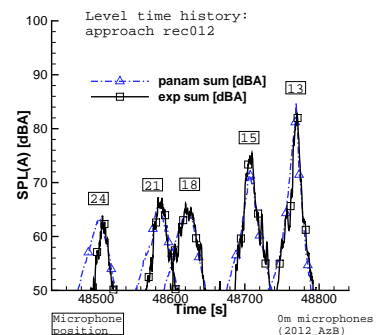
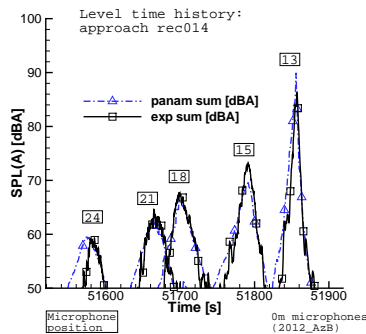
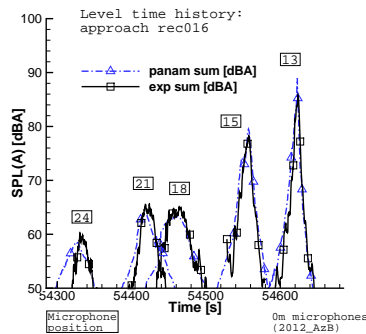
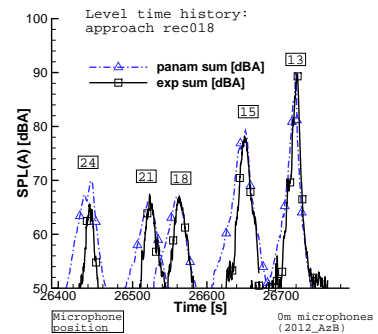
(a) *rec002*(b) *rec004*(c) *rec006*(d) *rec008*(e) *rec010*(f) *rec012*(g) *rec014*(h) *rec016*(i) *rec018*

Figure A.17: Predicted vs. measured approach SPL(A) time-history: ground mics along flight ground track

²Corrupted Measurements are indicated with gray dotted lines.

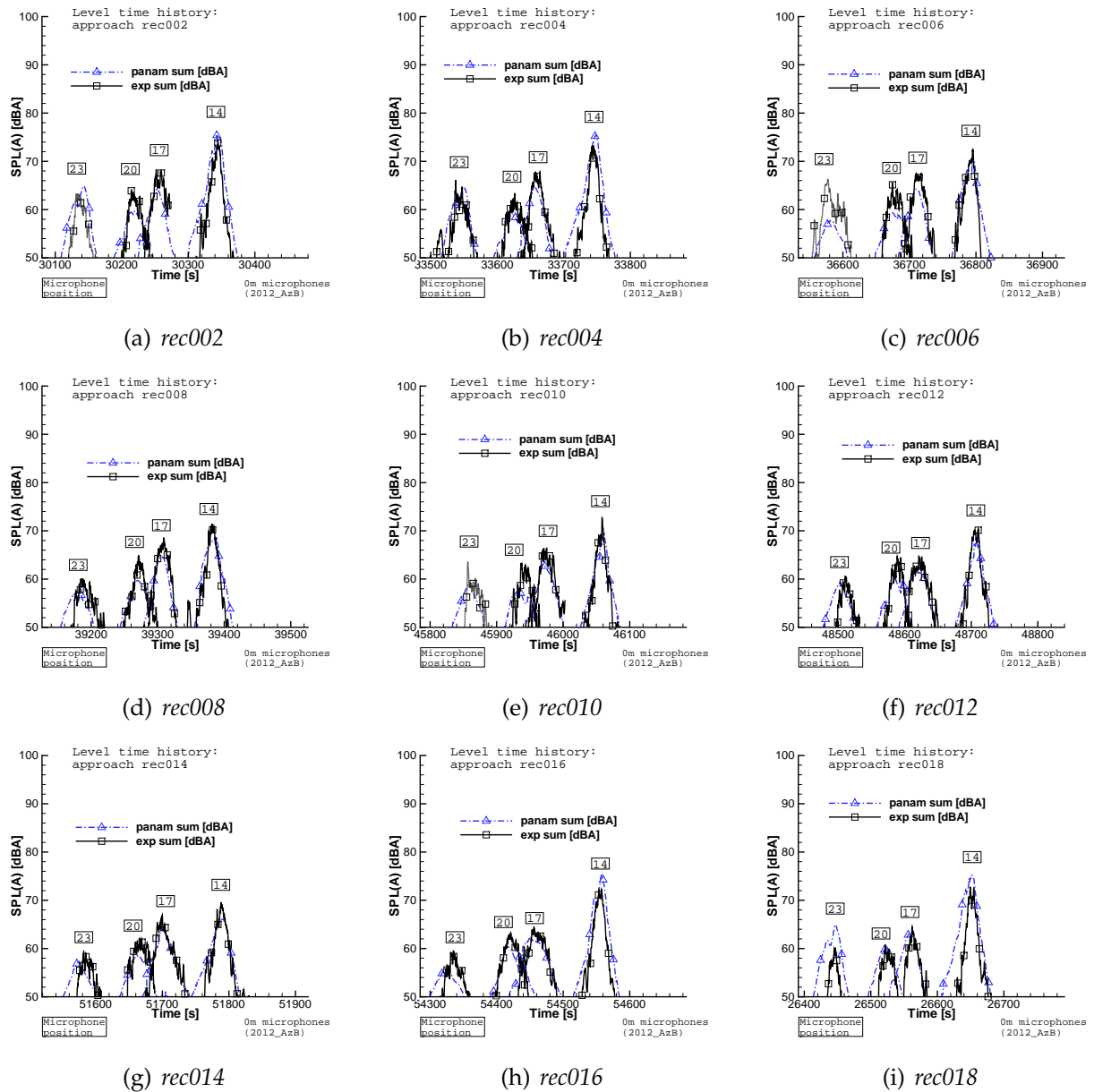


Figure A.18: Predicted vs. measured approach SPL(A) time-history: ground mics with lateral offset to flight ground track, 1

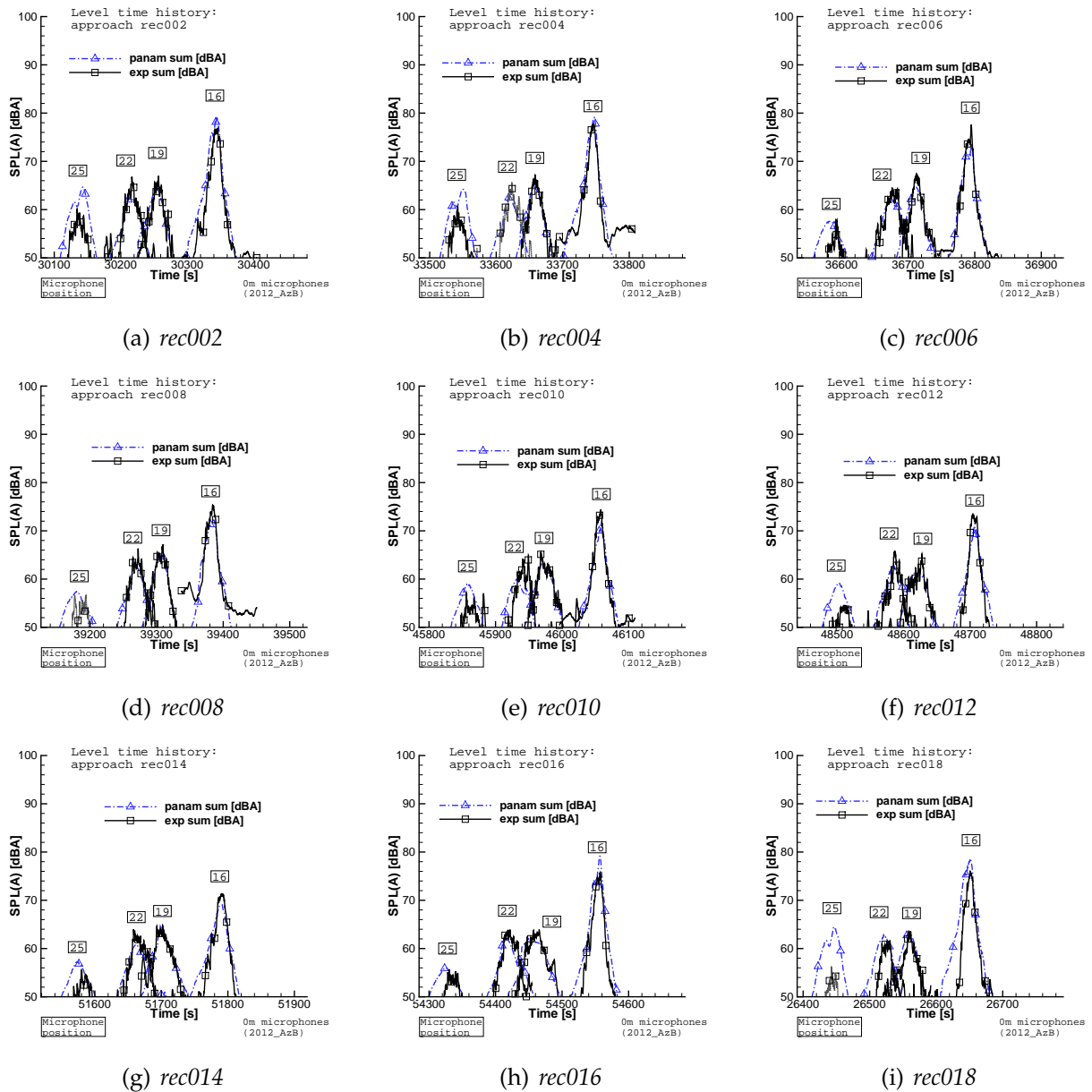
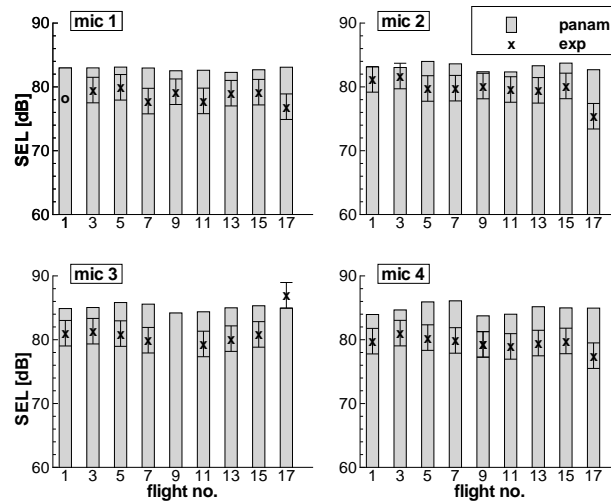
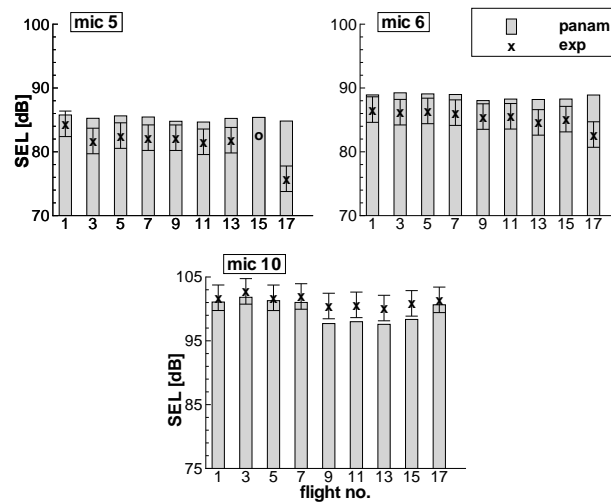


Figure A.19: Predicted vs. measured approach SPL(A) time-history: ground mics with lateral offset to flight ground track, 2

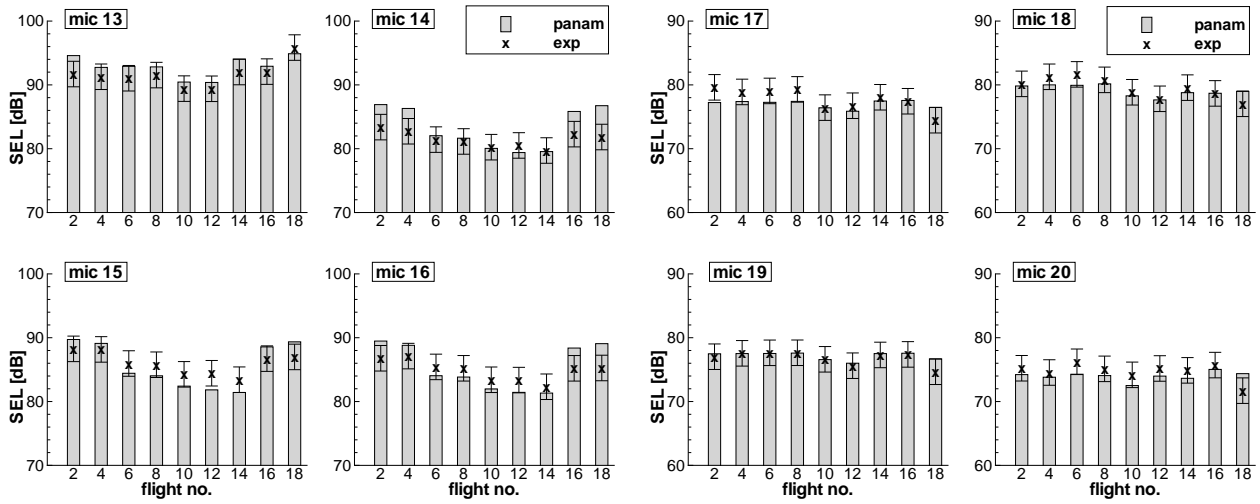


(a) mic locations 1-4



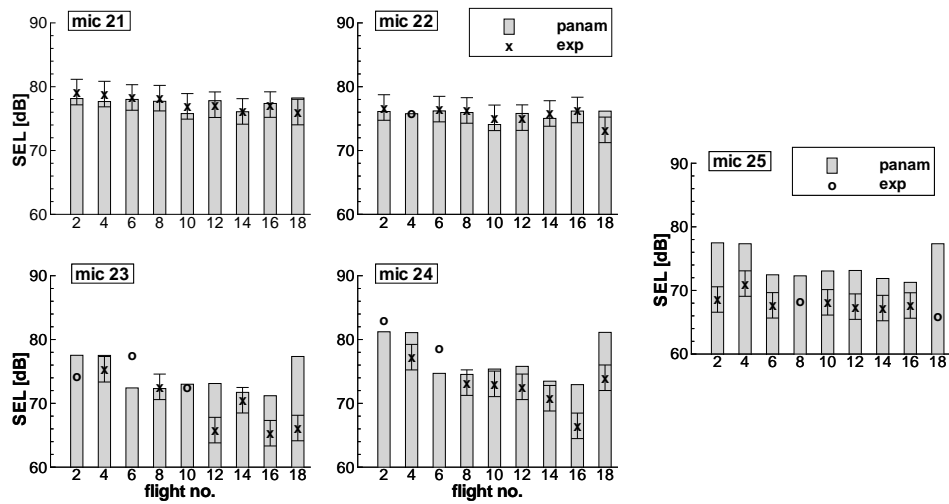
(b) mic locations 5-6, 10

Figure A.20: Parchim Campaign: Departure procedures, predicted vs. measured SEL ("o" indicates corrupted measurements)



(a) mic locations 13-16

(b) mic locations 17-20



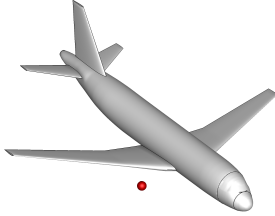
(c) mic locations 21-24

(d) mic location 25

Figure A.21: Parchim Campaign: Approach procedures, predicted vs. measured SEL ("o" indicates corrupted measurements)

A.4 Low-Noise Vehicle Design

Vehicle category $v-r$



$\Lambda_w \backslash A_w$	7.0	8.0	9.0	10.0	11.0
100.0	1	2	3	4	5
105.0	6	7	8	9	10
110.0	11	12	13	14	15
115.0	16	17	18	19	20
120.0	21	22	23	24	25
125.0	26	27	28	29	30
130.0	31	32	33	34	35

Figure A.22: $v-r$ vehicle layout: parameter variation 1

Table A.8: $v-r$ variants: parameter variation 1 (wing area & aspect ratio)

design	weights			performance			
	OEW [kg]	MTOW [kg]	MLW [kg]	flight speed [km/h]	block time [h]	balanced field length [m]	fuel req. [kg]
1	34730.07	57762.96	55166.97	813.34	4.32	2108.18	11037.1
2	35609.48	58188.24	55787.32	813.34	4.31	2095.42	10583.0
3	36466.28	58713.75	56455.88	813.34	4.31	2175.79	10251.7
4	37471.09	59469.67	57318.06	813.34	4.31	2258.10	10002.8
5	38695.33	60522.28	58445.11	813.34	4.31	2345.99	9831.2
6	35052.26	58070.72	55480.49	813.34	4.32	2032.48	11022.7
7	35814.43	58364.33	55975.75	813.34	4.31	2015.87	10554.1
8	36893.03	59149.63	56887.62	813.34	4.31	2101.07	10260.8
9	38022.32	60051.03	57886.78	813.34	4.31	2185.05	10033.0
10	39241.93	61101.08	59009.88	813.34	4.31	2269.67	9863.4
11	35215.89	58199.77	55624.87	813.34	4.32	1950.46	10988.1
12	36159.02	58715.51	56324.31	813.34	4.31	1948.09	10560.7
13	37125.99	59379.40	57118.25	813.34	4.31	2026.96	10257.7
14	38456.08	60507.91	58333.76	813.34	4.31	2114.82	10056.1
15	39706.36	61592.13	59489.62	813.34	4.31	2196.07	9890.0
16	35390.34	58359.57	55790.54	813.34	4.32	1879.21	10973.5
17	36495.35	59066.58	56668.89	813.34	4.31	1886.03	10575.5
18	37631.08	59922.01	57644.87	813.34	4.31	1967.76	10295.2
19	38883.60	60968.90	58780.54	813.34	4.31	2049.46	10089.5
20	40166.64	62096.91	59975.29	813.34	4.31	2128.92	9934.5
21	35650.56	58606.82	56043.35	813.34	4.32	1824.51	10960.5
22	36879.59	59475.34	57067.10	813.34	4.31	1830.52	10600.0
23	38043.89	60364.36	58074.35	813.34	4.31	1910.47	10324.7
24	39284.03	61399.90	59198.64	813.34	4.31	1988.40	10120.1
25	40765.39	62753.50	60607.05	813.34	4.31	2071.41	9992.3
26	36019.57	58996.12	56424.44	813.34	4.32	1781.59	10980.8
27	37152.60	59756.79	57344.86	813.34	4.31	1776.34	10608.4
28	38427.36	60773.53	58472.56	813.34	4.31	1856.06	10350.4
29	39825.23	61988.29	59766.46	813.34	4.31	1936.25	10167.3
30	41216.02	63246.54	61081.66	813.34	4.31	2014.21	10034.8
31	36392.25	59391.90	56809.87	813.34	4.32	1742.22	11003.9
32	37408.87	60036.17	57614.60	813.34	4.31	1724.23	10631.5
33	38824.78	61225.90	58901.53	813.34	4.31	1806.60	10405.4
34	40271.96	62495.13	60247.47	813.34	4.31	1885.97	10227.4
35	41780.32	63864.00	61676.37	813.34	4.31	1964.63	10087.9

Table A.9: $v-r$ global aircraft parameters: parameter variation 1

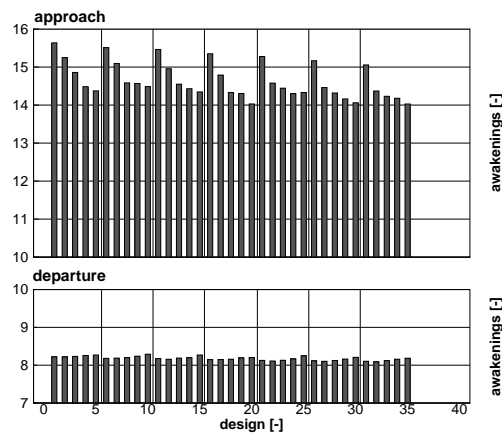


Figure A.23: v - r aircraft noise induced awakenings: parameter variation

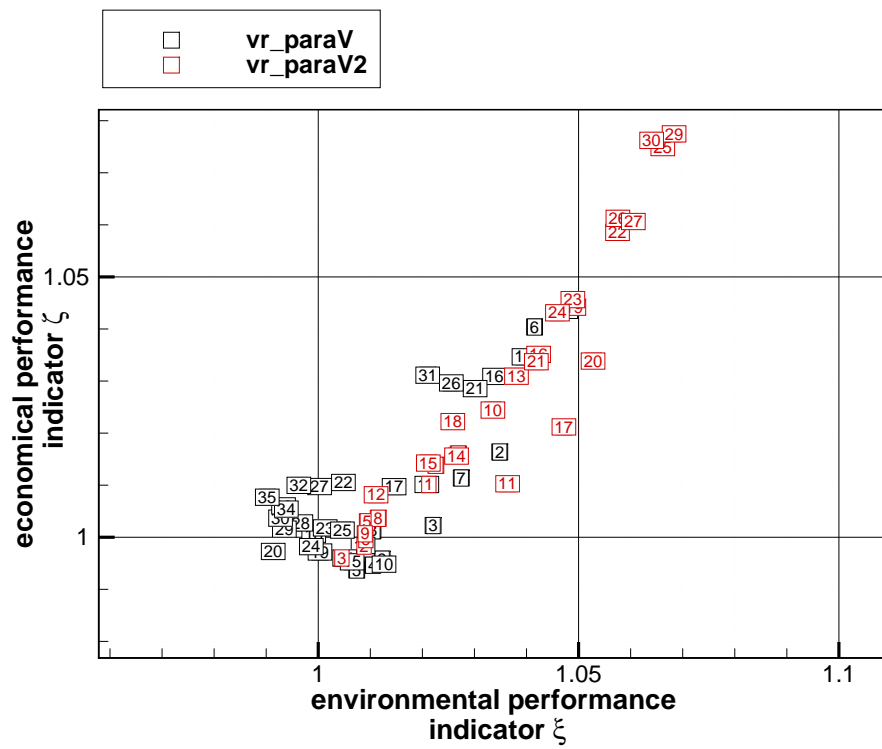
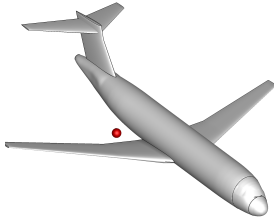


Figure A.24: Performance indicators: v - r variants

Vehicle category $v-0$

$v-0$: Parameter study 1



$\Lambda_w \backslash A_w$	7.0	8.0	9.0	10.0	11.0
100.0	1	2	3	4	5
105.0	6	7	8	9	10
110.0	11	12	13	14	15
115.0	16	17	18	19	20
120.0	21	22	23	24	25
125.0	26	27	28	29	30
130.0	31	32	33	34	35

Figure A.25: $v-0$ vehicle layout: parameter variation 1

Table A.10: $v-0$ variants: parameter variation 1 (wing area & aspect ratio)

design	weights			performance			
	OEW [kg]	MTOW [kg]	MLW [kg]	flight speed [km/h]	block time [h]	balanced field length [m]	fuel req. [kg]
1	34951.14	58530.63	55699.46	813.34	4.32	2266.90	11583.7
2	35941.32	59022.62	56405.59	813.34	4.32	2184.59	11085.5
3	36828.62	59556.49	57091.38	813.34	4.32	2167.00	10732.1
4	37965.63	60447.35	58088.52	813.34	4.31	2244.33	10486.0
5	39073.07	61391.26	59102.77	813.34	4.31	2323.97	10322.4
6	35313.75	58912.94	56073.09	813.34	4.32	2197.99	11603.4
7	36201.49	59308.01	56680.16	813.34	4.32	2104.88	11110.8
8	37304.04	60086.06	57597.69	813.34	4.32	2103.56	10786.3
9	38415.30	60946.63	58566.52	813.34	4.31	2166.39	10535.6
10	39641.87	62016.71	59703.76	813.34	4.31	2247.05	10379.1
11	35542.69	59160.57	56312.62	813.34	4.32	2125.17	11622.1
12	36568.48	59716.37	57070.71	813.34	4.32	2043.17	11152.1
13	37740.15	60569.79	58060.84	813.34	4.32	2043.47	10833.9
14	38900.25	61486.59	59082.86	813.34	4.31	2096.71	10590.6
15	40178.16	62610.91	60273.25	813.34	4.31	2173.91	10437.0
16	35854.70	59501.17	56641.05	813.34	4.32	2069.70	11650.7
17	36918.03	60101.61	57440.58	813.34	4.32	1986.85	11187.8
18	38142.29	61013.19	58486.82	813.34	4.32	1987.64	10875.1
19	39347.91	61986.99	59560.54	813.34	4.31	2029.99	10643.3
20	40746.18	63260.98	60887.87	813.34	4.31	2108.24	10519.0
21	36214.28	59880.22	57011.68	813.34	4.32	2026.36	11670.2
22	37409.59	60648.79	57963.94	813.34	4.32	1948.15	11243.4
23	38570.02	61486.83	58940.81	813.34	4.32	1939.45	10921.1
24	39789.53	62477.68	60029.90	813.34	4.32	1967.93	10692.4
25	41371.53	63965.69	61558.60	813.34	4.31	2049.47	10598.4
26	36539.20	60247.04	57360.44	813.34	4.32	1988.54	11712.1
27	37743.83	61027.62	58323.32	813.34	4.32	1902.35	11288.0
28	38989.36	61964.59	59393.52	813.34	4.32	1896.50	10979.5
29	40360.21	63121.93	60642.48	813.34	4.32	1927.23	10766.0
30	41789.14	64443.13	62010.20	813.34	4.32	1989.43	10658.2
31	36868.23	60623.43	57716.64	813.34	4.32	1972.16	11759.4
32	38036.69	61364.77	58641.57	813.34	4.32	1858.65	11332.3
33	39425.71	62462.52	59865.15	813.34	4.32	1859.51	11041.0
34	40900.97	63748.63	61232.19	813.34	4.32	1900.64	10851.9
35	42371.51	65108.90	62640.41	813.34	4.32	1950.40	10741.6

Table A.11: $v-0$ global aircraft parameters: parameter variation 1

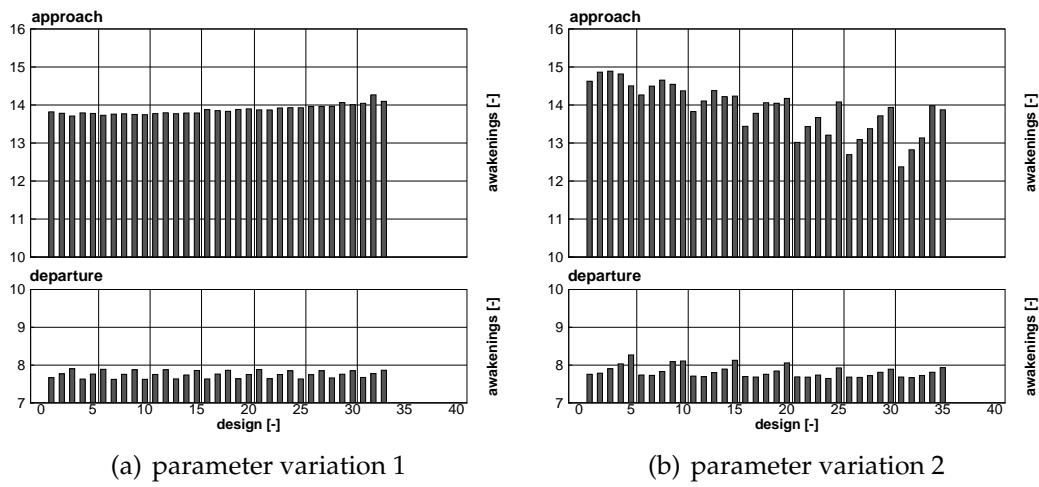
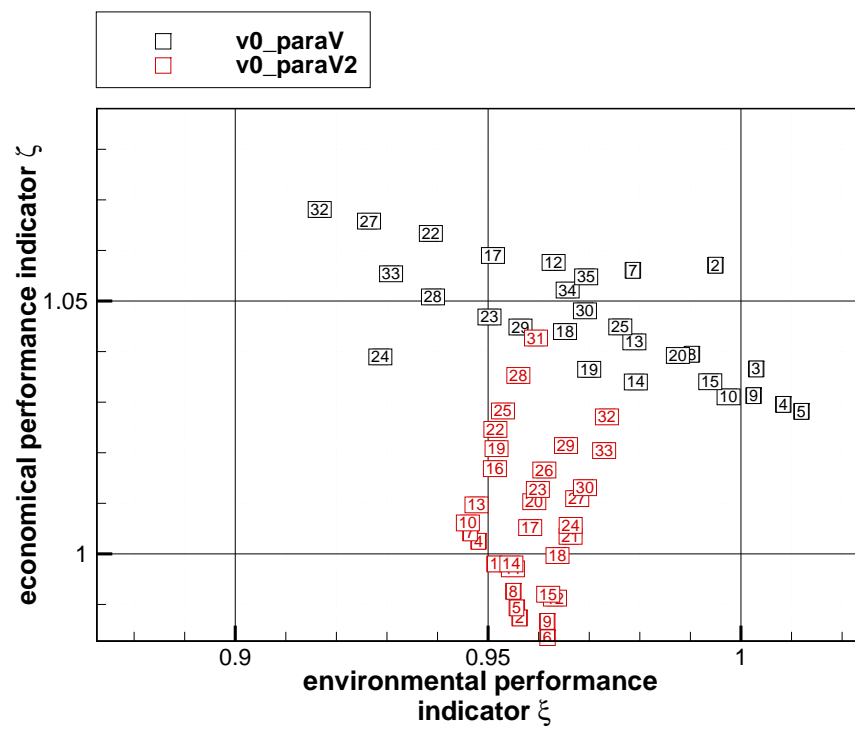
***v-0*: Parameter study 2**Figure A.26: *v-0* vehicle layout: parameter variation 2

Λ_w	8.0	9.0	10.0
x_w / l_f			
0.30	1	2	3
0.31	4	5	6
0.32	7	8	9
0.33	10	11	12
0.34	13	14	15
0.35	16	17	18
0.36	19	20	21
0.37	22	23	24
0.38	25	26	27
0.39	28	29	30
0.40	31	32	33

Table A.12: *v-0* variants: parameter variation 2 (wing location & aspect ratio)

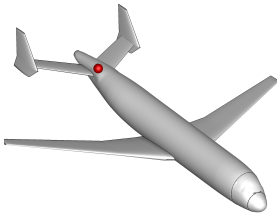
design	weights			performance			
	OEW [kg]	MTOW [kg]	MLW [kg]	flight speed [km/h]	block time [h]	balanced field length [m]	fuel req. [kg]
1	35432.27	57883.16	55537.33	813.34	4.31	1925.81	10455.1
2	36379.47	58543.60	56321.09	813.34	4.31	2004.87	10168.4
3	37366.52	59314.74	57184.84	813.34	4.31	2082.77	9952.5
4	35548.03	58051.43	55683.08	813.34	4.31	1931.44	10507.6
5	36352.84	58547.33	56311.47	813.34	4.31	2005.98	10198.7
6	37343.57	59319.54	57177.73	813.34	4.31	2082.58	9980.2
7	35497.15	58029.33	55648.23	813.34	4.31	1930.43	10536.4
8	36412.23	58648.74	56394.85	813.34	4.31	2007.80	10240.8
9	37416.69	59432.45	57273.64	813.34	4.31	2085.26	10020.0
10	35462.34	58026.80	55631.93	813.34	4.31	1929.36	10568.7
11	36555.12	58841.89	56566.44	813.34	4.31	2012.76	10291.0
12	37590.03	59655.00	57475.10	813.34	4.31	2091.67	10069.2
13	35540.03	58148.37	55734.65	813.34	4.31	1932.43	10612.6
14	36471.91	58781.01	56496.02	813.34	4.31	2010.24	10313.3
15	37492.12	59579.05	57389.57	813.34	4.31	2087.30	10091.2
16	35734.60	58429.72	55978.78	813.34	4.31	1936.56	10699.4
17	36701.89	59095.12	56774.06	813.34	4.31	2015.00	10397.5
18	37803.52	59972.89	57748.19	813.34	4.31	2095.01	10173.6
19	35819.48	58564.99	56092.42	813.34	4.32	1938.00	10749.7
20	36886.41	59336.93	56991.29	813.34	4.31	2019.66	10454.8
21	37931.02	60144.92	57901.36	813.34	4.31	2096.76	10218.1
22	35904.84	58699.36	56205.74	813.34	4.32	1938.10	10798.8
23	36911.97	59398.18	57037.58	813.34	4.31	2016.55	10490.5
24	37961.42	60207.18	57949.90	813.34	4.31	2093.22	10250.0
25	35942.60	58782.66	56269.64	813.34	4.32	1944.58	10844.3
26	37025.68	59560.19	57178.36	813.34	4.31	2015.57	10538.7
27	38182.66	60487.29	58204.64	813.34	4.31	2095.66	10308.9
28	36135.61	59044.70	56501.83	813.34	4.32	1969.86	10913.3
29	37190.08	59784.56	57376.85	813.34	4.31	2013.30	10598.7
30	38189.16	60531.74	58232.97	813.34	4.31	2086.40	10346.8
31	36293.48	59277.62	56702.44	813.34	4.32	1997.91	10988.4
32	37373.86	60039.16	57601.59	813.34	4.31	2010.75	10669.5
33	38494.88	60921.18	58586.46	813.34	4.31	2086.99	10430.5

Table A.13: *v-0* global aircraft parameters: parameter variation 2

***v-0*: Results**Figure A.27: *v-0* aircraft noise induced awakeningsFigure A.28: *v-0* performance indicators: parameter variation

Vehicle category *v-1*

v-1: Parameter study 1



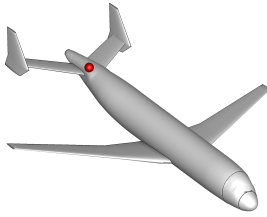
$\Lambda_w \backslash A_w$	7.0	8.0	9.0	10.0	11.0
100.0	1	2	3	4	5
105.0	6	7	8	9	10
110.0	11	12	13	14	15
115.0	16	17	18	19	20
120.0	21	22	23	24	25
125.0	26	27	28	29	30
130.0	31	32	33	34	35

Figure A.29: *v-1* vehicle layout: parameter variation 1

Table A.14: *v-1* variants: parameter variation 1 (wing area & aspect ratio)

design	weights			performance			
	OEW [kg]	MTOW [kg]	MLW [kg]	flight speed [km/h]	block time [h]	balanced field length [m]	fuel req. [kg]
1	35532.27	58772.12	56087.10	813.34	4.32	2151.64	11244.1
2	36386.97	59163.80	56677.65	813.34	4.32	2109.02	10781.1
3	37322.19	59779.20	57430.82	813.34	4.31	2184.88	10461.3
4	38294.28	60509.37	58265.14	813.34	4.31	2268.34	10219.3
5	39498.84	61551.43	59377.18	813.34	4.31	2357.92	10056.8
6	35848.93	59062.59	56388.80	813.34	4.32	2073.07	11217.9
7	36653.45	59402.01	56928.06	813.34	4.32	2025.01	10752.8
8	37649.69	60096.86	57752.71	813.34	4.31	2106.92	10451.4
9	38809.75	61040.89	58789.94	813.34	4.31	2194.30	10235.4
10	40046.18	62120.81	59937.00	813.34	4.31	2280.18	10078.9
11	36017.36	59192.11	56535.07	813.34	4.32	1989.59	11179.0
12	36963.76	59708.34	57236.08	813.34	4.32	1954.53	10748.8
13	37948.71	60396.45	58051.77	813.34	4.31	2035.34	10452.0
14	39192.04	61438.95	59181.28	813.34	4.31	2122.25	10251.1
15	40478.63	62574.78	60381.83	813.34	4.31	2206.00	10100.4
16	36190.35	59340.77	56694.18	813.34	4.32	1915.93	11154.7
17	37277.33	60024.61	57551.19	813.34	4.32	1891.44	10751.5
18	38445.69	60923.78	58566.30	813.34	4.31	1976.25	10482.3
19	39693.64	61975.78	59702.61	813.34	4.31	2059.25	10286.4
20	40949.77	63087.22	60876.46	813.34	4.31	2139.81	10141.7
21	36497.57	59632.69	56992.31	813.34	4.32	1860.55	11139.4
22	37692.02	60458.97	57977.27	813.34	4.32	1842.16	10771.2
23	38848.52	61348.10	58981.47	813.34	4.31	1918.73	10503.8
24	40088.39	62394.60	60111.20	813.34	4.31	1998.44	10310.4
25	41567.15	63760.87	61525.94	813.34	4.31	2083.50	10198.0
26	36862.02	60009.85	57364.34	813.34	4.32	1815.97	11152.1
27	37988.74	60760.24	58276.57	813.34	4.32	1788.98	10775.7
28	39254.22	61777.42	59400.92	813.34	4.31	1865.19	10527.4
29	40618.31	62966.50	60665.09	813.34	4.31	1946.30	10352.4
30	42020.48	64252.81	62001.15	813.34	4.31	2026.88	10236.6
31	37232.53	60399.17	57745.39	813.34	4.32	1776.37	11170.9
32	38333.16	61156.40	58650.34	813.34	4.32	1746.69	10827.5
33	39596.98	62185.30	59780.64	813.34	4.31	1814.68	10592.6
34	41131.74	63559.56	61223.91	813.34	4.31	1898.37	10432.1
35	42590.21	64881.53	62604.53	813.34	4.31	1976.37	10295.6

Table A.15: *v-1* global aircraft parameters: parameter variation 1

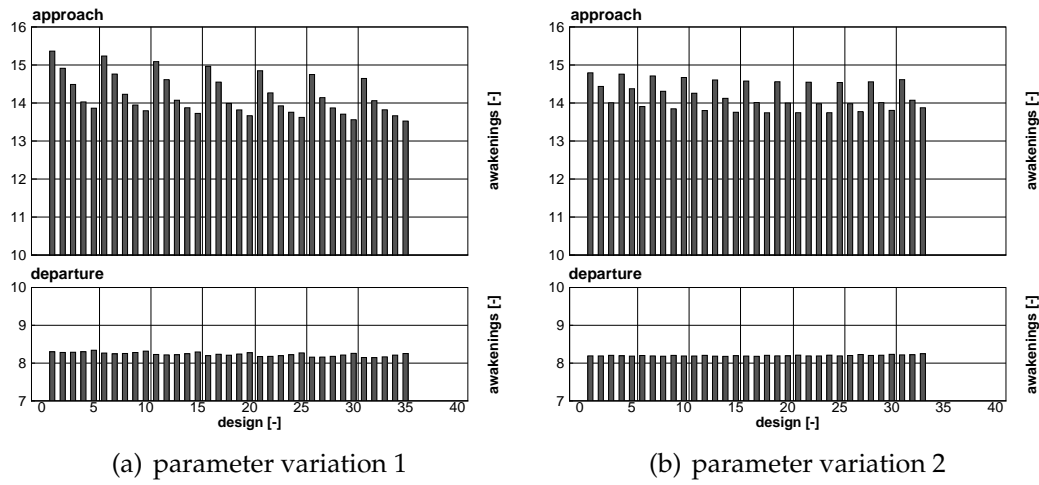
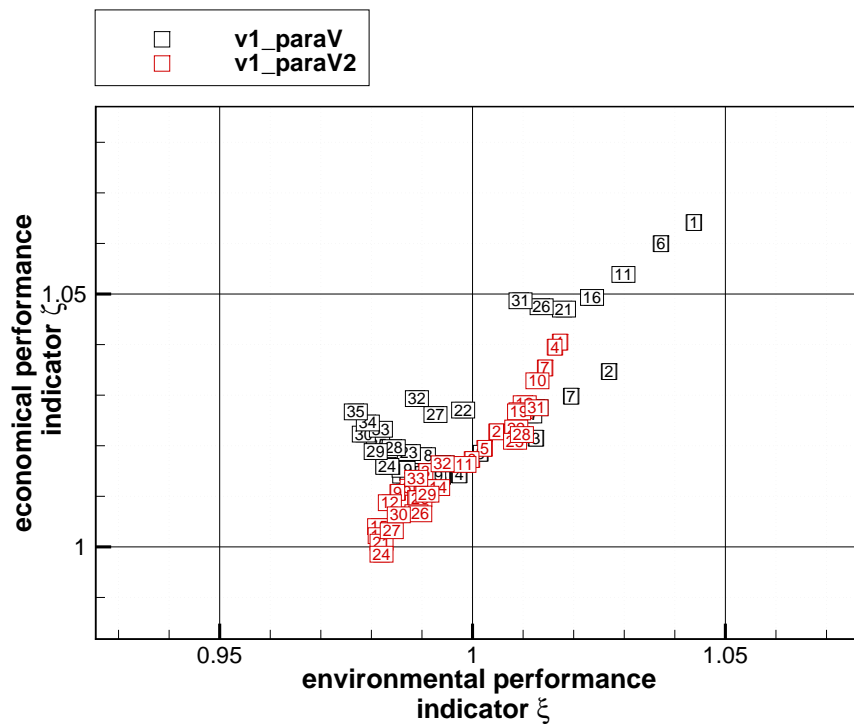
v-1: Parameter study 2Figure A.30: *v-1* vehicle layout: parameter variation 2

Λ_w x_w / l_f	8.0	9.0	10.0
0.30	1	2	3
0.31	4	5	6
0.32	7	8	9
0.33	10	11	12
0.34	13	14	15
0.35	16	17	18
0.36	19	20	21
0.37	22	23	24
0.38	25	26	27
0.39	28	29	30
0.40	31	32	33

Table A.16: *v-1* variants: parameter variation 2 (wing location & aspect ratio)

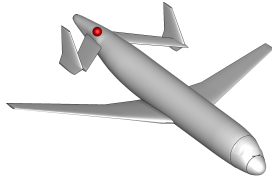
design	weights			performance			
	OEW [kg]	MTOW [kg]	MLW [kg]	flight speed [km/h]	block time [h]	balanced field length [m]	fuel req. [kg]
1	36377.19	59363.00	56787.15	813.34	4.32	1944.69	10990.1
2	37229.29	59897.10	57457.98	813.34	4.31	1937.43	10672.0
3	38270.04	60698.44	58362.05	813.34	4.31	1998.73	10432.6
4	36504.89	59464.22	56899.76	813.34	4.32	1947.67	10963.6
5	37217.24	59842.58	57421.46	813.34	4.31	1931.49	10629.6
6	38236.39	60615.72	58300.51	813.34	4.31	2007.38	10383.6
7	36450.07	59361.27	56817.19	813.34	4.32	1937.18	10915.4
8	37257.62	59839.95	57437.40	813.34	4.31	1941.90	10586.6
9	38375.39	60717.68	58418.42	813.34	4.31	2022.93	10346.5
10	36509.03	59380.24	56853.38	813.34	4.32	1935.09	10875.5
11	37391.11	59937.76	57550.66	813.34	4.31	1957.04	10550.9
12	38458.93	60753.59	58474.87	813.34	4.31	2038.43	10298.9
13	36447.67	59266.89	56762.34	813.34	4.32	1922.47	10823.5
14	37275.24	59755.76	57397.15	813.34	4.31	1967.89	10484.8
15	38353.98	60579.66	58330.64	813.34	4.31	2048.80	10229.9
16	36589.10	59373.65	56884.01	813.34	4.32	1927.34	10788.8
17	37445.77	59865.84	57533.10	813.34	4.31	1989.16	10424.3
18	38606.79	60769.25	58547.44	813.34	4.31	2072.92	10166.7
19	36731.95	59497.63	57016.24	813.34	4.32	1933.97	10769.9
20	37609.65	60006.59	57683.89	813.34	4.31	2002.73	10401.2
21	38706.42	60833.06	58626.66	813.34	4.31	2085.41	10130.9
22	36719.40	59440.11	56978.09	813.34	4.31	1932.78	10725.0
23	37595.02	59946.64	57643.47	813.34	4.31	2010.88	10355.9
24	38728.85	60812.03	58624.67	813.34	4.31	2094.91	10087.4
25	36719.33	59395.85	56952.93	813.34	4.31	1940.70	10680.8
26	37746.57	60075.65	57782.21	813.34	4.31	2021.47	10333.3
27	38921.40	61048.82	58842.54	813.34	4.31	2106.96	10131.7
28	36864.77	59544.38	57100.11	813.34	4.31	1947.94	10683.9
29	37794.75	60171.29	57857.46	813.34	4.31	2028.77	10380.8
30	38918.59	61088.89	58864.11	813.34	4.31	2111.18	10174.5
31	36963.76	59708.34	57236.08	813.34	4.32	1954.53	10748.8
32	37948.71	60396.45	58051.77	813.34	4.31	2035.34	10452.0
33	39192.04	61438.95	59181.28	813.34	4.31	2122.25	10251.1

Table A.17: *v-1* global aircraft parameters: parameter variation 2

v-1: ResultsFigure A.31: *v-1* aircraft noise induced awakeningsFigure A.32: *v-1* performance indicators: parameter variation 1 & 2

Vehicle category *v-1-1*

v-1-1: Parameter study 1



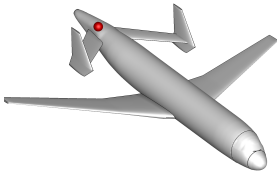
x_{vtp}/l_{htp} \ A_w	105.0	110.0	115.0	120.0	125.0
0.1	1	2	3	4	5
0.2	6	7	8	9	10
0.3	11	12	13	14	15
0.4	16	17	18	19	20
0.5	21	22	23	24	25
0.6	26	27	28	29	30
0.7	31	32	33	34	35
0.8	36	37	38	39	40

Figure A.33: *v-1-1* vehicle layout: parameter variation 1

Table A.18: *v-1-1* variants: parameter variation 1 (VTP positioning & wing area)

design	weights			performance			
	OEW [kg]	MTOW [kg]	MLW [kg]	flight speed [km/h]	block time [h]	balanced field length [m]	fuel req. [kg]
1	38313.44	60593.42	58321.15	813.34	4.31	2147.14	10284.2
2	38750.14	61056.41	58772.86	813.34	4.31	2078.69	10310.5
3	39188.52	61530.30	59231.55	813.34	4.31	2014.70	10346.0
4	39663.31	62051.68	59733.04	813.34	4.31	1957.28	10392.6
5	40113.87	62545.89	60208.51	813.34	4.31	1903.91	10436.3
6	38312.45	60591.51	58319.62	813.34	4.31	2147.08	10283.3
7	38750.14	61056.41	58772.86	813.34	4.31	2078.75	10310.5
8	39187.12	61527.95	59229.58	813.34	4.31	2014.69	10345.1
9	39661.42	62048.64	59730.43	813.34	4.31	1957.24	10391.5
10	40112.11	62542.82	60205.99	813.34	4.31	1903.97	10435.0
11	38311.28	60589.46	58317.93	813.34	4.31	2147.02	10282.4
12	38750.14	61056.41	58772.86	813.34	4.31	2078.79	10310.5
13	39185.51	61525.38	59227.40	813.34	4.31	2014.68	10344.1
14	39660.28	62046.43	59728.69	813.34	4.31	1957.22	10390.4
15	40110.42	62539.86	60203.57	813.34	4.31	1903.99	10433.7
16	38310.41	60587.79	58316.58	813.34	4.31	2146.97	10281.6
17	38750.14	61056.41	58772.86	813.34	4.31	2078.76	10310.5
18	39183.90	61522.77	59225.20	813.34	4.31	2014.67	10343.1
19	39659.24	62044.28	59726.99	813.34	4.31	1957.21	10389.3
20	40108.86	62536.96	60201.20	813.34	4.31	1903.95	10432.3
21	38308.86	60585.43	58314.57	813.34	4.31	2146.90	10280.8
22	38750.14	61056.41	58772.86	813.34	4.31	2078.74	10310.5
23	39182.82	61520.68	59223.52	813.34	4.31	2014.67	10342.1
24	39657.68	62041.60	59724.77	813.34	4.31	1957.19	10388.2
25	40107.17	62533.97	60198.76	813.34	4.31	1903.91	10431.0
26	38307.53	60583.21	58312.71	813.34	4.31	2146.84	10279.9
27	38750.14	61056.41	58772.86	813.34	4.31	2078.72	10310.5
28	39181.19	61518.04	59221.31	813.34	4.31	2014.66	10341.1
29	39656.02	62038.94	59722.54	813.34	4.31	1957.16	10387.2
30	40105.75	62531.31	60196.65	813.34	4.31	1903.87	10429.8
31	38307.23	60582.10	58311.94	813.34	4.31	2146.81	10279.1
32	38750.14	61056.41	58772.86	813.34	4.31	2078.70	10310.5
33	39179.81	61515.75	59219.41	813.34	4.31	2014.66	10340.2
34	39655.33	62037.25	59721.28	813.34	4.31	1957.16	10386.2
35	40104.31	62528.63	60194.46	813.34	4.31	1903.83	10428.6
36	38306.14	60580.22	58310.43	813.34	4.31	2146.75	10278.3
37	38750.14	61056.41	58772.86	813.34	4.31	2078.68	10310.5
38	39178.55	61513.49	59217.54	813.34	4.31	2014.66	10339.2
39	39653.85	62034.71	59719.19	813.34	4.31	1957.14	10385.1
40	40103.14	62526.27	60192.61	813.34	4.31	1903.81	10427.4

Table A.19: *v-1-1* global aircraft parameters: parameter variation 1

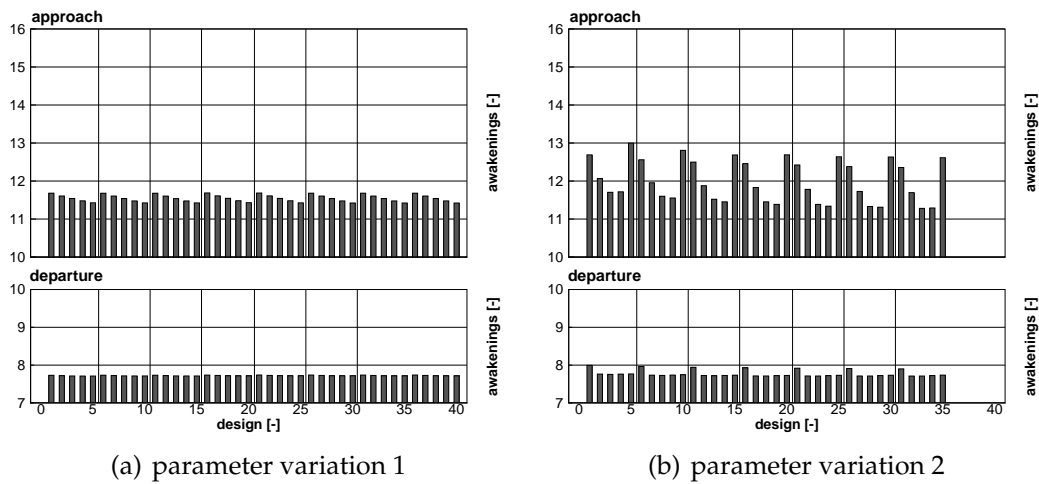
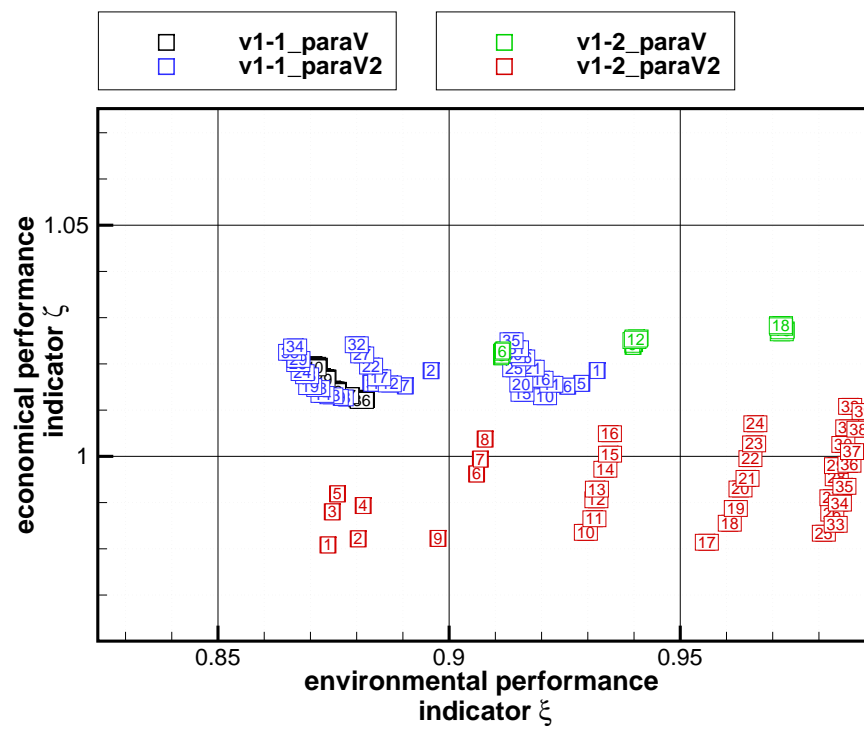
***v-1-1*: Parameter study 2**

x_{VTP} A_w	1.5	2.0	2.5	3.0	3.5
100.000	1	2	3	4	5
105.000	6	7	8	9	10
110.000	11	12	13	14	15
115.000	16	17	18	19	20
120.000	21	22	23	24	25
125.000	26	27	28	29	30
130.000	31	32	33	34	35

Figure A.34: *v-1-1* vehicle layout: parameter variation 2Table A.20: *v-1-1* variants: parameter variation 2 (wing area & VTP positioning)

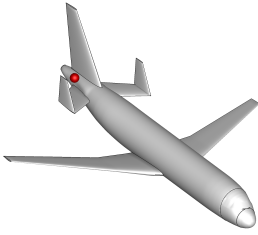
design	weights			performance			
	OEW [kg]	MTOW [kg]	MLW [kg]	flight speed [km/h]	block time [h]	balanced field length [m]	fuel req. [kg]
1	38027.56	60355.80	58063.08	813.34	4.31	2228.44	10332.5
2	38020.97	60349.50	58056.66	813.34	4.31	2228.13	10332.8
3	38013.71	60303.26	58027.19	813.34	4.31	2227.78	10293.8
4	38007.91	60298.08	58021.85	813.34	4.31	2227.49	10294.4
5	38003.90	60294.45	58017.46	813.34	4.31	2227.21	10294.8
6	38328.96	60645.57	58357.50	813.34	4.31	2147.83	10320.9
7	38323.59	60641.55	58352.91	813.34	4.31	2147.57	10322.2
8	38318.01	60598.68	58326.14	813.34	4.31	2147.26	10284.9
9	38313.62	60596.36	58323.01	813.34	4.31	2147.02	10287.0
10	38309.90	60595.38	58320.94	813.34	4.31	2146.78	10289.7
11	38763.80	61104.66	58806.02	813.34	4.31	2079.38	10345.1
12	38761.51	61103.67	58805.09	813.34	4.31	2079.26	10346.4
13	38752.34	61058.31	58774.76	813.34	4.31	2078.66	10310.2
14	38754.90	61065.27	58779.96	813.34	4.31	2078.32	10314.6
15	38756.47	61070.48	58783.41	813.34	4.31	2077.87	10318.3
16	39193.93	61565.93	59254.05	813.34	4.31	2015.84	10376.2
17	39193.76	61570.58	59256.73	813.34	4.31	2015.33	10381.1
18	39193.91	61537.34	59237.88	813.34	4.31	2014.76	10347.7
19	39194.41	61544.31	59242.15	813.34	4.31	2014.28	10354.1
20	39196.36	61554.36	59248.85	813.34	4.31	2013.81	10362.2
21	39665.09	62079.40	59749.48	813.34	4.31	1958.27	10418.5
22	39665.88	62087.14	59754.28	813.34	4.31	1957.80	10425.5
23	39669.05	62059.86	59740.20	813.34	4.31	1957.34	10395.1
24	39674.04	62074.80	59750.96	813.34	4.31	1957.04	10405.0
25	39678.83	62091.39	59762.57	813.34	4.31	1956.71	10416.8
26	40111.12	62564.25	60217.74	813.34	4.31	1904.85	10457.4
27	40115.35	62577.91	60227.40	813.34	4.31	1904.53	10466.8
28	40120.71	62556.05	60217.21	813.34	4.31	1903.79	10439.6
29	40127.28	62576.10	60231.64	813.34	4.31	1902.52	10453.1
30	40135.45	62599.55	60248.61	813.34	4.31	1901.17	10468.3
31	40493.86	62985.62	60622.28	813.34	4.31	1853.23	10496.0
32	40500.73	63005.74	60636.85	813.34	4.31	1851.95	10509.3
33	40507.48	62989.01	60630.28	813.34	4.31	1850.56	10485.8
34	40520.30	63018.78	60652.91	813.34	4.31	1849.46	10502.7
35	40532.07	63050.19	60675.98	813.34	4.31	1848.24	10522.4

Table A.21: *v-1-1* global aircraft parameters: parameter variation 2

***v-1-1*: Results**Figure A.35: *v-1-1* aircraft noise induced awakeningsFigure A.36: *v-1-1* performance indicators: parameter variation 1 & 2

Vehicle category *v-1-2*

v-1-2: Parameter study 1



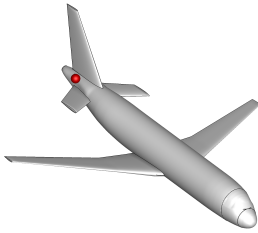
$\nu A_{vtp,1} - A_{vtp,2-3}$	20-8	22-7	24-6	26-5	28-4	30-3
-30.0	1	2	3	4	5	6
-35.0	7	8	9	10	11	12
-40.0	13	14	15	16	17	18
-45.0	19	20	21	22	23	24
-50.0	25	26	27	28	29	30

Figure A.37: *v-1-2* vehicle layout: parameter variation 1

Table A.22: *v-1-2* variants: parameter variation 1 (HTP sweep angle & VTP area ratios)

design	weights			performance			
	OEW [kg]	MTOW [kg]	MLW [kg]	flight speed [km/h]	block time [h]	balanced field length [m]	fuel req. [kg]
1	38656.28	61108.99	58762.21	813.34	4.31	2067.88	10456.9
2	38625.95	61073.49	58728.91	813.34	4.31	2066.97	10451.8
3	38653.19	61102.79	58757.36	813.34	4.31	2067.65	10453.8
4	38728.37	61187.84	58838.36	813.34	4.31	2069.65	10463.7
5	38710.46	61164.15	58817.11	813.34	4.31	2069.08	10457.9
6	38739.63	61194.49	58846.63	813.34	4.31	2069.83	10459.1
7	38776.78	61251.43	58895.42	813.34	4.31	2071.09	10478.9
8	38746.12	61215.04	58861.45	813.34	4.31	2070.14	10473.2
9	38772.91	61245.74	58890.31	813.34	4.31	2070.83	10477.1
10	38850.48	61336.09	58975.60	813.34	4.31	2072.98	10489.9
11	38830.64	61310.00	58952.06	813.34	4.31	2072.34	10483.6
12	38858.33	61339.56	58980.99	813.34	4.31	2073.08	10485.5
13	38917.29	61421.69	59053.12	813.34	4.31	2075.12	10508.6
14	38884.44	61382.83	59016.81	813.34	4.31	2074.09	10502.6
15	38910.58	61412.76	59045.17	813.34	4.31	2074.78	10506.4
16	38987.16	61502.07	59129.22	813.34	4.31	2076.60	10519.2
17	38964.37	61472.75	59102.63	813.34	4.31	2075.89	10512.6
18	38994.51	61504.96	59134.04	813.34	4.31	2076.48	10514.7
19	39063.12	61597.31	59216.18	813.34	4.31	2078.11	10538.4
20	39032.61	61561.25	59182.45	813.34	4.31	2077.16	10532.9
21	39057.91	61590.48	59210.05	813.34	4.31	2077.63	10536.8
22	39129.83	61675.50	59289.32	813.34	4.31	2079.20	10549.9
23	39112.32	61652.56	59268.70	813.34	4.31	2078.60	10544.5
24	39139.74	61681.87	59297.18	813.34	4.31	2079.13	10546.4
25	39231.09	61799.17	59403.40	813.34	4.31	2081.62	10572.3
26	39196.38	61758.35	59365.20	813.34	4.31	2080.53	10566.2
27	39220.51	61786.44	59391.59	813.34	4.31	2080.96	10570.2
28	39294.41	61873.20	59472.93	813.34	4.31	2082.63	10583.0
29	39274.13	61847.09	59449.30	813.34	4.31	2081.93	10577.2
30	39299.37	61874.10	59475.55	813.34	4.31	2082.41	10579.0

Table A.23: *v-1-2* global aircraft parameters: parameter variation 1

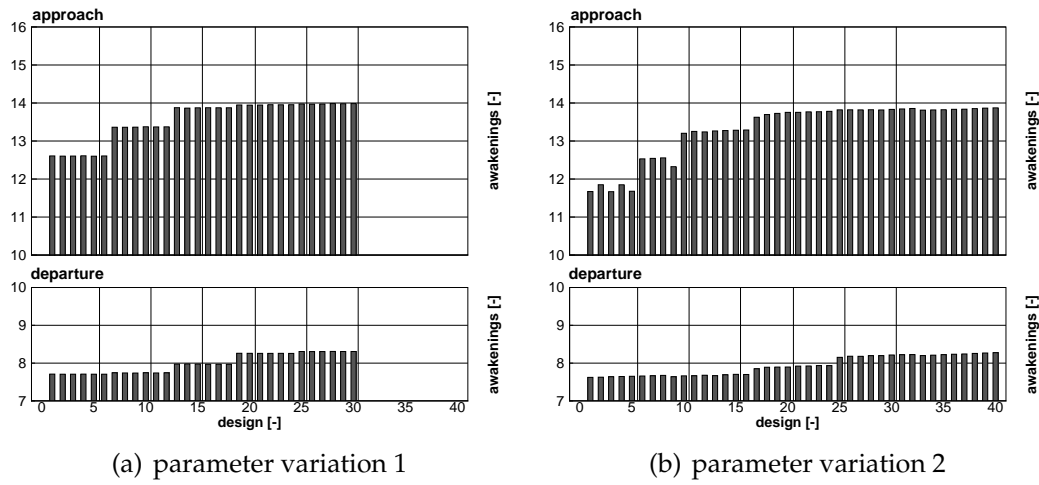
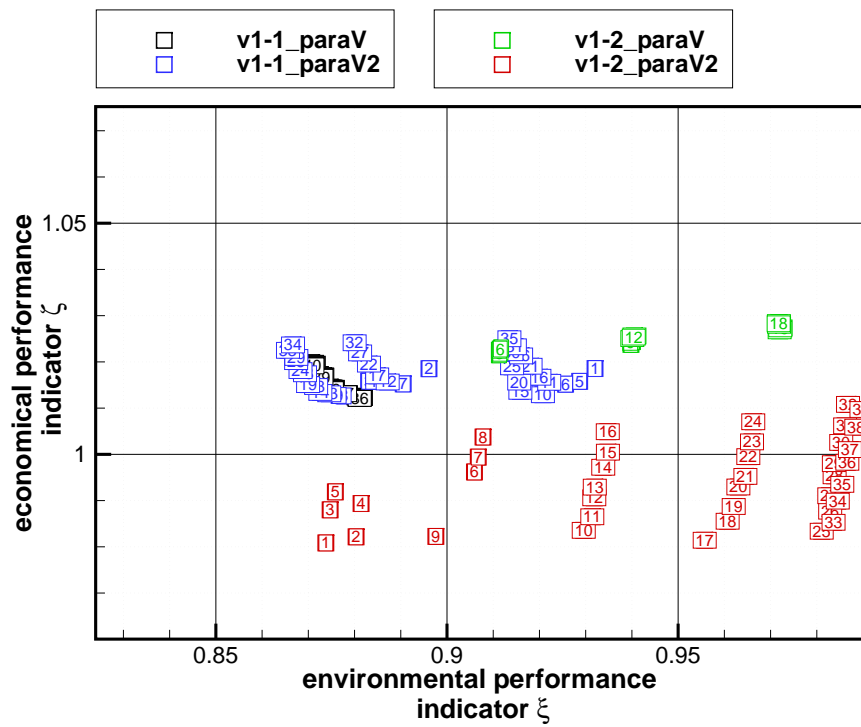
***v-1-2*: Parameter study 2**

$\nu \backslash A_{htp}$	22.0	24.0	26.0	28.0	30.0	32.0	34.0	36.0
-30.0	1	2	3	4	5	6	7	8
-35.0	9	10	11	12	13	14	15	16
-40.0	17	18	19	20	21	22	23	24
-45.0	25	26	27	28	29	30	31	32
-50.0	33	34	35	36	37	38	39	40

Figure A.38: *v-1-2* vehicle layout: parameter variation 2Table A.24: *v-1-2* variants: parameter variation 2 (HTP sweep angle & area)

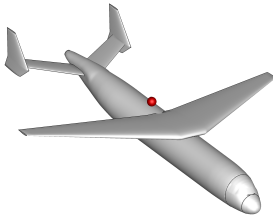
design	weights			performance			
	OEW [kg]	MTOW [kg]	MLW [kg]	flight speed [km/h]	block time [h]	balanced field length [m]	fuel req. [kg]
1	37905.33	59830.60	57710.61	813.34	4.31	2043.33	9929.5
2	37983.13	59919.90	57795.05	813.34	4.31	2046.05	9941.0
3	38063.82	60077.46	57919.51	813.34	4.31	2049.04	10017.9
4	38143.64	60169.04	58005.88	813.34	4.31	2051.86	10029.6
5	38177.75	60236.22	58058.84	813.34	4.31	2053.62	10062.7
6	38262.99	60375.36	58174.99	813.34	4.31	2056.73	10116.6
7	38342.47	60493.65	58276.68	813.34	4.31	2059.65	10155.4
8	38430.04	60635.63	58395.54	813.34	4.31	2062.84	10209.8
9	37976.10	59915.43	57789.43	813.34	4.31	2045.07	9943.6
10	38060.87	60010.75	57880.28	813.34	4.31	2047.93	9954.1
11	38148.57	60132.46	57987.34	813.34	4.31	2050.91	9988.1
12	38240.19	60274.77	58107.76	813.34	4.31	2054.05	10038.8
13	38283.21	60346.83	58167.35	813.34	4.31	2055.90	10067.9
14	38375.90	60492.85	58290.64	813.34	4.31	2059.13	10121.2
15	38464.64	60620.25	58401.64	813.34	4.31	2062.25	10159.8
16	38562.76	60773.10	58531.04	813.34	4.31	2065.67	10214.6
17	38054.57	59975.08	57857.18	813.34	4.31	2046.03	9924.7
18	38151.30	60121.81	57982.46	813.34	4.31	2049.73	9974.8
19	38249.00	60255.83	58100.76	813.34	4.31	2053.43	10011.1
20	38351.95	60410.02	58233.07	813.34	4.31	2057.04	10062.3
21	38403.73	60489.88	58300.92	813.34	4.31	2059.01	10090.4
22	38505.85	60644.15	58432.94	813.34	4.31	2062.43	10142.5
23	38600.88	60776.16	58549.20	813.34	4.31	2065.63	10179.5
24	38705.96	60934.27	58684.64	813.34	4.31	2069.17	10232.5
25	38142.18	60083.47	57956.71	813.34	4.31	2047.41	9945.5
26	38249.66	60243.36	58093.92	813.34	4.31	2051.25	9997.9
27	38358.82	60390.24	58224.73	813.34	4.31	2055.11	10035.7
28	38473.41	60556.10	58368.49	813.34	4.31	2059.13	10086.9
29	38530.94	60645.55	58444.54	813.34	4.31	2061.90	10118.9
30	38646.69	60816.47	58591.93	813.34	4.31	2066.05	10174.0
31	38760.03	60970.62	58728.49	813.34	4.31	2070.14	10214.8
32	38877.22	61143.81	58877.68	813.34	4.31	2074.06	10270.8
33	38237.89	60199.51	58063.79	813.34	4.31	2048.34	9965.9
34	38355.59	60371.76	58212.83	813.34	4.31	2052.88	10020.4
35	38476.70	60533.48	58357.19	813.34	4.31	2057.15	10061.0
36	38604.26	60717.84	58517.45	813.34	4.31	2061.48	10117.8
37	38676.54	60822.64	58608.31	813.34	4.31	2064.41	10150.3
38	38803.90	61007.93	58768.59	813.34	4.31	2068.75	10208.3
39	38930.90	61177.99	58920.30	813.34	4.31	2073.09	10251.3
40	39058.79	61320.34	59056.47	813.34	4.31	2077.37	10265.8

Table A.25: *v-1-2* global aircraft parameters: parameter variation 2

v-1-2: ResultsFigure A.39: *v-1-2* aircraft noise induced awakeningsFigure A.40: *v-1-1* and *v-1-2* performance indicators: parameter variation 1 & 2

Vehicle category $v2$

v -2: Parameter study 1



$A_w \Lambda_w$	7.0	8.0	9.0	10.0	11.0
100.0	1	2	3	4	5
105.0	6	7	8	9	10
110.0	11	12	13	14	15
115.0	16	17	18	19	20
120.0	21	22	23	24	25
125.0	26	27	28	29	30
130.0	31	32	33	34	35

Figure A.41: v -2 vehicle layout: parameter variation 1

Table A.26: v -2 variants: parameter variation 1 (wing area & aspect ratio)

design	weights			performance			
	OEW [kg]	MTOW [kg]	MLW [kg]	flight speed [km/h]	block time [h]	balanced field length [m]	fuel req. [kg]
1	36123.08	59485.01	56747.07	813.34	4.32	2189.10	11366.2
2	36777.28	59641.45	57117.80	813.34	4.32	2099.06	10868.4
3	37593.73	60124.01	57744.15	813.34	4.31	2148.47	10534.5
4	38609.82	60993.99	58677.26	813.34	4.31	2236.04	10388.4
5	39540.07	61735.57	59500.02	813.34	4.31	2317.54	10199.7
6	36328.30	59585.53	56892.72	813.34	4.32	2091.89	11261.5
7	37059.34	59849.49	57357.75	813.34	4.32	2013.23	10794.4
8	37909.14	60383.66	58027.37	813.34	4.31	2072.32	10478.8
9	38882.26	61213.12	58919.22	813.34	4.31	2155.67	10335.1
10	39955.42	62122.55	59899.14	813.34	4.31	2239.39	10171.4
11	36557.66	59728.24	57072.70	813.34	4.32	2007.81	11174.8
12	37374.09	60107.61	57640.19	813.34	4.32	1939.56	10737.8
13	38211.54	60636.64	58301.79	813.34	4.31	2002.74	10429.3
14	39239.18	61538.39	59258.33	813.34	4.31	2085.45	10303.4
15	40440.20	62596.54	60377.70	813.34	4.31	2169.20	10160.6
16	36717.34	59798.36	57181.31	813.34	4.32	1925.68	11085.3
17	37640.68	60312.35	57871.56	813.34	4.31	1869.14	10675.9
18	38535.72	60916.91	58601.03	813.34	4.31	1939.88	10385.4
19	39617.37	61894.17	59623.68	813.34	4.31	2021.32	10281.0
20	40880.23	63024.46	60810.79	813.34	4.31	2103.76	10148.5
21	36986.23	60000.01	57411.87	813.34	4.32	1861.81	11018.0
22	37932.82	60591.90	58156.24	813.34	4.31	1810.32	10663.3
23	38901.54	61399.83	59033.77	813.34	4.31	1884.54	10502.5
24	39996.52	62308.39	60022.86	813.34	4.31	1962.66	10316.1
25	41245.86	63423.20	61195.20	813.34	4.31	2042.24	10181.6
26	37285.35	60304.49	57714.23	813.34	4.32	1811.40	11023.4
27	38216.72	60891.31	58449.05	813.34	4.31	1757.76	10678.8
28	39282.74	61815.79	59434.83	813.34	4.31	1833.04	10537.3
29	40411.69	62764.58	60461.41	813.34	4.31	1909.70	10357.1
30	41725.83	63955.45	61705.12	813.34	4.31	1988.96	10233.9
31	37496.07	60521.37	57928.54	813.34	4.32	1758.61	11029.5
32	38535.13	61236.12	58782.65	813.34	4.32	1712.54	10705.2
33	39653.23	62225.65	59827.28	813.34	4.31	1784.98	10576.7
34	40853.85	63254.84	60930.99	813.34	4.31	1861.58	10405.2
35	42192.25	64453.05	62189.15	813.34	4.31	1939.42	10265.0

Table A.27: v -2 global aircraft parameters: parameter variation 1

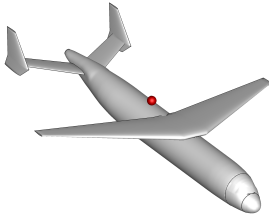
v-2: Parameter study 2

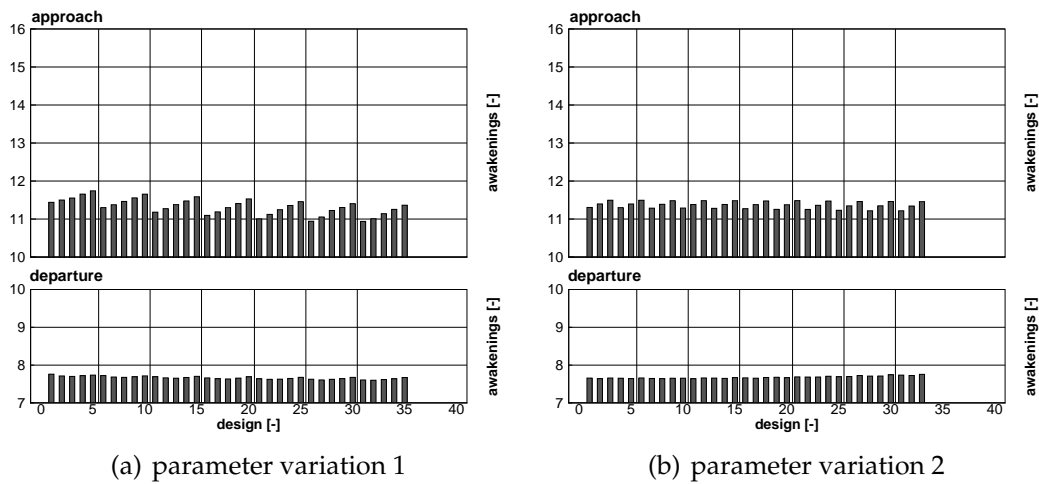
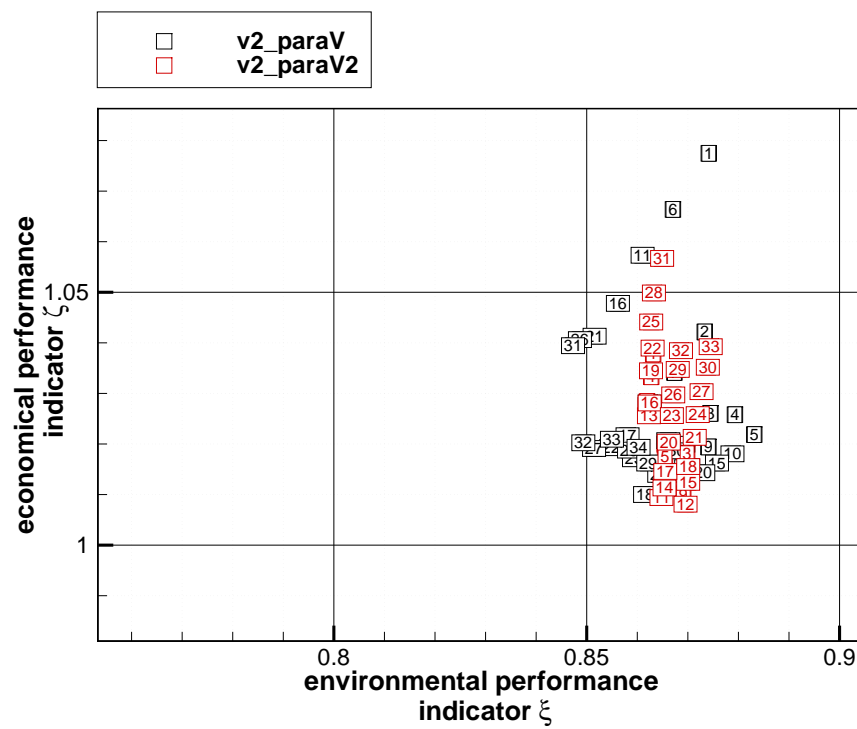
Figure A.42: v-2 vehicle layout: parameter variation 2

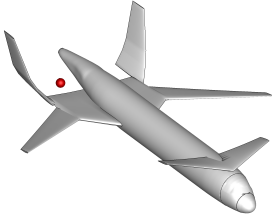
Λ_w	8.0	9.0	10.0
x_w / l_f			
0.30	1	2	3
0.31	4	5	6
0.32	7	8	9
0.33	10	11	12
0.34	13	14	15
0.35	16	17	18
0.36	19	20	21
0.37	22	23	24
0.38	25	26	27
0.39	28	29	30
0.40	31	32	33

Table A.28: v-2 variants: parameter variation 2 (wing location & aspect ratio)

design	weights			performance			
	OEW [kg]	MTOW [kg]	MLW [kg]	flight speed [km/h]	block time [h]	balanced field length [m]	fuel req. [kg]
1	37249.41	60133.81	57601.61	813.34	4.32	1939.88	10888.6
2	38010.22	60553.53	58168.06	813.34	4.31	1969.97	10547.5
3	39049.79	61426.48	59112.81	813.34	4.31	2051.31	10380.9
4	37259.39	60082.02	57576.33	813.34	4.32	1933.24	10826.9
5	38107.64	60598.34	58235.08	813.34	4.31	1982.12	10494.9
6	39117.08	61435.75	59147.01	813.34	4.31	2064.00	10322.9
7	37210.37	59970.60	57491.65	813.34	4.32	1925.91	10764.5
8	38100.02	60526.38	58191.18	813.34	4.31	1988.97	10430.6
9	39054.93	61300.59	59043.14	813.34	4.31	2067.98	10249.9
10	37313.43	60050.08	57581.25	813.34	4.32	1931.54	10740.9
11	38113.63	60478.53	58169.62	813.34	4.31	1992.50	10369.1
12	39193.04	61394.19	59155.65	813.34	4.31	2076.69	10205.4
13	37345.94	60049.90	57595.10	813.34	4.32	1932.52	10708.2
14	38232.66	60610.22	58295.83	813.34	4.31	2000.66	10381.8
15	39258.84	61513.58	59252.20	813.34	4.31	2082.63	10259.0
16	37374.09	60107.63	57640.03	813.34	4.32	1939.56	10737.8
17	38211.60	60636.69	58301.89	813.34	4.31	2002.74	10429.3
18	39239.29	61539.05	59258.12	813.34	4.31	2085.45	10304.0
19	37488.77	60294.28	57795.83	813.34	4.32	1955.89	10809.7
20	38344.92	60840.33	58475.28	813.34	4.31	2008.39	10499.7
21	39397.25	61765.92	59455.26	813.34	4.31	2090.02	10372.9
22	37501.22	60362.63	57840.38	813.34	4.32	1967.56	10865.7
23	38454.75	61016.63	58622.89	813.34	4.31	2011.17	10566.1
24	39499.79	61925.18	59590.27	813.34	4.31	2091.71	10429.6
25	37565.53	60487.79	57938.96	813.34	4.32	1980.41	10926.5
26	38534.12	61150.88	58733.73	813.34	4.31	2009.41	10621.0
27	39637.80	62120.01	59760.48	813.34	4.31	2090.40	10486.4
28	37653.37	60637.75	58062.18	813.34	4.32	2000.48	10988.6
29	38685.94	61365.14	58920.93	813.34	4.31	2008.92	10683.4
30	39811.76	62352.98	59968.11	813.34	4.31	2088.04	10545.5
31	37783.19	60838.89	58232.81	813.34	4.32	2025.29	11059.9
32	38723.89	61455.07	58988.40	813.34	4.32	2008.07	10735.4
33	39882.30	62482.71	60072.37	813.34	4.31	2081.32	10604.6

Table A.29: v-2 global aircraft parameters: parameter variation 2

v-2: ResultsFigure A.43: *v*-2 aircraft noise induced awakeningsFigure A.44: *v*-2 performance indicators: parameter variation 1 & 2

Vehicle category v - x 

$x_{vtp}/l_w A_w$	120.0	125.0	130.0	135.0	140.0
0.1	1	2	3	4	5
0.2	6	7	8	9	10
0.3	11	12	13	14	15
0.4	16	17	18	19	20
0.5	21	22	23	24	25
0.6	26	27	28	29	30
0.7	31	32	33	34	35
0.8	36	37	38	39	40

Figure A.45: v - x vehicle layout: parameter variationTable A.30: v - x variants: parameter variation (VTP positioning & wing area)

design	weights			performance			
	OEW [kg]	MTOW [kg]	MLW [kg]	flight speed [km/h]	block time [h]	balanced field length [m]	fuel req. [kg]
1	37073.01	59590.29	55614.06	813.34	4.31	2025.73	10521.5
2	37266.30	59739.31	55795.78	813.34	4.31	1961.05	10477.2
3	37393.54	59802.68	55905.06	813.34	4.31	1912.19	10413.4
4	38111.19	60599.20	56644.98	813.34	4.31	1867.93	10492.2
5	38531.42	61083.84	57083.13	813.34	4.31	1820.65	10556.7
6	37072.59	59587.35	55613.01	813.34	4.31	2026.02	10519.0
7	37268.48	59739.62	55797.43	813.34	4.31	1961.43	10475.4
8	37393.82	59800.96	55904.70	813.34	4.31	1912.53	10411.4
9	38111.19	60599.20	56644.98	813.34	4.31	1868.26	10492.2
10	38532.78	61082.79	57083.87	813.34	4.31	1821.01	10554.2
11	37073.73	59586.11	55613.39	813.34	4.31	2026.38	10516.6
12	37270.81	59741.25	55798.78	813.34	4.31	1961.82	10474.7
13	37396.50	59801.87	55907.00	813.34	4.31	1912.96	10409.6
14	38111.19	60599.20	56644.98	813.34	4.31	1868.58	10492.2
15	38535.87	61083.43	57086.27	813.34	4.31	1821.42	10551.8
16	37075.28	59585.47	55614.37	813.34	4.31	2026.75	10514.4
17	37271.36	59739.69	55798.79	813.34	4.31	1962.17	10472.6
18	37397.24	59800.69	55907.13	813.34	4.31	1913.31	10407.7
19	38111.19	60599.20	56644.98	813.34	4.31	1868.91	10492.2
20	38538.20	61083.36	57088.00	813.34	4.31	1821.80	10549.4
21	37077.55	59585.42	55616.10	813.34	4.31	2027.14	10512.1
22	37273.88	59740.15	55800.63	813.34	4.31	1962.56	10470.5
23	37399.41	59801.13	55908.82	813.34	4.31	1913.73	10406.0
24	38111.19	60599.20	56644.98	813.34	4.31	1869.24	10492.2
25	38538.61	61081.29	57087.60	813.34	4.31	1822.15	10546.9
26	37077.78	59583.28	55615.54	813.34	4.31	2027.47	10509.7
27	37275.36	59739.75	55801.67	813.34	4.31	1962.93	10468.6
28	37399.70	59799.30	55908.36	813.34	4.31	1914.08	10403.8
29	38111.19	60599.20	56644.98	813.34	4.31	1869.56	10492.2
30	38541.39	61081.68	57089.95	813.34	4.31	1822.55	10544.5
31	37077.96	59581.35	55616.13	813.34	4.31	2027.83	10507.6
32	37276.30	59738.96	55802.30	813.34	4.31	1963.29	10466.9
33	37403.72	59801.75	55912.06	813.34	4.31	1914.54	10402.3
34	38111.19	60599.20	56644.98	813.34	4.31	1869.89	10492.2
35	38543.63	61081.65	57091.49	813.34	4.31	1822.94	10542.3
36	37079.64	59580.41	55616.20	813.34	4.31	2028.18	10505.0
37	37281.38	59742.24	55806.78	813.34	4.31	1963.77	10465.1
38	37404.39	59800.62	55911.64	813.34	4.31	1914.89	10400.5
39	38111.51	60599.51	56645.30	813.34	4.31	1870.23	10492.2
40	38547.39	61083.11	57094.69	813.34	4.31	1823.38	10540.0

Table A.31: v - x global aircraft parameters: parameter variation 1

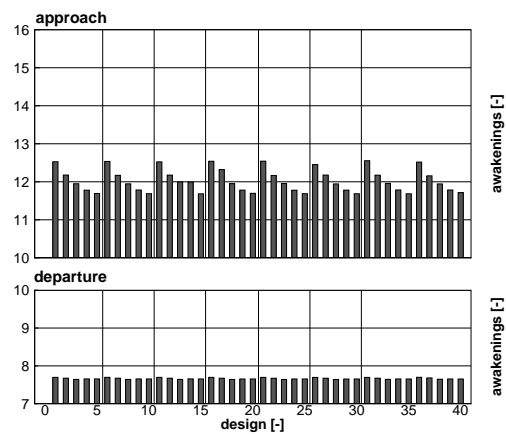


Figure A.46: v - x aircraft noise induced awakenings: parameter variation

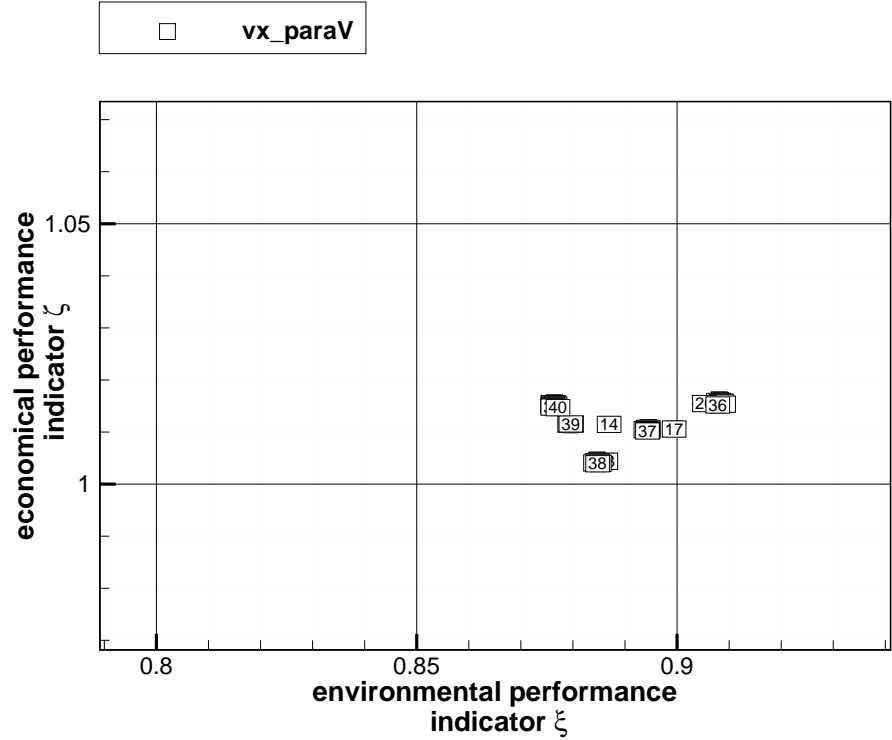


Figure A.47: v - x performance indicators: parameter variation

Vehicle Variant Ranking

scenario: eco-env. weighting	vehicle group	best design variant	2nd best	3rd best	4th best	worst
0: 0.0 - 1.0	vr	<i>vr : paraV(5)</i>	<i>vr : paraV(4)</i>	<i>vr : paraV(10)</i>	<i>vr : paraV(15)</i>	<i>vr : paraV2(31)</i>
	v0	<i>v0 : paraV2(3)</i>	<i>v0 : paraV2(6)</i>	<i>v0 : paraV2(9)</i>	<i>v0 : paraV2(2)</i>	<i>v0 : paraV(31)</i>
	v1	<i>v1 - 2 : paraV2(1)</i>	<i>v1 - 2 : paraV2(17)</i>	<i>v1 - 2 : paraV2(2)</i>	<i>v1 - 2 : paraV2(9)</i>	<i>v1 : paraV(1)</i>
	v2	<i>v2 : paraV2(12)</i>	<i>v2 : paraV2(11)</i>	<i>v2 : paraV2(9)</i>	<i>v2 : paraV(18)</i>	<i>v2 : paraV(1)</i>
	vx	<i>vx : paraV(38)</i>	<i>vx : paraV(33)</i>	<i>vx : paraV(28)</i>	<i>vx : paraV(23)</i>	<i>vx : paraV(1)</i>
1: 0.1 - 0.9	vr	<i>vr : paraV(5)</i>	<i>vr : paraV(4)</i>	<i>vr : paraV(15)</i>	<i>vr : paraV(10)</i>	<i>vr : paraV2(31)</i>
	v0	<i>v0 : paraV2(3)</i>	<i>v0 : paraV2(6)</i>	<i>v0 : paraV2(9)</i>	<i>v0 : paraV2(2)</i>	<i>v0 : paraV(1)</i>
	v1	<i>v1 - 2 : paraV2(1)</i>	<i>v1 - 2 : paraV2(2)</i>	<i>v1 - 2 : paraV2(9)</i>	<i>v1 - 2 : paraV2(3)</i>	<i>v1 : paraV(1)</i>
	v2	<i>v2 : paraV2(12)</i>	<i>v2 : paraV2(11)</i>	<i>v2 : paraV(18)</i>	<i>v2 : paraV2(9)</i>	<i>v2 : paraV(1)</i>
	vx	<i>vx : paraV(38)</i>	<i>vx : paraV(28)</i>	<i>vx : paraV(33)</i>	<i>vx : paraV(23)</i>	<i>vx : paraV(1)</i>
2: 0.2 - 0.8	vr	<i>vr : paraV(20)</i>	<i>vr : paraV(5)</i>	<i>vr : paraV(15)</i>	<i>vr : paraV2(3)</i>	<i>vr : paraV2(31)</i>
	v0	<i>v0 : paraV2(3)</i>	<i>v0 : paraV2(6)</i>	<i>v0 : paraV2(2)</i>	<i>v0 : paraV2(9)</i>	<i>v0 : paraV(1)</i>
	v1	<i>v1 - 2 : paraV2(1)</i>	<i>v1 - 2 : paraV2(2)</i>	<i>v1 - 2 : paraV2(9)</i>	<i>v1 - 2 : paraV2(3)</i>	<i>v1 : paraV(1)</i>
	v2	<i>v2 : paraV(18)</i>	<i>v2 : paraV2(12)</i>	<i>v2 : paraV2(11)</i>	<i>v2 : paraV2(9)</i>	<i>v2 : paraV(1)</i>
	vx	<i>vx : paraV(38)</i>	<i>vx : paraV(28)</i>	<i>vx : paraV(33)</i>	<i>vx : paraV(23)</i>	<i>vx : paraV(1)</i>
3: 0.3 - 0.7	vr	<i>vr : paraV(20)</i>	<i>vr : paraV(5)</i>	<i>vr : paraV(19)</i>	<i>vr : paraV(24)</i>	<i>vr : paraV2(31)</i>
	v0	<i>v0 : paraV2(3)</i>	<i>v0 : paraV2(6)</i>	<i>v0 : paraV2(2)</i>	<i>v0 : paraV2(9)</i>	<i>v0 : paraV(1)</i>
	v1	<i>v1 - 2 : paraV2(1)</i>	<i>v1 - 2 : paraV2(2)</i>	<i>v1 - 2 : paraV2(3)</i>	<i>v1 - 2 : paraV2(9)</i>	<i>v1 : paraV(1)</i>
	v2	<i>v2 : paraV(18)</i>	<i>v2 : paraV2(11)</i>	<i>v2 : paraV2(12)</i>	<i>v2 : paraV2(14)</i>	<i>v2 : paraV(1)</i>
	vx	<i>vx : paraV(28)</i>	<i>vx : paraV(38)</i>	<i>vx : paraV(33)</i>	<i>vx : paraV(23)</i>	<i>vx : paraV(1)</i>
4: 0.4 - 0.6	vr	<i>vr : paraV(20)</i>	<i>vr : paraV(29)</i>	<i>vr : paraV(24)</i>	<i>vr : paraV(19)</i>	<i>vr : paraV2(31)</i>
	v0	<i>v0 : paraV2(3)</i>	<i>v0 : paraV2(6)</i>	<i>v0 : paraV2(2)</i>	<i>v0 : paraV2(5)</i>	<i>v0 : paraV(1)</i>
	v1	<i>v1 - 2 : paraV2(1)</i>	<i>v1 - 2 : paraV2(2)</i>	<i>v1 - 2 : paraV2(3)</i>	<i>v1 - 2 : paraV2(5)</i>	<i>v1 : paraV(1)</i>
	v2	<i>v2 : paraV(18)</i>	<i>v2 : paraV2(11)</i>	<i>v2 : paraV(32)</i>	<i>v2 : paraV(27)</i>	<i>v2 : paraV(1)</i>
	vx	<i>vx : paraV(28)</i>	<i>vx : paraV(38)</i>	<i>vx : paraV(23)</i>	<i>vx : paraV(18)</i>	<i>vx : paraV(6)</i>
5: 0.5 - 0.5	vr	<i>vr : paraV(20)</i>	<i>vr : paraV(29)</i>	<i>vr : paraV(30)</i>	<i>vr : paraV(35)</i>	<i>vr : paraV2(31)</i>
	v0	<i>v0 : paraV2(2)</i>	<i>v0 : paraV2(3)</i>	<i>v0 : paraV2(5)</i>	<i>v0 : paraV2(6)</i>	<i>v0 : paraV(1)</i>
	v1	<i>v1 - 2 : paraV2(1)</i>	<i>v1 - 2 : paraV2(2)</i>	<i>v1 - 2 : paraV2(3)</i>	<i>v1 - 2 : paraV2(5)</i>	<i>v1 : paraV(1)</i>
	v2	<i>v2 : paraV(32)</i>	<i>v2 : paraV(27)</i>	<i>v2 : paraV(18)</i>	<i>v2 : paraV(22)</i>	<i>v2 : paraV(1)</i>
	vx	<i>vx : paraV(28)</i>	<i>vx : paraV(38)</i>	<i>vx : paraV(23)</i>	<i>vx : paraV(18)</i>	<i>vx : paraV(6)</i>
6: 0.6 - 0.4	vr	<i>vr : paraV(20)</i>	<i>vr : paraV(29)</i>	<i>vr : paraV(30)</i>	<i>vr : paraV(35)</i>	<i>vr : paraV2(31)</i>
	v0	<i>v0 : paraV2(2)</i>	<i>v0 : paraV2(5)</i>	<i>v0 : paraV2(7)</i>	<i>v0 : paraV2(3)</i>	<i>v0 : paraV(1)</i>
	v1	<i>v1 - 2 : paraV2(1)</i>	<i>v1 - 2 : paraV2(3)</i>	<i>v1 - 2 : paraV2(2)</i>	<i>v1 - 2 : paraV2(5)</i>	<i>v1 : paraV(1)</i>
	v2	<i>v2 : paraV(32)</i>	<i>v2 : paraV(27)</i>	<i>v2 : paraV(22)</i>	<i>v2 : paraV(18)</i>	<i>v2 : paraV(1)</i>
	vx	<i>vx : paraV(35)</i>	<i>vx : paraV(30)</i>	<i>vx : paraV(25)</i>	<i>vx : paraV(15)</i>	<i>vx : paraV(31)</i>
7: 0.7 - 0.3	vr	<i>vr : paraV(20)</i>	<i>vr : paraV(35)</i>	<i>vr : paraV(29)</i>	<i>vr : paraV(30)</i>	<i>vr : paraV2(31)</i>
	v0	<i>v0 : paraV(31)</i>	<i>v0 : paraV(24)</i>	<i>v0 : paraV(32)</i>	<i>v0 : paraV2(7)</i>	<i>v0 : paraV(5)</i>
	v1	<i>v1 - 2 : paraV2(1)</i>	<i>v1 - 2 : paraV2(3)</i>	<i>v1 - 2 : paraV2(5)</i>	<i>v1 - 2 : paraV2(2)</i>	<i>v1 : paraV(1)</i>
	v2	<i>v2 : paraV(32)</i>	<i>v2 : paraV(27)</i>	<i>v2 : paraV(22)</i>	<i>v2 : paraV(33)</i>	<i>v2 : paraV(1)</i>
	vx	<i>vx : paraV(35)</i>	<i>vx : paraV(30)</i>	<i>vx : paraV(25)</i>	<i>vx : paraV(15)</i>	<i>vx : paraV(31)</i>
8: 0.8 - 0.2	vr	<i>vr : paraV(20)</i>	<i>vr : paraV(35)</i>	<i>vr : paraV(30)</i>	<i>vr : paraV(29)</i>	<i>vr : paraV2(31)</i>
	v0	<i>v0 : paraV(31)</i>	<i>v0 : paraV(32)</i>	<i>v0 : paraV(26)</i>	<i>v0 : paraV(24)</i>	<i>v0 : paraV(5)</i>
	v1	<i>v1 - 2 : paraV2(1)</i>	<i>v1 - 1 : paraV2(33)</i>	<i>v1 - 2 : paraV2(3)</i>	<i>v1 - 1 : paraV2(28)</i>	<i>v1 : paraV(1)</i>
	v2	<i>v2 : paraV(32)</i>	<i>v2 : paraV(27)</i>	<i>v2 : paraV(31)</i>	<i>v2 : paraV(26)</i>	<i>v2 : paraV(1)</i>
	vx	<i>vx : paraV(35)</i>	<i>vx : paraV(30)</i>	<i>vx : paraV(15)</i>	<i>vx : paraV(25)</i>	<i>vx : paraV(31)</i>
9: 0.9 - 0.1	vr	<i>vr : paraV(20)</i>	<i>vr : paraV(35)</i>	<i>vr : paraV(30)</i>	<i>vr : paraV(29)</i>	<i>vr : paraV2(31)</i>
	v0	<i>v0 : paraV(31)</i>	<i>v0 : paraV(26)</i>	<i>v0 : paraV(32)</i>	<i>v0 : paraV(24)</i>	<i>v0 : paraV(5)</i>
	v1	<i>v1 - 1 : paraV2(33)</i>	<i>v1 - 1 : paraV2(34)</i>	<i>v1 - 1 : paraV2(28)</i>	<i>v1 - 1 : paraV2(29)</i>	<i>v1 : paraV(1)</i>
	v2	<i>v2 : paraV(32)</i>	<i>v2 : paraV(31)</i>	<i>v2 : paraV(26)</i>	<i>v2 : paraV(27)</i>	<i>v2 : paraV(5)</i>
	vx	<i>vx : paraV(35)</i>	<i>vx : paraV(30)</i>	<i>vx : paraV(15)</i>	<i>vx : paraV(25)</i>	<i>vx : paraV(31)</i>
10: 1.0 - 0.0	vr	<i>vr : paraV(35)</i>	<i>vr : paraV(20)</i>	<i>vr : paraV(30)</i>	<i>vr : paraV(33)</i>	<i>vr : paraV2(31)</i>
	v0	<i>v0 : paraV(31)</i>	<i>v0 : paraV(26)</i>	<i>v0 : paraV(32)</i>	<i>v0 : paraV(21)</i>	<i>v0 : paraV(5)</i>
	v1	<i>v1 - 1 : paraV2(33)</i>	<i>v1 - 1 : paraV2(34)</i>	<i>v1 - 1 : paraV2(28)</i>	<i>v1 - 1 : paraV2(29)</i>	<i>v1 : paraV(1)</i>
	v2	<i>v2 : paraV(31)</i>	<i>v2 : paraV(26)</i>	<i>v2 : paraV(32)</i>	<i>v2 : paraV(27)</i>	<i>v2 : paraV(5)</i>
	vx	<i>vx : paraV(15)</i>	<i>vx : paraV(35)</i>	<i>vx : paraV(30)</i>	<i>vx : paraV(25)</i>	<i>vx : paraV(31)</i>

Table A.32: Scenario dependent vehicle variant ranking

Final Vehicle Design

Design V-Rx

Weights	
operational empty	39972.15
max. take-off	61783.15
max. landing	59712.31
Geometry	
max. width [m]	35.59
max. height [m]	12.12
max. length [m]	33.84
wheel base [m]	10.16
wheel guage [m]	7.96
max. rotation angle [°]	15.18
max. bank angle [°]	15.72

Table A.33: V-Rx: Global aircraft parameters

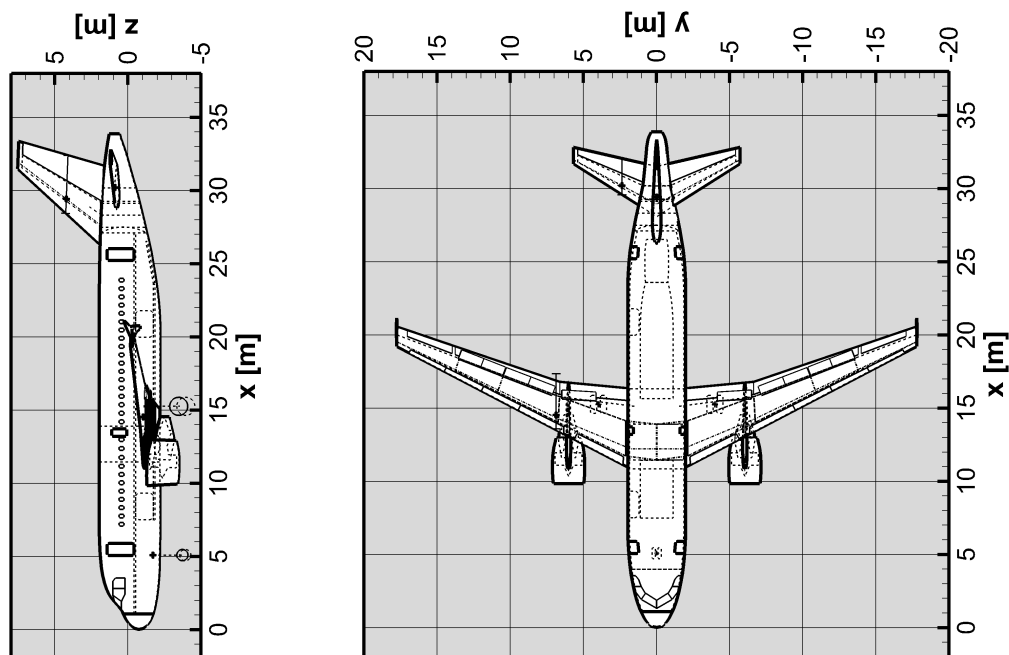


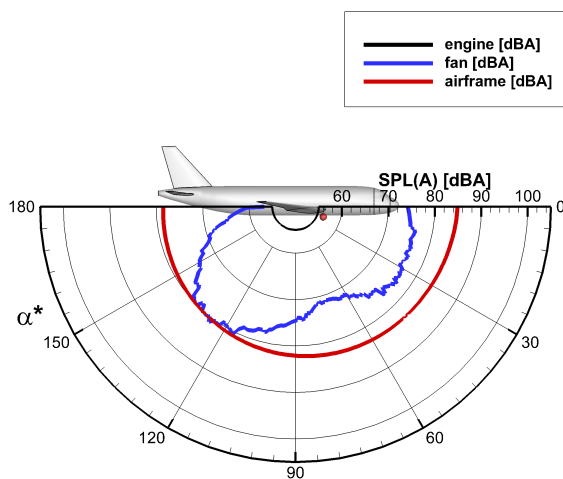
Figure A.48: V-Rx: Vehicle layout

Parameter	Wing	HTP	VTP
span width [m]	35.57	11.40	5.87
ref. area [m^2]	115.00	26.00	21.50
aspect ratio [-]	11.00	5.00	1.60
taper ratio [-]	0.25	0.33	0.35
root chord [m]	5.46	3.00	0.00
wing tip chord [m]	1.34	1.13	1.90
aerod. mean chord [m]	3.75	2.47	3.95
t/4 sweep angle [°]	24.52	27.91	37.20
leading edge sweep [°]	27.49	32.21	42.60
trailing edge sweep [°]	14.78	12.88	16.12
t/4 dihedral angle [°]	4.22	5.00	90.00

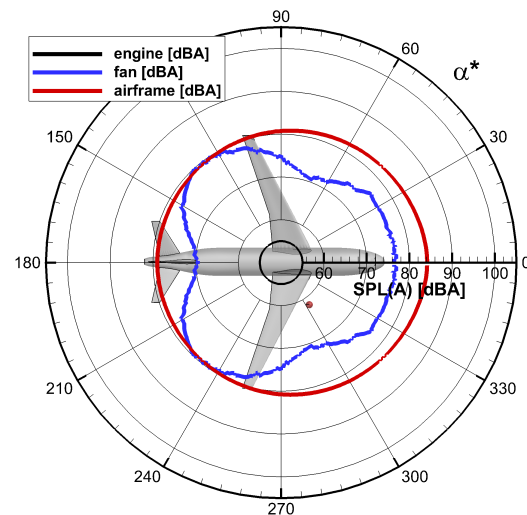
Table A.34: V-Rx: Lift and control surfaces

Design mission	
flight speed [km/h]	813.34
block time [h]	4.31
balanced field length [m]	2121.90
fuel req. [kg]	9815.24
Max. fuel mission	
max. fuel	17172.13
fuel req. [kg]	14492.63
range [km]	6614.00
Max. payload mission	
max. payload	16995.76
fuel req. [kg]	3146.62
range [km]	1249.47

Table A.35: V-Rx: Vehicle performance

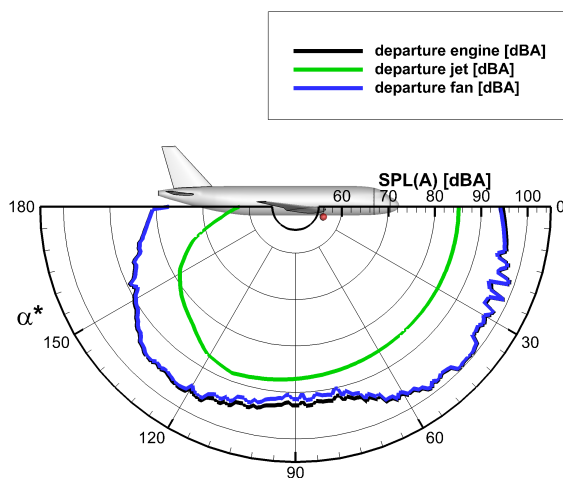


(a) polar directivity

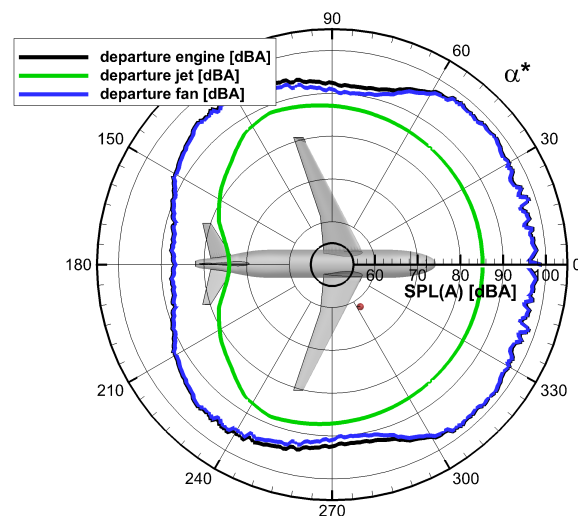


(b) lateral directivity

Figure A.49: V-Rx: Approach noise emission directivities



(a) polar directivity



(b) lateral directivity

Figure A.50: V-Rx: Take-off noise emission directivities

Design V-0

Weights	
operational empty	39649.72
max. take-off	62354.65
max. landing	59900.05
Geometry	
max. width [m]	34.66
max. height [m]	10.66
max. length [m]	37.37
wheel base [m]	12.70
wheel guage [m]	7.76
max. rotation angle [°]	16.04
max. bank angle [°]	13.99

Table A.36: V-0: Global aircraft parameters

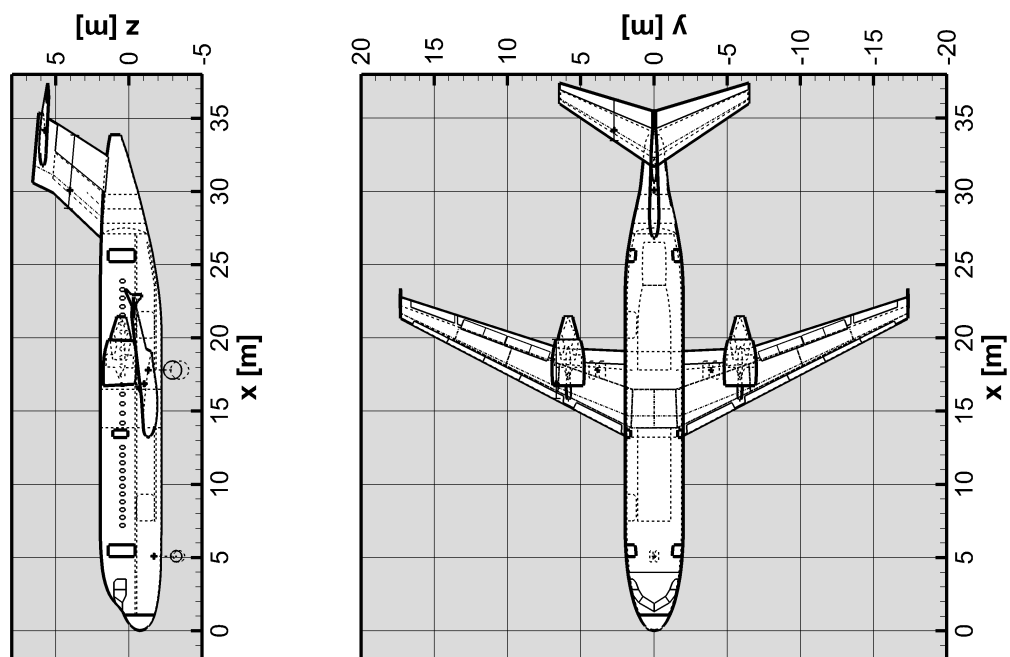


Figure A.51: V-0: Vehicle layout

Parameter	Wing	HTP	VTP
span width [m]	34.64	12.93	5.00
ref. area [m^2]	120.00	34.00	25.00
aspect ratio [-]	10.00	4.92	1.00
taper ratio [-]	0.25	0.38	0.86
root chord [m]	5.84	3.78	0.00
wing tip chord [m]	1.44	1.42	4.80
aerod. mean chord [m]	4.02	2.82	5.02
t/4 sweep angle [°]	24.20	29.52	37.46
leading edge sweep [°]	27.49	33.33	39.06
trailing edge sweep [°]	13.36	16.29	32.31
t/4 dihedral angle [°]	4.24	-2.92	90.00

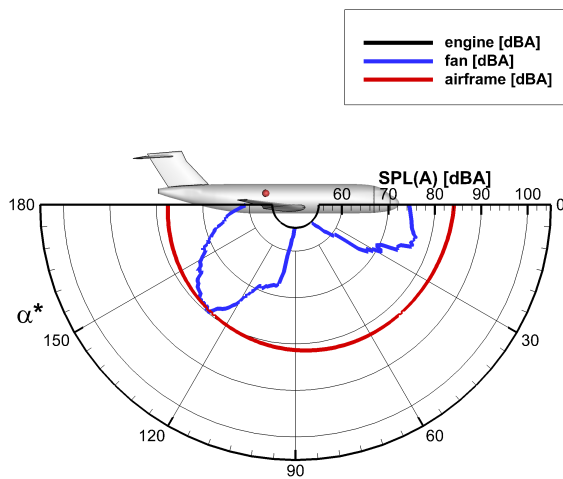
Table A.37: V-0: Lift and control surfaces

Design mission	
flight speed [km/h]	813.34
block time [h]	4.32
balanced field length [m]	1989.08
fuel req. [kg]	10709.18

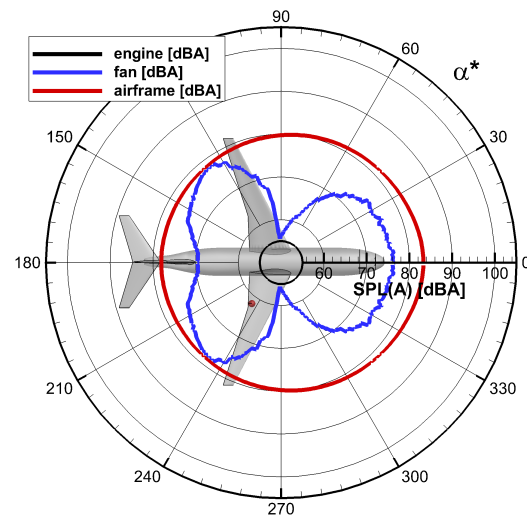
Max. fuel mission	
max. fuel	18462.90
fuel req. [kg]	15582.73
range [km]	6614.00

Max. payload mission	
max. payload	16995.76
fuel req. [kg]	3840.17
range [km]	1404.19

Table A.38: V-0: Vehicle performance

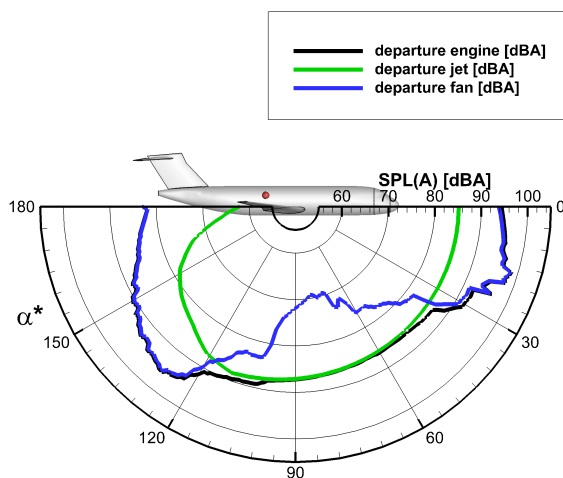


(a) polar directivity

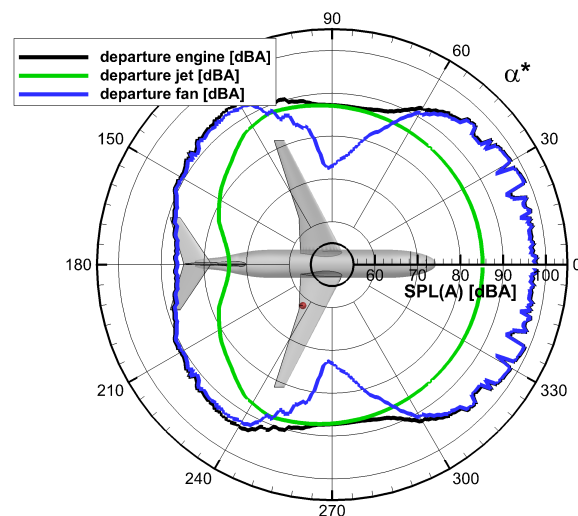


(b) lateral directivity

Figure A.52: V-0: Approach noise emission directivities



(a) polar directivity



(b) lateral directivity

Figure A.53: V-0: Take-off noise emission directivities

Design V-1

Weights	
operational empty	40109.25
max. take-off	62012.81
max. landing	59902.87
Geometry	
max. width [m]	34.81
max. height [m]	12.78
max. length [m]	35.22
wheel base [m]	12.16
wheel guage [m]	7.79
max. rotation angle [°]	16.89
max. bank angle [°]	15.98

Table A.39: V-1: Global aircraft parameters

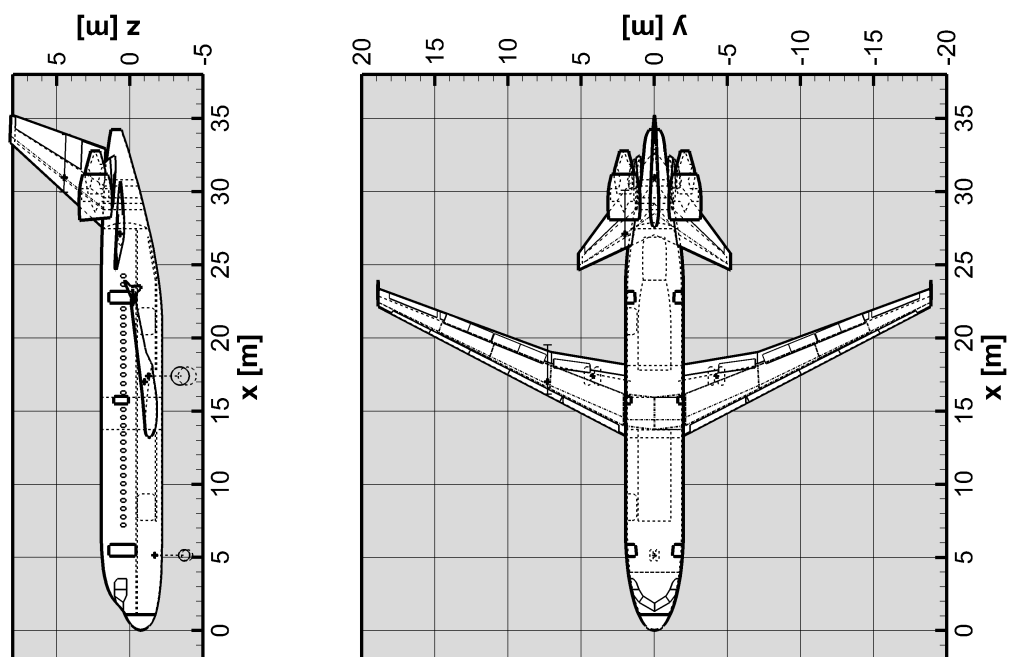


Figure A.54: V-1: Vehicle layout

Parameter	Wing	HTP	VTP
span width [m]	34.79	13.23	6.57
ref. area [m^2]	110.00	35.00	24.00
aspect ratio [-]	11.00	5.00	1.80
taper ratio [-]	0.25	0.74	0.35
root chord [m]	5.34	2.89	0.00
wing tip chord [m]	1.31	2.25	1.89
aerod. mean chord [m]	3.67	2.67	3.93
t/4 sweep angle [°]	24.51	-31.17	37.84
leading edge sweep [°]	27.49	-29.91	42.60
trailing edge sweep [°]	14.76	-34.77	19.67
t/4 dihedral angle [°]	4.22	5.00	90.00

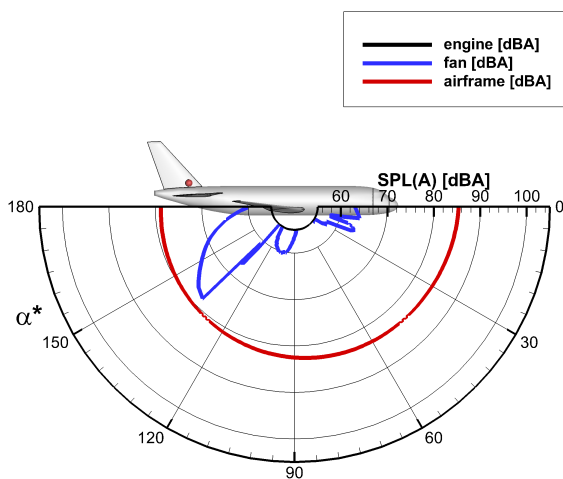
Table A.40: V-1: Lift and control surfaces

Design mission	
flight speed [km/h]	813.34
block time [h]	4.31
balanced field length [m]	2177.53
fuel req. [kg]	9907.81

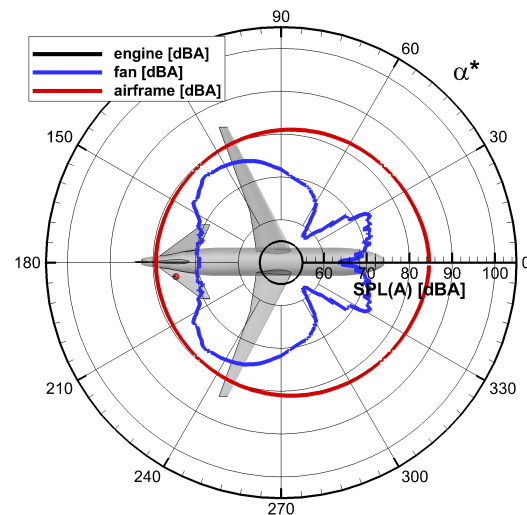
Max. fuel mission	
max. fuel	17115.63
fuel req. [kg]	14441.95
range [km]	6614.00

Max. payload mission	
max. payload	16995.76
fuel req. [kg]	3178.42
range [km]	1225.86

Table A.41: V-1: Vehicle performance

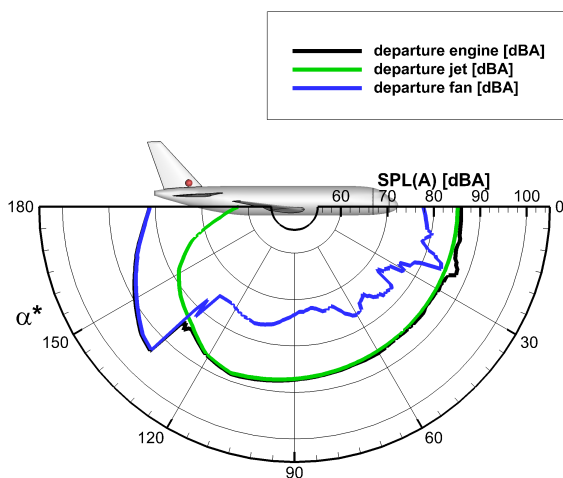


(a) polar directivity

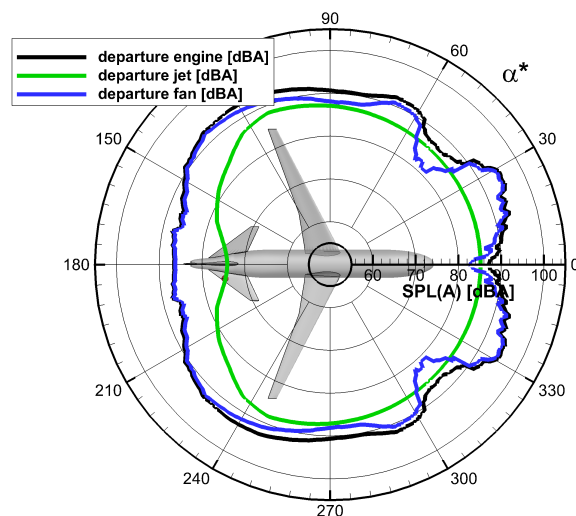


(b) lateral directivity

Figure A.55: V-1: Approach noise emission directivities



(a) polar directivity



(b) lateral directivity

Figure A.56: V-1: Take-off noise emission directivities

Design V-2

Weights	
operational empty	38005.21
max. take-off	60541.78
max. landing	58158.99
Geometry	
max. width [m]	31.64
max. height [m]	8.14
max. length [m]	36.61
wheel base [m]	12.38
wheel guage [m]	4.62
max. rotation angle [°]	10.94
max. bank angle [°]	20.63

Table A.42: V-2: Global aircraft parameters

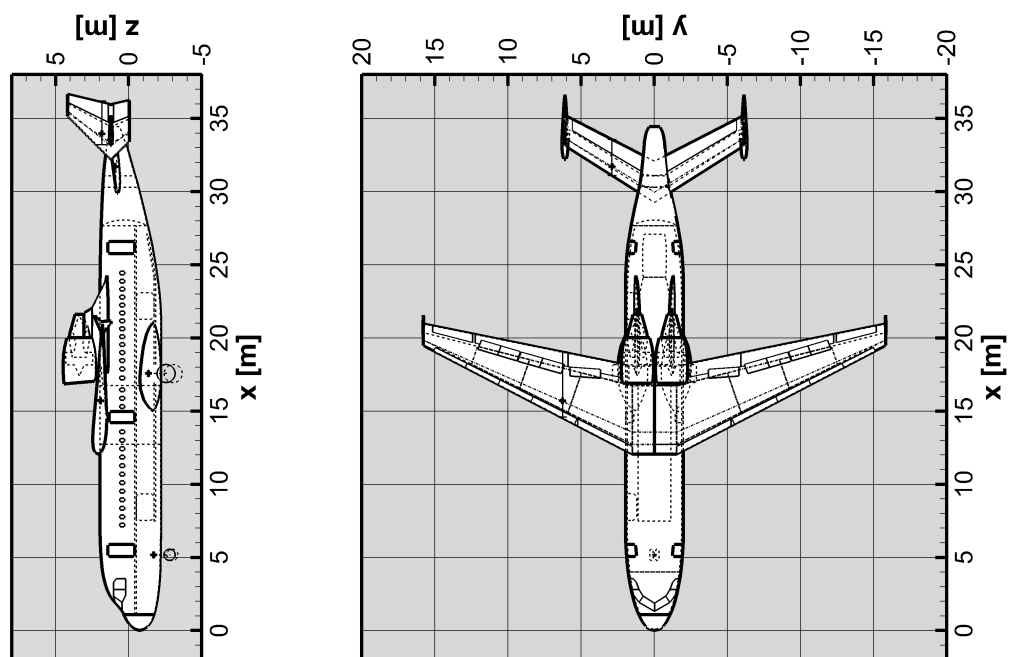


Figure A.57: V-2: Vehicle layout

Parameter	Wing	HTP	VTP
span width [m]	31.62	12.25	4.24
ref. area [m^2]	125.00	30.00	24.00
aspect ratio [-]	8.00	5.00	1.50
taper ratio [-]	0.25	0.74	0.40
root chord [m]	6.00	2.70	0.00
wing tip chord [m]	1.48	2.08	1.51
aerod. mean chord [m]	4.45	2.47	2.97
t/4 sweep angle [°]	23.29	30.98	17.98
leading edge sweep [°]	26.91	32.21	21.80
trailing edge sweep [°]	11.21	27.07	5.61
t/4 dihedral angle [°]	-0.70	5.00	90.00

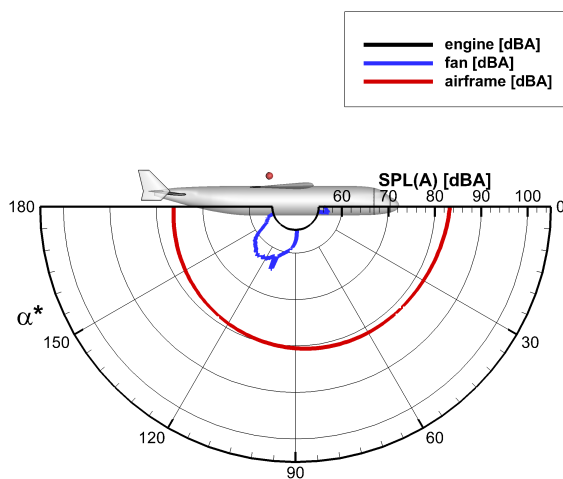
Table A.43: V-2: Lift and control surfaces

Design mission	
flight speed [km/h]	813.34
block time [h]	4.31
balanced field length [m]	1747.66
fuel req. [kg]	10540.80

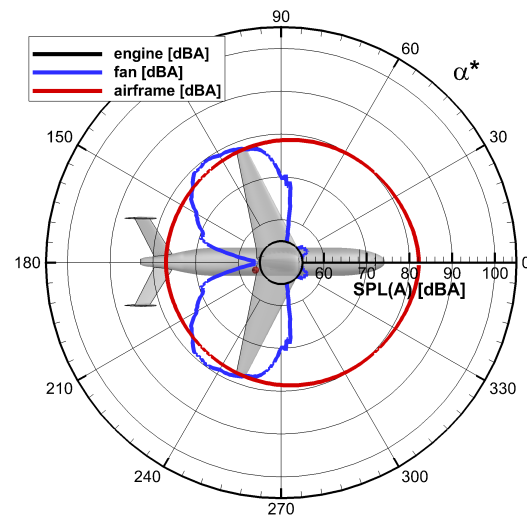
Max. fuel mission	
max. fuel	18137.88
fuel req. [kg]	15323.33
range [km]	6614.00

Max. payload mission	
max. payload	16995.76
fuel req. [kg]	3676.73
range [km]	1352.20

Table A.44: V-2: Vehicle performance

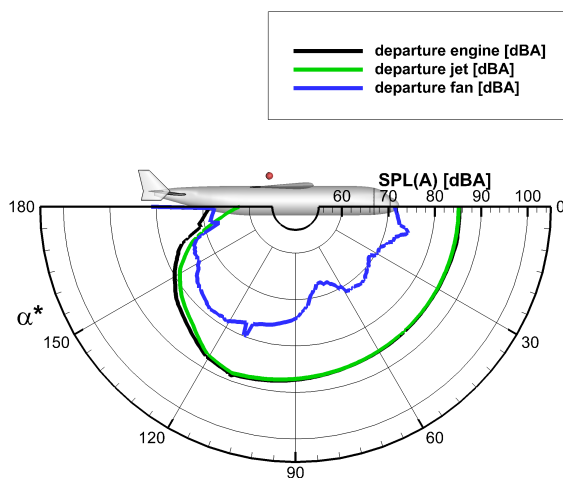


(a) polar directivity

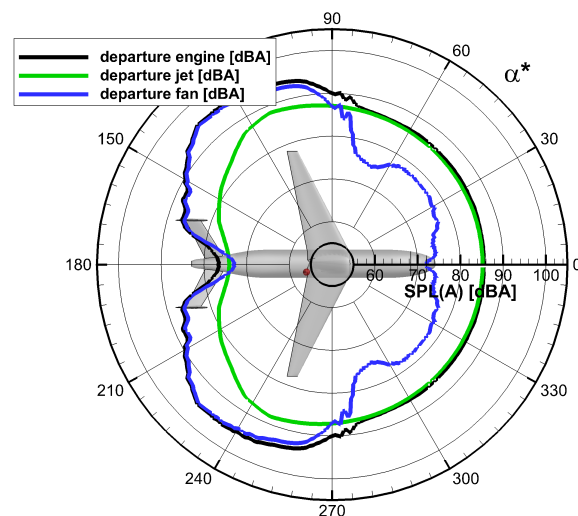


(b) lateral directivity

Figure A.58: V-2: Approach noise emission directivities



(a) polar directivity



(b) lateral directivity

Figure A.59: V-2: Take-off noise emission directivities

Design V-X

Weights	
operational empty	39165.80
max. take-off	61558.47
max. landing	57673.14
Geometry	
max. width [m]	31.77
max. height [m]	9.61
max. length [m]	34.64
wheel base [m]	18.37
wheel guage [m]	6.48
max. rotation angle [°]	20.54
max. bank angle [°]	17.39

Table A.45: V-X: Global aircraft parameters

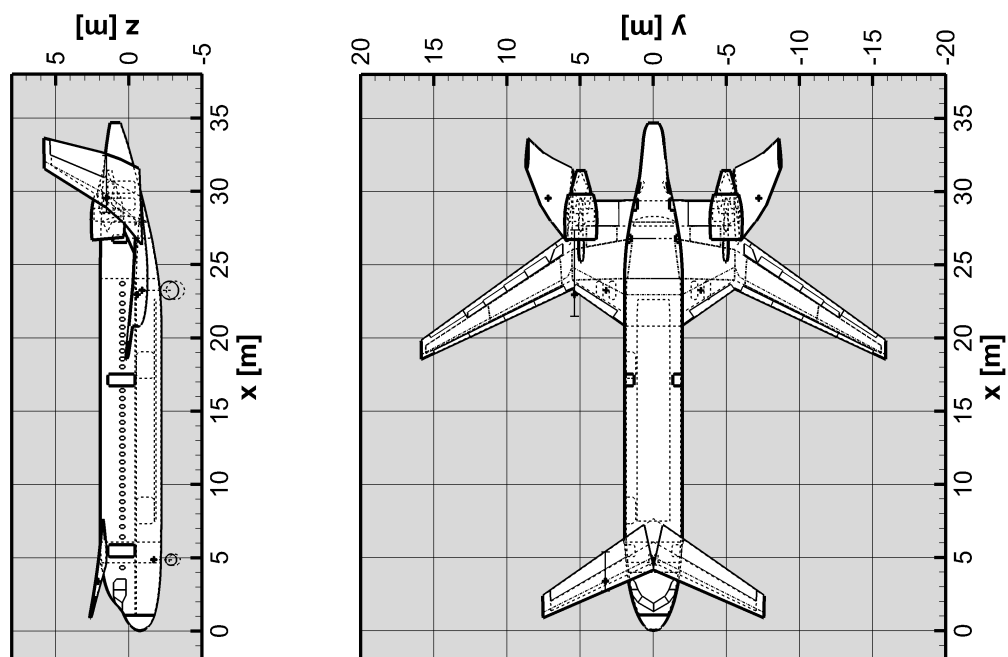


Figure A.60: V-X: Vehicle layout

Parameter	Wing	HTP	VTP
span width [m]	31.75	15.10	5.48
ref. area [m^2]	140.00	38.00	20.00
aspect ratio [-]	7.20	6.00	1.50
taper ratio [-]	0.15	0.44	0.40
root chord [m]	8.54	3.28	0.00
wing tip chord [m]	1.28	1.53	2.09
aerod. mean chord [m]	5.90	2.64	3.88
t/4 sweep angle [°]	-16.33	-26.44	31.35
leading edge sweep [°]	-9.25	-23.33	35.53
trailing edge sweep [°]	-34.35	-34.80	16.11
t/4 dihedral angle [°]	3.76	6.00	65.96

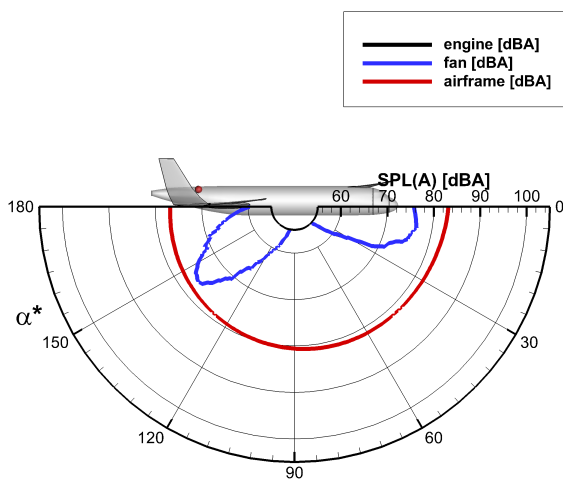
Table A.46: V-X: Lift and control surfaces

Design mission	
flight speed [km/h]	813.34
block time [h]	4.31
balanced field length [m]	1889.96
fuel req. [kg]	10396.91

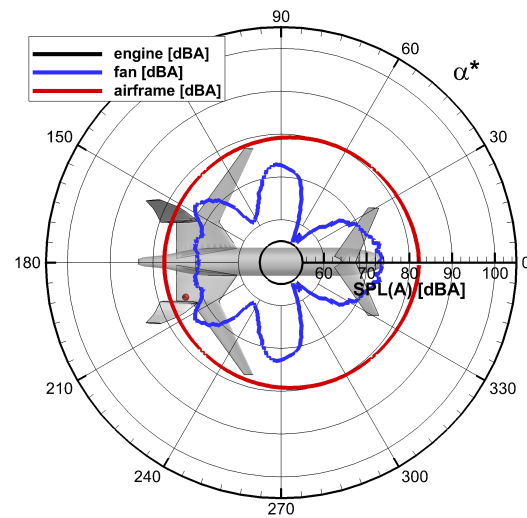
Max. fuel mission	
max. fuel	17735.18
fuel req. [kg]	14959.73
range [km]	6614.00

Max. payload mission	
max. payload	16995.76
fuel req. [kg]	3564.61
range [km]	1321.28

Table A.47: V-X: Vehicle performance

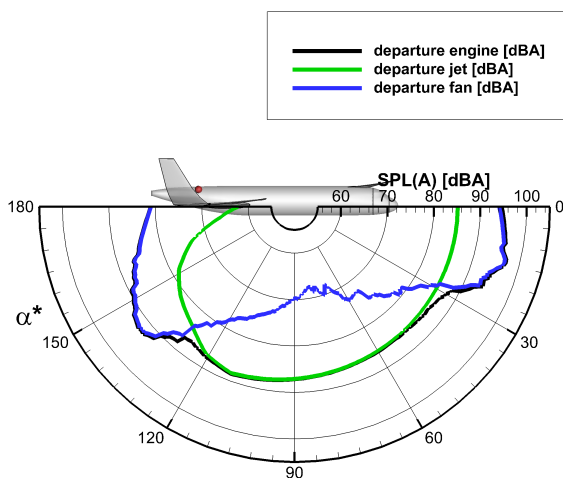


(a) polar directivity

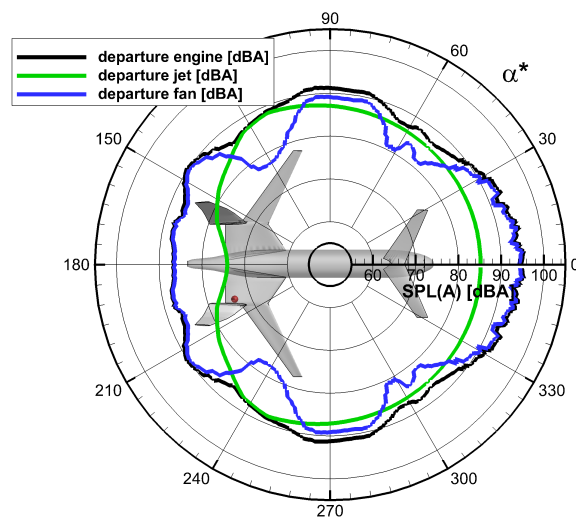


(b) lateral directivity

Figure A.61: V-X: Approach noise emission directivities



(a) polar directivity



(b) lateral directivity

Figure A.62: V-X: Take-off noise emission directivities

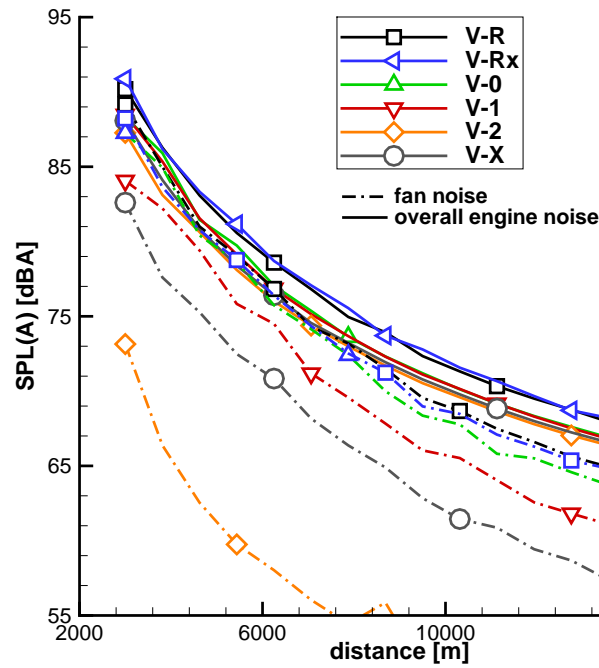


Figure A.63: Max. SPL(A) along departure flight ground track

Alternative weighting: STOL scenario

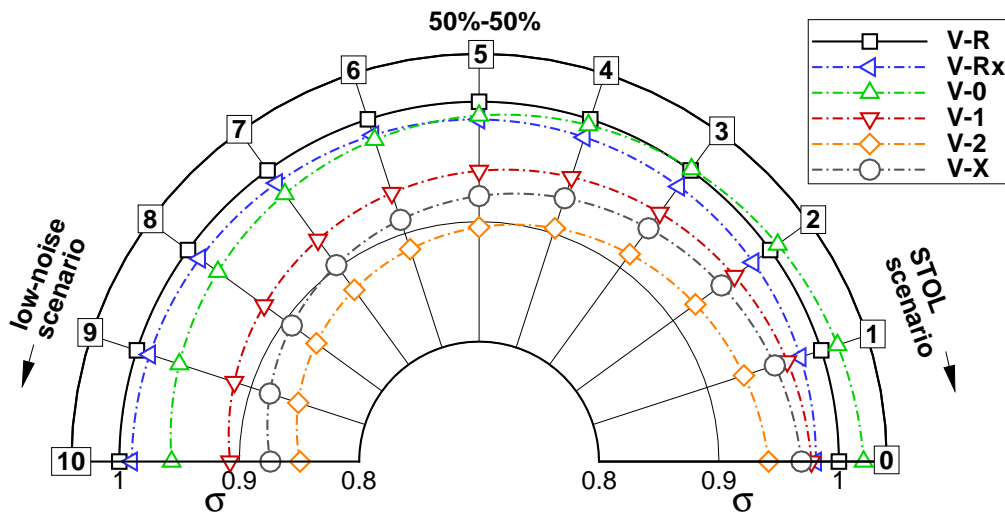


Figure A.64: Scenario dependent vehicle ranking: STOL scenario (60% weighting of field length req.)

B Additional Items

Equivalent jet model

According to Ref. [78], an equivalent jet model is implemented. The model is applied, whenever off-design operational conditions of the turbofan engine result in inverse jet velocities for core and bypass flow, i.e. $v_8 \leq v_{18}$.

For core and bypass flow, the velocity ratio η_v , the total Temperature ratio η_{Tt} , and area ratios η_A are known.

$$\begin{aligned}\eta_v &= \frac{v_{18}}{v_8} \\ \eta_{Tt} &= \frac{T_{t,18}}{T_{t,8}} \\ \eta_A &= \frac{A_{18}}{A_8}\end{aligned}\tag{B.1}$$

The area, velocity, and temperature of the equivalent jet can be defined as functions of these three ratios.

$$\begin{aligned}A_{eq} &= \pi \cdot A_8 \cdot \sqrt{(1 + \eta_v \cdot \eta_A) \cdot \frac{1 + \eta_v \cdot \eta_A \cdot \eta_T}{1 + \eta_v^2 \cdot \eta_A \cdot \eta_T}} \\ v_{eq} &= v_8 \cdot \frac{1 + \eta_v^2 \cdot \eta_A \cdot \eta_T}{1 + \eta_v \cdot \eta_A \cdot \eta_T} \\ T_{t,eq} &= T_{t,8} \cdot \frac{1 + \eta_v \cdot \eta_A}{1 + \eta_v \cdot \eta_A \cdot \eta_T}\end{aligned}\tag{B.2}$$

For this equivalent jet, the corresponding jet noise is then evaluated according to the implemented noise model for one single jet.

Multiple Flyover Evaluation

According to the definition in Ref. [90], continuous sound level L_{eq} can be predicted for N multiple flyover events.

$$L_{eq} = k \cdot \log_{10} \left(\frac{t_{ref}}{T} \cdot \sum_{i=1}^N g_i \cdot 10^{L_{E,i}/k} \right) + C\tag{B.3}$$

For the evaluation of L_{eq} at one observer location, all corresponding N flight movements within the reference time frame T are added up. In the definition of the L_{eq} , $L_{E,i}$ is a single event sound level for flight "i", t_{ref} is a reference time according to the definition of L_E , and g_i

is a time-dependent weighting function. For energy equivalent sound levels, the parameter k is equal to 10, otherwise the sound levels are not energy equivalent. Furthermore, an additional correction factor C can be applied. The following Tables list the available continuous sound levels for a PANAM simulation.

L_{eq}	$L_{E,i}$	k	C	time-dependent weighting g_i			
				0600-0700	0700-1900	1900-2200	2200-0600
$L_{eq(4)} - A$	L_{AZ}	13.3	0	1.5	1.5	1.5	0
$L_{eq(4)} - B$	L_{AZ}	13.3	0	1	1	1	5
L_{DN}	L_{AX}	10	0	10	1	1	10
L_{DEN}	L_{AX}	10	0	10	1	3.162	10
NEF	$EPNL$	10	-48.63	16.67	1	1	16.67

Table B.1: Standard output of continuous sound levels L_{eq} with corresponding parameter setting

L_{eq}	Nomenclature and reference time frame T
$L_{eq(4)} - A$	"aequivalenter Dauerschallpegel nach dem Gesetz zum Schutz gegen Fluglaerm", case A, 6 most busy months
$L_{eq(4)} - B$	"aequivalenter Dauerschallpegel nach dem Gesetz zum Schutz gegen Fluglaerm", case B, 6 most busy months
L_{DN}	Day-Night Average Sound Level, 1 year
L_{DEN}	Day-Evening-Night Sound Level, average day (yet not precisely defined)
NEF	Noise Exposure Forecast, 1 year

Table B.2: Continuous sound levels: Nomenclature

List of Figures

1.1	Ten thousands of people demonstrate in 2011 against Berlin's new international airport BBI ³	2
3.1	Noise prediction concept	16
3.2	Coordinate systems and emission angles	17
3.3	Impact of geometry parameters on noise emission (note: depicted is the cosine of the sweep angle)	28
3.4	Station numbering for turbofan and turbojet engines ¹⁰	29
3.5	Engine noise spectra, emission angle $\alpha^* = 40^\circ$	34
3.6	Engine noise spectra, emission angle $\alpha^* = 135^\circ$	34
3.7	PANAM acoustical analogous model	48
4.1	Reference Aircraft A319-100: PrADO payload range diagram	50
4.2	PrADO flight simulation for A319-100	51
4.3	SPL(A) emission directivities	52
4.4	Ground noise impact: Noise source ranking	53
4.5	Influence of source altitude and ground attenuation: max. levels and time-level-history	55
4.6	Influence of flight velocity: max. levels and time-level-history	57
4.7	Influence of configurational setting: max. level and time-level-history	58
4.8	Parchim Campaign 2006: Observer locations	60
4.9	Parchim Campaign 2006: departure <i>rec003</i>	61
4.10	Parchim Campaign 2006: approach <i>rec004</i>	63
4.11	Parchim Campaign: Sound Exposure Level (SEL)	64
5.1	Reference aircraft cabin layout	69
5.2	Design Evolution Chart	76
5.3	Performance indicators: all design variants	77
5.4	Scenario dependent vehicle ranking	81
5.5	Max. SPL(A) along approach flight ground track	82
5.6	Vehicle V-2: Engine noise SPL(A) directivities for geared turbofan versus scaled reference engine	85

5.7	CROR: vehicle layout	87
5.8	CROR: polar noise directivity	88
5.9	Frankfurt Airport: Departing and approaching Airtraffic routing ¹⁶	90
5.10	Helical Noise Abatement Procedure (HeNAP), Ref. [125]	91
5.11	Parametric Noise Prediction for Airspace Routing	92
6.1	Take-off SPL spectrum: <i>V-R</i> vs. <i>V-2</i>	94
A.1	Atmospheric sound absorption	107
A.2	Sound Pressure Level: A-weighting	107
A.3	Predicted ground attenuation for flyover event in 500 m altitude	107
A.4	EPNL predictions: Aircraft noise source ranking	108
A.5	Noise isocontour areas along simplified approach trajectory	108
A.6	Influence of flight velocity: noise emission directivity (in 80 m source distance)	109
A.7	Influence of configurational setting: noise emission directivity (in 80 m source distance)	110
A.8	<i>V-r</i> oew breakdown	112
A.9	<i>V-r</i> design mission mass breakdown	112
A.10	<i>V-r</i> geometry layout	112
A.11	<i>V-r</i> noise emission directivities	113
A.12	Parchim Flyover Campaign: Departure procedures	115
A.13	Parchim Flyover Campaign: Approach procedures	116
A.14	Predicted vs. measured departure SPL(A) time-history: ground mics along flight ground track	117
A.15	Predicted vs. measured departure SPL(A) time-history: ground mics with lateral offset to flight ground track, 1	118
A.16	Predicted vs. measured departure SPL(A) time-history: ground mics with lateral offset to flight ground track, 2	119
A.17	Predicted vs. measured approach SPL(A) time-history: ground mics along flight ground track	120
A.18	Predicted vs. measured approach SPL(A) time-history: ground mics with lateral offset to flight ground track, 1	121
A.19	Predicted vs. measured approach SPL(A) time-history: ground mics with lateral offset to flight ground track, 2	122
A.20	Parchim Campaign: Departure procedures, predicted vs. measured SEL ("o" indicates corrupted measurements)	123
A.21	Parchim Campaign: Approach procedures, predicted vs. measured SEL ("o" indicates corrupted measurements)	124
A.22	<i>v-r</i> vehicle layout: parameter variation 1	125
A.23	<i>v-r</i> aircraft noise induced awakenings: parameter variation	126
A.24	Performance indicators: <i>v-r</i> variants	126

A.25 <i>v-0</i> vehicle layout: parameter variation 1	127
A.26 <i>v-0</i> vehicle layout: parameter variation 2	128
A.27 <i>v-0</i> aircraft noise induced awakenings	129
A.28 <i>v-0</i> performance indicators: parameter variation	129
A.29 <i>v-1</i> vehicle layout: parameter variation 1	130
A.30 <i>v-1</i> vehicle layout: parameter variation 2	131
A.31 <i>v-1</i> aircraft noise induced awakenings	132
A.32 <i>v-1</i> performance indicators: parameter variation 1 & 2	132
A.33 <i>v-1-1</i> vehicle layout: parameter variation 1	133
A.34 <i>v-1-1</i> vehicle layout: parameter variation 2	134
A.35 <i>v-1-1</i> aircraft noise induced awakenings	135
A.36 <i>v-1-1</i> performance indicators: parameter variation 1 & 2	135
A.37 <i>v-1-2</i> vehicle layout: parameter variation 1	136
A.38 <i>v-1-2</i> vehicle layout: parameter variation 2	137
A.39 <i>v-1-2</i> aircraft noise induced awakenings	138
A.40 <i>v-1-1</i> and <i>v-1-2</i> performance indicators: parameter variation 1 & 2	138
A.41 <i>v-2</i> vehicle layout: parameter variation 1	139
A.42 <i>v-2</i> vehicle layout: parameter variation 2	140
A.43 <i>v-2</i> aircraft noise induced awakenings	141
A.44 <i>v-2</i> performance indicators: parameter variation 1 & 2	141
A.45 <i>v-x</i> vehicle layout: parameter variation	142
A.46 <i>v-x</i> aircraft noise induced awakenings: parameter variation	143
A.47 <i>v-x</i> performance indicators: parameter variation	143
A.48 <i>V-Rx</i> : Vehicle layout	145
A.49 <i>V-Rx</i> : Approach noise emission directivities	146
A.50 <i>V-Rx</i> : Take-off noise emission directivities	146
A.51 <i>V-0</i> : Vehicle layout	147
A.52 <i>V-0</i> : Approach noise emission directivities	148
A.53 <i>V-0</i> : Take-off noise emission directivities	148
A.54 <i>V-1</i> : Vehicle layout	149
A.55 <i>V-1</i> : Approach noise emission directivities	150
A.56 <i>V-1</i> : Take-off noise emission directivities	150
A.57 <i>V-2</i> : Vehicle layout	151
A.58 <i>V-2</i> : Approach noise emission directivities	152
A.59 <i>V-2</i> : Take-off noise emission directivities	152
A.60 <i>V-X</i> : Vehicle layout	153
A.61 <i>V-X</i> : Approach noise emission directivities	154
A.62 <i>V-X</i> : Take-off noise emission directivities	154

A.63 Max. SPL(A) along departure flight ground track	155
A.64 Scenario dependent vehicle ranking: STOL scenario (60% weighting of field length req.)	155

List of Tables

4.1	Reference Aircraft A319-100: PrADO (P) weight predictions vs. manufacturer data (M) [101]	49
5.1	Reference vehicle performance parameters	72
6.1	Environmental and economical vehicle performance	93
A.1	Horizontal, non-accelerated flight segments	108
A.2	Top Level Aircraft Requirements	111
A.3	<i>V-r</i> global aircraft parameters	111
A.4	<i>V-r</i> engine data	111
A.5	<i>V-r</i> lift and control surfaces	111
A.6	<i>V-r</i> vehicle performance	111
A.7	Parchim Flyover Campaign: Test Flights (standard procedures), according to Ref. [100]	114
A.8	<i>v-r</i> variants: parameter variation 1 (wing area & aspect ratio)	125
A.9	<i>v-r</i> global aircraft parameters: parameter variation 1	125
A.10	<i>v-0</i> variants: parameter variation 1 (wing area & aspect ratio)	127
A.11	<i>v-0</i> global aircraft parameters: parameter variation 1	127
A.12	<i>v-0</i> variants: parameter variation 2 (wing location & aspect ratio)	128
A.13	<i>v-0</i> global aircraft parameters: parameter variation 2	128
A.14	<i>v-1</i> variants: parameter variation 1 (wing area & aspect ratio)	130
A.15	<i>v-1</i> global aircraft parameters: parameter variation 1	130
A.16	<i>v-1</i> variants: parameter variation 2 (wing location & aspect ratio)	131
A.17	<i>v-1</i> global aircraft parameters: parameter variation 2	131
A.18	<i>v-1-1</i> variants: parameter variation 1 (VTP positioning & wing area)	133
A.19	<i>v-1-1</i> global aircraft parameters: parameter variation 1	133
A.20	<i>v-1-1</i> variants: parameter variation 2 (wing area & VTP positioning)	134
A.21	<i>v-1-1</i> global aircraft parameters: parameter variation 2	134
A.22	<i>v-1-2</i> variants: parameter variation 1 (HTP sweep angle & VTP area ratios)	136
A.23	<i>v-1-2</i> global aircraft parameters: parameter variation 1	136
A.24	<i>v-1-2</i> variants: parameter variation 2 (HTP sweep angle & area)	137

A.25 <i>v-1-2</i> global aircraft parameters: parameter variation 2	137
A.26 <i>v-2</i> variants: parameter variation 1 (wing area & aspect ratio)	139
A.27 <i>v-2</i> global aircraft parameters: parameter variation 1	139
A.28 <i>v-2</i> variants: parameter variation 2 (wing location & aspect ratio)	140
A.29 <i>v-2</i> global aircraft parameters: parameter variation 2	140
A.30 <i>v-x</i> variants: parameter variation (VTP positioning & wing area)	142
A.31 <i>v-x</i> global aircraft parameters: parameter variation 1	142
A.32 Scenario dependent vehicle variant ranking	144
A.33 <i>V-Rx</i> : Global aircraft parameters	145
A.34 <i>V-Rx</i> : Lift and control surfaces	146
A.35 <i>V-Rx</i> : Vehicle performance	146
A.36 <i>V-0</i> : Global aircraft parameters	147
A.37 <i>V-0</i> : Lift and control surfaces	148
A.38 <i>V-0</i> : Vehicle performance	148
A.39 <i>V-1</i> : Global aircraft parameters	149
A.40 <i>V-1</i> : Lift and control surfaces	150
A.41 <i>V-1</i> : Vehicle performance	150
A.42 <i>V-2</i> : Global aircraft parameters	151
A.43 <i>V-2</i> : Lift and control surfaces	152
A.44 <i>V-2</i> : Vehicle performance	152
A.45 <i>V-X</i> : Global aircraft parameters	153
A.46 <i>V-X</i> : Lift and control surfaces	154
A.47 <i>V-X</i> : Vehicle performance	154
 B.1 Standard output of continuous sound levels L_{eq} with corresponding parameter setting	 158
B.2 Continuous sound levels: Nomenclature	158

Curriculum vitae of Eberhard-Lothar Bertsch

Educational History

Feb 2006	Diplom-Ingenieur Luft- und Raumfahrttechnik , Department of Aerospace Engineering, Universität Stuttgart, Stuttgart
July '05 - Jan '06	Final thesis (towards Diplom): "Numerical investigation of turbine blade film cooling", Institute of Applied Thermodynamics ITLR, Universität Stuttgart, and Rolls Royce, Berlin (Aerodynamics and Cooling Group)
Aug '03 - Dec '04	Master of Science Aerospace Engineering , Department of Aerospace and Ocean Engineering, Virginia Polytechnic Institute and State University, Blacksburg, Virginia, USA
Jan '04 - Dec '04	Student thesis (towards Diplom): "Advanced Boundary Element Approximation And Sound Quality Evaluation", Department of Aerospace and Ocean Engineering, Virginia Tech, and Institute of Aero- and Gasdynamics IAG, Universität Stuttgart
Oct '99 - Sept '01	Vordiplom Luft- und Raumfahrttechnik, Department of Aerospace Engineering, Universität Stuttgart

Working Experience

April '12 - present	Research engineer at DLR's Institute of Aerodynamics and Flow Technology, Göttingen (aircraft system noise prediction) <ul style="list-style-type: none">• Initiator of an international workgroup on aircraft noise simulation; ANSWeR (2012)
April '06 - April '12	Research engineer at DLR's Institute of Aerodynamics and Flow Technology, Braunschweig (conceptual aircraft design and aircraft system noise prediction) <ul style="list-style-type: none">• Initiator and organisator of an international workshop on active high-lift technology (2011)• Initiator of and principal investigator for a dedicated fly-over noise campaign with DLR's flying testbed ATTAS (2009)• Work package leader and substitute project manager for DLR project QSTOL (2006-2010)• Scientific publications & presentations on national and international conferences, reviewer for the AIAA Journal of Aircraft

ISSN 1434-8454

ISRN DLR-FB-2013-20